Impulse Loading of 3D Prismatic Cellular Structures

A Dissertation

Presented to

the faculty of the School of Engineering and Applied Science

University of Virginia

---

in partial fulfillment

of the requirements for the degree of

Doctor of Philosophy

Materials Science and Engineering

Ryan L. Holloman

May 2014

APPROVAL SHEET

The dissertation is submitted in partial fulfillment of the

requirement for the degree of

Doctor of Philosophy

Ryan Holloman

Ryan L. Holloman, Author

This dissertation has been read and approved by the examining committee:

Haydn Wadley

Haydn N.G. Wadley, Advisor

James Fitz-Gerald

James M. Fitz-Gerald, Committee Chair

Sean Agnew

Sean R. Agnew

Hilary Bart-Smith

Hilary Bart-Smith

Arve Hanssen

Arve G. Hanssen

Accepted for the School of Engineering and Applied Science:

James H. Aylor, Dean
School of Engineering and Applied Science
May 2014

Abstract

A novel light metal cellular structure has been designed and fabricated from assemblies of square cross section tubes oriented in a cross-ply 2D and orthogonal 3D arrangements tailored to support different combinations of through thickness and in-plane loads. A simple dip brazing approach is used to fabricate these structures from extruded 6061-T6 aluminum alloy tubes. By varying the tube wall thickness, the resulting 3D cellular structures had relative densities between 11 and 43%. Using a combination of experimental testing and finite element simulation of the through thickness compression, it was found that the 3D orthogonal structures have an approximately linear dependence of modulus upon relative density. However their strength had a power law dependence upon density with an exponent of approximately 5/3. These cellular structures exhibit almost ideal plastic energy absorption at pressures that could be selected by adjustment of the vertical and in-plane tube wall thicknesses.

The dynamic compressive response of the 3D cellular structure, and the 2D $[0^o/90^o]_2$ array and out-of-plane tubes from which they were constructed, have also been

investigated using a combination of instrumented Hopkinson bar impact experiments, high speed video imaging and finite element analysis. It was found that the collapse strength was independent of compression rate for compression strain rates up to 2000 s^{-1}, despite a transition to higher order buckling modes at high strain rates. The study identifies a synergistic interaction between the co-linear aligned and out-of-plane tubes, observed during quasi-static loading, extends into the dynamic regime. Finite element simulations, using a rate dependent, piecewise linear strain hardening model with a von Mises yield surface and an equivalent plastic strain failure criterion, successfully predicted the compressive stress- displacement relations and the buckling response of the structures, and confirmed the absence of strain rate hardening in the 3D cellular structure. The simulations also reveal that the ratio of impact to back face stress increased with compression strain rate and with sample relative density; a result with potentially significant implications for shock load mitigation applications of these structures.

To investigate a shock loading application of the structure, a vertical pendulum apparatus has been developed and used to experimentally investigate the structures utility for impulse mitigation during explosive loading by wet sand. The test facility was used to measure the impulse and pressure applied by the impact of synthetic wet sand with an incident velocity of ~300 ms^{-1} to the flat surface of a back supported 3D cellular structure with thick (relatively rigid) and thin impact face sheets and was compared to that transferred by an incompressible solid aluminum test block of similar dimensions. By varying the distance between the sand layer and the impact face of the solid block, the transferred impulse and maximum pressure applied to the samples were both found to decrease with standoff distance. A particle based simulation method has been used to

model the sand impact with the test structure and was able to successfully predict both the impulse and pressure transferred during the tests. The simulated results agreed well with experimental data, and both showed that the impulse transferred to a solid test structure was approximately the same as that of the sand that intercepted the sample front face, consistent with sand stagnation against its planar surface. The results are consistent with no strong sand reflection back towards the source. Experiments and simulations of the 3D cellular structures revealed that 10-15% less impulse was transferred to the cellular structures than was transferred to a solid block of similar dimensions. Analysis of experimentally validated simulations indicated that the decrease in transferred impulse with increasing standoff distance arises because of a small reduction in sand particle velocity (resulting from momentum transfer from sand to air particles) and an increase in lateral spreading of the sand particles as the standoff distance increased. This spreading resulted in a smaller fraction of the sand particles intercepting and impacting the finite area of the reference block impact face.

Simulations of the sand interaction with the cellular structures revealed that a substantial part of the 10-15% impulse reduction for the 3D cellular structure was a result of a subtle interaction of the compressible sample and the aperture opening in the sand box lid within which the sand was accelerated. In solid samples, the sand stagnated against the bottom face of the sample and escaped though a gap between the sample bottom and the top of the sand box lid. This gap varied during the loading event because of elastic compression of the Hopkinson bars to which specimens were attached and flexure of the sand box lid due to sand impact on its underside. This gap remained small for the solid block and for cellular structures loaded to pressures less than their

compressive strength. However, when the cellular structures were loaded above their crush strength, the rapid motion of the front face during core crushing opened the gap and relived the sand pressure applied to the sample front face. This effect was enhanced for thin front face sheet samples by deflection of the front face at the sides of the sample. This created a convex shaped sand impact surface and the subsequent sand particle impacts did not fully transfer their vertical momentum to the structure. To further investigate the sand structure interaction additional simulations were conducted with the (now well validated) simulation code in which the top lid of the sandbox was removed and the impact face sheet made rigid. As the core strength was reduced (by reducing the yield strength of the material used to make the core) the plastic collapse of the core was shown to lead to a ~5% reduction in transferred impulse compared to a solid (incompressible) structure and the loading rate (acceleration) also was significantly reduced. These results support recent calculations of sand particle impact by other groups and confirm that the sand-structure interaction for sand impacts in the ~300 ms^{-1} range is small.

Acknowledgements

I thank my advisor Haydn Wadley for all his support and guidance. Haydn brought a tremendous amount of enthusiasm and a visionary approach to all our research endeavors. He taught me to approach problems on a deeper and more fundamental level than I was comfortable with when this journey started. I am truly grateful to have been associated with such a timely problem and have admired Haydn's ability to tackle big problems and form a tremendous network of collaborators. Being part of an international collaboration so early in my career was extremely valuable for my growth.

I would also like to acknowledge my committee members, Sean Agnew, Hilary Bart-Smith, James Fitz-Gerald, and Arve Hanssen, for their advisement and review of all my work.

Arve Hansson and Lars Olovsson, I am truly grateful for our many conversations. It was very exciting to be part of IMPETUS Afea and to watch it develop and flourish. Arve, my trip to Flekkefjord, Norway will always be a highlight of my graduate school years. Thanks to you and your family for being such gracious hosts.

I wish to thank Vikram Deshpande and Karthik Kandan of Cambridge University for allowing me to conduct experiments with their gas gun and Hopkinson pressure bar facility. I am indebted to Vikram for reviewing all my publications and providing brilliant insight into my work.

I am extremely grateful to Keith Williams for opening up his test range (and home) in South Carolina. None of this work would be possible without you and your crew. Many good memories were had during our countless test days in the South Carolina heat.

I would also like to thank my fellow lab mates and IMP staff members: Kumar Dharmasena, Tommy Eanes, Tochukwu George, David Glover, Rich Gregory, Toni Kember, Adam Malcom, Mark O'Masta, Sherri Sullivan, and J.J. Wetzel. To the staff members, I appreciate all the help that was provided in every aspect of my graduate work. To my lab mates, thank you for all the camaraderie each of you provided.

Thank you to Amber Aiken and Thad Lewis for all their support while juggling work and school obligations. They both went above and beyond all expectations and I could not have done it without their unwavering support.

Thank you to my family for being so patient and supportive during this long and demanding venture. I am grateful to my parents for instilling in me a strong work ethic and the ability to persevere, which were both valuable during grad school. Thank you for supporting me from my earliest academic endeavors and always reminding me that there is "Justification for Higher Education."

To my wife Katie, thank you for all your love, support, and sacrifice. This work brought us together, and for that it was a blessing. However, it also kept us apart for far too long, and I truly appreciate your continual patience. Thank you for always believing in me and providing me with encouragement on my toughest days. I love you and can't wait to begin our next journey in life together.

Table of Contents

List of Figures

List of Tables

List of Symbols

A	Initial yield strength (Johnson-Cook Parameter)
A_B	Cylindrical cross section of Hopkinson bar
A_0	Initial cross section of tensile coupon
A_{Sample}	Sample area loaded by sand
B	Hardening parameter (Johnson-Cook)
c	Extensional wave speed of the aluminum Hopkinson bar
C	Strain rate hardening parameter (Johnson-Cook Parameter)
C_0	Coefficient for square tubes
D	Damage parameter
E	Young's modulus
E_{cell}	Modulus of cellular structure
E_m	Energy absorbed per unit mass
E'_m	Theoretical energy absorbed per unit mass

E_s	Modulus of the solid
E_v	Energy absorbed per volume
$f\left(\epsilon_{eff}^{P}\right)$	A piecewise linear function of the effective deviatoric strain
F	Force
F_{Total}	Sum of Hopkinson bar forces
g	Acceleration due to gravity
$h(t)$	Height pendulum traveled with time
GF	Gauge factor
l	Outer tube width
L_1	Initial gauge length
L_2	Extended gauge length
m	Thermal softening parameter (Johnson-Cook Parameter)
m_i	Mass of i-th particle
m_p	Mass of pendulum
n	Hardening parameter (Johnson-Cook)
P_h	Hydrodynamic pressure
t	Tube wall thickness
t_{end}	The end time for loading during simulation
t_h	Co-linear tube wall thickness
t_v	Out-of-plane tube wall thickness
T_0	Ambient temperature (Johnson-Cook Parameter)

T_m	Melting temperature (Johnson-Cook Parameter)
v_i	Velocity of i-th particle
v_0	Initial impact velocity of projectile
$v(t)$	Out-of-plane velocity time function used during quasi-static simulations
V_o	Output voltage
V_i	Input voltage
w	Crushing displacement used during simulations
W_c	Critical damage parameter
x, y	Length and height of out-of-plane tube notch
ε	Engineering strain
ε_D	Densification strain
ε_e	Elastic component of strain
ϵ_{eff}	Equivalent plastic strain (Johnson-Cook)
ε_L	Logarithmic strain
ε_0	Strain rate parameter (Johnson-Cook)
ε_p	Plastic component of strain
v	Poisson ratio
$\bar{\rho}$	Relative Density
ρ_s	Density of a solid material
σ_{02}	Nominal stress at 0.2% offset strain

σ_c	Cauchy stress
σ_{cell}	Peak strength of the cellular structure
σ_p	Peak stress
σ_s	Peak strength of the solid
σ_u	Ultimate tensile stress
σ_y	Yield stress

Chapter 1. Introduction

1.1. Background

Engineering structures are susceptible to failure during impulsive loading events in modes that are sometimes difficult to understand because both the stresses that activate deformation and the rate dependent failure modes are hard to predict [1]. The impact of a vehicle with a rigid object [2, 3], or a ship hull by water propagated shock fronts from underwater explosions [4, 5] or just the dropping of a delicate instrument [6] can all cause great damage to a structure, and has led to numerous efforts to create impulsive load mitigation concepts. One approach is to convert the kinetic energy of the impact to (stored) potential energy by plastic deformation of the structure [7]. However, it is also important to simultaneously control the forces applied during this momentum transfer and energy conversion process. This has generated interest in compressible cellular

structures as a replacement for solid load supporting structures since the energy conversion with these materials can be very high and the transmitted pressure, and in some special cases, even the momentum per unit area (impulse) can be controlled by the compressible cellular materials mechanical properties and density [6].

1.2. Cellular Metal Structures

Typically, porosity is avoided in bulk materials because it results in degradation of structural properties; however, nature has shown that structures such as bone [8], coral [9], and wood [10] exploit cellular structures with high pore volume fractions and are efficient at supporting bending loads, especially when higher density (less porous) material is located on the surfaces of the structures far from the neutral axis [11]. These naturally occurring sandwich structures provide the inspiration for synthetic cellular sandwich structures that minimize weight while maximizing bending resistance and strength. The remarkable properties of these naturally occurring structures has led to the rapidly growing area of metallic sandwich structures [12]. The cellular cores of metallic sandwich structures can be divided into two categories: stochastic foams [13] or periodic (lattice) cellular materials [14].

1.2.1. Stochastic Metal Foams

Gibson and Ashby [15] provided the first comprehensive analysis of the deformation mechanisms of metal foams. Their work established scaling relations for the mechanical properties of foams that are dependent on the relative density, $\bar{\rho}$, defined as the ratio of the density of the cellular structure to that of the material from which it is made. Open cell foams are bending-dominated structures, and their resulting stiffness scales with $\bar{\rho}^2$ (and linearly with the solid materials stiffness) while their strength scales with $\bar{\rho}^{3/2}$ (and again linearly with the strength of the solid from which it is made). Closed cell foams can theoretically exhibit a stiffness and strength that scales linearly with relative density, as a result of membrane-stretching that occurs within the cell faces [15]. However, the fabrication methods used to make metal foams often result in random cell architectures and the cell wall curvatures contain many defects. These induce premature cell wall-bending under compression loading, which degrades the compressive stiffness and strength of the structures. Due to their inherent bending-dominated deformation, the structure is often outperformed by other core topologies that are stretch dominated. Also, their use in structural applications is severely limited by the low elastic moduli and weak indention strengths of the low relative density cores that optimize bending resistance at minimum mass per unit area [13].

1.2.2. Periodic Topologies

Unlike the stochastic cellular metals, the deformation of many periodic cores is stretch-dominated; the cell structure predominantly experiences axial stresses (tension and compression) as opposed to bending [16]. This results in the out-of-plane stiffness and strength of various stretch dominated topologies scaling linearly with relative density [17], until the onset of strut or web buckling at very low relative density.

Closed cell honeycomb structures [18,19] display exceptional transverse shear stiffness and are considered the standard for lightweight sandwich cores. They have a higher bending stiffness than equivalent mass per unit area monolithic (solid) plates and have been used extensively for aerospace applications. The most common honeycomb has a hexagonal geometry, Figure 1.1. However, honeycombs with square and even triangular topologies have also attracted interest because of their superior in-plane bi-axial stretch resistance, and reduced susceptibility to buckling (because of their smaller web height to width ratios) at equivalent relative density. The mechanical properties of honeycomb structures have been investigated for many decades. Gibson et al.[20] were the first to propose models to predict the in-plane and out-of-plane properties of hexagonal honeycomb structures. They showed that while the out-of-plane strengths are high, in-plane deformation of hexagonal honeycombs occur by bending at plastic hinges at the nodes which results in negligible in-plane strength. However, they can be oriented in ways to improve the in-plane strength, which has made them favorable for high intensity loading scenarios [21]. Although the structures are standards in load bearing

sandwich structures, they offer limited multifunctionality because of their closed cells and the difficulty form curved shapes with them. The closed cells also trap moisture and this leads to corrosion and de-bonding of the faces and cores.

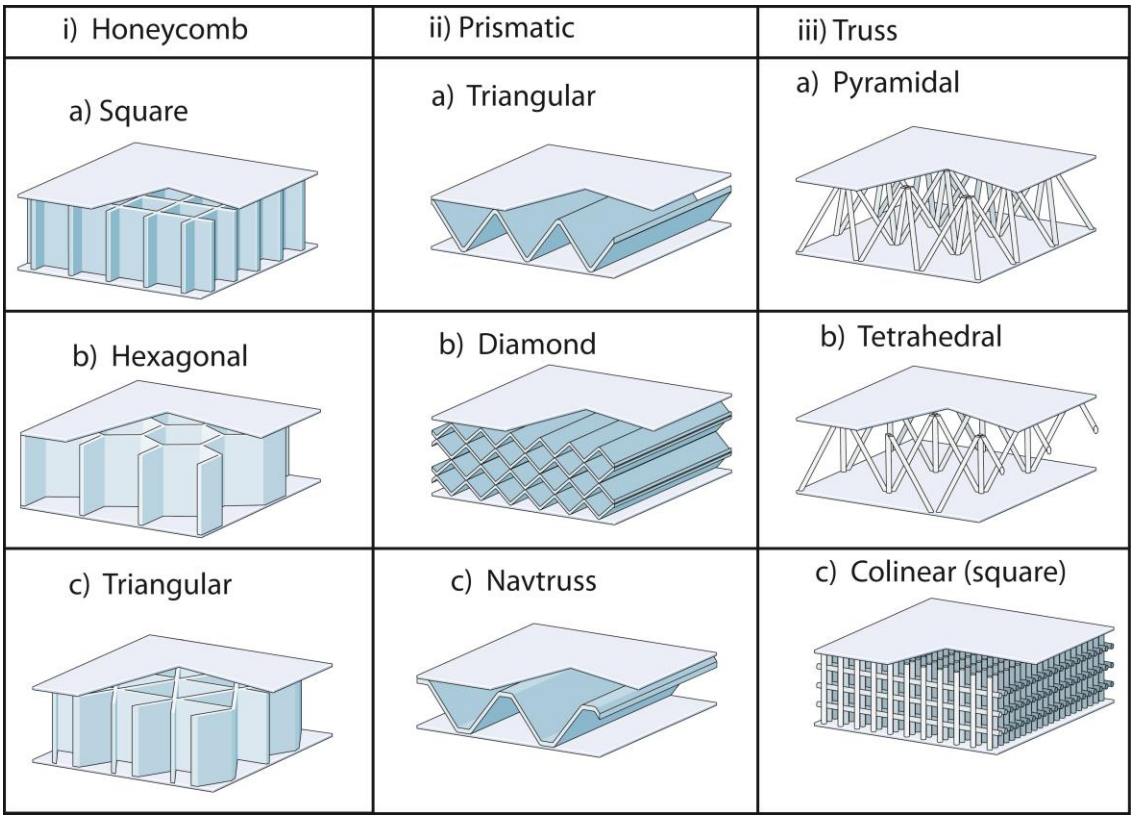

Figure 1.1 Schematic illustration of periodic cellular core topologies.

Prismatic cellular structures [22] have open cells that run the length of a sandwich panels. These structures can have a wide variety of cross sectional shapes and are easily manufactured, since a sheet bending process can used. Of the cores displayed in Figure 1.1(ii), the triangular prismatic core topology is superior for structural

applications since it enables the webs of the core cells to be in tension or compression with no bending during loading. The diamond and Navtruss prismatic cores behave similarly. Prismatic cores can be layered with an in-plane rotation relative to one another to vary the anisotropy. They are also considered to have intermediate crush and stretch performance, and have been studied for high intensity loading by Deshpande and Fleck [23]. McShane et al. [24] provided numerical and analytical evidence that suggests prismatic cores are good candidates for blast resistant sandwich structures in water. Also, unlike honeycomb structures, their open channels with high surface area make them attractive candidates for heat dissipation and would limit corrosion.

Three-dimensional truss structures have completely open cores, Figure 1.1(iii), which make them the most attractive multifunctional candidates [25]. However, they are more challenging to fabricate. Sypeck and Wadley [26, 27] have developed a textile-based method using transient liquid phase bonding to join metallic nickel wires. Pyramidal and tetrahedral lattice structures are amenable to fabrication of (multiply) curved sandwich panels. However ultimately the higher fabrication costs, and low in-plane stretch resistance limit the use of these structures for high intensity loading applications.

Many of the cellular core topologies identified above have been investigated for dynamic loading applications including honeycombs with in-plane stretch resistant square [28] or triangular [29, 30] cells, as well as more compressible prismatic topologies

based upon corrugations (with stretch resistance in only one direction) [31]. Concepts such as flex honeycomb [19] or lattice truss cores [32] have been proposed for curved sandwich panels, but these cores are significantly less stretch resistant.

1.3. Crash Box (Square Tube) Approach

The sandwich panel approach is not widely used to mitigate automobile impacts. Instead this community has focused upon crash box (tube) designs that absorb the kinetic energy during frontal vehicle impact [33, 34], and control force transmission to levels that remain below the injury threshold for vehicle occupants. An ideal crash box design provides close to theoretical plastic energy absorption at predictable (constant) force through progressive buckling and plastic deformation of the box/tube structure, Figure 1.2. However, the crush response of tubes is highly impact orientation dependent [35, 36]. More isotropic aluminum foams [37], and foam filled tubes [38, 39, 40] have therefore received attention for these structural impact problems. These foam-based structures are highly compressible, and can undergo compression at nearly constant (plateau) stress to plastic strains of 60% or more, making them efficient impact energy absorbers. However, they possess little (or none) of the in-plane stretch resistance that is utilized in sandwich panel - based mitigation approaches.

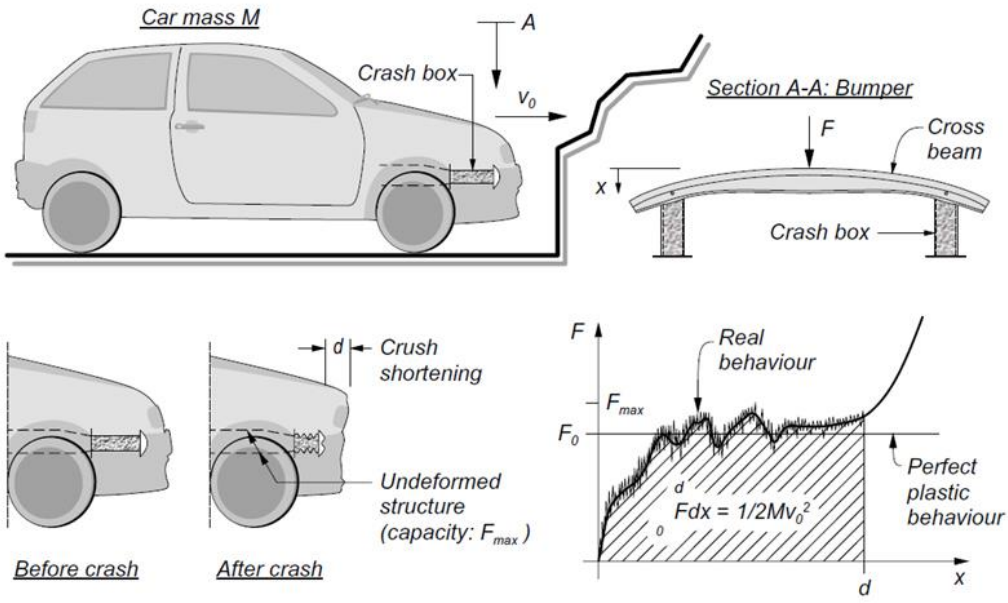

Figure 1.2 A crash box being used to absorb the kinetic energy of a frontal vehicle impact and an idealized plastic energy absorption curve for the crash box.[33]

1.3.1. Loading Rate Effects

The compressive stress versus strain response of cellular structures is frequently found to depend upon the rate of straining [41, 42]. This can arise from material strain rate hardening [12], changes in the deformation modes of the cells [15] and from inertial effects [43]. To design a structure whose energy absorption and stress transfer are insensitive to the rate or direction of compression, it is necessary to understand the significance of each of these factors to the overall response.

1.4. Fluid-Structure Interactions

The pressure applied to the surface of an elastic half-space by the reflection of acoustic (low amplitude) pulses propagated through water or air is twice that of the incident disturbance because the reflected and incident amplitudes are equal and in-phase at the surface [44]. For a perfect reflection, conservation of momentum dictates the impulse (momentum per unit area) transferred to the half-space is also twice that of the incident pulse. Analogous amplifications of impulse and pressure accompany the reflection of high intensity shock fronts with engineering structures, causing sometimes large permanent deformations and fracture. In this case, the nonlinear behavior of the fluid in which the high intensity shock is propagated can lead to even higher reflection coefficients, especially in air [45], but even in water when the structure is close to the source of the disturbance. As a result, the investigation of materials and structures with improved resistance to impulsive loads applied by the impingement of shocks propagated through air [46, 47, 48, 49] and in water [21, 45, 47, 50] has attracted considerable interest.

Foundational work by G. I. Taylor [51] during World War II showed that the shock reflection from a thin, air-backed movable plate was substantially reduced for water propagated pulses because plate motion (away from the impinging shock) resulted in the development of a tensile reflected pulse, which cannot be supported in shallow water, leading to its cavitation. This fluid structure interaction (FSI) at the surface of low

inertia plates substantially reduces the pressure and impulse applied to a light (thin) movable plate. Several studies have subsequently confirmed this prediction [45, 52], and led to an interest in the use of sandwich panels with thin faces supported by a compliant core to mitigate shock loads [53, 54, 55], Figure 1.3. Controlled experiments conducted in the laboratory with air [56] and water shock tubes [57, 58] have enabled the conditions needed to induce strong FSI effects to be experimentally studied. Other studies with explosive charges have been used to impulsively load instrumented targets to record the transmitted pressure and impulse [5, 28]. Numerous analytic and numerical simulation studies have also explored cavitation at the fluid-structure interface, and investigated structural designs that exploit the underwater FSI phenomenon [52, 59, 60, 61]. Analogous studies have also investigated structures that mitigate the effects of air shock loading where the beneficial FSI with thin plates is more difficult to exploit [30, 62, 63].

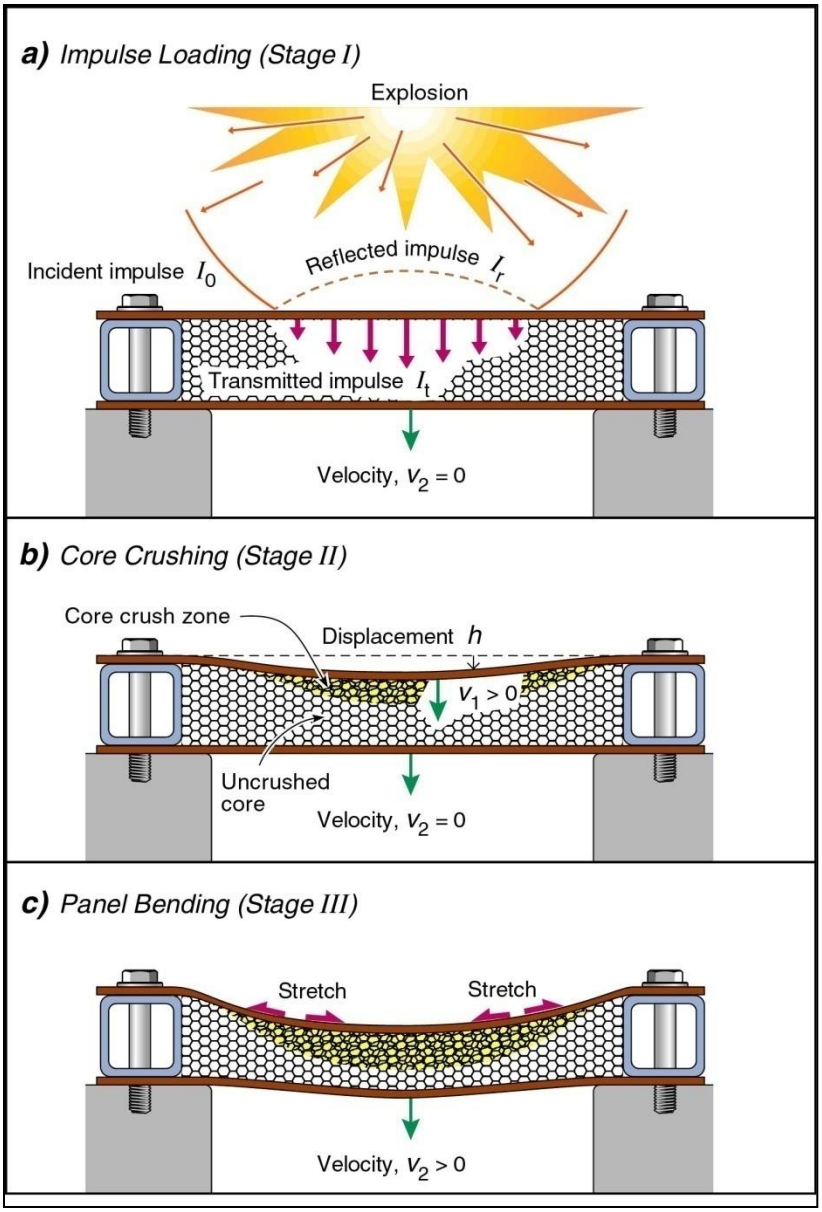

Figure 1.3 Response of a sandwich beam to impulsive loading. (a) Impulse loading (stage I); (b) core crushing (stage II); (c) panel bending (stage III).

While the response of structures to nearby air and underwater explosions is now quite well understood, the design of structures to resist the impulsive loads resulting from shallow buried explosions in soil is much less well developed. This is partly a

consequence of the difficulty of conducting controlled experiments where the loading of a structure can be understood [48, 64, 65]. It is also compounded by the complexity of the analytical and numerical analysis required to understand the mechanisms by which the detonation of a buried explosive accelerates soil, and the loads this subsequently applies to a nearby structure [66, 67]. Together, they have delayed a comprehensive characterization of the soil- structure interaction, and have hampered the development of mitigation concepts.

Experimental work by Bergeron et al. [68] has provided important basic insight into the phenomena activated during the detonation of a small explosive charge buried at various depths within dry sand. They used high speed photography and pulse X-ray methods to characterize the sand plume, Figure 1.4. These observations led Deshpande et al. [69] to identify three temporal regimes associated with the detonation of a buried explosive. Initially, immediately following detonation, a compressive shock pulse travels through the soil [67, 68, 70]. Once the shock reaches the soil/air interface, the pulse is reflected, and sign converted to a tensile shock within the soil, as a result of the large acoustic impedance difference between soil and air. The tensile pulse then results in spallation of the surface soil. The second regime coincides with expansion of the high pressure gaseous detonation products which push the soil; especially in the direction of least resistance which is normal to the soil surface for a shallow buried explosive. This causes the soil to acquire a velocity and momentum that are complicated functions of the soil density, composition, and the depth of burial, mass, type, shape and manner of detonation of the explosive, and various properties of the foundation upon which the

explosive is supported (soil type, degree of compaction and moisture content). This leads to the third regime of soil propagation; in our case, toward a target where it is arrested or undergoes reflection. If simply arrested at a surface oriented perpendicular to the direction of propagation, the soil would transfer its incident momentum to the structure, but if it were strongly reflected back towards the source, substantial impulse amplification would arise from momentum conservation.

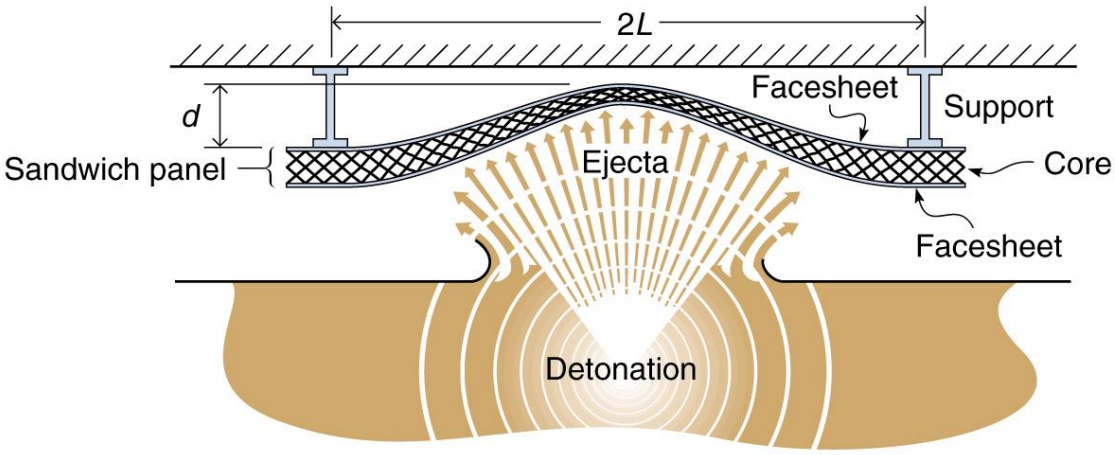

Figure 1.4 Example of a sandwich panel structure whose core undergoes localized compression transverse shear, and membrane stretching during high intensity impulsive loading. The core in this example exhibits modest resistance to in-plane stretching.

A variety of numerical modeling approaches have been used to analyze the velocity and density distributions, and thus momentum distribution, within a soil plume ejected by a buried explosion, and to investigate the ensuing soil - structure interaction during impact with a target [71, 72]. These numerical schemes include coupled

Lagrangian-Eulerian techniques implemented in commercial codes such as LS-DYNA [65, 67] and ANSYS AUTODYN [66], as well as gridless Lagrangian approaches such as Smooth Particle Hydrodynamics (SPH) [73]. The Euler-Lagrange based methods require the use of a soil constitutive model that approximates the response of the soil during its initial compressive shock loading, during spallation, propagation through air, and upon impact with a structure. Either an empirical three-phase model [71]; a modified form of the Drucker-Prager [74] approach, or a porous-material compaction model [75] have been widely used for this with varying levels of success. Deshpande et al [69] recently proposed a micromechanics based approach to better model both wet and dry soil. While this approach held promise for analyzing the shock compaction process densely packed soil (where the particle-particle contacts were semi-permanent), implementations within LS-DYNA failed to properly analyze the ejection of low density sand from the surface. Furthermore, this model, like all other soil constitutive models, required calibration for each soil type and moisture level combination [76], since each have strong effects upon ejecta momentum. However, such calibrations also compensate for other effects such as non-modeled physics, inaccuracies of the numerical implementation scheme or the many other, often uncontrolled factors (such as the soil type below the explosive charge) that influence the characteristics of ejecta from buried tests.

To side-step many of the practical problems with soil impact experiments, Park et al. [77] recently reported a laboratory method for creating cylindrical sand slugs whose axial velocity (in the 50-100 ms^{-1} range) could be well characterized by high speed video

techniques. They used a piston to push water saturated, moist, or dry sand columns through cylindrical tubes, which resulted in the ejection of sand slugs with an axial velocity gradient, Figure 1.5. By impacting sand slugs with axial velocities up to ~100 ms^{-1} against an instrumented Hopkinson pressure bar, they measured the pressure exerted by the sand, showing it to be well approximated by the sand stagnation pressure, ρv^2 where ρ is the instantaneous incident sand density and v its axial velocity just prior to impact with the flat end of the bar. They also discovered that the impulse transmitted to the bar was almost identical to that of the incident sand, consistent with a weak reflection of sand from the bar surface. These experiments then provided a data set that could be used to evaluate numerical simulation schemes.

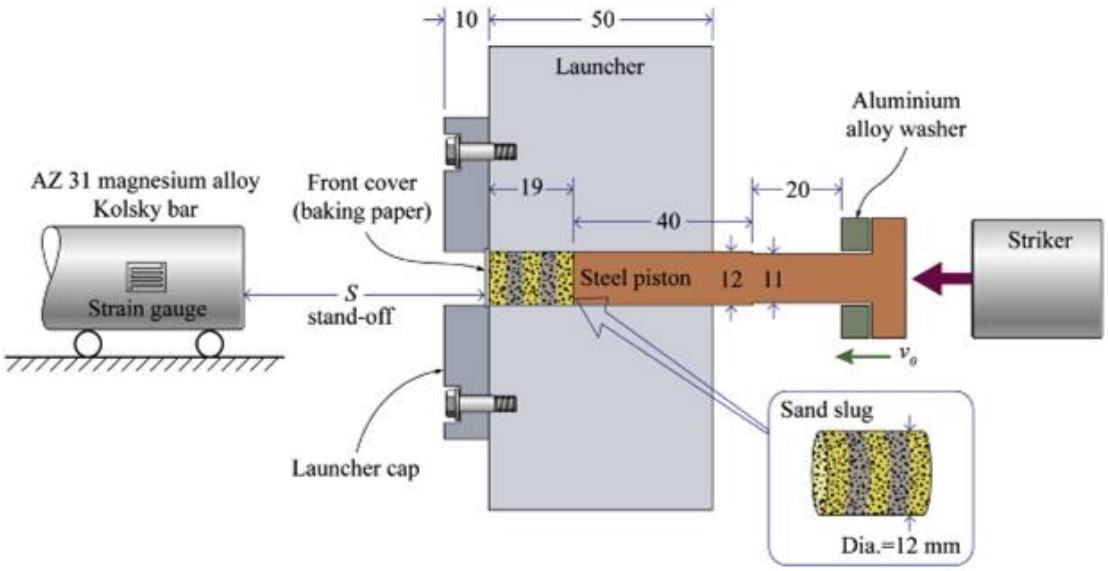

Figure 1.5 The apparatus used to launch a sand slug. An instrumented direct impact Kolsky bar (or Hopkinson bar) was used to measure the stress imparted by the sand slug. All dimensions are in mm. [77]

Pingle et al. [78] and Liu et al. [79] proposed a discrete particle method to simulate the impact of a sand column aggregate. In this approach a particle contact law defined inter-particle contact forces. The behavior of a sand aggregate during its propagation could then be simulated using a molecular dynamics method, and interfaced with a finite element package to analyze the response of a structure impacted by a sand column. This simulation methodology successfully predicted the experiments of Park [77], and confirmed that the impulse transferred to a rigid, back supported solid plate by a sand slug impacting a rigid plate at zero obliquity was no more than 10% higher than that of the incident impulse, Figure 1.6.

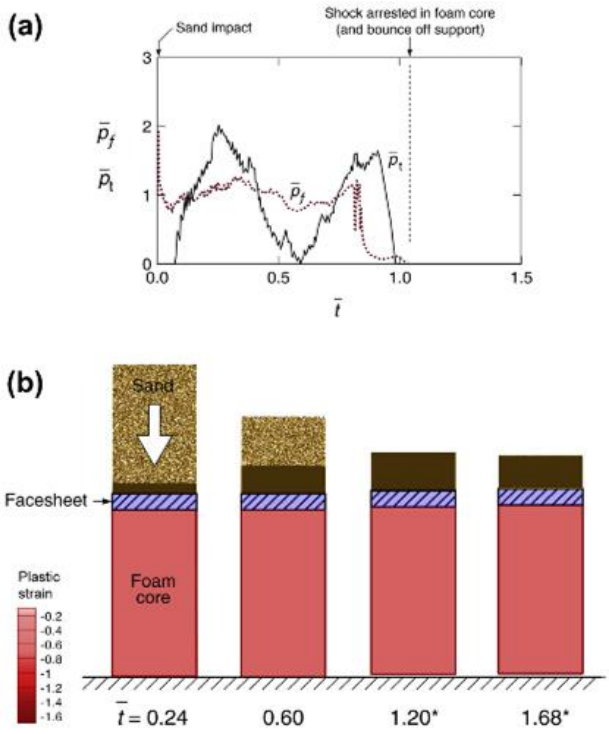

Figure 1.6 Discrete/continuum simulation predictions for the unattached buffer plate. (a) The time evolution of the normalized front, p_f, and transmitted pressures, p_t. (b) Snapshots showing the deformation of the buffer plate and sand slug at selected normalized time.[79]

Recently, an analogous coupled discrete particle-finite element based approach [80], has been combined with particle-based models of explosive events to simulate the interactions between high pressure explosive detonation products, sand, and air particles. This simulation has been interfaced to a robust finite element analysis method incorporating node splitting and element deletion methods to address crack growth, and used to investigate the effect of soil impact upon the deformation and failure of structures. The method is based on a Lagrangian formulation for the structure, but uses the particle based approach for the soil to avoid the errors often associated with arbitrary Lagrangian-Eulerian (ALE) methods and the computational expense of Eulerian approaches [81]. A second advantage is that the corpuscular method allows a simple treatment of the discrete particle interactions with the finite element modeled structure, which is difficult to represent with ALE or Eulerian methods. The method has been implemented commercially as the IMPETUS Afea Solver [82], and experimentally validated with dry and fully water saturated, spherically symmetric synthetic sand shells that were explosively accelerated by spherical charges against edge-clamped metal plates [83].

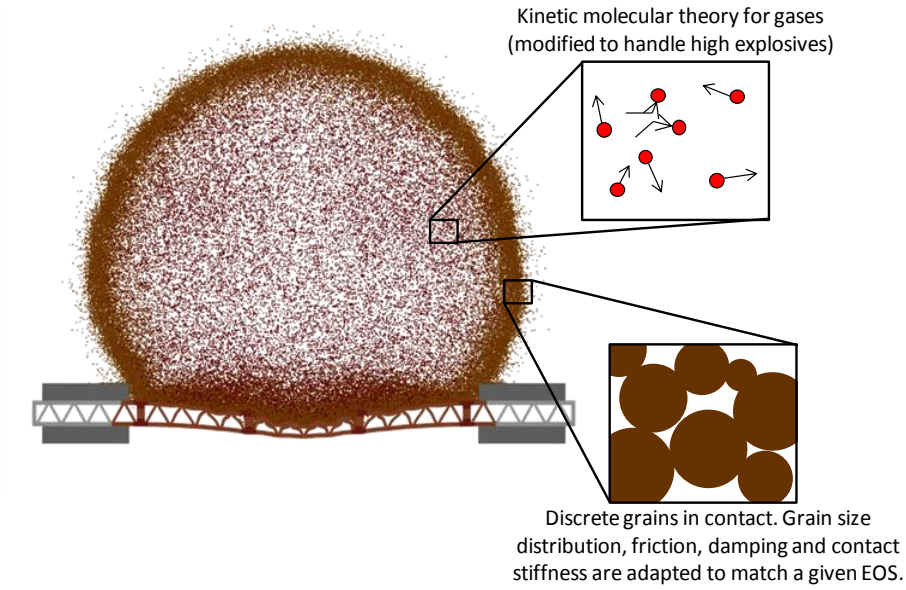

*Figure 1.7 Synopsis of numerical modeling approach.[*83*]*

1.5. Compressible Cellular Structures for Shock Mitigation

Compressible cellular materials are widely used for protecting structures from impulsive loads created by impacts [6, 84]. For example, light, low compressive strength polymeric foams are widely used as part of packaging systems to protect fragile objects during transport, and in protective helmets as a key component of a protection strategy to reduce the risk of traumatic brain injury [85]. In both applications, the stress applied to the protected object is controlled by the compressive strength of the cellular material. When these cellular materials are integrated into structures with strong faces, localized (impact) loads are also spatially and temporally dispersed, further reducing the risk of

damage or injury, Figure 1.8 The emergence of strong metallic cellular structures [13] has led to an interest in the extension of these concepts to the protection of structures from high intensity impulsive loads caused by nearby underwater explosions [61, 86, 87].

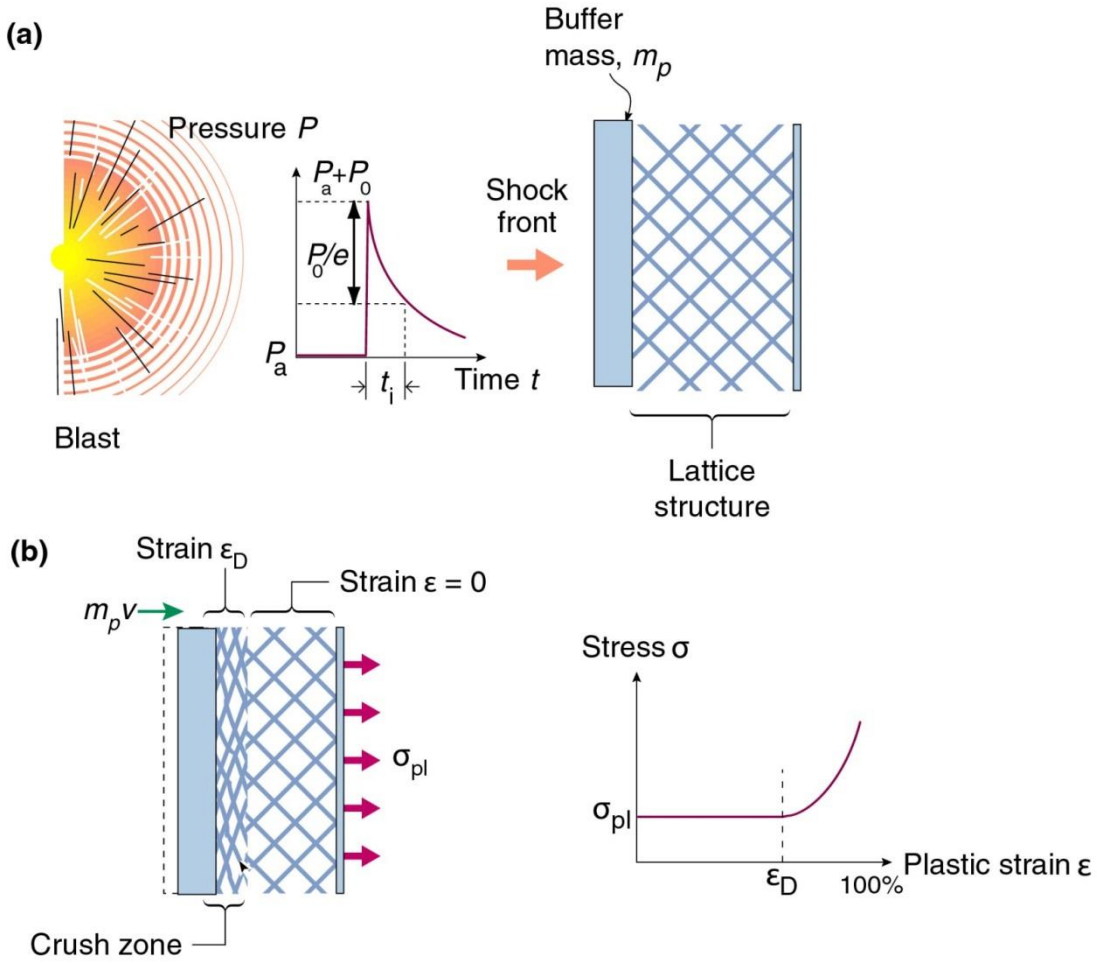

Figure 1.8 A schematic of the passive blast mitigation system. In (a) the detonation creates a shock with a peak overpressure p_0 and a decay time, t_i. The impulse, I_0, impinges onto a buffer, imparting momentum and causing it to accelerate to an initial velocity that varies inversely with its mass per unit area. In (b) the kinetic energy of the buffer is dissipated by the dissipation that occurs upon crushing of the cellular medium. The transmitted stresses are controlled by the flow strength of the cellular medium, which depends upon its topology, relative density and the material from which it is made.[48]

In the underwater loading studies the cellular structures were configured as the cores of sandwich panels with faces made of the same alloy as the core. The impact of one of the face sheets by a water propagated shock resulted in a transfer of momentum to the face sheet, Figure 1.9. The momentum transfer is governed by a fluid structure interaction (FSI) [21, 51, 60]. For rigid structures, the momentum transferred to the structure was twice the incident value, but this could be substantially reduced by decreasing the mass per unit area of the front face sheet and the core compressive strength. The ensuing motion of the impacted face sheet was then arrested by reaction forces arising from core compression and face sheet and core stretching. These forces could be controlled by the core topology, its relative density and the mechanical properties of the material used to fabricate it. The use of light (thin) front face sheets and weak cores whose dynamic crush strength was less than the pressure applied by the shock front enabled significant (up to 50%) reductions in impulse transferred to the protected structure (by reducing the shock reflection coefficient) [88, 89, 90].

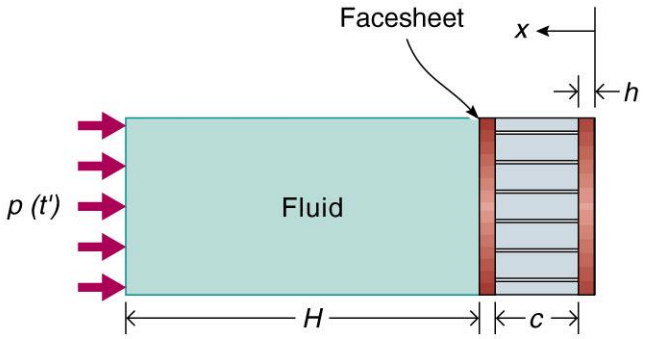

Figure 1.9 A one-dimensional boundary value problem analyzed to investigate the response of the sandwich panels in the "dynocrusher" tests.[92]

Underwater experiments [91, 92] utilizing instrumented Hopkinson pressure (or Kolsky) bars attached to back supported impulsively loaded structures have been used to study pressure (and impulse) transmission during quasi-planar shock front loading of cellular core sandwich structures, Figure 1.10.

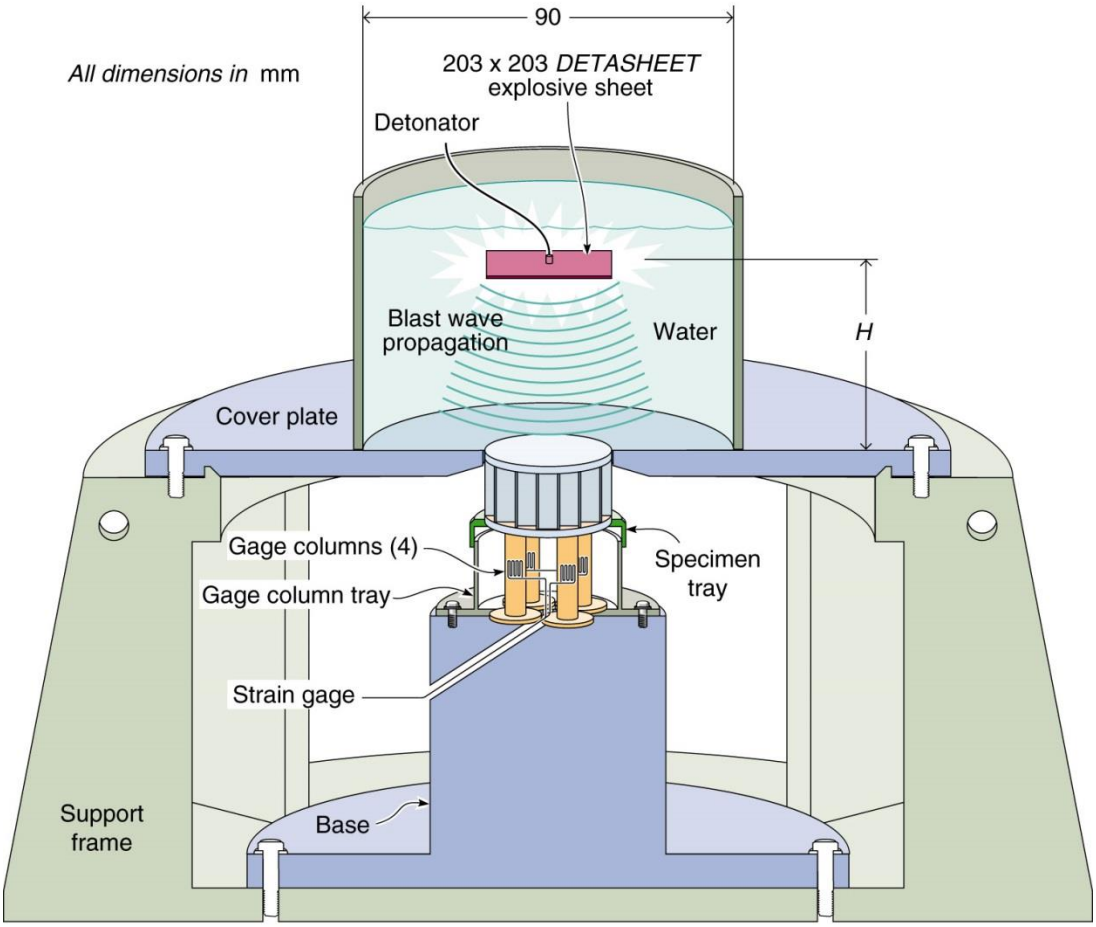

Figure 1.10 A sketch of the apparatus used to measure blast loads transmitted through the sandwich panel.[92]

Many core topologies fabricated from corrosion resistant stainless steels [29, 93, 94] have been investigated for mitigating high intensity underwater impulse loading

including honeycombs [91], corrugated structures [92], and lattices with a pyramidal truss arrangement [5]. All were able to significantly reduce the transferred impulse and pressure in back supported configurations. These studies showed that significant reductions in transmitted pressure (and momentum) could be realized when weak core systems were utilized. They also showed that when the shock pressure was sufficient to completely collapse (densify) the cellular structure, slap of the front face sheet against the densified core caused a rise in pressure and impulse transfer, but this was much less than model predictions.

Efforts to extend the protection concept to edge supported test configurations revealed the important role of the core in supporting panel stretching [51]. Since the pyramidal lattice offers little in-plane stretch resistance, the corrugated and square or triangular honeycomb cores [95] were preferred with corrugations being easier to fabricate. Related studies have also investigated the response of edge clamped sandwich panels to explosive shock loading in air and led to the discovery of significant reductions of back face sheet deflection compared to equivalent monolithic plates [5, 96]. Until recently, relatively little experimental work had investigated momentum transfer by the impact of explosively accelerated soil against sandwich structures with compressible cores [66, 67, 97, 98, 99, 100]. The soil-structure interaction (SSI) has remained relatively un-explored for compressible cellular structures for the same numerical limitations described in Section 1.4.

1.6. Dissertation Goals

This dissertation is motivated by interest in mitigating the impulse loads applied to structures by explosively accelerated soil. The forces created against a structure as the soil is brought to rest can be very large and depend upon the type of soil (especially its density), its velocity and angle of impact with the structure. To simplify the problem investigated here, the dissertation utilizes a synthetic soil made of glass microspheres and develops a novel aluminum alloy cellular structure whose quasi-static and dynamic deformation and failure modes are investigated experimentally and by finite element analysis. This dissertation explored a cellular structure made from a 3D arrangement of square cross section, extruded tubes of a heat treatable 6061 aluminum alloy. The structure contains $[0^o/90^o]_2$ oriented in-plane tubes that provide in-plane stretch resistance, while the through thickness tubes resist compression in analogous fashion to that of a crash box design. The goals of the dissertation are to: *(i)* design and develop a method for fabricating a sandwich structure with a cellular structure core well suited for impact mitigation; *(ii)* characterize the energy absorbing capabilities of the structure; *(iii)* investigate the effects of compression rate upon the cellular structures modes of compression; *(iv)* investigate the pressure and momentum transferred to an incompressible aluminum block and a compressible back-supported cellular structure by an idealized buried explosive event; and *(v)* analyze the results, in conjunction with discrete particle based simulations, to investigate the nature of the soil-structure interaction.

1.7. Dissertation Outline

The dissertation is organized as follows: Chapter 2 presents the fabrication technique used to build the rectilinear cellular sandwich structure and characterizes the age-hardened 6061 aluminum material. Chapter 3 describes the quasi-static compressive response for the sandwich structure measured in the out-of-plane direction. The energy absorbing capabilities of the tube core are also investigated and compared to other ideal energy absorbing structures. Chapter 4 investigates the dynamic out-of-plane compressive response of the sandwich structure. The dynamic crushing resistance and collapse mode mechanisms are explored via direct impact Hopkinson bar experiments that utilized high speed photography. Finite-element analysis was also used to investigate the dynamic deformation modes, and to estimate the stresses at the impact and distal faces of the structure. Chapter 5 experimentally investigates the pressure and momentum transferred to an incompressible back-supported aluminum block by an idealized buried explosive event. The results are then used, in conjunction with discrete particle based simulations to investigate the nature of the soil-structure interaction. Chapter 6 investigates the pressure and momentum transferred to the back-supported cellular sandwich structure by an idealized buried explosive event. The thickness of the samples front face sheet was varied to investigate its effect on the soil-structure interaction. Discrete particle based simulations were used to interpret the experimental findings. Chapter 7 uses the validated particle based model developed in Chapters 5-6 to further analyze in detail the cause for impulse mitigation for a cellular structure when compared to an incompressible solid block. Chapter 8 then discusses the significance of

all these results in the context of the goals of the dissertation, and Chapter 9 summarizes the conclusions of the dissertation.

Chapter 2. Cellular Structure Design, Fabrication and Alloy Characterization

This chapter explores the design and fabrication of bonded square hollow tube cellular structures. Two rectilinear cell topologies with and without tubes oriented in the out-of-plane direction are proposed, and a method for their manufacture from extruded aluminum tubes is presented. The tubes can be assembled in a 2D cross-ply (rectilinear), or 3D orthogonal geometry. The in-plane tubes provide stretch resistance while the through thickness tubes resist out-of-plane compression. The topology affords future multifunctionality [101] such as cross flow heat exchange via the open channels that extend within the structure [102].

2.1. Cell Geometry

Rectalinear cellular tube structures can be assembled from square cross-section tubes to create many topologies two of which are shown in Figure 2.1. The 2D structure,

Figure 2.1(a) can be assembled by simply laying down a co-linear layer of square cross section tubes each spaced a tube width apart. A second similarly spaced layer is then orthogonally placed on the first layer, and the assembly sequence repeated until a desired thickness is achieved. The 3D topology, Figure 2.1(c) can be assembled from the 2D structure by simply inserting additional tubes in the out-of-plane (vertical) void space between the cross-ply oriented tubes. The tubes could be bonded with polymeric adhesives or more robustly by dip or vacuum brazing. Dip brazing was chosen here. To facilitate complete fluid penetration during dip braze bonding of the structure to face sheets, the vertically inserted tubes can be notched as shown, Figure 2.2. In principle, the wall thicknesses of the tubes in each orthogonal direction could be different, enabling tuning of properties in the various directions.

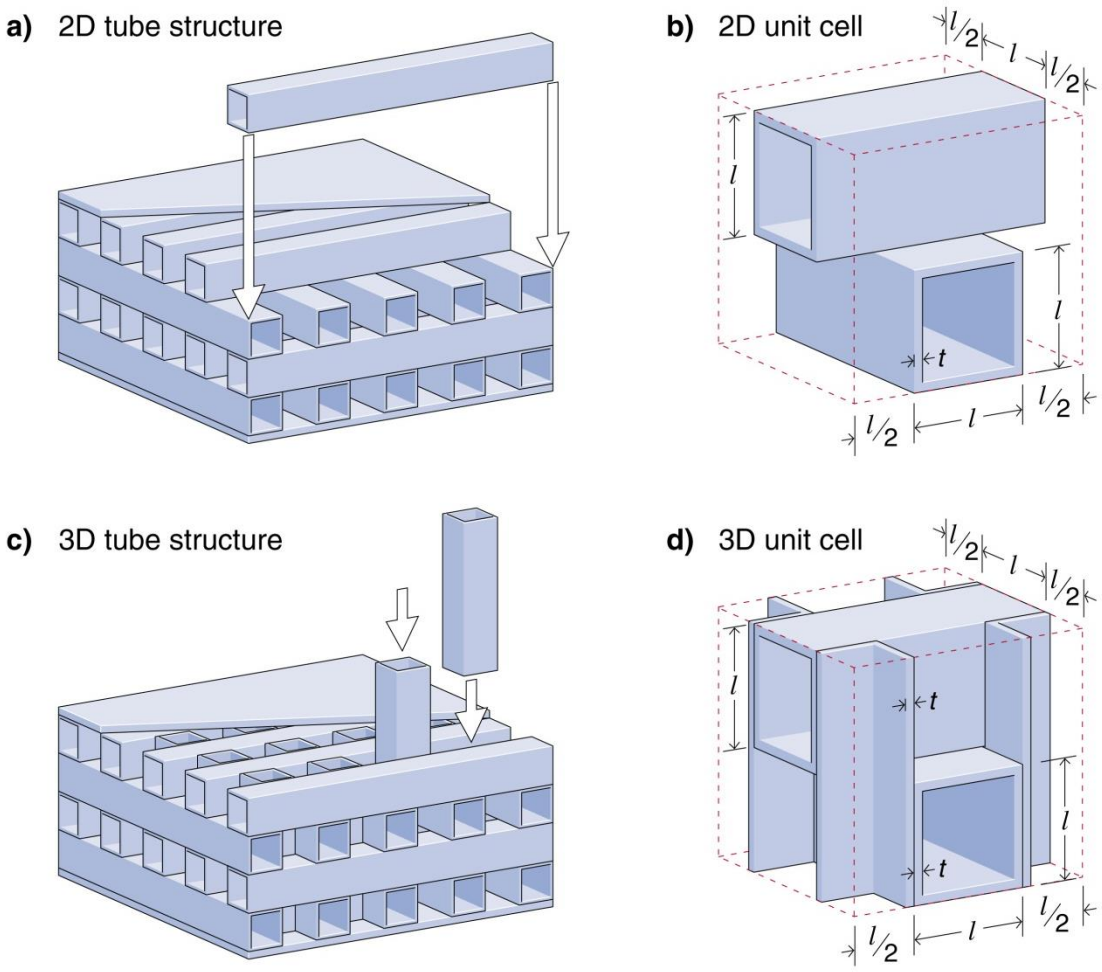

Figure 2.1. Examples of cellular structures fabricated from square extruded tubes. a) 2D structure made by bonding 0/90 layers of co-linear tubes. b) The unit cell of the 2D structure. c) A 3D tube structure where the through thickness gaps in the 0/90 assembly are filled with vertical tubes. d) Unit cell of the 3D tube structure.

The two structures are periodic, and their unit cells are shown in Figure 2.1(b) and (d) and Figure 2.2(b). The relative density, $\bar{\rho}$, of each topology is the fraction of unit cell volume occupied by solid. The relationship between $\bar{\rho}$, the tube wall thickness (t), and outer tube width (l) for the 2D topology can be found by dividing the volume of solid (l^3) by that of the unit ($16lt(l-t)$) and is given by;

$$\bar{\rho} = \frac{2(l-t)t}{l^2} \tag{2.1}$$

The 3D topology assembled from identical tubes in all three directions can be shown to have a relative density given by ;

$$\bar{\rho} = \frac{3(l-t)t}{l^2} \tag{2.2}$$

However, if notched vertical tubes are used, and the rectangular notches are of length *x* and height *y*, the reduced relative density for the 3D assembly is;

$$\bar{\rho} = \frac{2 * t_v^2(y-2l) - t_v\big(2xy + l(y-4l)\big) - 8t_h(t_h-l)l}{4l^3} \tag{2.3}$$

where the in-plane and through thickness oriented tubes can have different wall thicknesses of t_h and t_v, respectively. Figure 2.1 shows that when the cellular tube structures are bonded to face sheets to create sandwich panels, they have a large core to face sheet interfacial area with potentially benefial consequences for the robustness of intensely loaded panels.

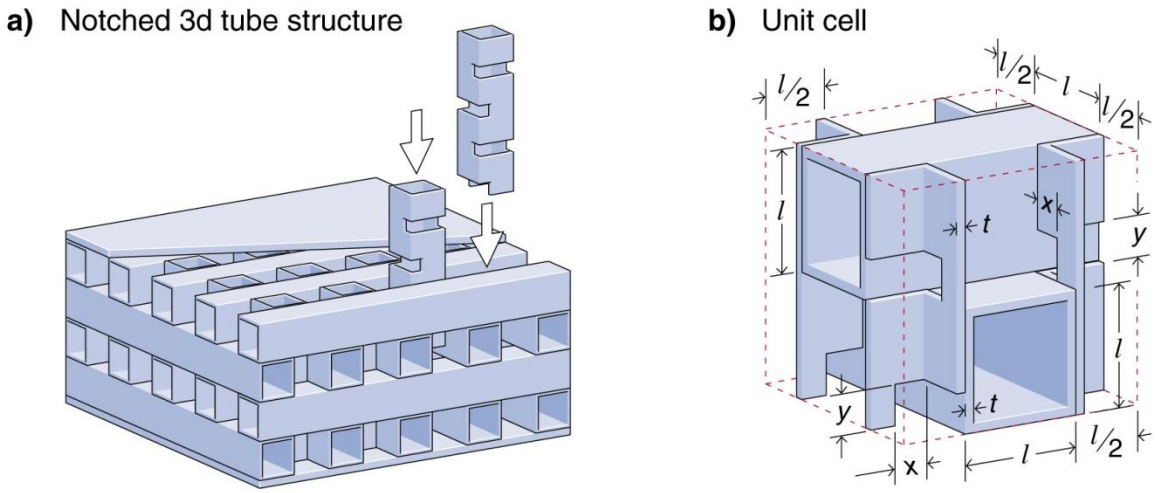

Figure 2.2. A modified 3D structure in which the vertical tubes were notched to allow removal of salts used for dip braze bonding. b) The unit cell of the modified 3D structure with the notch geometry incorporated. For all experiments reported here, x=y=6.35mm.

2.2. Cellular Tube Structure Fabrication

The 3D orthogonal geometry assembled from tubes of the same size, will be shown later to behave well under compressive loading, and so samples were also assembled from tubes of various wall thickness and outer tube widths to investigate the effect of these geometric parameters upon energy absorbtion and collapse mechanisms. A 2D struture was also examined to reveal the effect of using no vertical tubes upon the compressive response. The geometries of all the structures investigated are summarized in Table 2.1. Since there was a variability in the wall thickness of the tubes, the wall thickness of fifty tubes was measured and the mean thickness was calculated and this is reported in the table. The standard deviation in tube wall thickness was also determined and found to be ±0.14 mm for all the tubes. These wall thickness variations were

accounted for by the introduction of imperfections in the FE models that are described later (Chapter 3).

Table 2-1. Tube geometries and predicted relative densities for tube-based cellular structures.

Topology	Average in-plane tube wall thickness (mm)	Average in-plane tube width (mm)	Average out-of-plane tube wall thickness (mm)	Average out-of-plane tube width (mm)	Relative density, $\overline{\rho}$
3D	3.47	19.05	3.47	19.05	42.7
3D	3.27	19.05	1.52	19.05	35.1
3D	1.53	19.05	3.30	19.05	28.6
3D	1.45	19.05	1.45	19.05	20.1
3D	0.74	11.48	0.74	11.48	11.6
3D-Not Notched	1.44	19.05	1.44	19.05	21.0
2D	1.70	19.05	-	-	16.3
1D Array	-	-	1.52	19.05	6.7

Samples of each cell topology were fabricated from square cross-section, 6061-T6 aluminum alloy extrusions using a simple dip brazing process followed by an aging heat treatment. Square cross-sectional extruded 6061-T6 aluminum alloy tubes were obtained from Argyle Industries Inc. (Branchburg, NJ, USA). To facilitate compression testing, a face sheet was attached to opposing sides of the samples to create sandwich panels. The

4.76 mm thick 6061-T6 aluminum alloy face sheet material was supplied by BMG Metals (Richmond, VA, USA).

A schematic illustration of the fabrication process for making the 3D orthogonal topology structure is shown in Figure 2.3. An analogous sequence was used for the 2D topology. All the test structures were dip brazed using a facility and process developed at Coleman Microwave Co. (Edinburg, VA, USA). This process involves a prebraze cleaning, dip brazing, and a postbraze heat treatment [103]. The AA6061-T6 parts were first subjected to a degreasing/chemical deoxidation process to remove the thick oxide films that form during extrusion processing and subsequent heat treatments. This involved soaking the tubes in a degreasing solution (Hurrisafe 950 supplied by PCI of America of Rockville, Md, USA) at 65° to 82°C to remove hydrocarbon residues. After rinsing in warm water, the parts were dipped in a caustic bath (Isoprep 35 supplied by MacDermid of Denver, CO) for 30 seconds to lightly etch the surface. After a second warm water rinse, the parts were dipped for 30 seconds in a neutralizing acid bath (Gil-Sparkle C solution diluted 50% with de-ionizing water). The parts were again rinsed in a warm water bath before dipping for 45 seconds in a deoxidizing solution containing ferric sulfate, sulfuric acid, and nitric acids followed by rinsing in warm water and air drying. Once cleaned, the extrusions were assembled into the appropriate sandwich geometry. During assembly, Lynch Metal (Union, NJ) grade 4047 Al-Si filler foil was applied to the surfaces of the cellular structure as shown in Figure 2.3. Filler alloy 4047 was used due to its improved fluidity (wetting action) and for minimizing solidification cracking. A bead of AA 4145 filler paste (Omni/Lucas Milhaupt grade LTB 37-SSK) was also

applied to any small gaps within the assembly. In the case of the 3D structures, it is assumed that AA4145 was used in very limited quantities and only along small joints at the edge of the 3D structure. Table 2-2 summarizes the compositions of the AA6061, AA4047, and AA4145 alloys, whose compositions and braze process conditions governed the microstructure [104]. It should be noted that perfect tube alignment for all tested structures was dificult to maintain with the fabrication method used here. The tubes slid and it was difficult to attain perfect alignment even with clamping the face sheets. Both tube wall thickness variablility and misalignment are imperfections that trip tube buckling modes during subsequent compression testing.

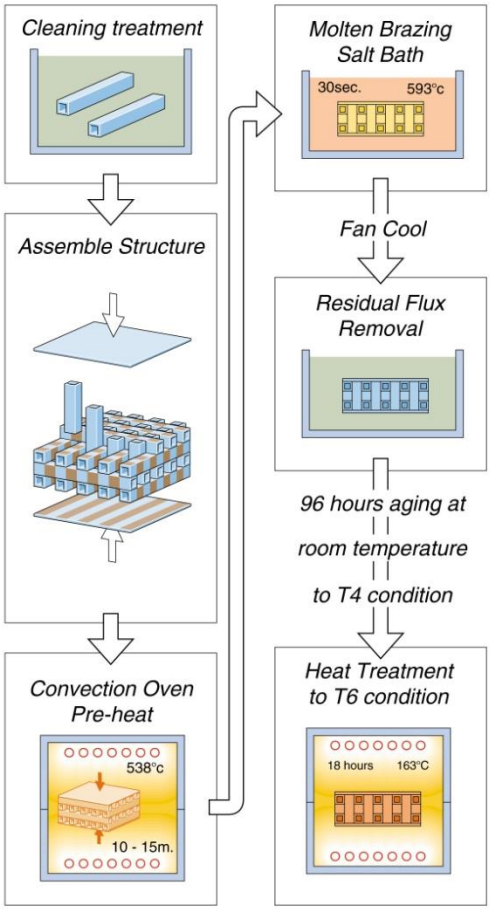

Figure 2.3. A process flow chart for the manufacturing sequence used to fabricate the cellular tube structures.

After assembly, the cellular structure was clamped to the top and bottom face sheets and the entire assembly mounted on a rack for dip brazing. The assembly was preheated for 10-15 minutes at 538˚C (just slightly below the brazing temperature) in a hot air convection oven to remove moisture [103]. The structures were then quickly transferred to a 593˚C bath of molten brazing flux (Alu-braze 960, Park Metallurgical, Detroit, MI) for approximately 30 seconds, this acted as both a heating medium and deoxidizer. During this emersion, the molten braze alloy flowed (by capillary action) to

fill the joints. After removal from the molten flux bath, molten salt was drained from the structure, and it was fan cooled to room temperature at rates ranging from 0.08 to 0.32 K/s, depending on the size of the structure. The structure was then soaked in hot-agitated water and Gil-Sparkle C solution with a 50% de-ionized water. After these fabrication steps, the structure was slow-aged at room temperature for 96 hours to the T4 condition and then peak hardened (to the T6 condition) by ageing at 163˚C for 18 hours followed by water quenching.

Table 2-2. Composition of extruded material (AA6061) and filler materials used to braze the tube profiles. [105], [106]

	Composition (wt%)							
Material	Si	Cu	Mg	Mn	Fe	Cr	Zn	Mg/Si
AA 6061	0.4-0.8	0.15-0.4	0.8-1.2	0-0.15	0-0.7	0.04-0.35	0-0.25	0.5-1.5
AA 4047	11.0-13.0	0.3	0.1	0.15	0-0.8	0	0-0.2	0.009_{max}
AA 4145	9.3-10.7	3.3-4.7	0.15	0-0.15	0-0.8	0	0-0.2	0.016_{max}

2.3. Material Characteristics

2.3.1. Microstructure Characterization

Micrographs of the parent alloy and brazed regions of one of the structures studied here are shown in Figure 2.4, all samples were electropolished [104] prior to

imaging. Figure 2.4(a) shows a backscattered SEM micrograph of the tube wall material for a region more than 125μm from a brazed joint. In the post brazed and heat treated condition, the tube wall material has an average grain size of 20μm. The grain boundaries were decorated by large β-Mg_2Si and Q-$Al_4Cu_2Mg_8Si_7$ phase precipitates as predicted by Chakrabarti [107]. Fleming [104] has conducted a detailed examination of the microstructure evolutions accompanying the dip braze bonding process used here. The large β-phase grain boundary particles are consistent with the time-temperature transformation curves calculated by Fleming and the slower than normal rate of cooling after brazing. The brazed regions between the tubes, Figure 2.4(b) consisted of a eutectic structured region and a transition zone to the parent alloy microstructure. Within the brazed joint, the AA 4047 braze foil had fully melted and an fcc aluminum solid solution and diamond cubic silicon eutectic microstructure had formed upon cooling. Both β and Q-$Al_4Cu_2Mg_8Si_7$ phases were predicted [104] to be responsible for the strengthening in this region. The Vickers microhardness in the brazed and mixed regions was measured to be approximately 90HV30 and 98HV30, respectively; equivalent to tensile strengths of 285 and 300 MPa. In the mixed zone on either side of the original braze foil location, Figure 2.4(c), resolidified AA6061 formed coarse grains with Al-Si eutectic at solidification boundaries. Kinetic models and composition profiles [104] have shown that significant outward diffusion of silicon and inward diffusion of magnesium had occurred in a zone that extended 125 μm from the edge of the brazed zone. Strengthening in this region resulted from precipitated Si, as well as β, and Q phase precipitation in Al-rich phase [104].

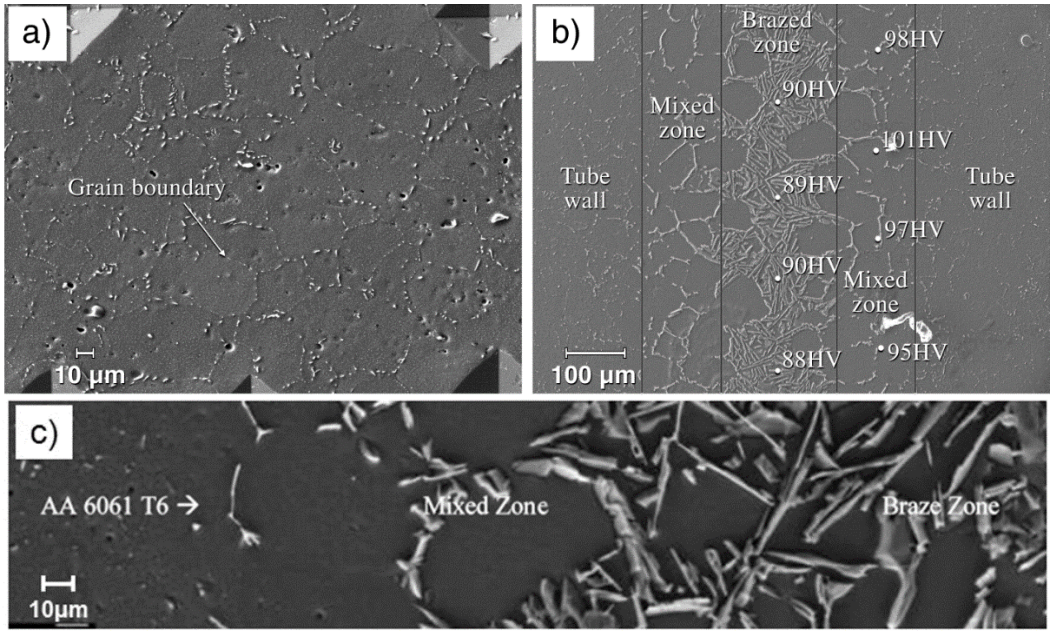

Figure 2.4. SEM images of the post-brazed and heat treated AA6061-T6 material. a) Backscatter electron image of the extruded tube wall showing precipitate phases decorating the grain boundaries. b) The brazed region between two tubes showing silicon rich phases. Microhardness values are shown within the brazed and mixed zones. c) A higher magnification view of the brazed and mixed zone regions.

2.3.2. Alloy Mechanical Properties

An optical image of a polished cross section cut from a 3D structure is shown in Figure 2.5. Microhardness measurements were made at various locations (all further than 125 µm from any brazed region) to investigate the local strength of the post brazed/artificially age hardened extrusion region of the structure. These hardness values and approximate location of the measurement are shown in Figure 2.5. The measured Vickers microhardness lay in the range of 102±7.5HV30; equivalent to an alloy tensile strength of approximately 330 MPa, which is consistent with the T6 condition of the

6061 alloy. Indents made in the outer surface of the tube wall, indicated a hardness that deviated very little from 107HV. However, when measured on a plane transverse to the extruded direction, the microhardness was roughly 10HV smaller, and fluctuated between 95HV and 102HV. The microhardness indention diameter was about 0.1 mm, while half the tube wall thickness was 0.8 mm. As a result the distance to the free surface from the middle of the tube wall was about eight times the indent diameter, and proximity to the free surface may have reduced lateral constraint during indentation. Hardness measured in the same orientation near the two (horizontal) brazed joints, indicated a hardness that varied between 101 and 110 HV consistent with better lateral constraint. We conclude that the strength of the tube wall alloy after brazing was approximately isotropic and independent of orientation.

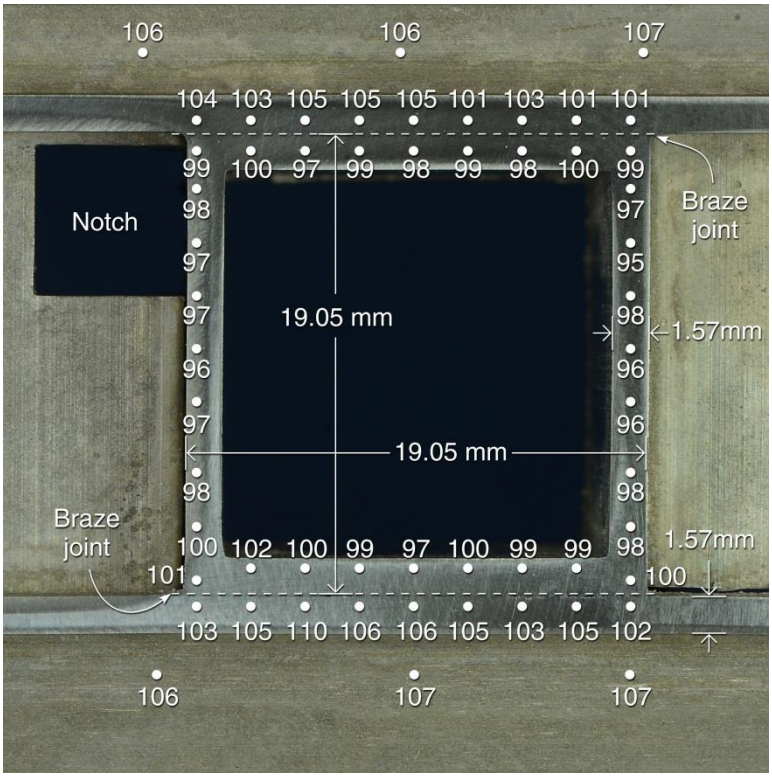

Figure 2.5. A photograph of a polished cross sectional slice through the 3D tube structure with measured Vickers microhardness values superimposed. A notch in one of the vertically oriented tubes can be seen in the upper left. All microhardness measurements are located in the AA6061-T6 extrusion region.

Quasi-static tensile tests were used to determine the stress-strain response of the post-brazed and T6 aged 6061 tube wall alloy. The tensile test specimens were cut so that the loading direction was in the axial (extrusion) direction of the tubes. The test coupons were prepared according to ASTM standard B557-06 and tested on a 50kN screw driven universal testing machine (Instron Model 4208, Instron Corp, Canton, MA, USA) at 25^{o}C at a strain rate $\dot{\varepsilon}$ of 10^{-4} s^{-1}. The specimen's axial displacement was determined with a laser extensometer (Electronic Instrument Research, Model LE-01,

Irwin, PA, USA). The specimens were tested to failure and the Cauchy stress, σ_c and the logarithmic strain, ε_L, up to diffuse necking were calculated from;

$$\sigma_c = \frac{F}{A_0(1+\varepsilon)}, \qquad \varepsilon_L = ln\frac{L_2}{L_1} \tag{2.4}$$

where F is the force, A_0 is the initial cross section of the tensile coupon, ε is the engineering strain, L_1 the initial gauge length and L_2 the extended length.

To verify that material in the post brazed 3D orthogonal assembly had the same mechanical properties throughout its interior, tests were performed on material extracted from the walls of tubes located at the surface and the interior of the sample. Two samples from each location within a 3D cellular structure in the post brazed and peak hardened condition were obtained and tested (measured at 25°C and a strain rate of 10^{-4} s^{-1}). In addition, the AA6061-T6 face sheet material was also tested in the rolling and transverse directions. Figure 2.6 shows the cauchy stress - logarithmic strain curve for one of the tube wall material samples. This curve was subsequently used to deduce the material properties for the numerical simulations of the 3D orthogonal assembly. A summary of the mechanical test results for all the samples is shown in Table 2-3. It is evident that there is little variation in the mechanical properties within the tube structure, and the ultimate strengths are consistent with the microhardness measurements.

Table 2-3. Mechanical properties of 3D orthogonal structure and face sheet.

Direction	Modulus, E_s (GPa)	Yield Strength, σ_{02} (MPa)	Ultimate Strength, σ_u (MPa)	Total Strain to Failure ε_f (%)
Exterior Region of 3D Structure				
Axial	70.5	278.2	310.5	5.3
Axial	69.9	280.9	311.5	5.1
Interior Region of 3D Structure				
Axial	68.5	284.5	313.6	4.9
Axial	68.3	283.2	312.8	4.9
Face Sheet Material				
Tranverse	69.4	265.9	346.8	12.5
Rolling	71.4	281.4	344.3	12.7

The mechanical response of the brazed joint was also investigated using a lap shear test in accordance with test standards specified by ASTM D1002-05. The test specimens were cut in the length direction of the extruded tube and underwent the same brazing and age-hardening process described in Section 2.2. Tests were conducted at a strain rate of 10^{-5} s^{-1} in the specimens gauge area. In three tests, the AA6061-T6 material failed prior to the braze joint near the grips at a tensile stress of 247 MPa. The corresponding shear stress within the joint at the point of material failure was measure to be 165 MPa. Since no nodal fracture was observed at the brazed lap joint during these tests, the nodes of the adjacent tubes in the FE models (Chapter 3) were merged prior to simulations.

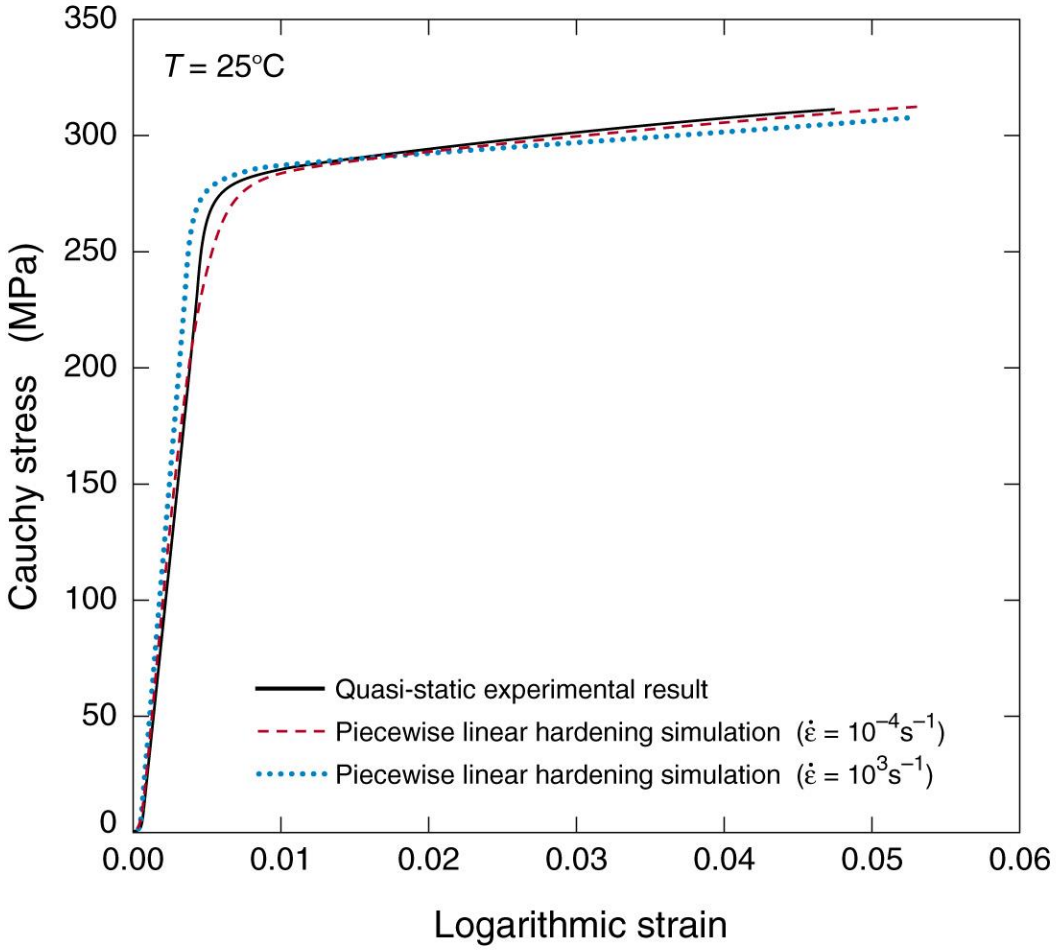

Figure 2.6. Measured true stress - logarithmic strain curve for post-brazed and fully age hardened AA6061-T6 tube wall material tested in uniaxial tension to fracture at room temperature. The stress-strain curve predicted by a piecewise linear hardening constitutive model used in subsequent simulations is also included.

Chapter 3. Compressive Response of Cellular Structures

This chapter investigates the quasi-static mechanical response of the tube based structures described in Chapter 2. By using different wall thicknesses for the in-plane and through thickness tubes, it is possible to independently control the in-plane stretch resistance and the through thickness crush strength. The large nodal contact areas also improve load transfer within the core and between cores and face sheets. It is shown that a 3D orthogonal arrangement of tubes offers effective crushing resistance and appears well suited for impact energy absorbing applications.

3.1. The 2D Cellular Structure

The compressive stress strain response of the cellular structures were measured following the guidelines of ASTM C 365/C for sandwich panel testing at an applied engineering strain rate of 10^{-4} s^{-1}. A laser extensometer was used to measure the compressive displacement and thus nominal strain.

The out-of-plane compressive response of a 2D structure with $\bar{\rho} = 16.3\%$ is shown in Figure 3.1. The stress linearly increased with an elastic modulus (measured during unloading) of 3.2 GPa (see yellow inset in Figure 1.1). The structure exhibited an initial peak in strength of 13.2 MPa. Continued loading resulted in rapid softening and a significant period of compression at almost no stress. This was then followed by a second rise in stress to a peak value of 3.1 MPa at a strain of 0.19 followed again by rapid softening. A third stress peak was observed with a maximum stress of 11.8 MPa at a strain of 0.35. Further loading again resulted in rapid softening until densification (and rapid hardening) set in at a strain of 0.64.

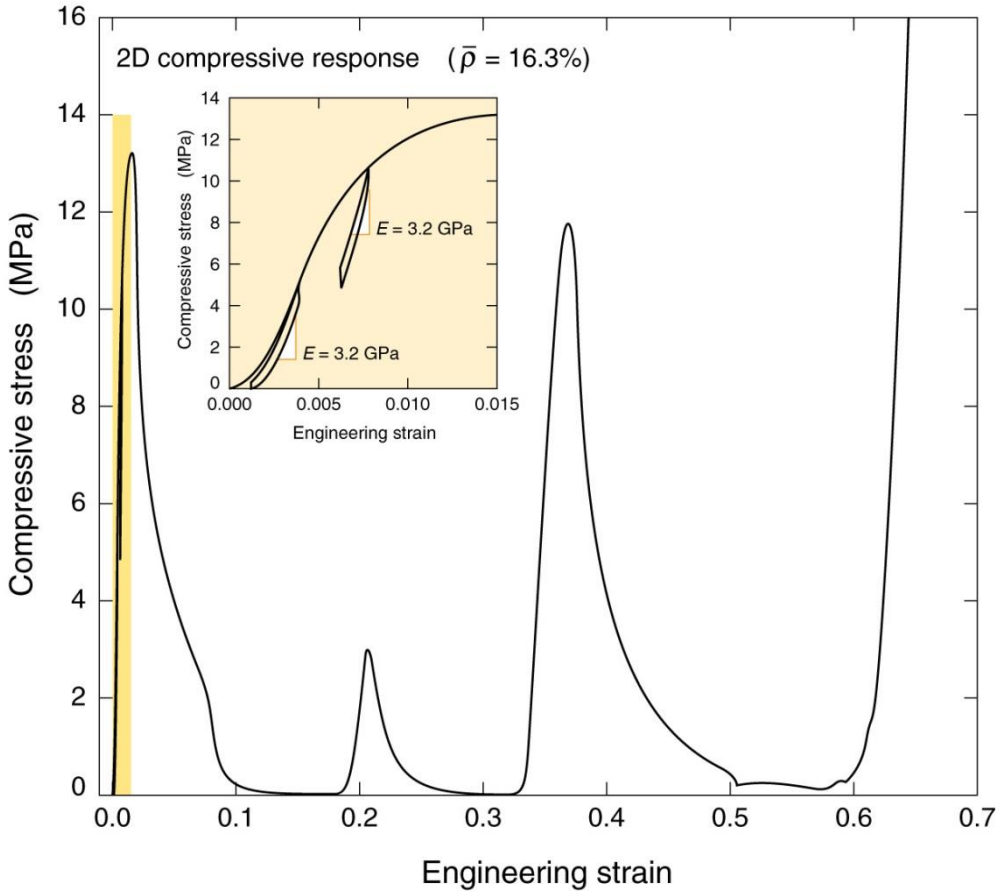

Figure 3.1. The compressive stress- strain response of a 2D cellular structure with a relative density of 16.3%. The inset shows an expanded view of the nominally elastic loading region of the test where the unloading modulus was measured.

Figure 3.2 shows a series of photographs of the 2D structure at various stages of the test. A comparison of Figure 3.2(a) and (b) shows that the initial peak in strength was controlled by concertina buckling of layers 1 and 3 in which the tubes on either side of a horizontal plane rotate in opposite directions forming a chevron pattern, Figure 3.2(c). Figure 3.2(d) indicates that the second stress peak results from the complete collapse of layer 1. Examination of Figure 3.2(e) and (f) show that the third stress peak resulted

from collapse of layers 2 and 4 by the concertina buckling mode. Some variability of response was also observed. In some tests, the stress-strain response exhibited only two peaks that resulted from simultaneous collapse of layers 1 and 3, and then layers 2 and 4. Apparently small imperfections in the structure influenced the details of the buckling sequence, but not the generally unstable response of this structure.

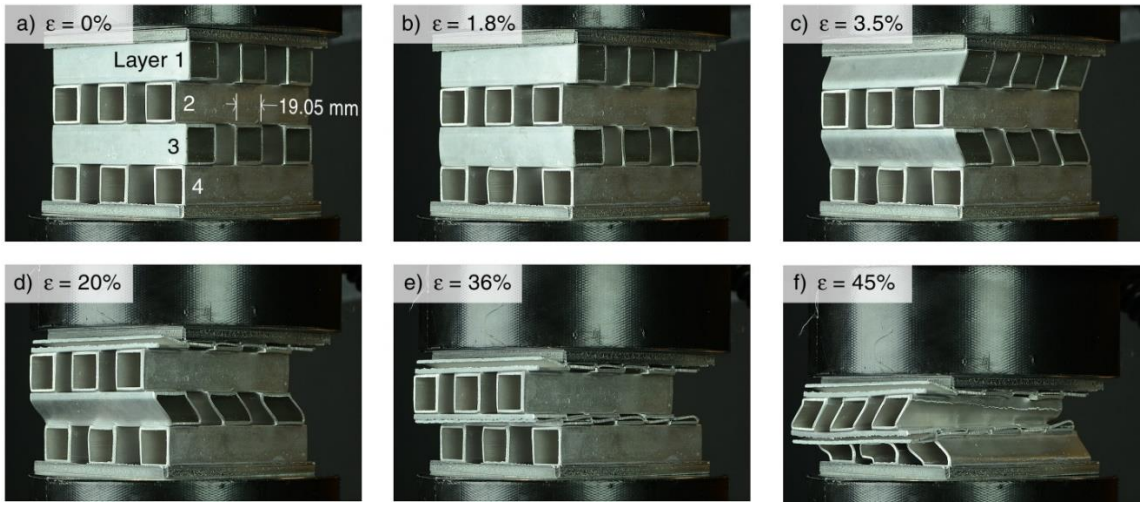

Figure 3.2. A photographic sequence showing the unstable collapse modes of a 2D cellular structure with a relative density of 16.3%.

The total absorbed (plastically stored) energy per unit volume, E_v, was obtained from the area under the stress-strain curve shown in Figure 3.1. The integration is usually terminated at the densification strain, ε_D defined here as the strain where the flow stress reaches the initial yield stress ($\varepsilon_D = 0.64$ for this sample). This gave an energy absorbed per volume, $E_v = 1.2 * 10^6\ J/m^3$. Dividing this by the core density $\bar{\rho}\rho_s = 0.163 \cdot 2.7x10^3 kg \cdot m^{-3} = 440.1\ kg \cdot m^{-3}$ (where ρ_s is the density of the solid) gave an

energy absorbed per unit mass, $E_m = 2.72\ J/g$. If the stress achieved at the first peak had remained constant until densification, the energy absorbed per unit mass in the 2D structure would have been the theoretical limit, $E_m^* = 19.1\ J/g$. Defining the energy absorbing efficiency as the ratio of measured energy absorption, E_m, to the theoretical limit, E_m^* , the 2D structure has an energy absorption efficiency of 14.2%. The low efficiency is a result of the unstable buckling response of the structure, and makes the 2D structure poorly suited for impact energy absorption applications. It was therefore investigated no further.

3.2. The 3D Cellular Structure

The 3D cellular structures defined in Table 3-1 had relative densities of 42.7, 20.1, and 11.6% and were made of tubes of identical wall thickness in each orthogonal direction. The 20.1% relative density structure represents the 2D structure, but with a notched tube inserted into the void of the co-linearly aligned tubes, Figure 2.2 (a). It's out-of-plane compressive response is shown in Figure 3.3(a). The structures unload modulus during initial loading was 3.1 MPa. It reached an initial peak in strength of 20.9 MPa, and then underwent moderate softening before hardening twice more to reach a strength about equal to that of the first peak. The sample then began to densify at a strain $\varepsilon_D = 0.61$. The notched structure had an absorbed energy per unit volume, $E_v = 10 *$

$10^6\ J/m^3$ and an energy absorbed per unit mass of $E_m = 19.2\ J/g$. Its energy absorption efficiency was 81.0%.

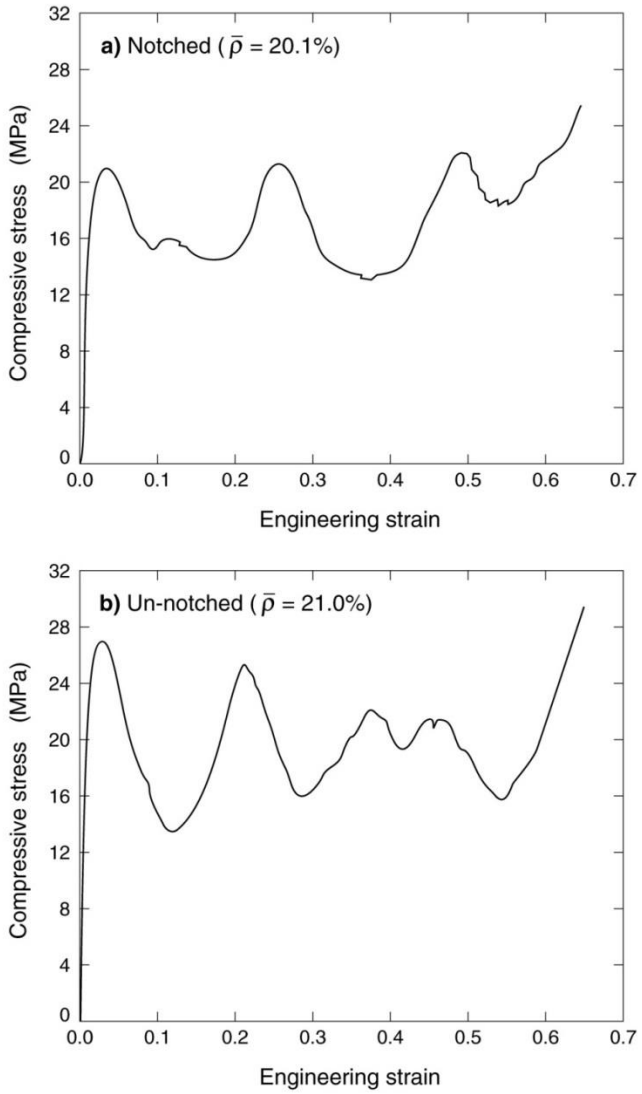

Figure 3.3. A comparison of the compressive stress - strain responses for 3D cellular structures assembled using (a) notched and (b) un-notched vertical tubes. The small difference in relative density results from removal of the notch material.

To ascertain the effect of notching the out-of-plane tubes, an otherwise identical cellular structure to that with a relative density of 20.1% was fabricated without notches in the through thickness tubes, and its compressive stress-strain response is shown in Figure 3.3(b). The slightly higher relative density of the un-notched structure (21.0%) was due to additional mass of the un-notched vertical tubes. It can be seen that notching reduced the initial peak strength of the 3D structure from 27.1 MPa to 20.9 MPa but also reduced the amplitude of the stress fluctuations. The energy absorbed per unit volume for the un-notched sample $E_v = 12.45 * 10^6\, J/m^3$ while $E_m = 21.94\, J/g$, which were both higher than those of the notched structure. However, the large stress drops observed in the sample with no axial tube notches reduced its energy absorption efficiency from 81.0 to 72.3%.

A photograph of the notched 3D structure with a relative density of 20.1% taken at the first peak in stress (at a strain of 0.04) is shown in Figure 3.4(b)(i). The drop in strength at the first peak resulted from the onset of buckling of the set of tubes oriented in the through thickness direction. This was nucleated at the notches in the tubes shown in the photographs of Figure 3.4(b). Continued loading resulted in softening to a relatively constant stress of approximately 15 MPa, Figure 3.5. At this stage, the buckles were fully developed in the through thickness tubes, and the side walls of the cross-ply tubes then began to buckle, Figure 3.4(b)(ii). This was accompanied by a second rise in stress at a strain of 0.21 that reached a peak value of 21.8 MPa as densification of layer 2 occurred, Figure 3.4(b)(iii). This process was repeated until each of the four cross-ply tube layers had densified at a strain $\varepsilon_D = 0.61$.

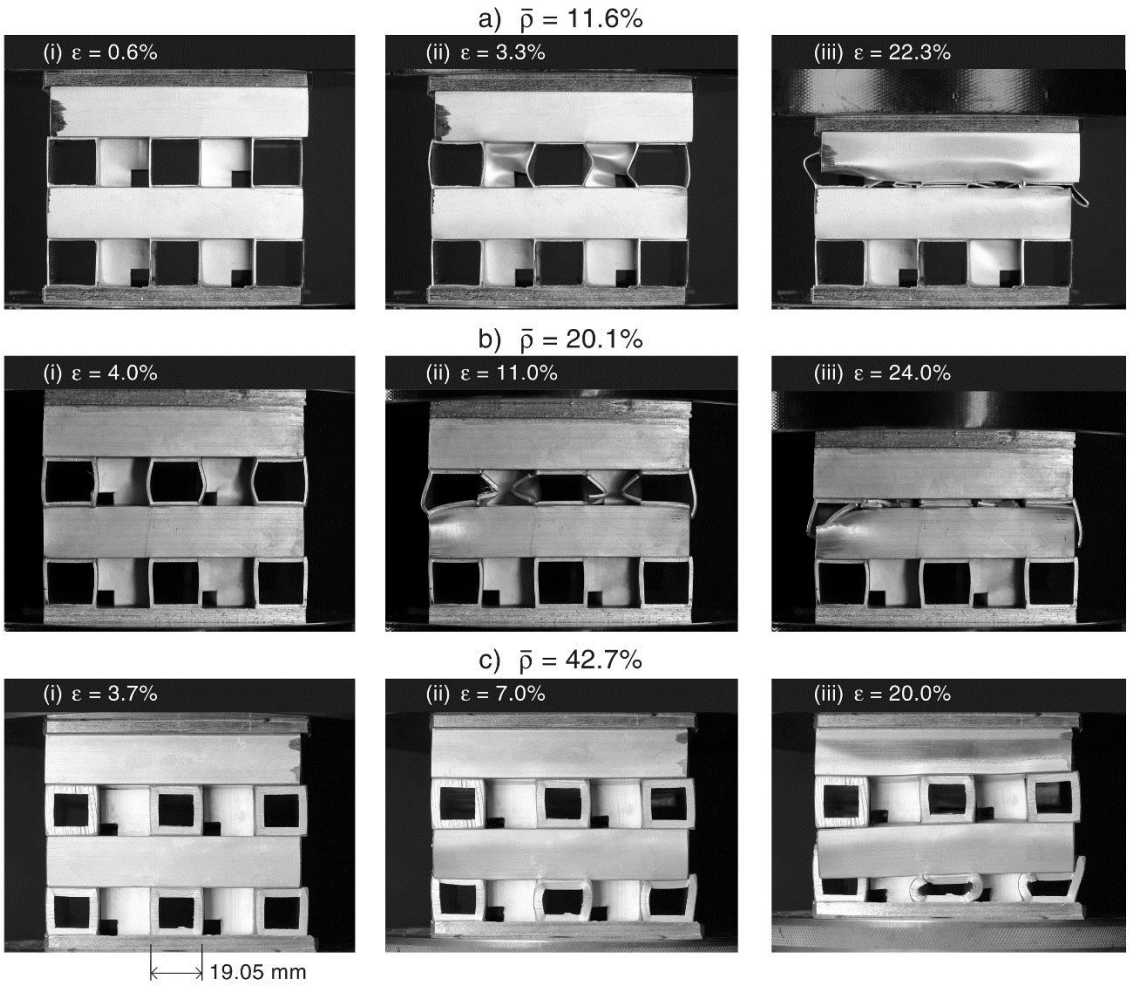

Figure 3.4. Photograph sequence of the collapse modes for 3D structures with relative densities of (a) 11.6, (b) 20.1, and (c) 42.7%. The strains at which each photograph was taken are indicated on Figure 3.5

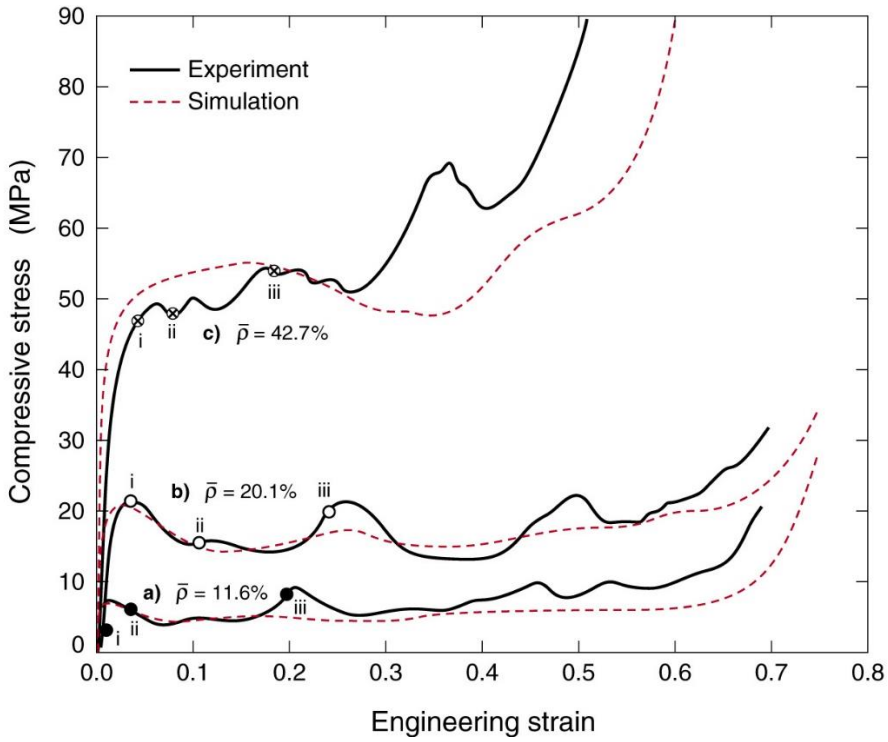

Figure 3.5. The compressive stress- strain responses of notched 3D cellular structures made from uniform wall thickness tubes with relative densities of 11.6, 20.1 and 42.7%. The structures exhibit a relatively flat stress-strain response after initial yield until attainment of a density dependent "densification strain" whereupon the stress rises sharply. The dashed curves correspond to FEA simulations discussed later.

The out-of-plane compressive response for cores with three different relative densities is compared in Figure 3.5. The ultimate peak strength of the 42.7, 20.1, and 11.6% relative density structures were 69.1, 21.8, and 9.7 MPa respectively, and was controlled by buckling of the through thickness tubes, Figure 3.5(a) - (c). This buckling is clearly seen in Figure 3.4(a) (ii). Further collapse results from the folds in the vertical tube walls buckling into the cross-ply oriented tubes. The stress-strain curves of all three structures exhibit relatively constant stress until their (density dependent) densification

strain was reached. Table 3-1 summarizes the measured mechanical properties for all the samples.

Table 3-1. Energy absorption values for tested tubular cellular structures

Topology	Relative Density, $\bar{\rho}$	Peak Stress, σ_p (MPa)	ε_D	E_v (MJ/m^3)	E_m (J/g)	Theoretical E_m^* (J/g)	Energy Absorbing Efficiency
3D	42.7	69.1	0.45	24.4	21.2	29.4	0.73
3D	35.1	53.3	0.51	23.8	25.1	27.5	0.91
3D	28.6	36.8	0.50	14.7	19.0	23.1	0.82
3D	20.1	21.8	0.61	10.4	19.2	23.7	0.81
3D	11.6	9.7	0.59	3.9	12.7	13.7	0.92
3D No notch	21.0	27.1	0.63	12.5	21.9	30.1	0.72
2D	16.3	13.2	0.64	1.2	2.7	19.1	0.14
1D array	6.7	4.7	0.72	1.7	18.0	35.2	0.51

3.3. Effect of the Tube Wall Thickness

Figure 3.6(a) shows the stress-strain responses of 3D structures in which the wall thicknesses of the in- and out-of-plane tubes were different. Recall that the 3D structure

with equal tube thickness in all directions had a relative density of 42.7%. Its stress-strain response was shown in Figure 3.4(c). The wall thickness of just the out-of-plane tubes was reduced by a half, and the relative density decreased to 35.1% (82% of the isotropic structure), but the strength dropped by only 5%, Figure 3.6(a). A larger decrease in strength occurred when only the in-plane tube wall thicknesses were reduced by one half (while keeping the of the out-of-plane tubes at the original wall thickness). In this case, the relative density decreased to 28.6% (66% of the isotropic structure) and the peak strength was reduced by approximately 54%. From the images in Figure 3.6(b) and (c), the initial peak strength is seen to be controlled by a similar mechanism to that observed in isotropic samples with identical tube wall thicknesses. We also note that the structures with relative densities of 35.1% and 28.6% had excellent energy absorbing characteristics, with efficiencies of 91% and 82%, respectively, Table 3-1.

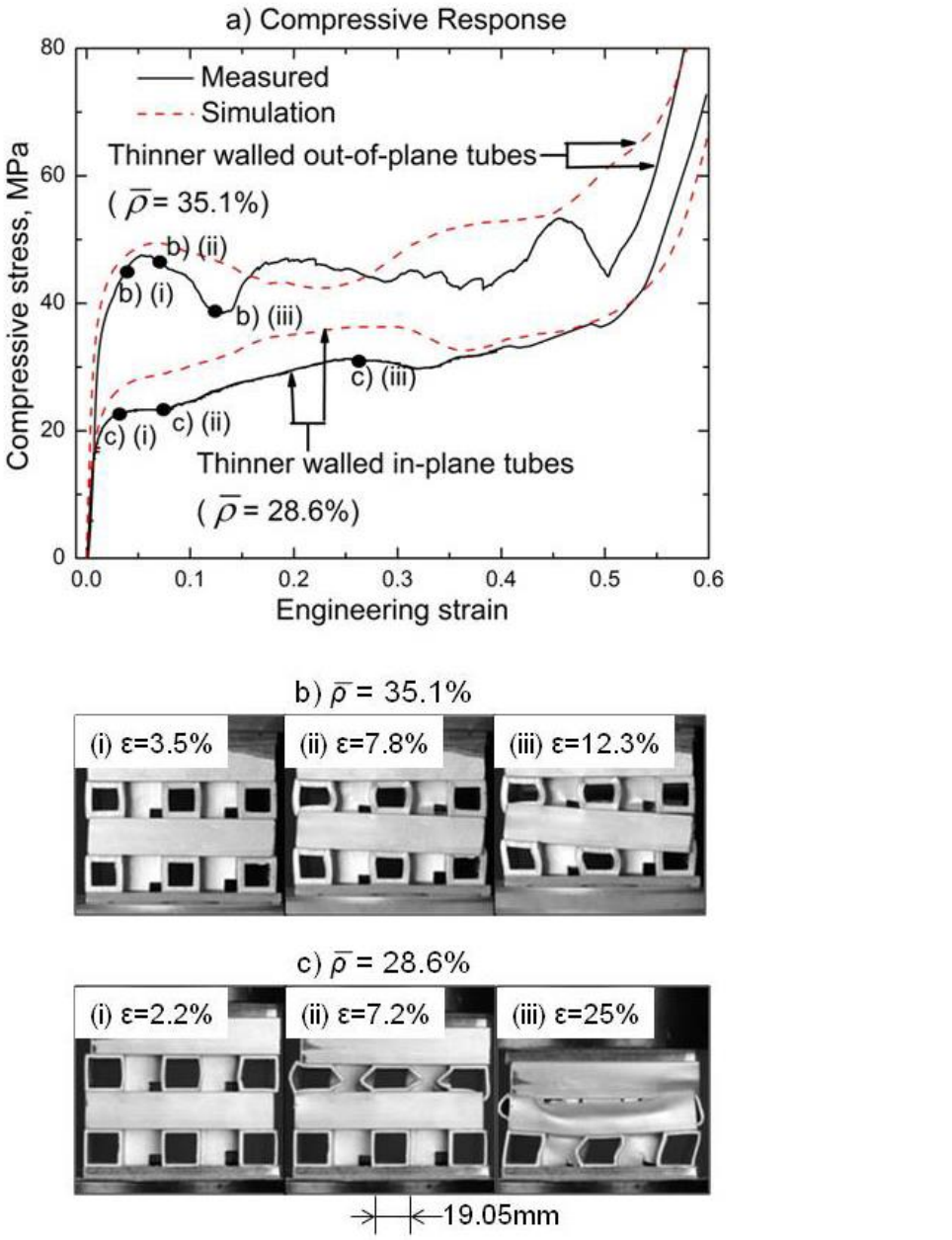

Figure 3.6. (a) The compressive stress-strain responses for notched 3D cellular structures in which the tube wall thicknesses in the vertical and horizontal directions were different. The sample with a relative density of 28.6% density used in-plane tubes with a reduced wall thickness (of 1.57mm). The sample with a relative density of 35.1% was constructed using vertical tubes with a reduced thickness of 1.57mm. The dashed curves correspond to FEA simulations discussed later. (b) and (c) show the collapse modes of the two structures. The in-plane tubes buckle first in c) while the vertical tubes initiate failure in b).

3.4. Tube Interactions

To experimentally investigate possible interactions between tubes in the in- and out-of-plane directions, only the co-linearly aligned (in-plane) tubes from the 3D structure with a relative density of 16.3% were tested in out-of-plane compression, Figure 3.7(a). The vertical notched tubes in this co-linear tube structure were then also tested in (axial) compression. The response of this 1D array structure is shown in Figure 3.7(b). The stress- strain response for a 3D structure made by combining both sets of tubes is shown in Figure 3.7(c). The in-plane and out-of-plane tube cells have initial peak strengths of 13.2 and 4.7 MPa, respectively. The addition of these strengths (17.9 MPa) is seen to be less than that of the fully assembled 3D structures first peak (20.8 MPa).

The experiment indicates the existence of a synergistic interaction between the co-linear aligned and vertical tubes. In the same way that the peak strength of the 3D assembly cannot be reproduce by summation of the co-linear and vertical tubes acting separately, the energy absorbed per unit volume for the 3D assembly also cannot be achieved by summing that of its components. The energy absorption per unit volume is increased in the 3D core by more than the summed energy absorbing capacities for the 1D array and 2D cores (from 2.79 MJm^{-3} to 10.4 MJm^{-3}), Figure 3.7(c). The energy absorbed per unit mass is also increased in the 3D core compared to the summed 1D array and 2D cores (from 5.21 J/g to 19.2 J/g), Figure 3.7(c). Table 3-1 summarizes the energy absorption values for the individual cores examined in this aspect of the study.

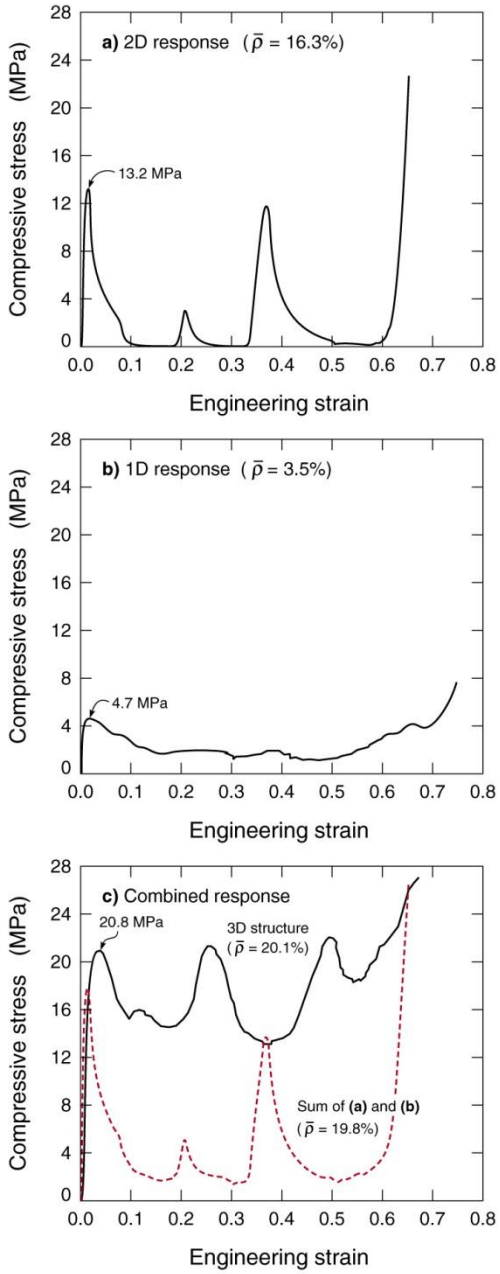

Figure 3.7. Measured stress-strain curves for a structure composed of (a) co-linear aligned (0/90) tubes and (b) only the vertical tubes used in the 3D assembly. (c) Compares the summed response of (a) and (b) with that measured for the 3D structure. Note the considerable increase in energy storage of the 3D structure.

3.5. Energy Absorption Comparisons

The energy absorbed per unit mass for the 3D structures is plotted against the peak stress and compared to a selection of aluminum foams [108, 109, 110] and the upper bound limit for axially compressed square cross section tubes of various wall thicknesses to tube width ratios, Figure 3.8.[A] The line for the upper bound absorbed energy per unit mass, E_m, has been derived (see Appendix A) from the average crush force of tubular extrusions calculated by Hanssen et al. [111];

$$E_m = \sigma_p \left[\rho_s \frac{\sigma_p}{c_0 \sigma_0}\right]^{-3/5} \qquad (3.1)$$

where $\sigma_0 = 0.5(\sigma_{02} + \sigma_u)$, is the extruded tube strength, $\sigma_{02} = 278.2MPa$ is the nominal stress at 0.2% offset strain, $\sigma_u = 310.5MPa$ is the ultimate tensile stress, $\rho_s = 2700kg \cdot m^{-3}$ is the solid density of aluminum, and $C_0 = 1.30$ is a coefficient for square tubes. Using the measured uniaxial tensile test results for the material studied here gives, $\sigma_0 = 294.4\ MPa$. Examination of Figure 3.8 shows that the 3D structures outperform all metal foams and falls just below the tube upper bound curve. It should be noted that the energy absorbed per unit mass for the un-notched vertical tubes fell just under the tube upper bound in Figure 3.8. We also note that unlike metal foams and arrays of axially compressed tubes which resist only crushing, the 3D structure has both excellent crush and stretch resistance.

[A] The energy absorption for the 3D structures and metal foams was always calculated by measuring the area under the stress-strain curve until the onset of densification (defined as the strain at which the stress reached that of the peak in crush strength).

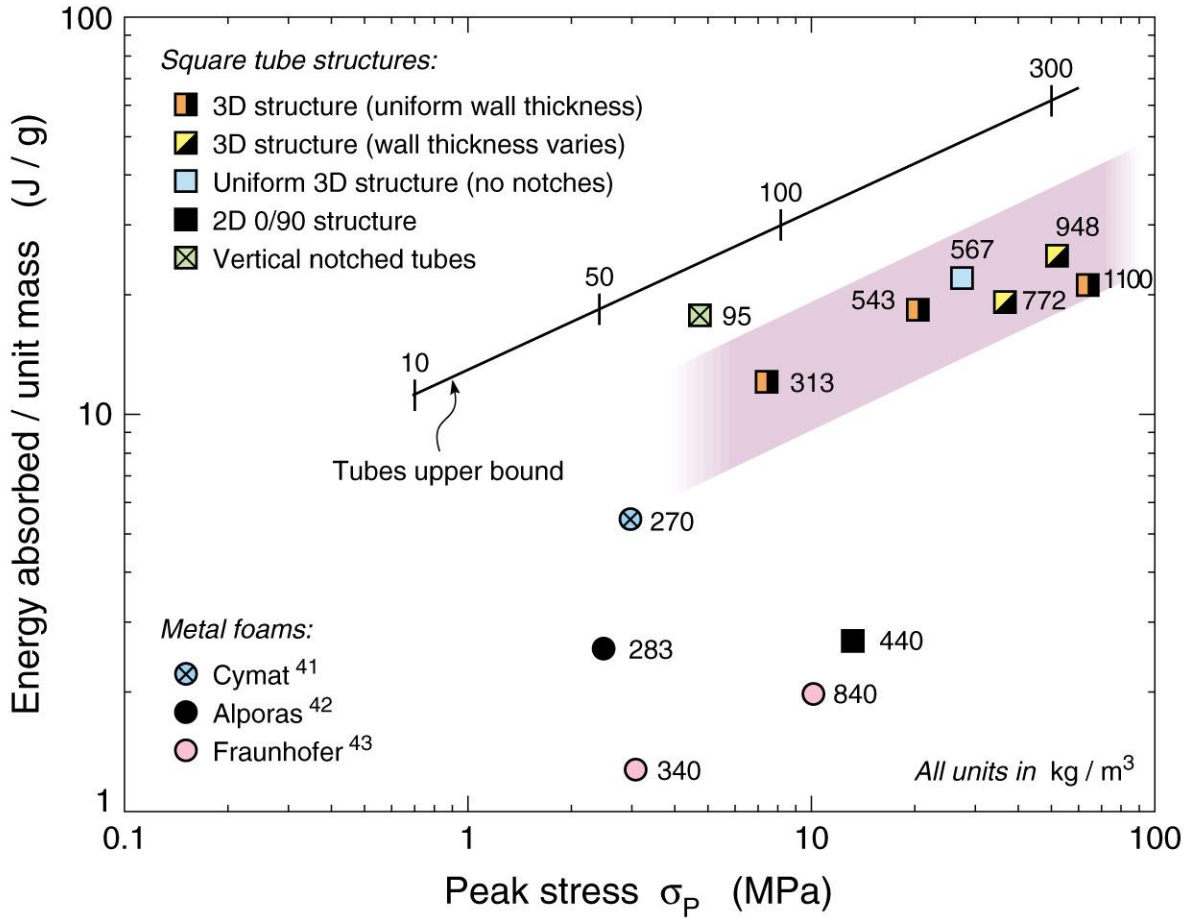

Figure 3.8. The energy absorbed per unit mass by the cellular structures investigated in this study compared to commercially available aluminum foams. Each cellular metal foam is labeled with its density in kg/m3.The wall thickness to tube width ratio is shown for the tube upper bound relation.

3.6. Finite Element Study

Finite element techniques have been used to investigate the failure mechanisms responsible for the mechanical responses of the cellular structures.

3.6.1. Finite Element Investigation

All the finite element simulations were conducted using the explicit version of the commercial, non-linear finite element package IMPETUS Afea Solver® [112]. The geometry and relative density of the modeled tube specimens was identical to those reported in Table 2-1. The initial models did not incorporate the defects in alignment and tube wall thickness seen in the experiments. The FE models were constructed using cubic hexahedral elements. A mesh sensitivity study indicated an in-plane nodal spacing approximately equal to the wall thickness (t) was sufficient to provide converged solutions. One cubic hexahedral element was therefore used through the thickness of each tube wall. The nodes of the adjacent tubes were merged prior to the simulation, thus representing a perfect braze zone with no interface failure criterion. The contact formulation in the software is based on a penalty formulation. All the simulations used rigid front face sheets constrained by the general boundary condition option of IMPETUS Afea Solver to move only in the through thickness direction while the rigid back face sheet was clamped in all directions. The simulations were conducted by applying an out-of-plane velocity-time function, $v(t)$, to the front face sheet given by;

$$v(t) = \frac{w}{t_{end}}\left(1 - \cos\frac{360t}{t_{end}}\right) \tag{3.2}$$

where w is the crushing displacement of the sample (6 cm) and t_{end} is the end time for the loading (1 ms), which results in a maximum initial displacement rate of 6 m/s.

3.6.2. Material Properties

The experimentally recovered Cauchy stress-true strain response of the 6061-T6 alloy undergoing uniaxial tensile testing was presented in Figure 2.6. The Cauchy stress, σ_c, versus true strain, ε, relation for an elastic-plastic material under uniaxial straining can be written:

$$\varepsilon = \varepsilon_e + \varepsilon_p = \frac{\sigma_c}{E} + \varepsilon_p \tag{3.3}$$

where ε_e and ε_p are the elastic and plastic components of strain and E is Young's modulus. Having performed the uniaxial tensile test shown by Figure 2.6, the true stress vs. plastic strain curve was tabulated. From the true stress verses plastic strain curve, the hardening curve used for all FE simulations was extracted, and the true stress at 230.7 MPa was calibrated to zero plastic strain for the isotropic hardening assumption. This hardening tabulation was applied in IMPETUS Afea Solver using the general piecewise linear constitutive model prescription given by:

$$\sigma_y = f\left(\epsilon_{eff}^P\right)\left(1 - \left(\frac{T - T_0}{T_m - T_0}\right)^m\right)\left(1 + \frac{\dot{\epsilon}_{eff}^P}{\epsilon_0}\right)^c \quad (3.4)$$

The piecewise linear hardening constitutive model option for IMPETUS-Afea Solver defined by Equation (3.4) includes thermal softening and strain rate hardening parts; however, these gave negligible contributions to the response and so for all tests, the yield stress was only defined by $f\left(\epsilon_{eff}^P\right)$, a piecewise linear function of the effective deviatoric strain, which was obtained from the hardening behavior. The 6061-T6 alloys constitutive response was modeled using a multi-axial von Mises yield criterion assuming isotropic hardening. The solid density $\rho_s = 2700\ kg \cdot m^{-3}$, Young's modulus $E = 70.5\ GPa$, and Poisson ratio $v = 0.3$. Using the material model described above, a uniaxial tensile test was simulated and compared to the measured Cauchy stress-logarithmic strain curve in Figure 2.6. The fit was good and these material properties were then used for all further simulations.

To account for softening created by tube wall fracture on the tensile side of severe buckles, the Cockcroft-Latham failure criterion [113] was implemented for all the compression simulations. Failure was defined to occur when a damage parameter, D, reached unity. The damage parameter was calculated as:

$$D = \frac{1}{W_c}\int_0^{\epsilon_{eff}^P} \max(0, \sigma_1)\, d\epsilon_{eff}^P \quad (3.5)$$

where σ_1 is the first principle stress. The critical damage parameter, W_c =85 MPa was obtained by fitting the simulated measured stress-strain response of a single tube lateral

compression test (Appendix B). The general node splitting feature in the IMPETUS code was turned on. In this feature the damage variable is allowed to evolve without any change to the constitutive response of the AA6061-T6 alloy until D=1. At that instant, the AA6061-T6 alloy is assumed to have failed and nodes of the elements where this failure has occurred are split apart.

The 3D tube structure models were each built from 3,106 cubic hexahedra elements with 107,348 nodes. The wall thicknesses were homogenous throughout the meshed structures and their dimensions were set to match the 3D topologies in Table 2-1 with $\bar{\rho} = 11.6\%$, $\bar{\rho} = 20.1\%$, $\bar{\rho} = 28.6\%$, $\bar{\rho} = 35.1\%$, and $\bar{\rho} = 42.7\%$. The perfectly aligned models gave much higher strengths than those seen in the experiments and so imperfections to the geometry of the FE models were introduced to trip buckling and provide a better fit to the measured stress-strain curves. The imperfections were modeled as a displacement of the lowest order measured eigenmode. The eigenmode amplitudes were altered by collecting all the internal tube wall faces with the general IMPETUS command used to define a surface from a seed node, and then pressurizing the 3D profiles from their inside walls using the general load pressure option of IMPETUS Afea Solver.

3.6.3. Simulation Results

The simulated stress-strain curves are compared to the measured stress-strain compressive curves in Figure 3.5 and Figure 3.6. First order eigenmode amplitudes of 2, 1.5, 2.6, 1.4 and 1.4 times the tube wall thickness were employed to trip buckling for the 11.6%, 20.1%, 28.6%, 35.1% and 42.7% relative density structures, respectively. These imperfection amplitudes are consistent with: (1) the significant misalignment of the 2D tubes at the boundary regions, (2) variations of tube wall thickness throughout the cellular structure, and (3) other random alignment errors as a result of tube slippage during dip brazing preparation. The laterally compressed tube simulations shown in Appendix B indicate that by alleviating these fabrication errors the need for large eigenmode amplitude imperfections can be avoided.

The collapse modes for each of the relative density samples are shown by Figure 3.8. The large initial eigenmode amplitudes are apparent in the early stages of strain, Figure 3.8(a)(i), (b)(i), and (c)(i). The strains in Figure 3.8 correspond to those shown in Figure 3.5, which also provide support for the large eigenmode imperfections introduced to the FE simulations. The buckling phenomenon observed during experiments (where the initial stress peak is controlled by through thickness tube buckling into a series of folds that initiate at the top of the tubes) is clearly observed in the simulations. Figure 3.10, for the 20.1% relative density structure, shows the buckling modes of the through thickness tubes in more detail by hiding two co-linear tubes that block their view in

Figure 3.9. In regions where the vertical tubes are not confined by the co-linear tubes, the vertical tube walls buckle into the cavity spaces with a first order eigenmode in Figure 3.10(a). The notches at each through thickness layer nucleate the buckling of the through thickness tubes due to material failure (node splitting), shown in detail by Figure 3.11 (green tube at a strain of 3.7%). Figure 3.10(b) and (c) show that the vertical tubes buckle most intensely in the bottom two layers of the structure, causing densification at this location first. As the vertical walls fold into the cavity spaces, the folds aid in crushing the co-linear tubes below the folds.

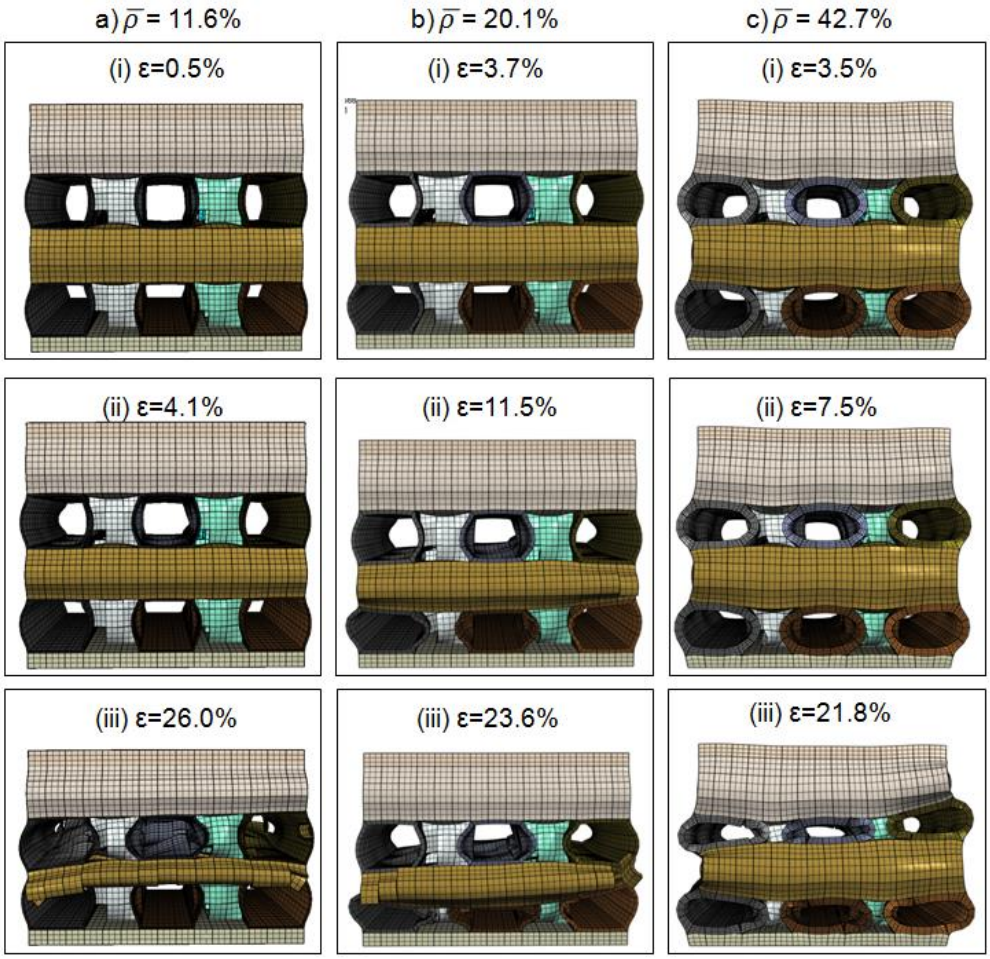

Figure 3.9. Images of the simulated collapse modes for 3D cellular structures with relative densities of (a) 11.6%, (b) 20.1%, and (c) 42.7%. The strain sequence corresponds to that of Figure 3.5. The colors are used only to aid visualization of the deformations of each tube.

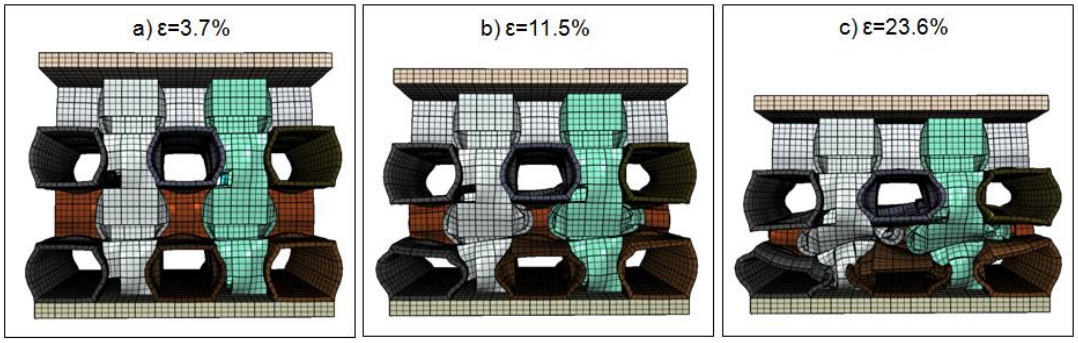

Figure 3.10. Images of the simulated collapse modes for 3D cellular structures with a relative density of 20.1%. Two co-linear tubes have been hidden to show the collapse mode of the axial aligned tubes more clearly. The colors are used to improve visualization of the core deformations.

The collapse modes in the void spaces (plane A in Figure 3.11(a)) can be seen in Figure 3.11(b), where all the walls buckle uniformly towards the void center as a result of reduced confinement. However, when all tube walls are brazed together at plane B (Figure 3.11a), non-uniform buckling of the co-linear tubes side wall occurs on the side connected to the notch as a result of the notch collapse, Figure 3.11(c). The side of the co-linear tube opposite the notch has a uniform collapse, but its first order eigenmode amplitude is less than the co-linear tube that is not contained by the vertical tube, due to increased mass. In addition, the simulated densification strains exhibit a polynomial relationship upon relative density, by equation (3.2).

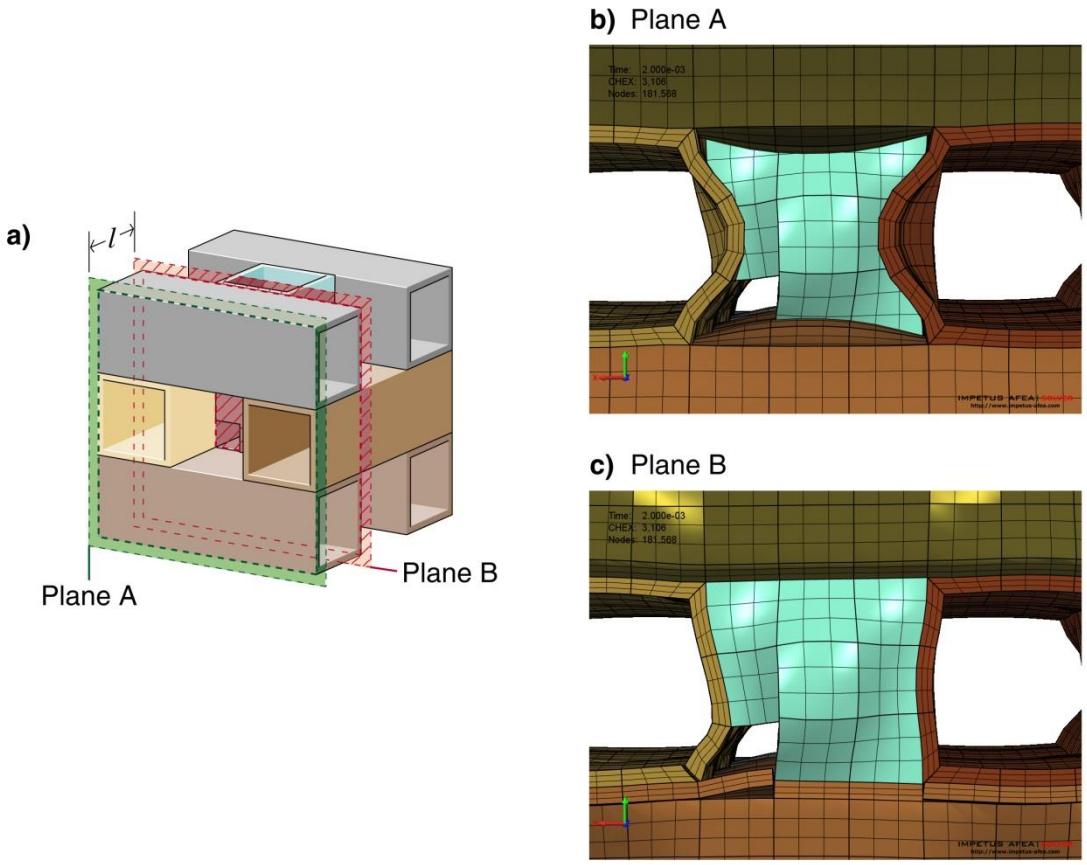

Figure 3.11. Simulated images of the collapse mode of a notched 3D cellular structure with a relative density of 20.1%. (a) Location of image planes (b) In-plane tube wall buckling at Plane A. (b) Buckling on plane B located deeper within the sample. Note the constraint imposed by the vertical tube upon the amplitude of the in-plane tube buckling mode.

The strength, modulus, and energy absorption of cellular foams was shown by Maiti et.al. [15], to be controlled by the relative density of the structure. This could be altered here by varying the tube wall thicknesses. Figure 3.12 shows that for relative densities between 11 and 42% the measured and predicted modulus of the 3D structures, E_{cell} scaled by that of the aluminum alloy, E_s, has a linear dependence upon relative density;

$$E_{cell}/E_s = 3.6\bar{\rho} \tag{3.6}$$

This is consistent with an initially stretch-dominated response [114]. The modulus of 3D orthogonal tube structures studied here is significantly higher than that of bending governed metal foams of similar relative density and material.

The peak strength of the 3D structure σ_{cell}, scaled by the strength of the alloy from which it is made, σ_s, has a power dependence upon relative density;

$$\sigma_{cell}/\sigma_s = 1.05\bar{\rho}^{5/3} \tag{3.7}$$

Using an energy balance argument, Wierzbicki [115] showed that the average axial crushing stress for an array of vertical tubes scaled with relative density to the power 5/3. This seems to agree well with both the experimental data and FE predictions presented here for the 3D structures whose response is dominated by the vertical tubes. We note that the 2D structure (which contains no vertical tubes aligned with the loading direction) deforms by transverse tube crushing and is expected to be a bending dominated system whose strength will scale with relative density to the power 3/2 like open cell foams, which are also bending dominated structures [15].

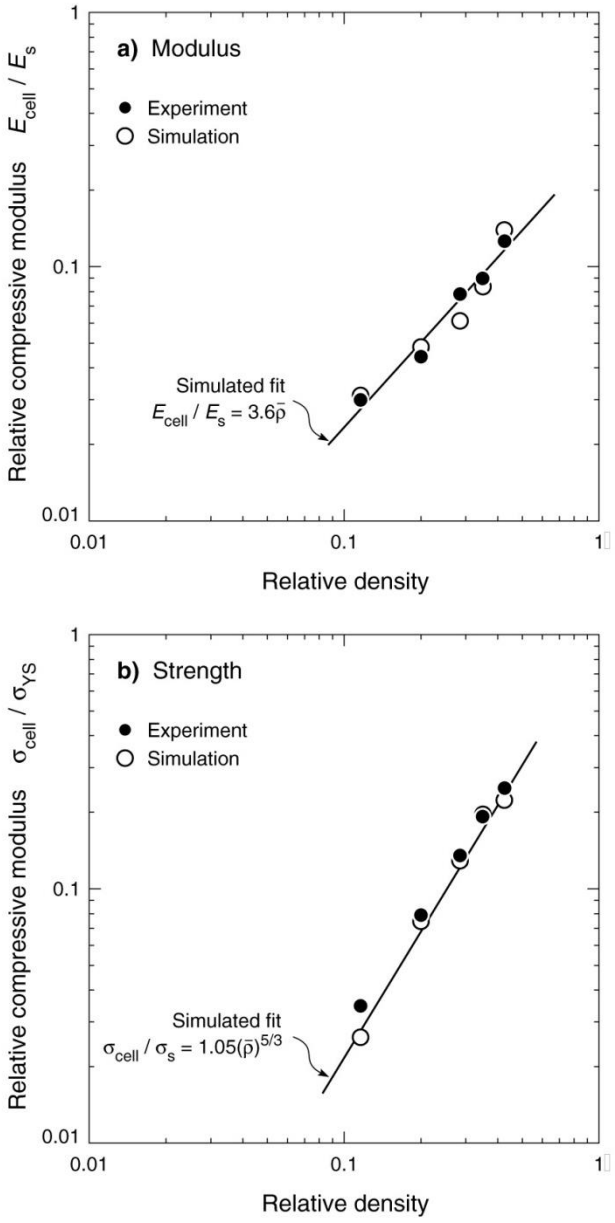

Figure 3.12 . Dependence of (a) compressive modulus and (b) compressive strength upon relative density. Empirical fits to the data are also shown.

Table 3-2 summarizes the energy absorption for the simulated 3D structures. A comparison of Table 3-1 and Table 3-2 shows only small differences between the measured and simulated energy absorptions. The insignificant deviations demonstrate the good predictive accuracy of the simulations. However, the energy absorption efficiency showed more significant variability between measurements and simulations. This arose because of the product of the simulated densification strain and peak strength was less accurately estimated.

Table 3-2. Energy absorption values for simulated 3D structures

Topology	**Relative Density, $\bar{\rho}$**	**Peak Stress, σ_p (MPa)**	ε_D	E_v **(MJ/m^3)**	E_m **(J/g)**	**Theoretical E_m^* (J/g)**	**Energy Absorbing Efficiency**
3D	42.7	62.0	0.49	25.7	22.3	22.7	0.97
3D	35.1	53.8	0.45	21.0	22.1	23.1	0.95
3D	28.6	36.0	0.47	15.7	20.3	20.6	0.98
3D	20.1	20.7	0.64	10.9	20.3	23.6	0.85
3D	11.6	7.3	0.70	3.5	11.2	16.4	0.68

Chapter 4. Dynamic Core Response

This chapter investigates the dynamic out-of-plane compressive response of the same structure explored quasi-statically in Chapter 3. The dynamic crushing resistance and collapse mode mechanisms are explored via direct impact Hopkinson bar experiments that utilized high speed photography. Finite-element analysis is also used to investigate the dynamic deformation modes, and to estimate the stresses at the impact and distal faces of the structures.

4.1. Experimental Protocol

The dynamic out-of-plane compressive response of the core structures were measured using a series of direct impact Hopkinson bar tests where the force was

measured on the samples back face with a strain-gauged Hopkinson [116] bar while synchronously recording the strain with a high speed video camera, Figure 4.1. Each specimen was attached to the end of a stationary 2 m long, 7.62 cm diameter Hopkinson bar using Loctite Super Glue adhesive. A striker projectile was accelerated with a gas gun towards the front face of the specimen, and the force transmitted by the sample was measured by diametrically opposed strain gauges placed 0.76 m from the impact end of the Hopkinson bar. The striker diameter was equal to both the inner diameter of the gas gun barrel and the diameter of the Hopkinson bar. The gas gun barrel measured 4.50 m in length; to achieve an impact velocity $v_0 \leq 75\ ms^{-1}$, the projectile was positioned 3.2 m from the exit of the barrel. Higher velocities were achieved by placing the striker projectile 3.8 m from the gun barrel exit. All initial striker velocities were measured near the barrel exit using four laser velocity gates each spaced 20 mm apart as shown in Figure 4.1. The figure also defines all other relevant geometrical parameters of the test set-up. The Hopkinson bar was made from aluminum alloy 6082-T6 whose yield strength was 310 MPa and measured longitudinal elastic wave speed $c = 5108\ ms^{-1}$. A time window of 485.5 μs was therefore available for measurements before elastic reflections from the distal end of the Hopkinson bar complicated interpretation.

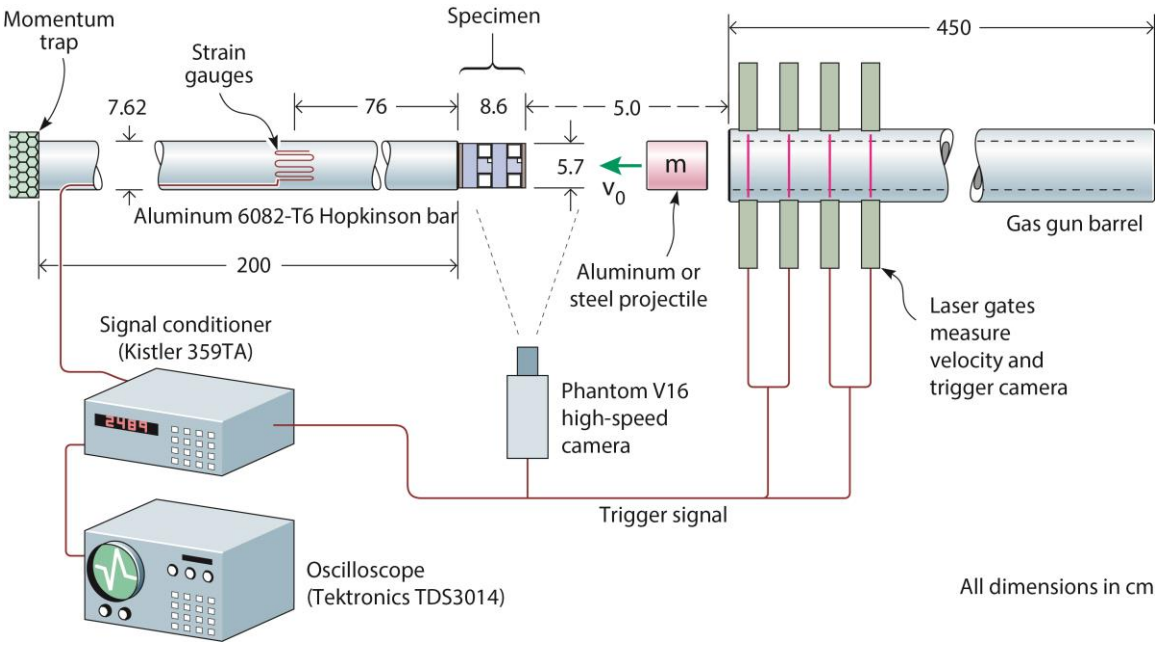

Figure 4.1. Schematic diagram of the Hopkinson bar arrangement used for dynamic testing.

The precision of the measurements was derived from multiple calibration tests. An example of one of the results is shown in Figure 4.2(a). The aluminum Hopkinson bar was impacted by an aluminum projectile that was 7.6 cm in diameter, 54.0 cm in length, and had a mass of 6124 g. In this example, it impacted the Hopkinson bar with an initial (pre-impact) velocity, $v_0 = 7.3\, ms^{-1}$. Figure 4.2(a) has set time *t = 0* as the first arrival of the stress pulse at the strain gauges, and shows that the rise time of the stress pulse at the gauge location was 35 μs for the bar/strain gauge system used here. This rise time limitation only became significant at the highest impact velocities where substantial specimen compression could occur within the first 5 μs after impact.

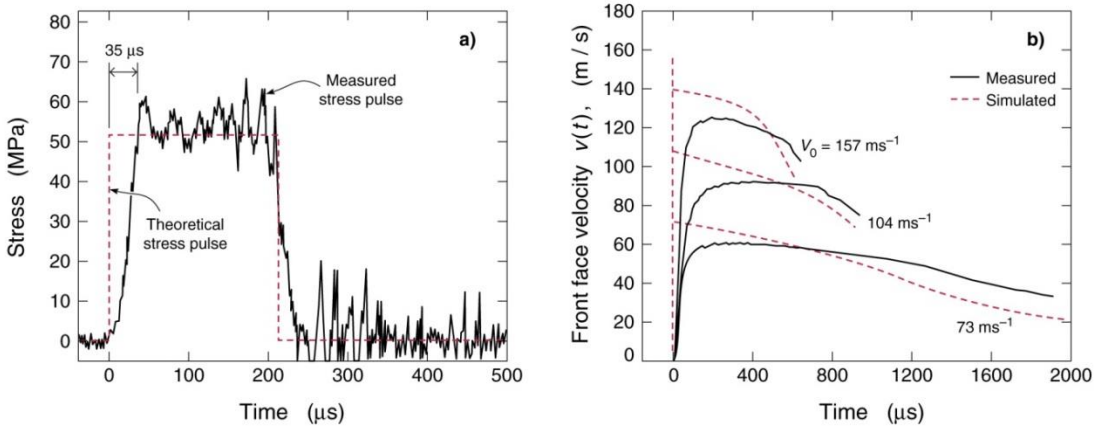

Figure 4.2. a) Transmitted stress versus time history of the aluminum Hopkinson bar following impact by a 54.0 cm long, 7.6 cm diameter aluminum striker with a mass of 6.124 kg and velocity $v_0 = 7.3ms^{-1}$. *The axial stress in the aluminum Hopkinson bar (predicted by 1D elastic wave theory) was 51.3 MPa (dashed curve). b) The measured front face velocity for a 3D tube structure with* $\bar{\rho} = 20.1\%$. *Simulated data is also shown.*

Elastic wave theory [117] gives the axial stress transferred to the aluminum Hopkinson bar in this test as $\rho c v_0/2 = 51.3\ MPa$, where $\rho = 2755\ kg * m^{-3}$ is the density and $c = 5108\ ms^{-1}$ is the extensional wave speed of the aluminum Hopkinson bar. The predicted axial stress pulse (red dotted curve in Figure 4.2(a)) is within 16% of the first stress measured peak (61.2MPa), and is reasonably close to the average measured stress. The measured calibration test stress drops to zero at $t = 236\mu s$ which corresponds to the arrival of the elastic stress pulse reflected from the free end of the striker.

Russell et al. [118] have shown that the striker projectile kinetic energy governs the compressive strain of a crushable sample and the transient velocity imposed upon the impacted end of the specimen. For the samples tested here, impact experiments were performed at nominal impact velocities of 75, 100, and 150 ms^{-1}. A steel striker of mass M = 2.5 kg was used for impact velocities $v_0\ of\ 75\ and\ 100\ ms^{-1}$ and it imparted sufficient momentum to crush most of the samples beyond their densification strain. An aluminum striker of mass M = 0.75 kg was used for tests at impact velocity $v_0 \geq 150\ ms^{-1}$. High speed video images of the samples were recorded using a Phantom V16 high speed camera to measure the compression rate, to identify failure modes and to confirm that the striker kinetic energy was sufficient to provide a constant velocity sample compression up to nominal strain of at least 50%. Inter-frame times of 10 μs and exposure times of 0.5 μs were used by the high speed camera. Figure 4.2(b) shows a typical impact face velocity result for a 3D structure with $\bar{\rho} = 20.1\%$; the front face velocity rose quickly upon striker impact to a peak crushing velocity and then fell slowly during continued crushing. The actual crush velocity was always slightly less than that of the striker just prior to impact, and remained relatively constant during crushing to the densification strain. As the relative density was increased to $\bar{\rho} = 42.7\%$, constant velocity compression ceased at a core compressions of 20% and the samples were not completely crushed even with the more massive striker. In the results to follow, we designate each test by the incident impact velocity, v_0, of the striker.

4.2. Finite Element Analysis Protocols

Finite element (FE) techniques have been used to study the 1D, 2D, and 3D tubes dynamic compression. The aims of this aspect of the investigation were to; (*i*) validate the analysis method by comparing the predicted and measured dynamic crush resistance of the tube structures; (*ii*) investigate the dynamic collapse mechanisms responsible for the mechanical responses of the cellular tube structures; (*iii*) determine the stresses imposed on the front (not experimentally measured), and (*iv*) rationalize the absence of strain rate strengthening of the structure.

4.2.1. The FE Model

All the tests were analyzed using finite element simulations conducted using the explicit version of the commercial, non-linear finite element package IMPETUS Afea Solver® [119]. The geometry and relative density of the modeled tube specimens were designed to be the same as the measured specimens, reported in Table 4-1, but following the usual practice [120, 121, 122], small imperfections (described below) were incorporated in the models to account for the manufacturing defects such as tube misalignment and tube wall thickness variability seen in the tested specimens. The modeled sandwich structure geometry was merged with a modeled Hopkinson bar of the same dimensions and strain gauge placement as shown in Figure 4.3. The Hopkinson bar

model included a cylindrical gridded region, at the same location as the experimental strain gauges, where the axial displacements and forces could be inferred.

The FE models were constructed using cubic hexahedral elements. Meshing specifics are summarized in Table 4-1. A mesh sensitivity study indicated an in-plane nodal spacing approximately equal to the tube wall thickness (t) was sufficient to provide converged solutions for impacts with tube core structures. One cubic hexahedral element was therefore used through the thickness of each tube wall. The nodes of the adjacent tubes were merged prior to the simulation, thus representing a perfect braze zone with no interface failure criterion [123]. The contact formulation in the software is based on a penalty formulation [127]. Simulations with uniform wall thickness models resulted in higher strengths than observed experimentally, and so imperfections to the geometries were introduced to trip buckling and better predict the stress-strain curves. The imperfections were modeled as a displacement of the lowest order measured eigenmode to each tube wall. For most modeled structures the first order eigenmode amplitude was set at 0.1 times the tube wall thickness; however, the un-notched tube structure required a larger amplitude imperfection (0.3 the tube wall thickness) to match the experiments.

Table 4-1. Tube geometries and velocity-time function values used during FE simulations.

Topology	Relative Density, $\bar{\rho}$	Cubic hexahedra elements	Linear hexahedra elements	Nodes
1D	6.7	2,176	_	88,958
2D	16.3	5,440	_	297,854
3D	20.1	7,264	_	403,838
3D	11.6	5,356	1,936	345,958
3D	42.7	4,592	_	253,294
1D, No Notches	7.3	450	_	28,192
3D, No Notches	21.0	2,240	450	205,376

All the simulations introduced a cylindrical projectile with the same dimension and mass as the experimented projectile. An initial velocity (v_0) was applied to the simulated projectile that matched the measured projectile velocity recorded by the laser gates in the experiment. Conservation of momentum during the inelastic collision between the projectile and the specimen resulted in a decrease in projectile velocity, as shown in Figure 4.2(b).

4.2.2. Material Properties

The material properties described in section 3.6.2 for the cellular sandwich structure were also used for this aspect of the dissertation. Using the AA6061-T6 piecewise linear strain hardening model with a von Mises yield surface and an equivalent plastic strain failure criteria model, a uniaxial tensile test was simulated at the measured strain rate and test temperature (25°C), and compared well to the measured Cauchy stress- logarithmic strain curve, Figure 2.6. The response at a strain rate of $10^3 s^{-1}$ is also shown, and confirms the modest strain rate dependence of the alloy.

The Hopkinson bar was fabricated from a general AA6082-T6 and the von Mises flow stress is defined by a form of the Johnson-Cook constitutive model:

$$\sigma_y = (A + B(\epsilon_{eff})^n) \cdot \left(1 + C \cdot \ln\left(\frac{\dot{\epsilon}_{\text{eff}}}{\epsilon_0}\right)\right) \cdot \left(1 - \left(\frac{T - T_0}{T_m - T_0}\right)^m\right) \qquad (4.1)$$

where ϵ_{eff} is the equivalent plastic strain and A, B, n, C, and m are material constants. The first term on the right hand side of Eq. (4.1) governs the strain hardening and the constant A represents the initial yield strength, and B and n are both hardening parameters. The second term on the right hand side of Eq. (4.1) governs strain rate hardening and the constant *C* is the strain rate hardening parameter, and ϵ_0 is a user defined reference strain rate parameter. The last term of Eq. (4.1) controls thermal softening of the material. The coefficients used in conjunction with Eq. (4.1) to model the Hopkinson bar, aluminum projectile, and steel projectile are provided in Table 4-2,

which were derived for a general AA6082-T6 [124], AA6061-T6 material [125] and 4340 steel [126].

Table 4-2. Material constants for AA6082-T6 Hopkinson bar, AA6061-T6 projectile and 4340 steel projectile

Material	**Elastic constant and density**			**Yield stress and strain hardening**			**Strain rate hardening**		**Temperature softening and adiabadic heating**		
	E (GPa)	v	ρ $(kg \cdot m^{-3})$	A (MPa)	B (MPa)	n	ϵ_0 (s^{-1})	C	T_0 (K)	T_m (K)	m
AA6082	70	0.3	2700	428	327	1.008	$5*10^{-4}$	0.007	293	855	1.31
AA6061	70	0.3	2700	270	98	6.0	$5*10^{-4}$	0.001	293	893	1.0
4043 Steel	210	0.3	7850	796	510	0.26	$1*10^{-2}$	0.014	293	1793	1.03

4.3. Dynamic Compression Results

We begin by examining the dynamic compression of the components (single axial and 2D tube arrays) of the 3D cellular structure, and then investigate the fully integrated structure at three relative densities. Finite element analysis is used to resolve the tube collapse modes and to estimate the impact face pressure.

4.3.1. Axially Loaded Tubes

4.3.1.1. Notched Tube Response

The back face pressure versus core strain response of notched tubes impacted at the three velocities is given in Figure 4.3(b), (c) and (d), and compared with the quasi-static result in Figure 4.3(a). The core strain, ε_c for the impacted samples was defined as $\varepsilon_c = h^{-1}\int_0^t v(t)dt$, where $v(t)$ was the measured sandwich panel impact face velocity as a function of time t, and h the initial core height (85.7 mm). The predicted back face stress versus imposed nominal strain results are overlaid on the experimental data in Figure 4.3, and found to be in good agreement with the measured back face stress. Under quasi-static loading, examination of Figure 4.3(a) shows a plateau-like stress versus strain response after an initial peak in compressive stress of σ_p=4.7MPa. During dynamic impact at 72 m/s, Figure 4.3(b), the stress-strain response remained plateau-like, but with a smaller initial stress peak of 2.9±0.3 MPa for the three impact velocities; consistent with an absence of strain rate (or inertial) hardening. However after the initial peak in resistance, the measured and simulated flow stresses of the dynamically loaded samples gradually increased with strain, especially at the highest strain rate, and also exhibited several small additional stress peaks before the onset of densification (where the stress rose rapidly towards 25 MPa and beyond) at a strain ε_D=0.62±0.06 which was less than the value of 0.72 measured under quasi-static deformation. These results are summarized in Table 4-3.

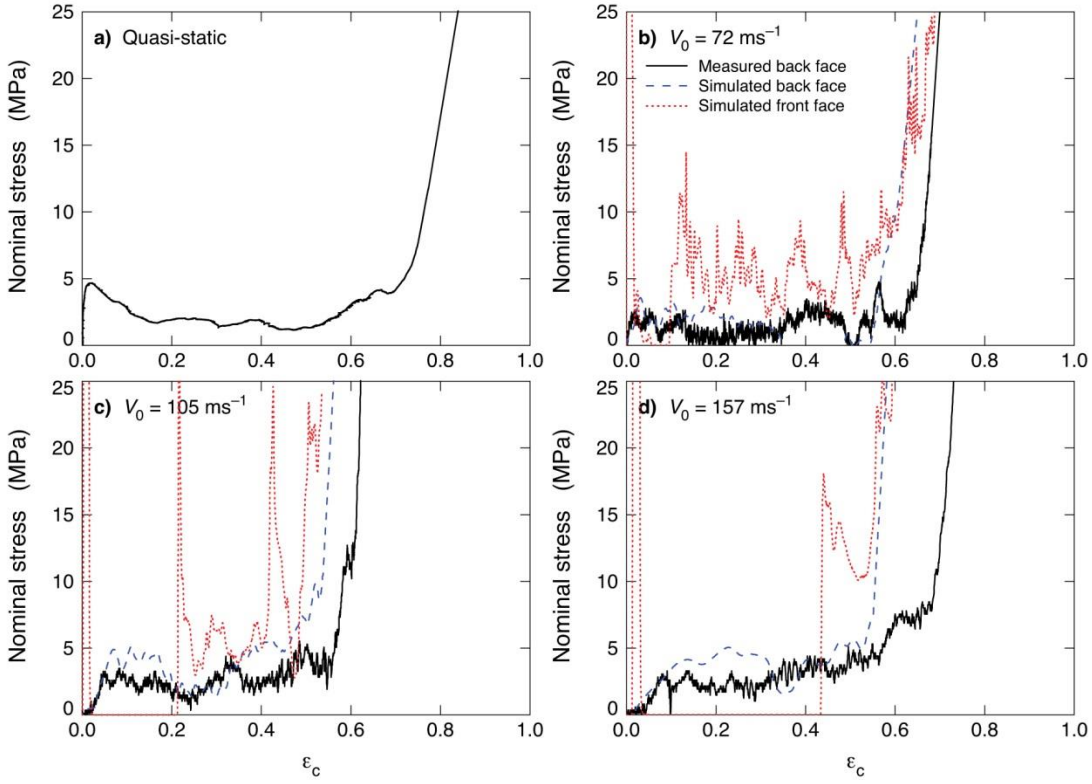

Figure 4.3. The measured and simulated back face stress versus nominal compressive strain for a notched (1D) tube which contributed 6.7% to the relative density of a 3D structure. a) The quasi-static compression response followed by responses after impact at b) 72 m/s, c) 105 m/s, and d) 157 m/s. Simulation results are also shown for the specimens front (impacted) face pressure.

A sequence of high speed video images and corresponding simulations for the notched tube impacted at $v_0 = 72ms^{-1}$ are shown in Figure 4.4. The initial strain suffered by an impacted tube occurred by axial plastic compression of the tube walls at the notches. However, after a small shortening period as the tube walls at the notch compressed, the initial peak in strength was reached as the tube began to buckle about a notch, Figure 4.4(a). This was initiated at the right hand notch (nearest to impact end of the tube) at a nominal strain of slightly less than 0.04, and correlated well with the first

stress peak in Figure 4.3(b). As the nominal strain increased, new notch buckling events progressed from notches at the impact end of the sample towards those at the distal end, Figure 4.4(a) to (b). At a nominal strain of 0.34, the tube walls near all the notches had suffered significant buckling deflections, Figure 4.4(c), and material near the impact end had rotated about the notch. Further axial compression resulted in fracture of the buckled tube wall at the most distal notch, and contact of the tube walls on either side of this notch, Figure 4.4(d). This self-contact coincided with stiffening of the structure, and a rise in compressive flow stress to 4.7 MPa at a nominal strain of 0.56, Figure 4.3(b). This process then progressed from right to left along the tube, resulting in densification at $\varepsilon_D = 0.65$, Figure 4.3(b).

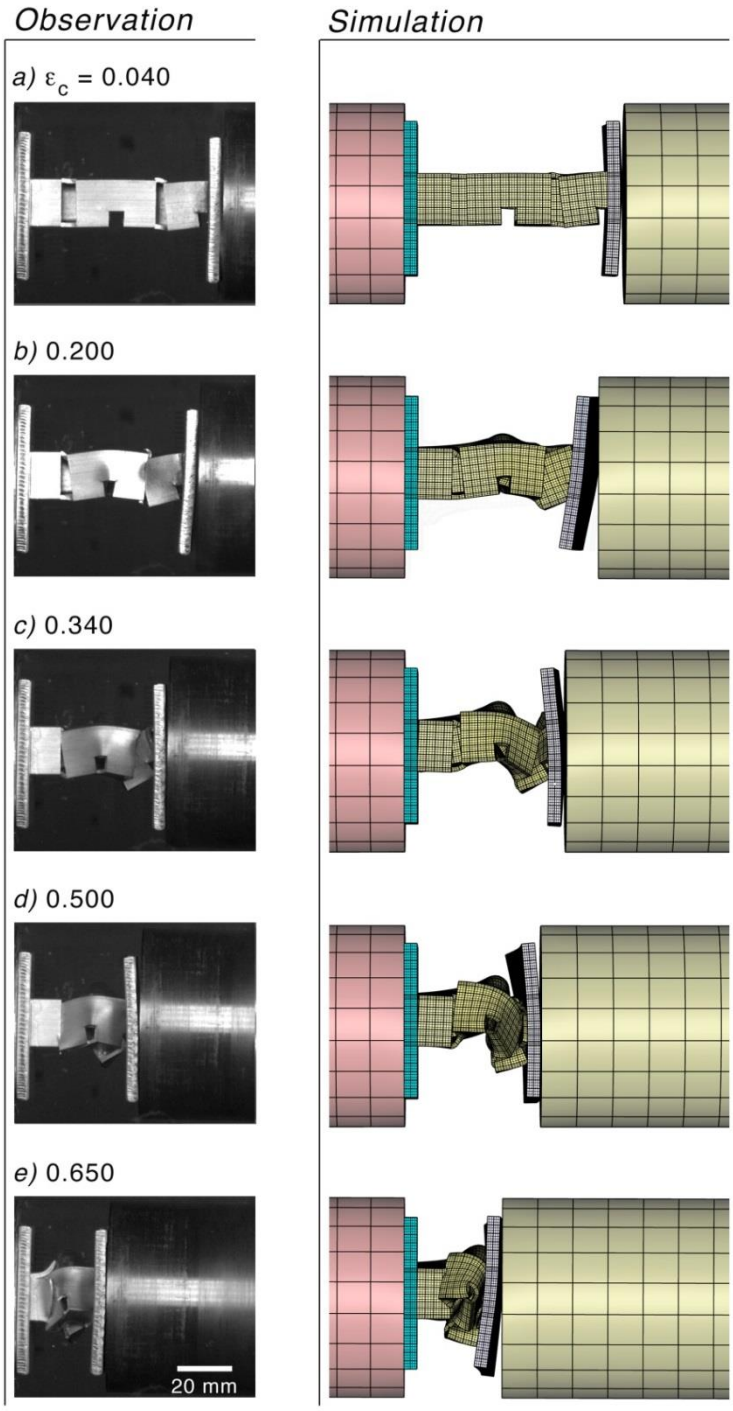

Figure 4.4. Observed and simulated deformation sequence for a notched tube (1D) specimen impacted at an initial velocity $v_0 = 72\ ms^{-1}$. Impact occurs on the right side of both the photographs and the FE simulations.

If the four notches had buckled (without tube rotation) until tube wall contact was established across the 6.35 mm wide notch, the axial displacement of the 76.2 mm long tube would have been 25.4 mm; a strain of 33%. Since the densification strain was about twice this value, we conclude that the combination of tube rotation and axial compression of the tube walls between the notches contributed about the same level of strain as notch deformation to the densification limit. We note that simulation images compared well to those observed with the high speed camera, Figure 4.4. The comparison was best when the strain was below 0.300. Beyond this strain, tube rotations were increasingly difficult to precisely predict due to the global nature of failure, and its sensitivity to imperfections. The simulations verified that the strength was governed by buckling collapse of the tubes, and that this was initiated at the right hand notch nearest to the impact.

Increasing the impact velocity resulted in a similar deformation sequence, but the degree of tube rotation decreased with increased impact velocity, Figure 4.5. This was observed in both the experimental data and that obtained by simulation. Since tube rotation is an inertially sensitive failure mode, and was active during the nominal plateau region of the crush response, its decrease with increase in impact velocity may be responsible for the more rapid rise in plateau flow stress as the impact velocity increased, Figure 4.3(b)-(d). This would prolong axial tube compression (a harder mode) as opposed to tube rotation.

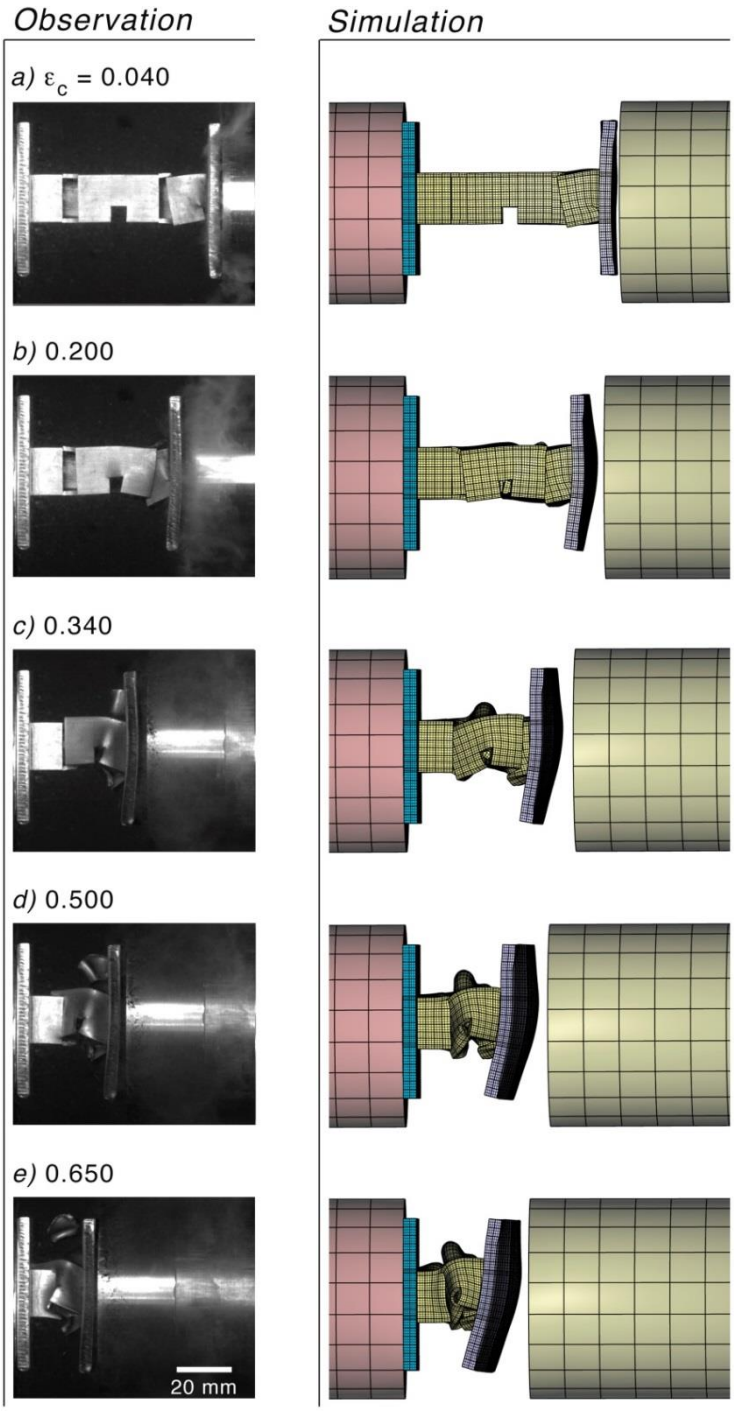

Figure 4.5. Experimentally observed and simulated deformation sequence for a notched tube (1D) specimen impacted at an initial velocity, $v_0 = 157\ ms^{-1}$.

The total absorbed (plastically stored) energy per unit volume, E_v, was obtained from the area under the stress-strain curve shown in Figure 4.3(b). The integration was terminated at the densification strain, where the flow stress began to increase sharply due to material self-impingement. This gave a volumetric absorbed energy, $E_v = 1.0\ MJ/m^3$. Dividing this by the core density $\bar{\rho}\rho_s = 0.067 \cdot 2.7Mg \cdot m^{-3} = 180.9\ kg \cdot m^{-3}$ gives a gravimetric absorbed energy, $E_m = 5.5\ J/m$. If the stress achieved at the first stress peak had remained constant until densification, the gravimetric absorbed energy would have been the theoretical limit of the structure, $E_m^* = 9.2\ J/g$. The notched 1D structure impacted at $v_0 = 72\ ms^{-1}$ therefore had an energy absorption efficiency of 59.0%. The energy absorption and energy absorption efficiency of the tubes rose with impact velocity as the cores peak strength also increased, Table 4-3, and increased beyond unity (using the first stress peak to define the theoretical energy absorption) because of the gradual rise in plateau-region flow stress with strain in the most rapidly crushed samples. The FEA results slightly under-predicted the measured densification strains, most notably for the test at $v_0 = 157ms^{-1}$.

The simulations permit calculation of the front face pressure for each test, and this is overlaid on the experimental and predicted back face responses of Figure 4.4. The initial inelastic impact resulted in very large contact stresses on the front face sheet, and a significant momentum transfer to the lighter sandwich structure, leading to its loss of contact with the striker. As the tube crushing reaction forces decelerated the impact face, the striker eventually re-contacted the sample, and the stress once again increased. The

repletion of this process is responsible for the series of stress peaks observed in the front face stress - strain profiles, Figure 4.4.

Table 4-3. Measured mechanical properties and energy absorption values for tested tubular cellular structures.

Topology	Relative Density, $\bar{\rho}$	Impact Velocity, (m/s^2)	Compressive Strengths, σ_p (MPa)	ε_D	E_v (MJ/m^3)	E_m (J/g)	Theoretical E_m^* (J/g)	Energy Absorbing Efficiency
1D Notched tube	6.7	0	4.7	0.72	11.7	9.4	18.7	0.50
		72	2.6	0.65	1.0	5.5	9.2	0.59
		105	3.2	0.56	1.4	7.7	9.6	0.80
		157	3.0	0.68	2.3	12.7	10.9	1.16
1D tube	7.3	0	10.3	0.79	5.3	26.9	39.6	0.68
		73	10.2	0.77	1.9	9.6	37.2	0.26
		108	11.6	0.75	3.3	16.7	40.8	0.41
		157	11.2	0.72	4.3	21.8	37.1	0.58
2D $0/90_2$	16.3	0	13.2	0.64	1.2	2.7	19.2	0.14
		73	15.4	0.62	2.8	6.4	21.2	0.30
		104	13.4	0.59	4.3	9.7	17.3	0.56
		156	13.5	0.59	4.8	10.9	17.0	0.64
3D cellular structure	20.1	0	20.8	0.61	10.4	19.2	23.4	0.82
		73	18.2	0.59	8.4	15.5	18.2	0.85
		104	17.5	0.56	9.3	17.1	17.0	1.00
		157	17.2	0.56	8.8	16.2	16.6	0.98
3D cellular structure (no notches)	21.0	0	27.1	0.63	12.5	22.0	30.1	0.73
		74	24.6	0.72	10.8	19.0	30.7	0.62
		108	21.8	0.66	10.5	18.5	24.5	0.75
		154	19.5	0.63	9.6	16.9	20.7	0.82
3D cellular structure	11.6	0	7.3	0.59	3.9	12.7	13.7	0.92
		72	7.0	0.73	2.8	8.9	16.3	0.55
		156	7.1	0.73	3.5	11.2	16.5	0.68
3D cellular structure	42.7	0	49.8	0.45	24.4	21.2	29.4	0.73
		73	53.2	–	–	–	–	–
		105	51.4	–	–	–	–	–
		157	56.6	–	–	–	–	–

4.3.1.2. Regular Tube Response

The impact response of a vertical tube without notches is shown in Figure 4.6(b, c, and d), and compared with that measured during quasi-static testing in Figure 4.6(a). The initial peak stress was again unaffected by impact velocity, but had a much higher value of ~11 MPa than that of a notched tube (~2.9 MPa). The flow stress then dropped with continued loading, exhibiting numerous oscillations of stress, until the onset of densification at a very high densification strain $\varepsilon_D = 0.8$. The simulated back face stress-strain responses are compared to experimental results in Figure 4.6, and are in reasonable agreement with the measurements provided they accounted for the experimental (small) variability in the tube orientation. The measured peak strength and energy absorption for the samples are summarized in Table 4-3. Even though the initial peak strength was about four times that of the notched structure, and it had a higher densification strain, the volumetric energy absorption was only about twice that of the notched structure because of the substantial fall in strength following the initial peak in stress, and the highly oscillatory plateau region's response.

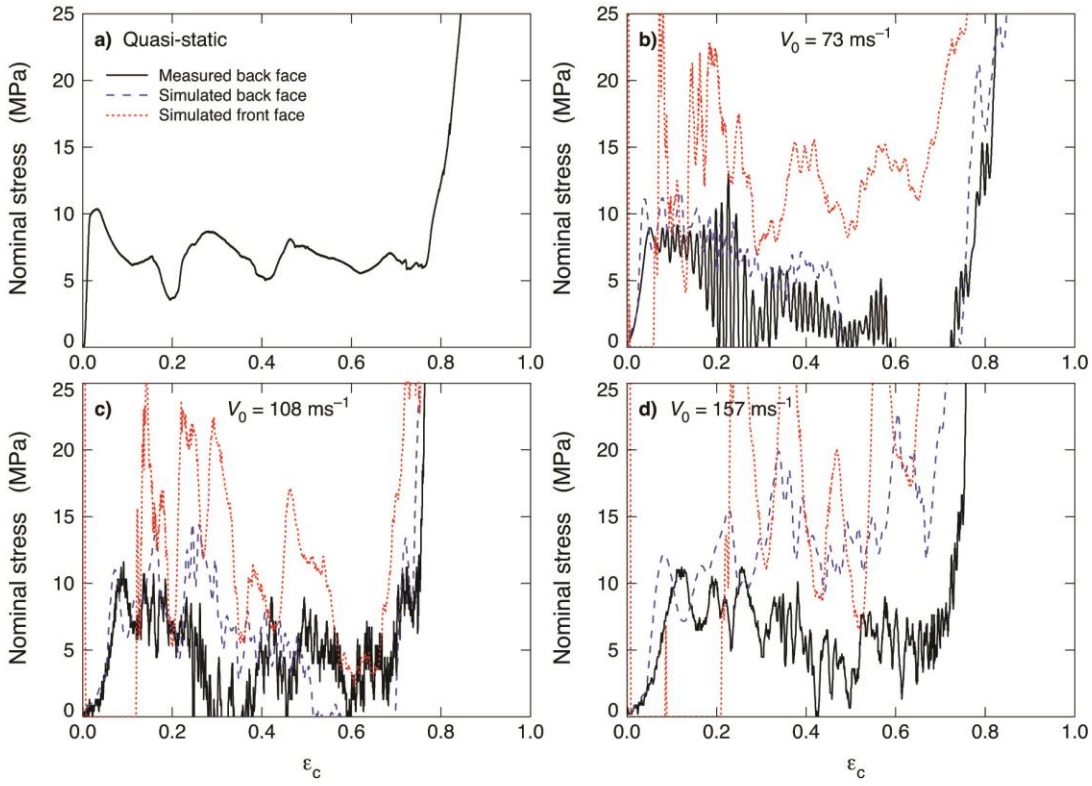

Figure 4.6. The measured and simulated back face stress versus nominal compressive strain of an un-notched 1D tube structure which contributed 7.3% to the relative density of an un-notched 3D structure. a) Quasi-static response, and for impacts at b) 73 m/s, c) 108 m/s, and d) 157 m/s. Simulation results are also shown for the front face of the specimen.

High speed video and simulated images of the collapse process are shown in Figure 4.7. At low strains, the tubes underwent plastic compression and the initial peak in strength at $\varepsilon = 0.04\%$, was correlated with tube wall buckling, Figure 4.7(a). This was followed by failure of the tube-front face bond, rotation of the tube, and tube wall fracture at the apex of buckles, Figure 4.7(b). This process continued resulting in fragmentation (and loss) of the tube walls. This delayed the onset of material self-impingement, and was the origin of the higher than normal densification strain, Figure

4.7(e). The simulated damage progression in Figure 4.7 also shows the significant tube rotation and fragmentation of the tube during dynamic loading[B] observed experimentally. The "spikey" character of the measured stress profile was also seen in the simulation, and the transient partial load drops were linked to tube fracture events. The progressive drop in flow stress with continued straining arose from continued fragmentation at the distal end of the tube until densification at a strain of 0.8.

[B] The response of the tube was highly sensitive to small changes in its orientation. When tubes were perfectly aligned, progressive concertina plastic buckling of the tubes was observed. However, introduction of the small misalignments present in the experiments resulted in the modes shown in the figures.

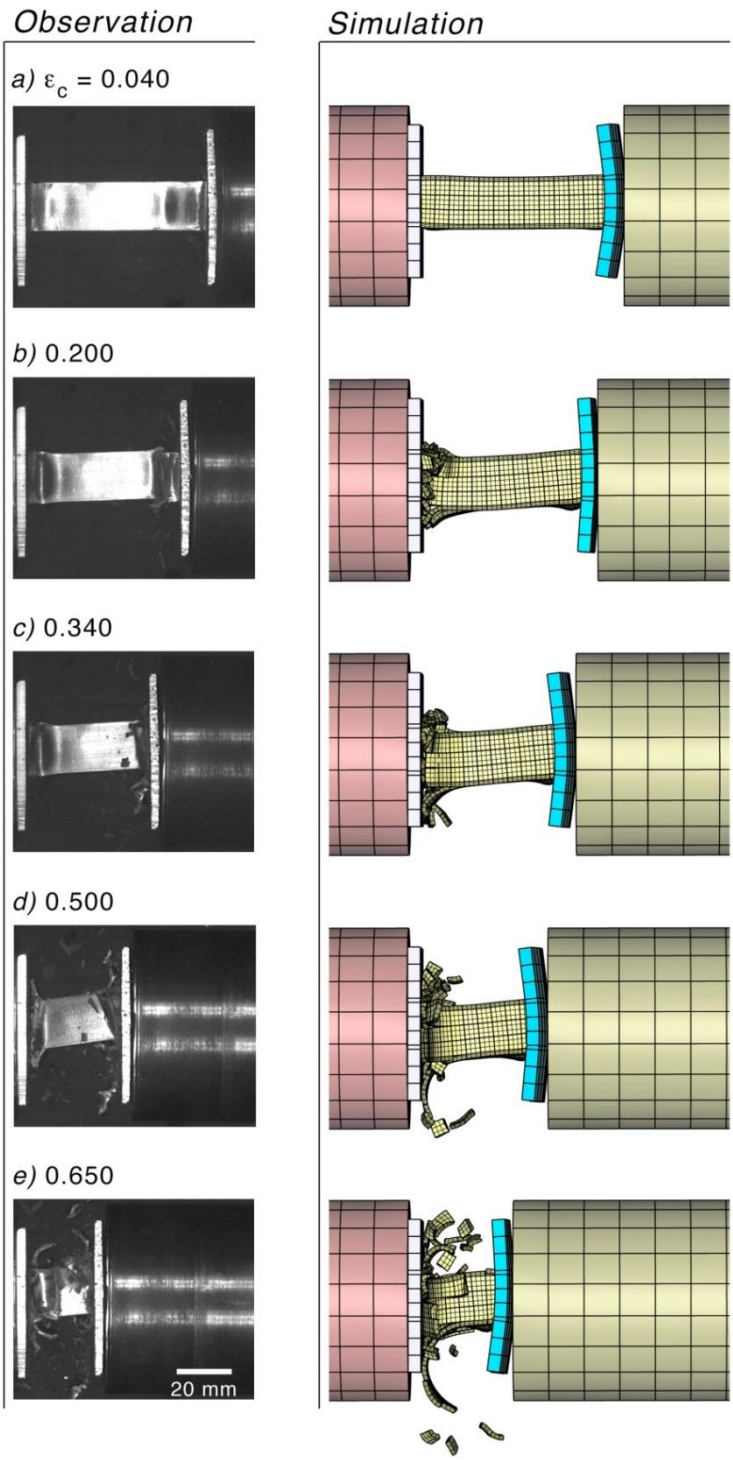

Figure 4.7. Observed and simulated deformation sequence for a 1D tube specimen with a relative density of 7.3% and no notches impacted at an initial velocity, $v_0 = 73\ ms^{-1}$.

4.3.2. Two Dimensional Tube Arrays

The measured and simulated compressive stress versus strain response of the dynamically tested 2D structure is shown in Figure 4.8 (b), (c) and (d) and compared to the quasi-static result in Figure 4.8(a). The stress versus strain responses at all loading rates exhibit three peaks followed by densification. The initial peak stress, σ_p was again independent of loading rate; consistent with minimal strain rate hardening. The load drops after each peak in stress resulted in a low volumetric and gravimetric energy absorptions, Table 4-3, but these (and the energy absorption efficiency) increased with impact velocity because the stress drops decreased in amplitude at higher velocities, Figure 4.8.

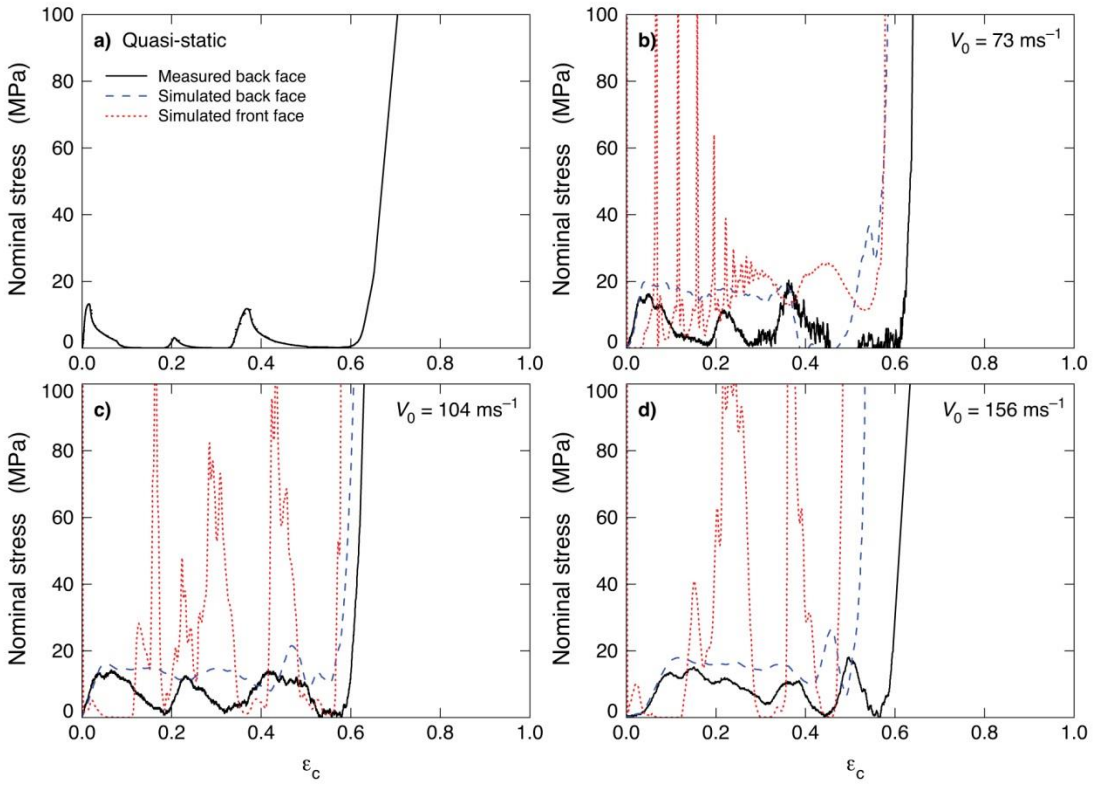

Figure 4.8. The measured and simulated dynamic stress versus normalized nominal strain responses of a 2D tube structure with a relative density of 16.3%; a) quasi-static response, and following impact at b) 73 m/s, c) 104 m/s, and d) 156 m/s.

High speed video observations and simulations, Figure 4.9, indicate that the initial rise to the first stress peak was always correlated with the onset of a high order (short wavelength) buckling mode of the axially aligned walls of the tube layer nearest the impacted face, Figure 4.9(a,b). As the sample continued to undergo compression, the buckling behavior became impact velocity dependent. At an impact velocity of 73 m/s, buckling of the first to buckle (right hand) layer stopped, Figure 4.9(b), and further strain was achieved by initiation of a low order mode of buckling of the other three tube layers.

As the compressive strain reached a value of about 0.2, the deformation localized into the tube layer second from the right, Figure 4.9(c), and the second peak in stress then corresponded to the collapse (aided by wall fracture) of this layer. The third stress peak corresponded to collapse of the tube layer third from impacted end of the sample, Figure 4.9(d). Collapse of the first impacted layer then coincided with the onset of densification, Figure 4.9(e), at a strain of 0.62. As the velocity of impact increased, the initial impact provided sufficient pressure to cause complete (but still high order mode) buckling of the right hand tube layer, and this collapse corresponded to the first peak in stress, Figure 4.10(a and b). The other peaks then corresponded with the progressive collapse of the layers from right to left, Figure 4.10(c to e).

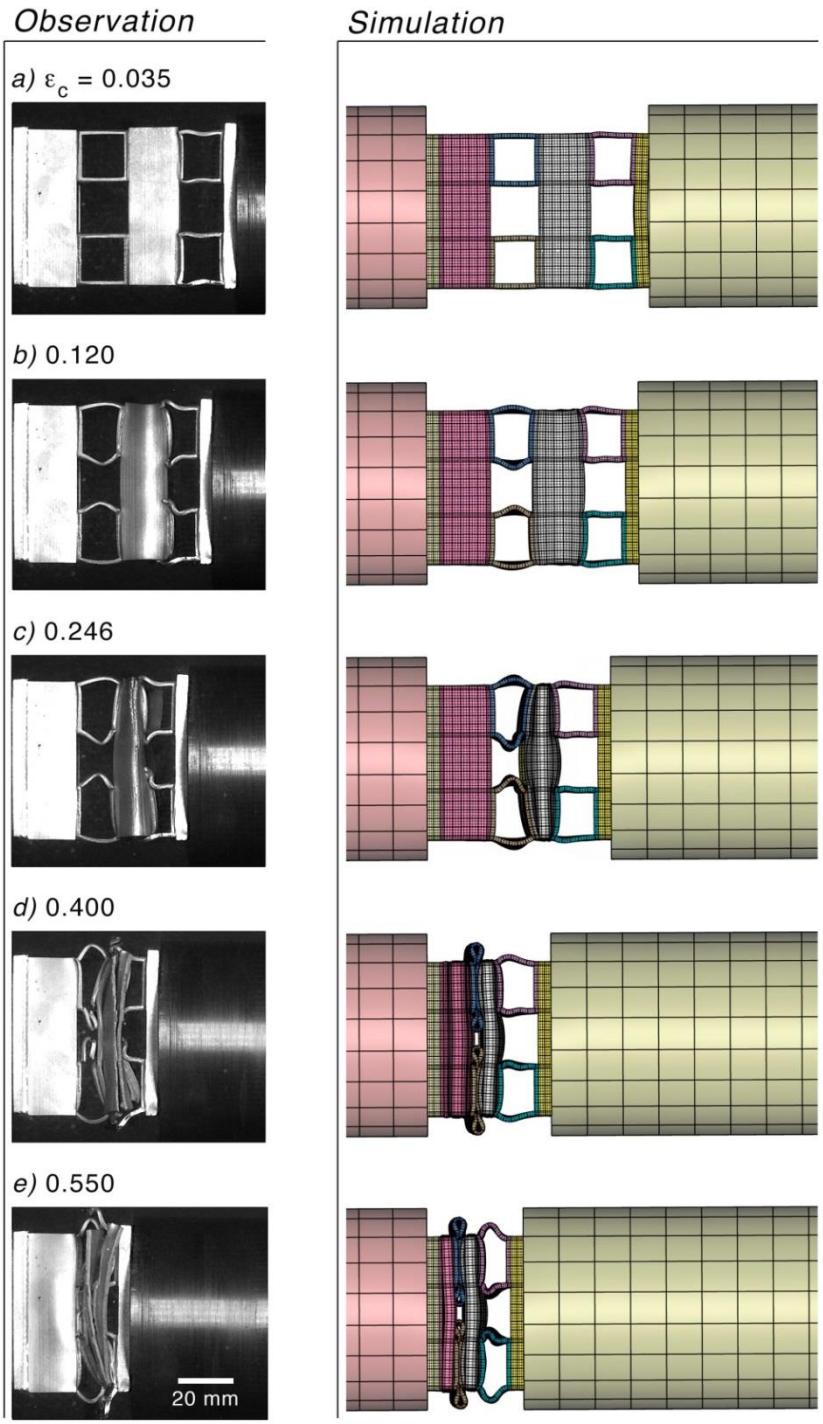

Figure 4.9. Observed and simulated deformation sequence for a 2D specimen impacted at an initial velocity $v_0 = 73\, ms^{-1}$.

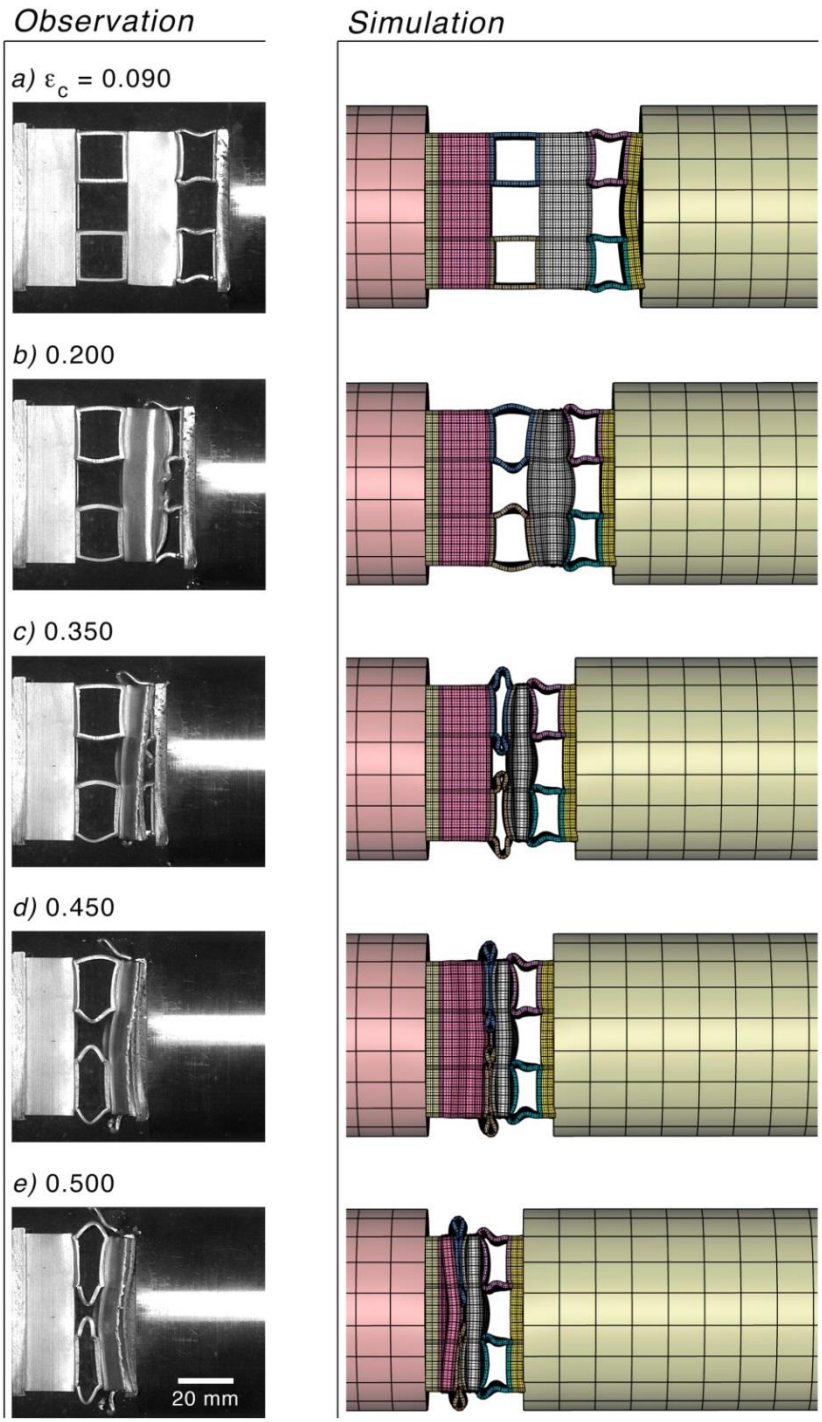

Figure 4.10. Observed and simulated deformation sequence for a 2D specimen impacted at an initial velocity $v_0 = 156\ ms^{-1}$.

The simulated nominal stress versus applied nominal strain results shown in Figure 4.8(b), (c), and (d) compared well with experimental results. While the three peaks in stress are well predicted, the simulations do not fully capture the unloading instability, suggesting that the simulated tube wall fracture process is not completely captured by the approximate approach used here.

4.3.3. Three Dimensional Tube Cores

4.3.3.1. Notched Vertical Tube Response

The 3D structures dynamic responses are shown in Figure 4.11(b), (c) and (d) and again compared to the quasi-static result in Figure 4.11(a). The 3D cores initial quasi-static peak strength, σ_p, was 20.9 MPa while dynamically it was slightly less (varying from 17.2 to 18.2 MPa), and independent of impact velocity, Table 4-3[C].

[C] The difference in strength was consistent with small tube misalignments which have a significant effect upon the small samples tested here. To illustrate, Figure 14 (a), shows a high speed video image of the sample tested at $v_0 = 73ms^{-1}$, and reveals that one of the in-plane tubes side-walls (at the top right of the sample) was not in full contact with the underlying in-plane tube wall, causing it to prematurely fail.

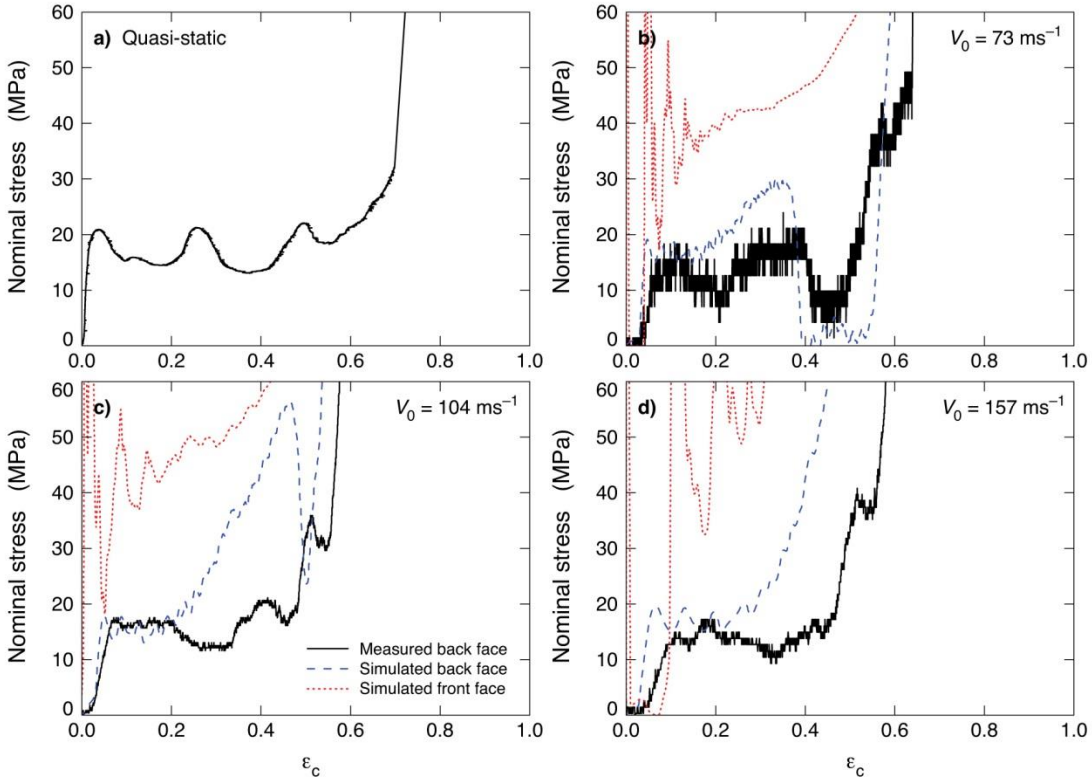

Figure 4.11. The measured and simulated dynamic stress versus nominal strain responses of a 3D tube structure (containing notched out-of-plane tubes) with a relative density of 20.1%. a) quasi-static response, and after impact at b) 73 m/s, c) 104 m/s, and d) 157 m/s.

In general, the dynamically deformed samples exhibited plateau-like compression responses with three small stress peaks like those associated with sequential collapse of the 2D in-plane tubes discussed above. The 3D structures volumetric and gravimetric energy absorptions, Table 4-3, were independent of compression rate. The average volumetric energy absorbed for the four loading rates, was 9.2MJm^{-3}. This significantly exceeded that for the average absorbed energy of 5.8 MJm^{-3} for the components of the 3D system (one notched tube and the 2D tube array, Table 4-4). The energy absorption

efficiency of the 3D structure was independent of compression rate, and varied between 82 and 100%. The high efficiency resulted in part from the rising back ground stress just before densification was reached. This high efficiency, combined with the plateau-like compressive stress – strain response to compressive strains of about 50%, indicates the 3D tube structure to be well suited for impact mitigation applications.

Table 4-4. Summed response of 1D and 2D cores.

Topology	**Sum† of relative densities, $\bar{\rho}$**	**Impact velocity (ms^{-1})**	**Sum of compressive strength, σ_p (MPa)**	**E_v (MJ/m^3)**	**E_m (J/g)**
Notched 1D tube + 2D core	23.0	0	17.9	2.8	5.2
		72	17.4	4.4	8.2
		105	17.3	7.2	13.3
		157	16.8	8.9	16.4
Un-notched 1D tube + 2D core	23.6	0	23.2	6.1	9.5
		73	25.1	4.8	8.5
		108	25.6	8.7	15.4
		157	25.6	11.5	20.3

† The sums of the 1D and 2D cores do not match the measured relative density of the 3D core because of variability in tube wall thickness resulting from the extrusion process and an effect of the braze layer.

The rear face pressure responses from the finite element simulations were in good agreement with the measurements at the lowest impact velocity, Figure 4.11(b). During quasi-static loading, three stress peaks were superimposed on a constant stress plateau response, Figure 4.11(a). However, during dynamic loading, the third peak occurred on a

rising back ground stress response and was most pronounced in the sample tested at the highest impact velocity, Figure 4.11(d). This rising background stress was a characteristic of the vertical notched tube response, Figure 4.3(c and d). A rise in predicted stress during the plateau response was also observed, but for the two most rapidly loaded samples, exceeded that measured beyond a core strain of 20%. The small drops in flow stress after each peak were correlated with the buckling instability and fracture of the walls of one of the collapsing tube layers of the four tube layer, $0/90_2$ in-plane tube system.

The collapse mechanisms were investigated by examining a sequence of high speed video images and finite element analyses. The result for an impact at $v_0 = 73ms^{-1}$ is shown in Figure 4.12. The initial peak in stress occurred at a strain of 0.10, Figure 4.11 (b). From the experimental observations shown in Figure 4.12(b) this was correlated with both notch induced out-of-plane tube collapse and the initiation of buckling of the in-plane tube walls, and was identical to the mechanism previously observed at quasi-static strain rates [123]. By using the FEA post-processor to make the in-plane tubes transparent after a simulation, Figure 4.13(a), we see that by a core strain of 0.04, the notched tube had begun to buckle at the two notches nearest the impacted face. We were also able to confirm that notch tripped buckling of the out-of-plane tube was coincident with in-plane buckling; a result consistent with the earlier observations that the components (single axial and 2D tube arrays) of the 3D cellular structure also buckled at the same strain (4%).

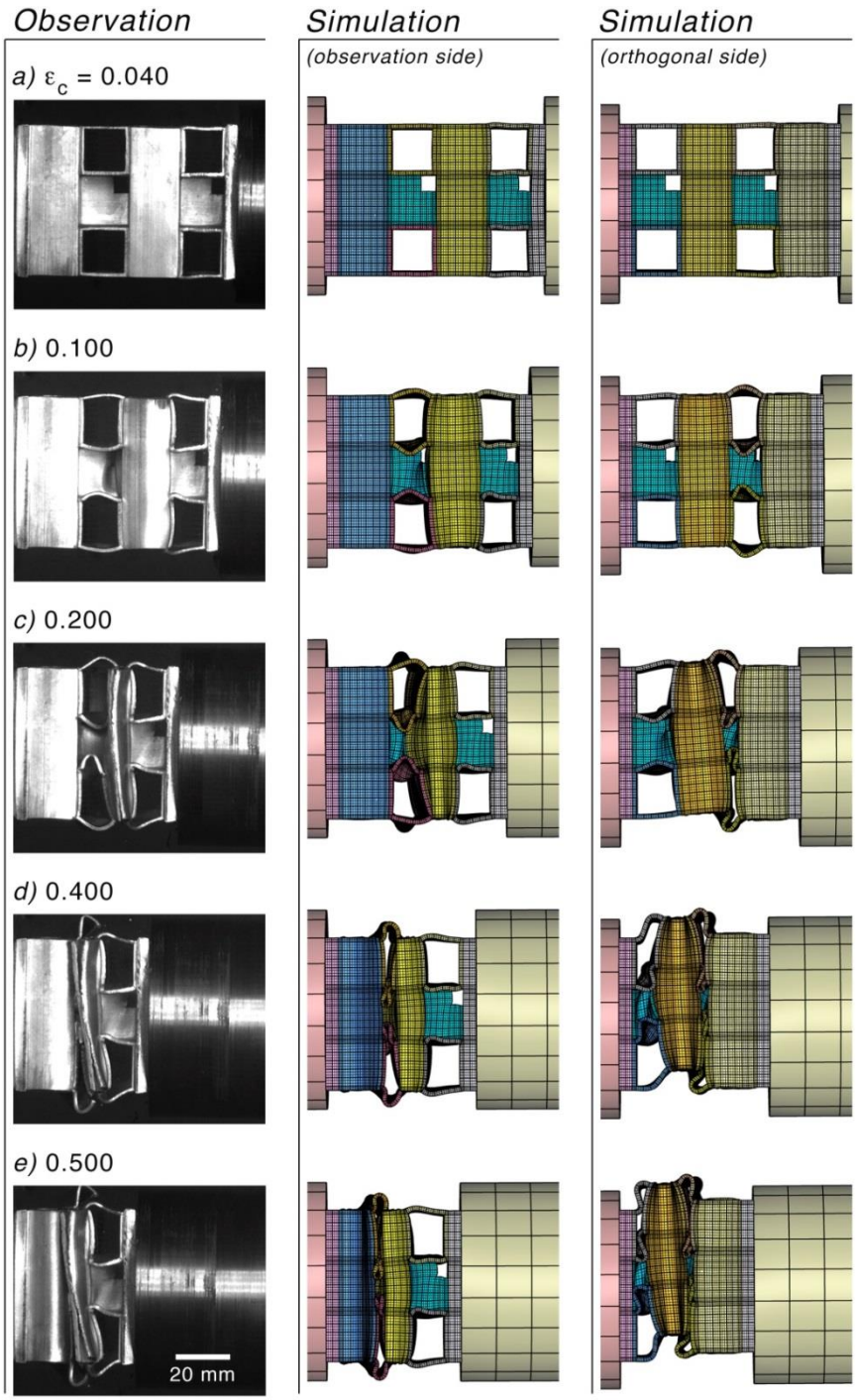

Figure 4.12. Observed and simulated deformation sequence for a 3D specimen with a relative density of 20.1% after impact at an initial velocity $v_0 = 73\ ms^{-1}$. Two sides of the simulated FE model are shown to more clearly reveal the deformation sequence.

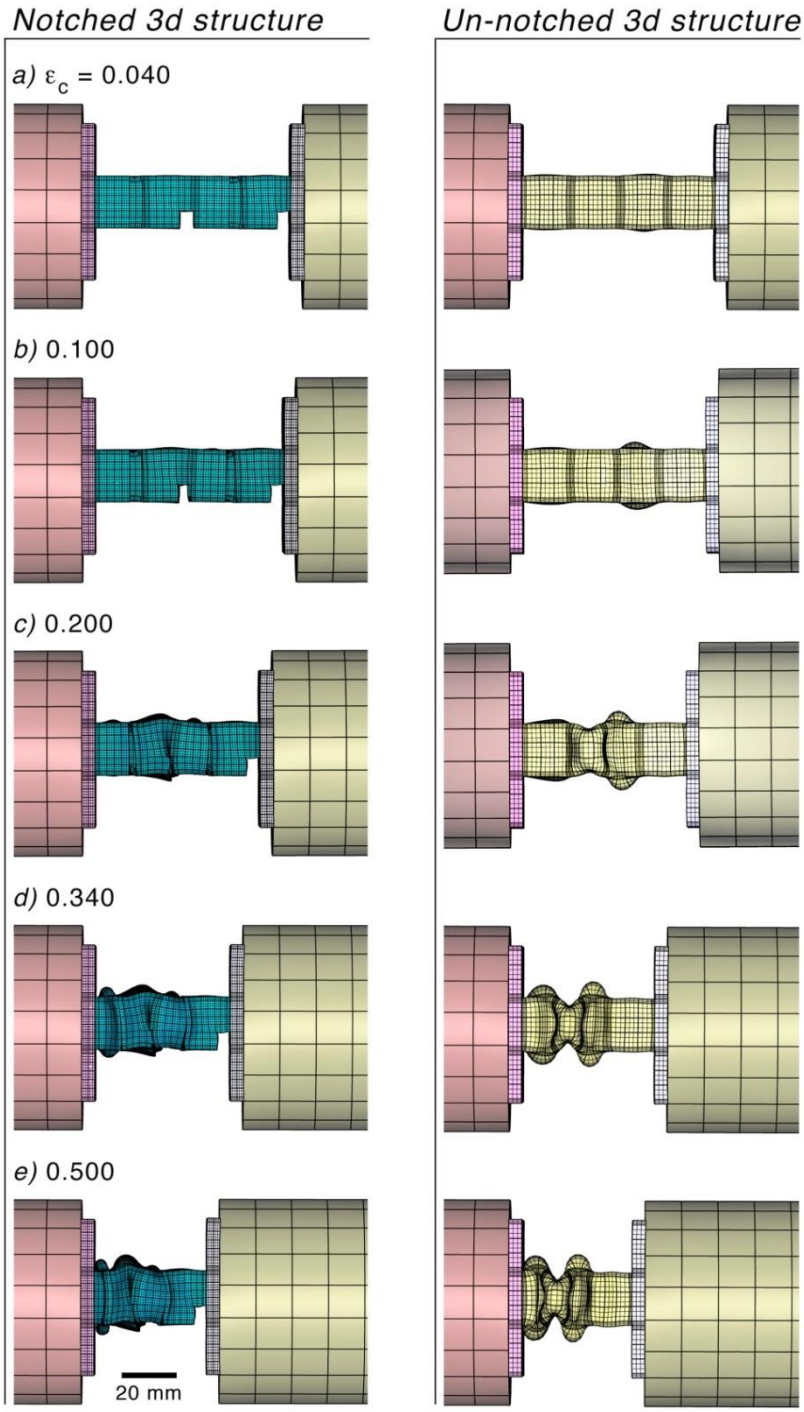

Figure 4.13. Deformation sequence showing the 3D notched and un-notched structures when the co-linear tubes have been made transparent to show the collapse mode of the axial aligned tubes following impact at an initial velocity $v_0 = 73\ ms^{-1}$.

Further compression beyond the initial stress peak resulted in the flow stress softening to a strain of ~20%. The high speed video images and the simulations, Figure 4.12(c), indicate this corresponded with continued buckling of the second in-plane tube layer from the strike face, consistent with observations of the 2D in-plane structure at this impact rate, Figure 4.9(a). Collapse of the second layer, rather than that nearest the strike face appears to have resulted from its higher order buckling mode which requires a higher stress to continue collapse. Following this softening, the tested structure hardened to a second stress peak at a strain of 0.38 followed by a sharp drop in stress at a strain of 0.41. The mechanism responsible for the structures rapid stress drop can be seen by comparing the high speed images and simulations in Figure 4.12(c) and (d). It resulted from the buckling collapse of the third layer of tubes from the strike face. The orthogonal simulated view of the collapse process in Figure 4.12also reveals a significant lateral (transverse shear) displacement as the axial strain increased to 0.4. The simulations also revealed that the second and fourth notches from the impact face contributed to the shearing of the second and fourth in-plane tube layers. This mechanism is not apparent in the high speed video images due to the orientation of the specimen. Further collapse of the structure resulted in core densification (with additional shear of the second and fourth in-plane tube layers) as the fourth in-plane layer and the first in-plane tube layer buckled at $\varepsilon_D = 0.61$.

It is interesting to note that as the impact velocity increased, the transverse (shear) displacement was reduced, and at the highest impact velocity the structure collapsed axially with no transverse displacement, and was observed by both experiment and

simulation, Figure 4.14. This change in deformation mode appears to be linked with the collapse of the vertical notched tube which during isolated testing, Figure 4.4 and Figure 4.5, exhibited significant rotation and transverse displacement at low velocity, but deformed in a more axial manner at the highest impact velocity. To investigate this we show the simulated deformation sequence of the axial tubes of 3D sample tests conducted at 73 and 157 m/s in Figure 4.15. It can be seen that a significant lateral deformation accompanies the low velocity test, but at high velocity, the sample progressively collapsed with no transverse motion.

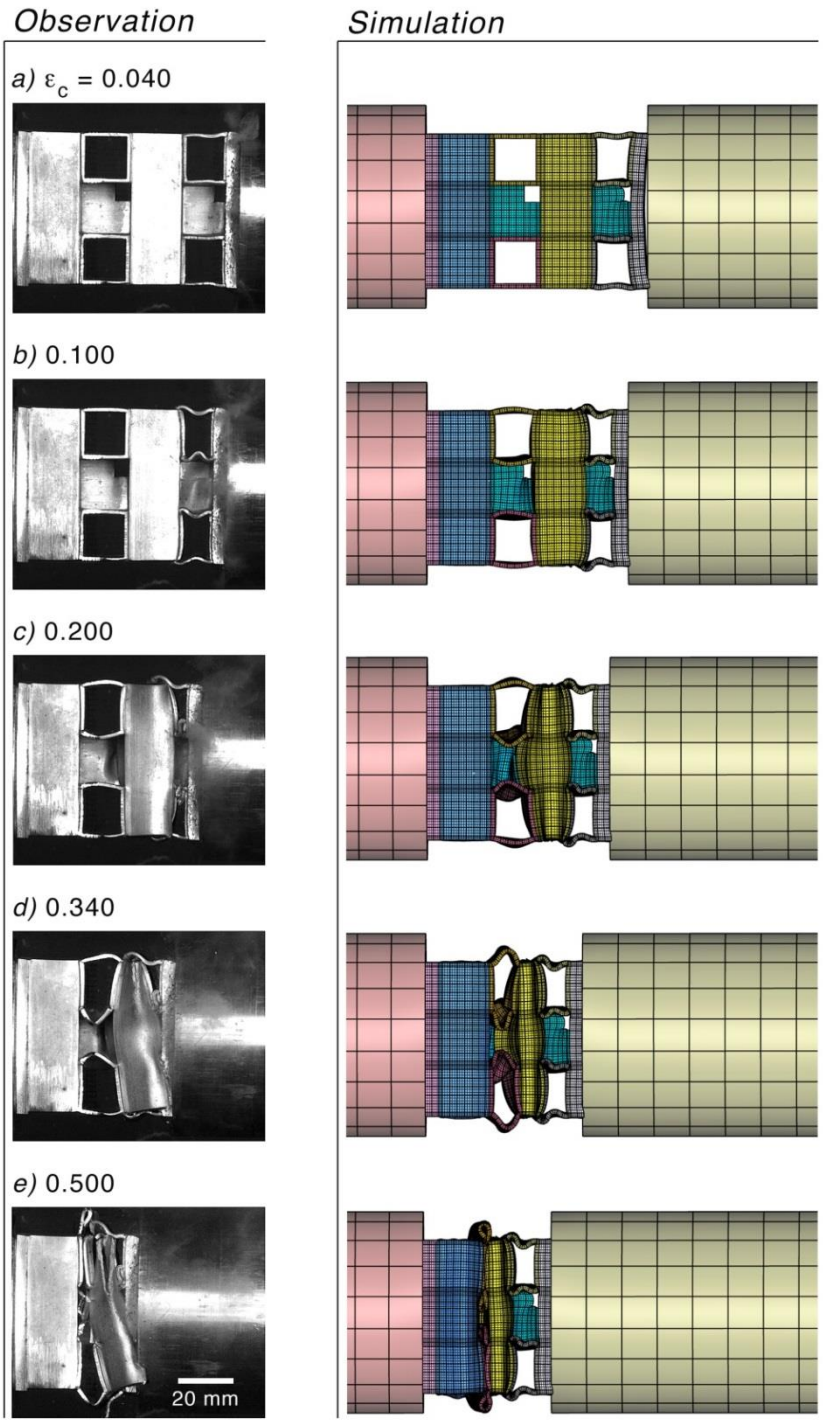

Figure 4.14. Observed and simulated deformation sequence for a 3D specimen with a relative density of 20.1% after impact at an initial velocity $v_0 = 157\ ms^{-1}$.

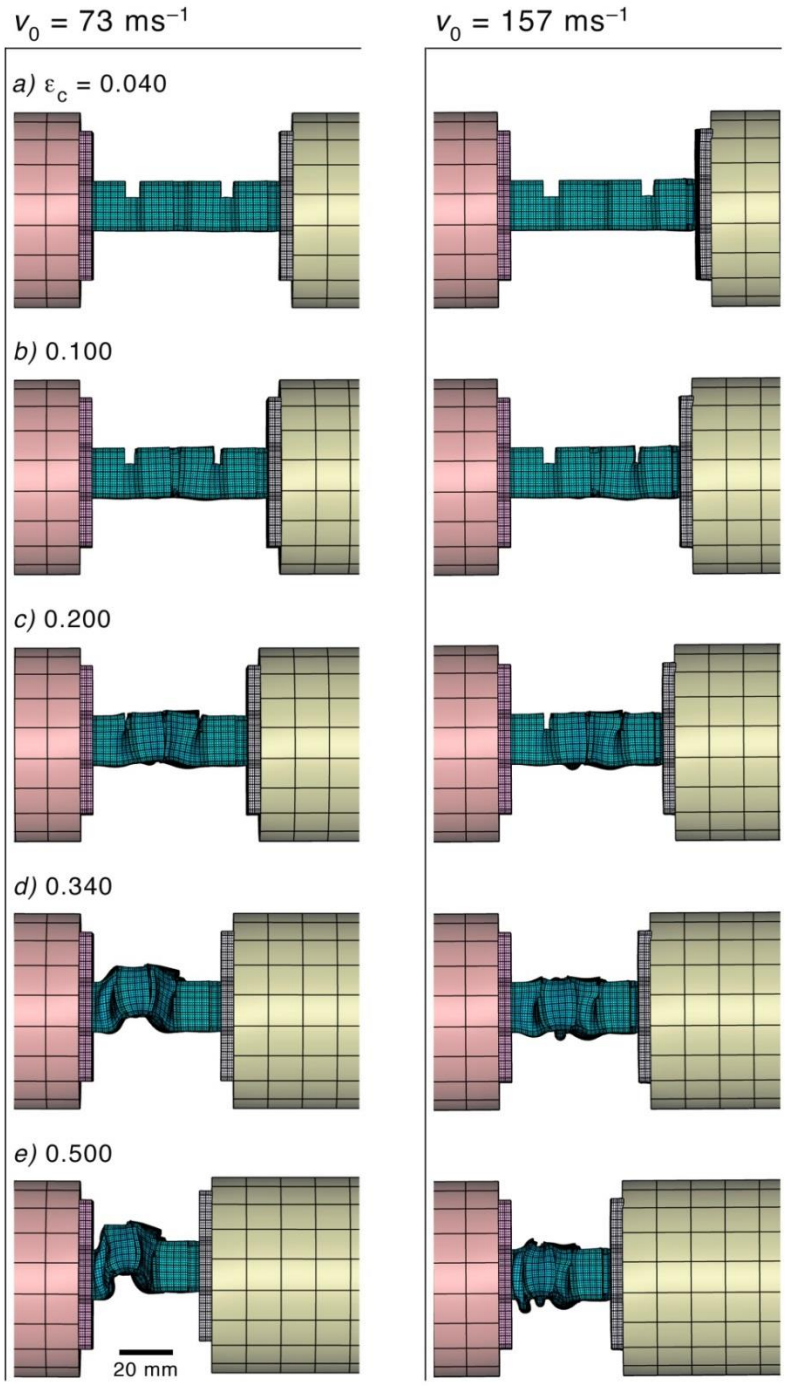

Figure 4.15. Deformation sequence showing the orthogonal side of the 3D notched structure after the co-linear tubes have been made transparent.

The simulations indicate the initial contact stresses between the projectile and the front face sheet increased from 764 to 1520 MPa as the impact velocity increased from $73\ to\ 157\ ms^{-1}$, and greatly exceed those at the distal end of the samples, Figure 4.11 (b), (c), (d). Following striker impact at $v_0 = 73\ ms^{-1}$, the 3D sample was brought into equilibrium much more quickly than the 1D or 2D cores because of its higher mass and core strength. However, as the initial impact velocity was increased, larger amounts of energy were transferred to the specimen during initial contact, and the contact force briefly dropped to zero for impact at $v_0 = 157\ ms^{-1}$, Figure 4.11(d), as sample face sheet-striker separation occurred.

Three dimensional tube cores with relative densities $\bar{\rho} = 11.6\ and\ 42.7\%$, were also tested and the results are summarized in Table 4-4. The structure with $\bar{\rho} = 11.6\%$ was observed to fail in a similar fashion to the $\bar{\rho} = 20.1\%$ structure. At the lowest impact velocity transverse (shear) displacement was present, but at the highest impact velocity the structure collapsed axially with no transverse shear, which resulted in increased flow stress. The 3D cores with a relative density of 42.7% were not completely crushed during dynamic loading, even though the striker was reflected from the specimen (thereby increasing the transferred momentum and applied pressure). While the initial strength could be measured (and is given in Table 4-3), it was not possible to determine the densification strain or energy absorbed by this structure. Simulations indicated that the out-of-plane notched tube in the highest density structure showed no rotation, ever at the lowest impact velocity, where rotation was observed in the other two structures.

4.3.3.2. Regular Vertical Tube 3D Case

The 3D core without notches in the vertical tubes ($\bar{\rho} = 21.0\ \%$)[D] was tested dynamically to determine the role of the notches upon the response of the 3D structure. The measured and simulated compressive stress – strain responses for impacts at various velocities are shown in Figure 4.16. The samples tested at impact velocities of 73 and 108 m/s exhibited several small peaks in stress during the region of plateau response like those seen in the 2D and 3D structure with notched axial tubes. These stress peaks corresponded to the sequential collapse of three of the in-plane tube layers, Figure 4.17. Collapse of the fourth layer coincided with densification (in simulations, the first layer was responsible for densification). The sample tested at the highest impact velocity, Figure 4.16(d), exhibited almost no secondary peaks and had an almost ideal plateau response to a densification strain of about 0.6 (about the same as the quasi-static test).

[D] Its density was less than the sum of the 1D tube and 2D structure due to variations of ±0.14mm in the thickness of the tube walls.

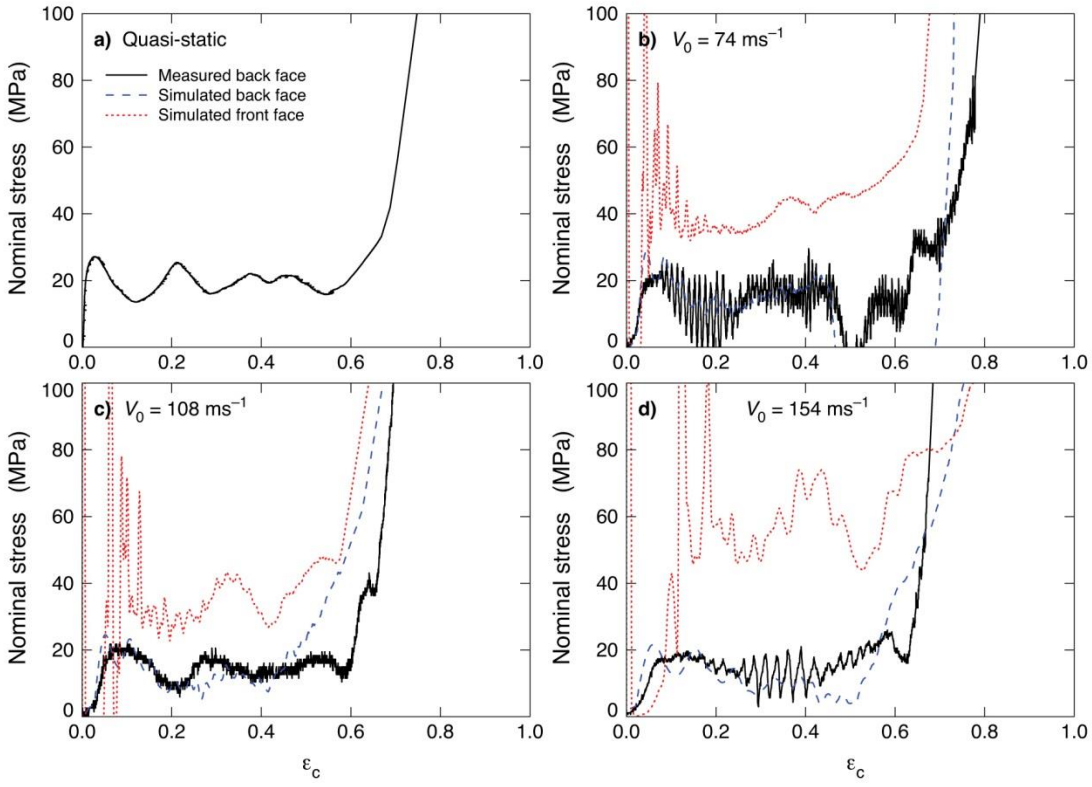

Figure 4.16. The measured and simulated dynamic stress versus normalized nominal strain responses of a 3D tube structure that used out-of-plane tubes without notches. Its relative density was 21.0%. a) Quasi-static response, and following impact at b) 74 m/s, c) 108 m/s, and d) 154 m/s.

The mechanical properties of the cores are summarized in Table 4-3. The cores were slightly stronger than the notched counterpart, consistent with the higher strength of the un-notched out-of-plane tube. The first peak stress and densification strains were again independent of impact velocity. The average volumetric energy absorbed was 10.9 MJm^{-3} compared to 7.8 MJm^{-3} for the average of the summed component tubes (see Table 4.4) indicating much less of a synergistic energy absorption effect in this 3D

structure. The energy absorption efficiencies range between 62 and 82% (Table 4-3) for these cores, making them quite efficient.

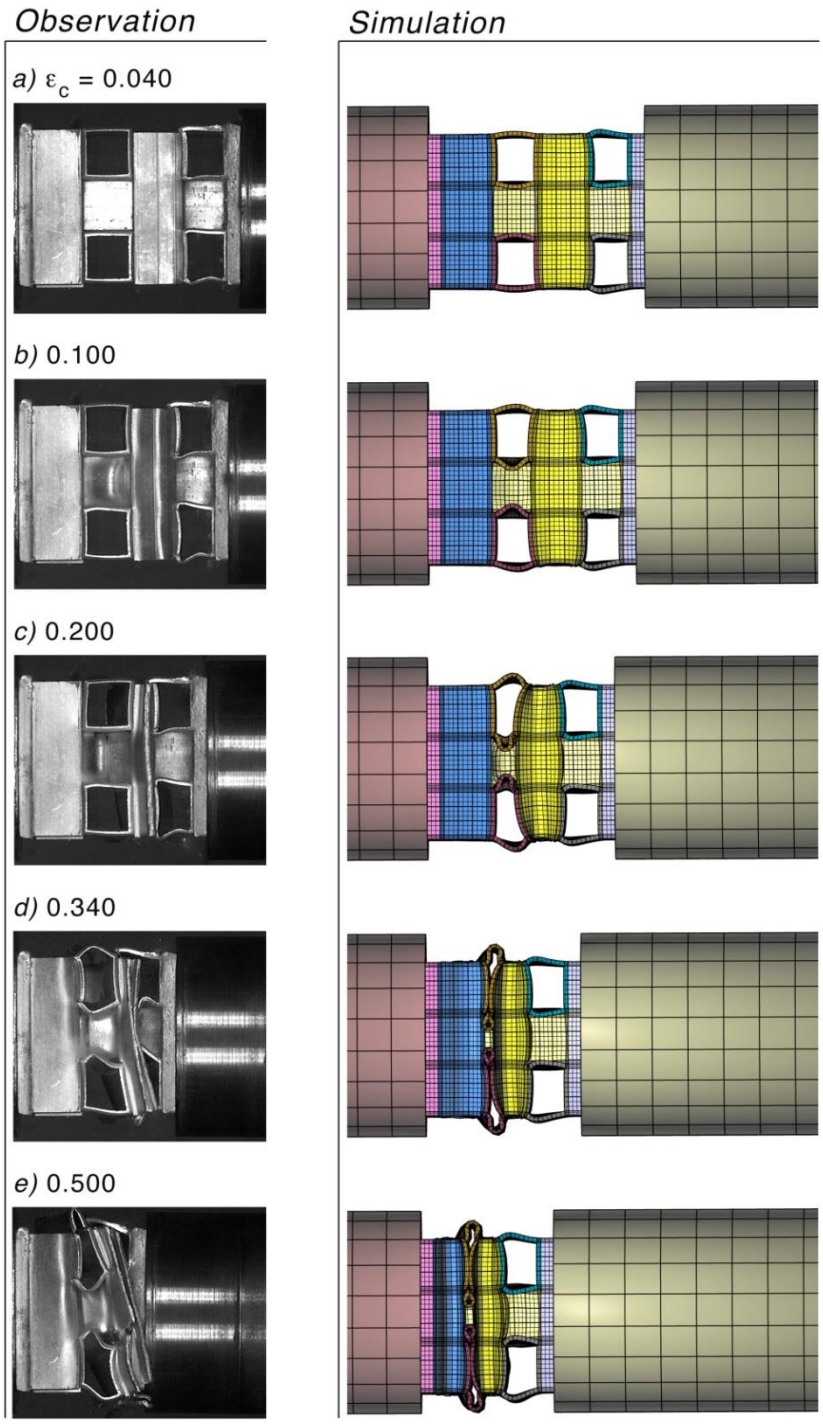

Figure 4.17. Observed and simulated deformation sequence for a 3D specimen whose four vertical tubes had no notches in the axial aligned tube. The sample relative density was 21.0% and was impacted at an initial velocity $v_0 = 74\ ms^{-1}$.

Recall that in section 4.3.1 a regular tube not in perfect axial alignment with the striker underwent tube rotation and buckling with fragmentation. Stress drops were observed to accompany the fracture events. Comparison of the single tube, Figure 4.6, and 3D responses, Figure 4.16, reveal significantly reduced load drops suggesting that vertical tube fragmentation was suppressed. Using the FEA post-processor to make in-plane tubes transparent, the out-of-plane (un-notched) tube walls are shown to have concertina buckled in Figure 4.13 as opposed to the rotation, buckling and fragmentation fracture, Figure 4.7. This appears to be the origin of the extra energy absorbed in the 3D structures compared to their 1D and $[0°/90°]_2$ tube components.

4.3.4. Dynamic Results

Figure 4.18(a) summarizes the dependence of the initial compressive peak stress, σ_p, for the 3D notched structures and their components as a function of the impact velocity v_0 and applied strain rate $\dot{\varepsilon}_c = v_0/h$ (upper scale). The results confirm that the structures initial compressive strength is insensitive to the rate of loading for strain rates up to 2000 s^{-1}. Detailed observations indicate that the axial compression of single notched tubes proceeds by plastic compression of the tube walls followed by buckling at the notches and then of the tube segments between the notches, Figure 4.4and Figure 4.5. The rotation of the tubes became increasingly relevant after crushing to strains of 20%, and was reduced by increasing the rate of compression, consistent with a Calladine and English [43] Type II structure. The suppression of the Type II behavior in rapidly

compressed samples was linked with a rise in flow stress with plastic strain during plateau region compression of single tubes and the 3D structures that contained them (see Figure 4.11).

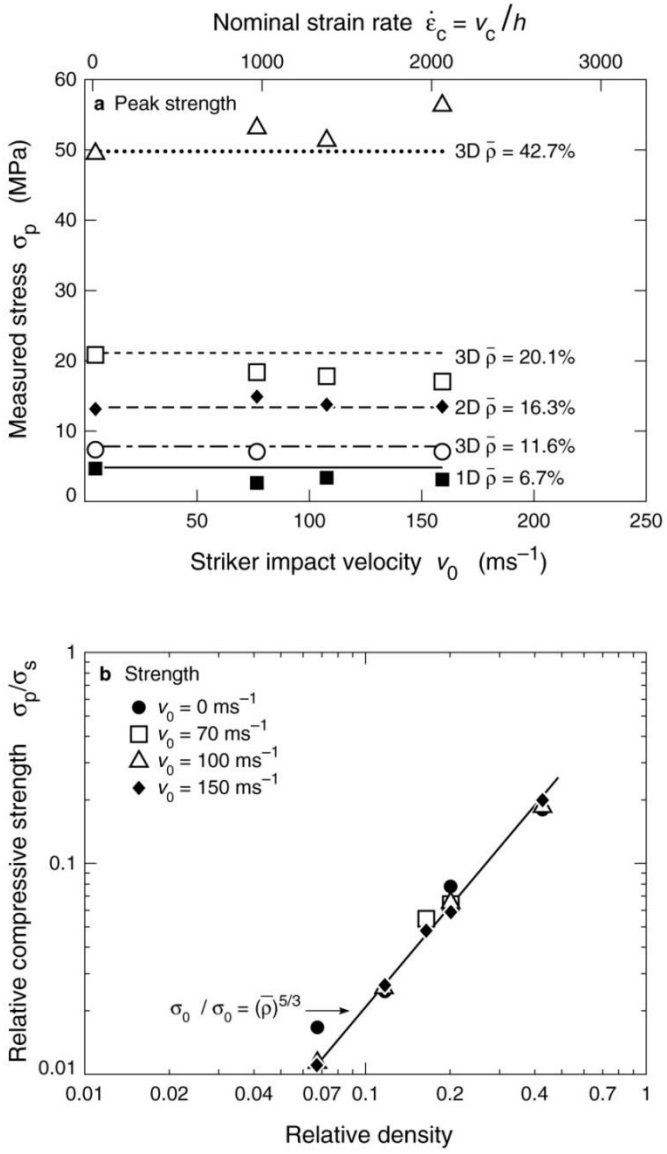

Figure 4.18. (a) Measured back face stresses for the notched tube core structures as a function of impact velocity on applied strain rate for the initial stress profile peak. The horizontal dashed lines correspond to an extension of the quasi-static strength. (b) Dependence of compressive strength upon relative density with an empirical fit.

The $[0^o/90^o]_2$ in-plane tube structures failed by plastic buckling of the tubes walls aligned with the crush direction, and was accompanied by three significant load drops. At low impact velocities, lateral displacement of the tubes (transverse to the loading direction) also occurred. As this lateral displacement was suppressed at higher impact velocities, the drop in load was reduced and the average stress prior to densification increased, Figure 4.8.

The combination of the notched vertical tubes and 0/902 lay-up to form the 3D structure resulted in an increase in plastic energy absorption that significantly exceeded the sum of the energy absorptions of the individual vertical tubes and 2D lay-up, Table 4-4. Analysis of the finite element simulations has revealed that it was a result of suppression of the vertical notched tubes rotation by the in-plane tubes. The axial strain was then achieved by a greater contribution from plastic compression of the tubes walls – a more energy absorbing mechanism than rotation.

Removal of the notches from the vertical tubes increased the axial compressive strength of the tubes. Their mode of compression when made from an alloy in its peak aged state was highly dependent upon the orientation of tubes. The small misalignments present in experiments resulted in a low order buckling mode during initial deformation, followed by rotation and progressive fragmentation. Numerous load drops associated with the fragmentation were observed, and the rotation resulted in a general reduction in compression resistance. Inserting the un-notched tubes in the 3D structure increased the

strength of the structure over that of a similar density 3D structure containing notched tubes, and led to a synergistic effect upon the energy absorption. In this case, detailed analysis of the finite element simulations revealed that the in-plane tubes suppressed rotation and forced the vertical tubes to concertina buckle with additional energy absorption.

Figure 4.18(b) shows that the variation in peak strength, σ_p, of the notched 3D structures with relative densities between 11 and 43% scaled by the strength of the alloy from which it is made, σ_s. The strength exhibits a power dependence upon relative density;

$$\sigma_p/\sigma_s = (\bar{\rho})^{5/3} \qquad (4.2)$$

This agrees with both the experimental data and FE predictions for the structures tested quasi-statically, Chapter 3. The dynamically tested structures at all tested impact velocities scale with relative density to the power 5/3, and like the quasi-static results, this suggests the response is dominated by the out-of-plane tubes. By tailoring the in- and out-of plane tube walls the 3D structure can be made anisotropic and the compressive strengths will be based on the power law, Eq. 4.2, as shown quasi-statically in Chapter 3

The simulation procedure used here has successfully modeled both the rear face pressure verses compression strain response and the mechanisms of core collapse. It was therefore used to estimate the front (impact) face contact pressure which was not

measured in these experiments. During an impact, the contact pressure and frontal displacement determine the work done by the impact mitigator's. The simulations indicate that the ratio of the front to rear face pressure is linearly related to the impact velocity and inversely dependent upon the relative density of the cellular structure, Figure 4.19. However, the front face pressure is much higher than that at the rear of the specimens and increases with both core density and impact velocity, suggesting that this structure may be well suited for mitigating high intensity dynamic loads.

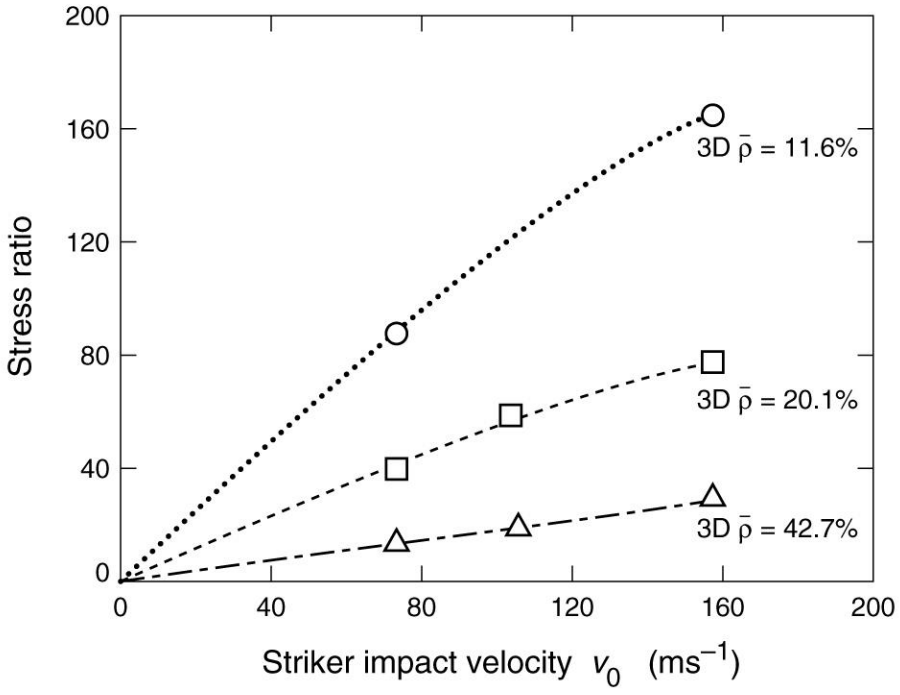

Figure 4.19. Simulated stress ratio based on the initial peak stress calculated for the front and back faces of the sandwich structures with notched cores.

Chapter 5. Impulse Transfer during Sand Impact with an Incompressible Solid Aluminum Block

The aim of chapter 5 is to experimentally investigate the pressure and momentum transferred to an incompressible, back-supported aluminum block by a model buried explosive event. Hopkinson pressure bars were attached to the rear of the aluminum block so that the transmitted pressure resulting from the sand impact could be measured, and its time integral (the impulse) determined. In a second series of experiments, the bars and apparatus that support them were clamped together and allowed to rise following impact of the aluminum block by the ejecta, thereby enabling the apparatus to act as a vertical pendulum, and the impulse transferred by the event to be independently measured. The results are then used, in conjunction with discrete particle based simulations to investigate the nature of the soil – structure interaction for this test geometry. It is shown that the simulation methodology predicts the impulse and pressure applied to the rigid structure, and the effects of varying the distance between the

explosive charge and the test structure. It also reveals new insights into the subtle, but significant interactions of sand particles with an elastically deflecting test structure.

5.1. Test Methodology

The impulse and pressure transferred to a back-supported solid aluminum block following impact by explosively accelerated wet synthetic sand was measured in a vertical impulse test apparatus constructed for the study at a test site operated by NEWTEC Services Group, Inc. (Edgefield, SC, USA).

5.1.1. Test Geometry and Procedures

The test sample, Figure 5.1, consisted of a solid Al6061-T6 block with a square, 203.2 mm by 203.2 mm impact face and thickness of 82.6 mm, welded to a 4.76 mm thick square plate of the same alloy. Since the back plate supported only compressive loads, it was designed to be relatively thin. It contained a hole pattern to enable bolting to a vertical impulse test apparatus shown in Figure 5.2. The pendulum was constructed from four Al6061-T6 vertical rods that were each 2 m in length and 5.08 cm in diameter, and also served as Hopkinson pressure bars. The large diameter was chosen to reduce the likelihood of plastic deformation at the impacted end of the bars. A variable mass weight could be bolted to the top of the pendulum to control the pendulum mass, and thus jump

height during subsequent testing. The lower end of the four aluminum bars were connected with counter-sunk screws to a 2.54 cm thick by 30.48 cm x 30.48 cm Al6061-T6 plate. A concentric hole pattern in the pendulum base plate matched the hole pattern of the back face sheet of the solid test structure, Figure 5.1, and allowed the test structure to be mounted to the pendulum. An A514 grade B steel box was constructed to contain the sand and the buried explosive. The sand box rested on a concrete pad and was partially filled with dry building sand (Type II sand). The support structure for the vertical pendulum was also attached to this concrete pad with four ties. Some tests were conducted with the aluminum bars clamped in position in order to measure the pressure applied to the test structure. In others, the Hopkinson bar arrangement was allowed to freely rise so that the rig functioned as a vertical pendulum.

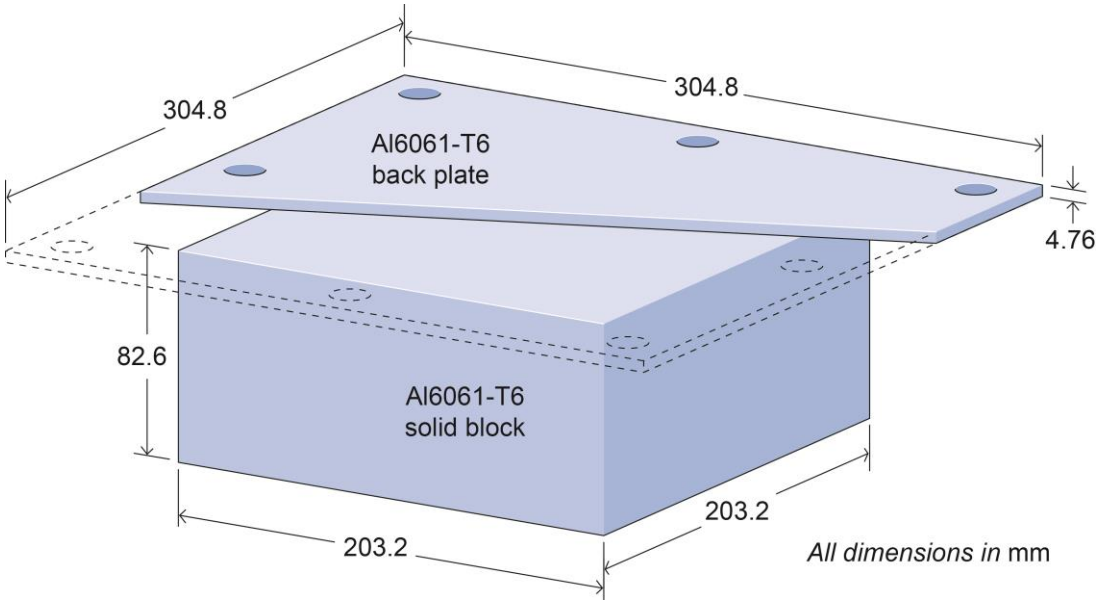

Figure 5.1. The aluminum solid block test specimen used for sand impact experiments. The block was welded to a 4.76 mm thick Al 6061-T6 back face sheet. The hole pattern on the back face sheet was used to attach the test specimen to a vertical impulse test apparatus.

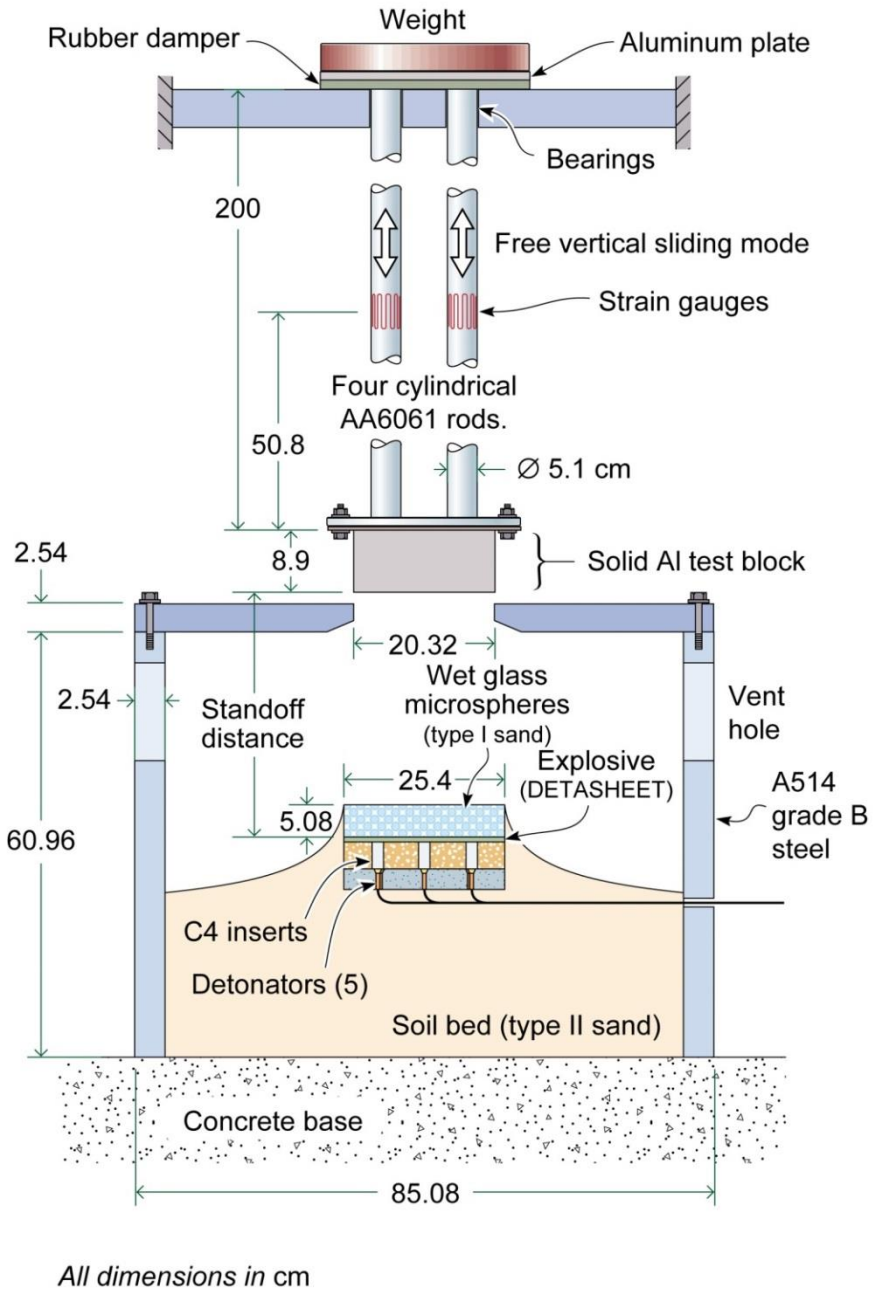

Figure 5.2. The vertical impulse test apparatus used to measure impulse and pressure transmission during synthetic sand impact. The four vertical Hopkinson bars had strain gauges attached to them to record the pressure verses time response of the system. The standoff distance was varied by raising or lowering the location of the explosive sheet and soil bed.

A test charge, Figure 5.3, was assembled on the dry Type II sand bed. It utilized a square Detasheet® explosive[E] and five detonators to accelerate a planar, 50 mm thick layer of partially water saturated (Type I) synthetic sand consisting of approximately 150-200 μm diameter amorphous silica particles (grade GL-0201Silica Glass Spheres, Mo-Sci Corporation). A layer of polystyrene foam was used to support five, millisecond delay, electric detonators (Dyno Nobel Electric Super SP/MS). A polyurethane foam pad with a hole pattern drilled to match the location of the detonators in the polystyrene layer was used to support a 300 g, 25.4 cm by 25.4 cm, by 3 mm thick Detasheet®. These five holes were each filled with 10 g of C4 plastic explosive to boost the detonation event. The polystyrene and polyurethane foams both had a density of approximately 33 kg/m^3, and were used since they quickly disintegrate to effectively form an air cavity below the charge, and thereby reduced sensitivity of the tests to the properties of the foundation upon which the tests were conducted.

[E] Detasheet is composed of 63% pentaerythritol tetranitrate **(**PETN), 8% nitrocellulose, and 29% acetyl tributyl citrate (ATBC) as an organic plasticizer (for simplicity it was modeled 100% PETN in subsequent simulations).

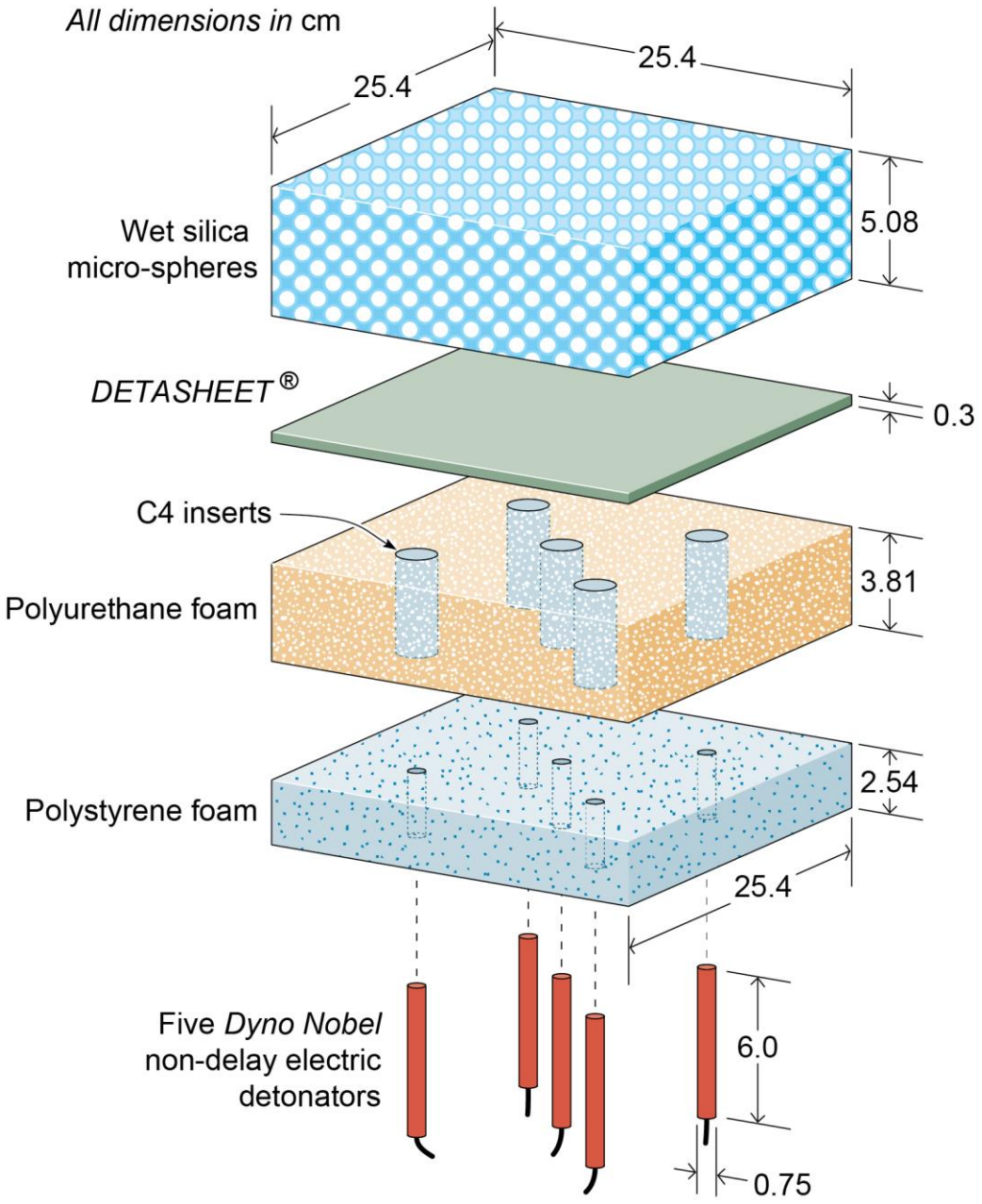

Figure 5.3. The test charge design used to accelerate wet silica micro-spheres.

The steel box had a 25.4 mm thick steel top with a 203.2 mm by 203.2 mm square opening at its center through which the explosively accelerated sand was directed at the test sample. The aperture was designed to be the same size as the bottom surface of the

test block so only the bottom surface of the sample was directly impacted by the sand; the soil bed largely remained trapped inside the steel box or was expelled though circular side vents on the steel box, Figure 5.2. The standoff distance between the top of the Datasheet® and the lower surface of the sample was systematically varied between 14 and 40 cm to modify the density and impulse of the sand column that impacted the test sample. The standoff distance was varied by adjusting the level of the test charge in the steel box while maintaining the lower surface of the test sample 8 mm above the opening of the steel plate covering the top of the box.

The set-up of a test began by adjusting the level of the Type II soil bed within the steel box. The test charge assembly was then centrally positioned on the sand bed, and a 50 mm high, 254 mm by 254 mm hollow aluminum guide box was placed on top of the Detasheet® to create a cavity. The Type II soil bed was then built up around the external sides of the aluminum guide with a steep angle to the soil bed below. The 5 cm deep aluminum mold cavity was then filled with 5.6 kg of a water saturated mixture of the silica micro-spheres (4.4 kg of the silica microspheres and 1.2 kg of water), and the aluminum guide removed. Finally, the A514B steel lid with its 203.2 mm by 203.2 mm central aperture, was attached to the top of the steel box, Figure 5.2. The time between pouring the water saturated sand and initiating detonation of the charge was typically 30 minutes. Laboratory experiments indicated that approximately 20% (220 g) of the water drained from the Type I sand into the surrounding Type II sand during this 30 minute period.

5.1.2. Sand Velocity Measurement

In order to characterize the sand front shape and its speed in the direction of the test sample, the pendulum and sand box cover plate were temporarily removed to enable the explosively accelerated silica micro-sphere overburden to be observed with a high speed Vision Research Phantom V12 camera. Figure 5.4 shows a time sequence of images collected during the first 426 μs following detonation. Detonation of the test charge configuration resulted in a relatively planar sand front, but with several higher speed sand spikes, Figure 5.4(f), that extended beyond the primary sand front. Figure 5.4 (d) shows that at 284 μs after detonation, the left side of the sand front had a slightly higher velocity than the right, which may have resulted from detonator firing delay, would result in non-uniform loading of some samples. The average sand front speed for test charges consisting of 300 g Detasheet plus an additional 50 g of C4 inserts with a 50 mm thick wet sand overburden, was approximately 300 m/s; just below the sound speed of air at the test site.

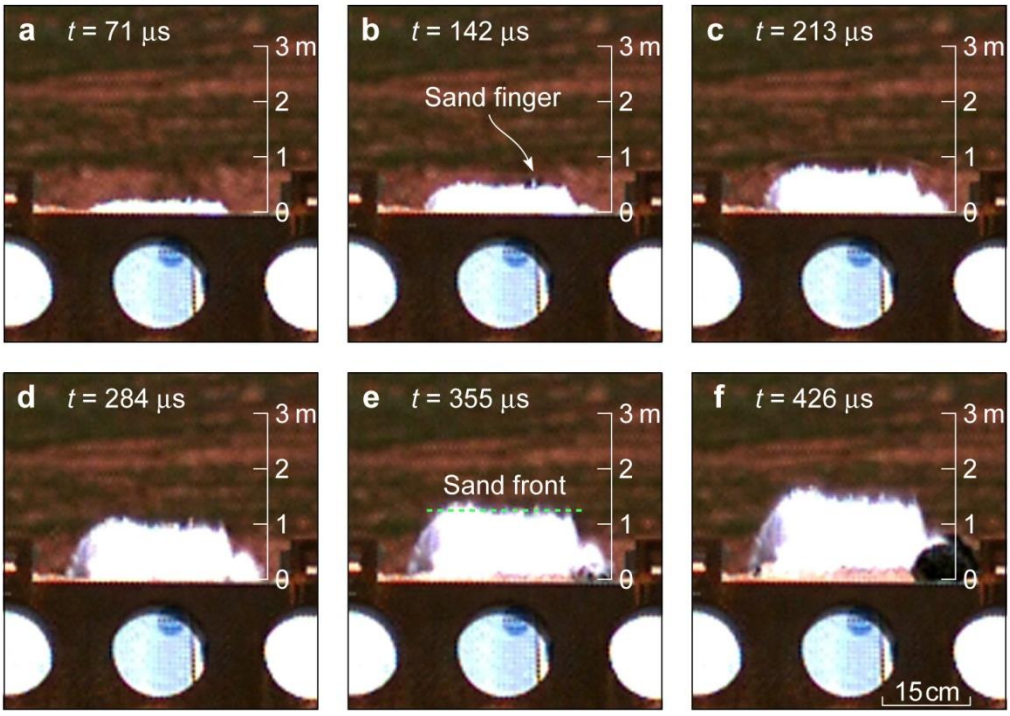

Figure 5.4. Sequence of high speed camera images following the detonation at t=0 µs of a 300 g Detasheet buried below a 5cm thick layer of wet silica glass micro-spheres. The lid of the containment structure has been removed to visualize the sand front. The measured sand front speed in the vertical direction was 300 m/s.

5.1.3. Vertical Pendulum Test Mode

A photograph of the vertical pendulum with a solid test sample attached is shown in Figure 5.5(a). The total weight of the pendulum consisting of the four Hopkinson bars (43.7 kg), the bottom 2.54 cm thick aluminum plate (6.064 kg), the top cylindrical aluminum plate (12.6 kg), the solid aluminum block (11.65kg), and attachment hardware (3.8 kg) was 77.8 kg. Trial tests indicated that reducing the standoff distance increased the pendulum's jump height. To keep the pendulum arms from exceeding their 2 m jump

height limit, steel weights each weighing 7.2 kg were added to the aluminum plate at the top of the Hopkinson bars, Figure 5.2 and Figure 5.5. Table 5-1 lists the mass of the pendulum, sample, and the counterweights for each test. During a test, impulse was transferred to the pendulum causing a time dependent rise in its height, $h(t)$, that could be measured using a Vision Research Phantom V12 video camera. The images shown in Figure 5.5 are still frames from the high speed camera for a test conducted at a standoff distance of 19 cm at (a) the moment of detonation, $t = 0\ ms$ and (b) at $t = 472\ ms$ when the pendulum had reached its peak jump height.

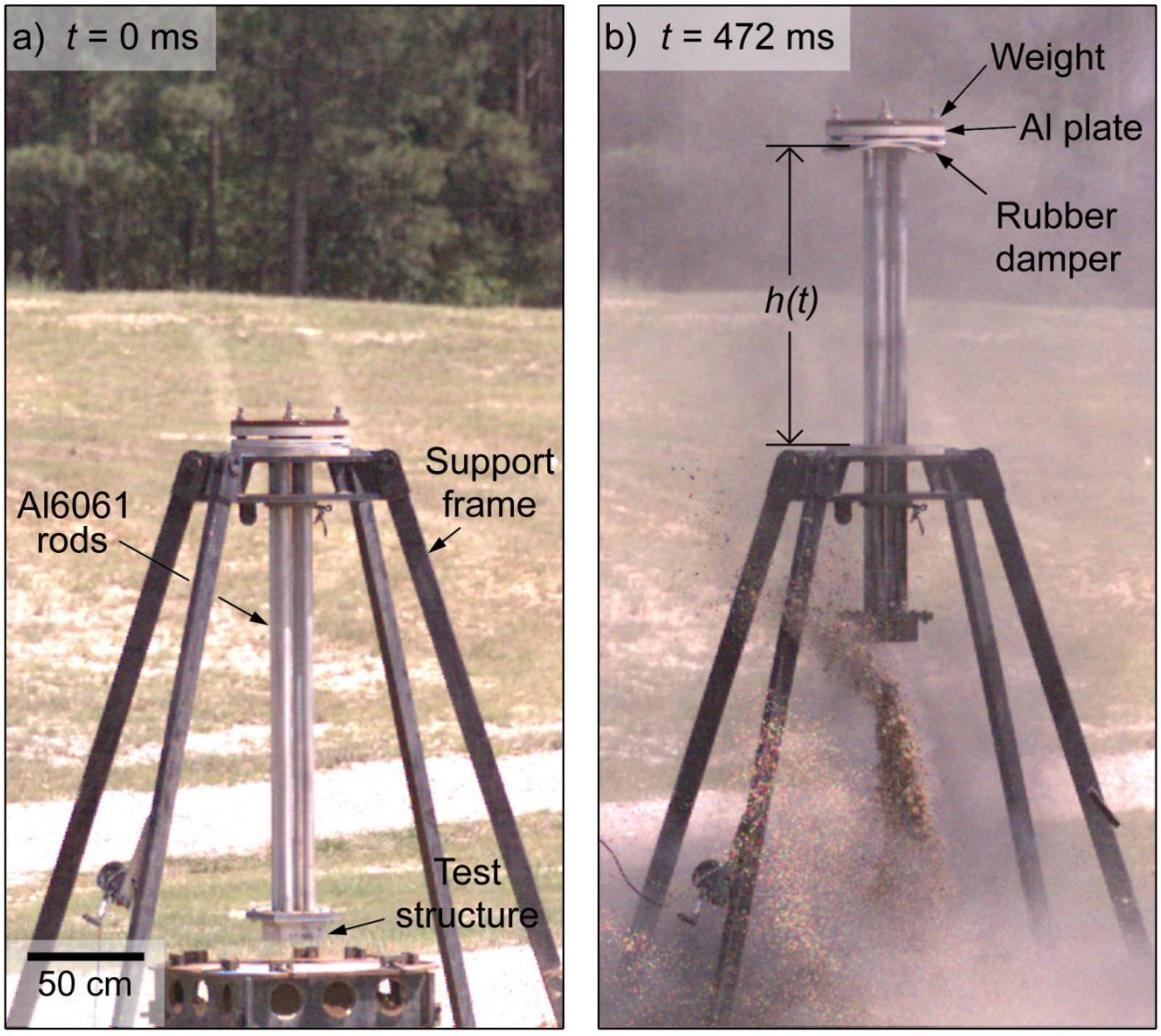

Figure 5.5. Images from a high speed camera showing the pendulum jump in height, $h(t)$, for a 19 cm standoff test. a) Time $t = 0\ ms$ corresponds to the time of detonation and b) $t = 472\ ms$ corresponds to the time at which the pendulum reached its peak height.

Table 5-1. Transmitted impulse for solid block test specimens

Standoff Distance (cm)	***Charge Mass (C4 Insert Mass) (g)***	***Mass of Pendulum with Sample and Counterweights (kg)***	***Maximum Jump Height, h, (m)***	***Transferred Impulse ($kPa \cdot s$)***
14	300 (50)	106.6±0.15	1.49±0.17	13.9±0.8
19	300 (50)	92.3±0.15	1.46±0.21	12.0±0.9
29	300 (50)	85.1±0.15	1.26±0.24	10.2±1.0
40	300 (50)	85.1±0.15	0.84±0.17	8.3±0.8

The impulse per unit area *I*, transferred to a rigid plate of area *A* positioned at the lower end of a pendulum due to the application of a force, *F(t)*, for time $t_i \; to \; t_f$ is:

$$I = \frac{1}{A}\int_{t_i}^{t_f} F(t)dt, \tag{5.1}$$

This impulse causes a change in linear momentum, Δp, of a pendulum with mass, m_p, causing its velocity to rise from $v_1 \; to \; v_2$:

$$\Delta p = m_p(v_2 - v_1) = m_p v_2, \quad for \; v_1 = 0, \tag{5.2}$$

A pendulum launched upwards at velocity v_2, does work against gravity in rising a distance, $h(t)$. Conservation of energy can be used to relate the change in the kinetic energy of the pendulum to its work against gravity:

$$\frac{1}{2}m_p v_2^2 = m_p g h(t). \quad (5.3)$$

where g is the gravitational constant (6.67×10^{-11} N·(m/kg)^2). Solving Eq. (5.3) for velocity, $v_2 = \sqrt{2gh}$, where h is the maximum jump height, results in an expression for the impulse transmitted to the pendulum through the test structure:

$$I = m_p\sqrt{2gh} \quad (5.4)$$

5.1.4. Hopkinson Pressure Bar Mode

The vertical impulse test apparatus shown in Figure 5.2 was also used to measure the transmitted pressure. The four 2 m length pendulum arms were replaced with dimensionally identical Hopkinson bars that each had two strain gauges (manufacture by Vishay Precision Group) attached diametrically to the bar surface, 50.8 cm from the lower end of each bar. A protective layer of epoxy was applied to the surface of the bar where the strain gauges were attached to avoid detachments of the sensors during high intensity loading. The top of the bars were bolted to the test apparatus frame to eliminate bar sliding. The strain gauges attached to each bar formed a full Wheatstone bridge circuit, and the output voltage signal was amplified using a series of operational amplifiers. Each pair of sensors on a bar were connected to separate input channels of an analogue to digital converter which allowed four separate output voltage signals for the four bars to be recorded. Recording was initiated by a trigger signal coincident with the electrical pulse used to initiate charge detonation, and continued for a period of 4 ms.

The voltage-time waveforms recorded for a sand impact test with the solid aluminum block was used to determine the pressure applied by the back of the specimen to each bar. The pressure-time waveform for each bar was deduced from the axial strain of the bar, ε, which could be determined from the voltage-time waveform using a relationship between the output and input voltage of the full Wheatstone bridge given by:

$$\frac{V_o}{V_i} = \frac{GF * \varepsilon(1+v)}{2 + GF * \varepsilon(1-v)} \tag{5.5}$$

where the gauge factor $GF = 2.15$, Poisson's ratio $v = 0.33$, the input voltage $V_i = 10V$, and the sensor output voltage, V_o, is the output from each amplifying circuit. The stress at the sensor location on each bar was than calculated using Hooke's law:

$$\sigma_i = E\varepsilon_{i,} \tag{5.6}$$

where σ_{ii} is the stress, ε_i the axial strain in the *i*-th bar, and *E*=70 GPa is Young's modulus of the aluminum bar. The force applied to each bar, F_i, was given by:

$$F_i = \sigma_i A_{B,} \tag{5.7}$$

where A_B is the cylindrical cross-sectional area for each of the four bars. The pressure applied to the test structure was assumed to be given by:

$$P = \frac{F_{Total}}{A_{sample}}, \tag{5.8}$$

where F_{Total} is the sum of the four forces supported by the bars and A_{sample} = 0.04 m^2 is the test sample area impacted by sand.

Integration of the pressure-time curve was also performed to deduce the impulse-time relationship until elastic wave reflections from the upper end of the bars interfered with the signal. The time before the first reflection arrives can be deduced from the measured longitudinal elastic wave speed of Al6061-T6 which was $5350\ ms^{-1}$. Since the strain gauges were placed 50.8 cm from the impacted end of the 2 m long bars, the first (sign reversed) reflection from the distal end of the bar arrived $558\ \mu s$ after the direct signal. The next (twice reflected, non-sign reversed) arrival from the bottom of bar arrived $190\ \mu s$ after the first reflected arrival.

5.2. Experimental Results

We begin by experimentally examining the sand loading against the solid aluminum block and explore the impulse and pressure that are transferred. Simulations using the IMPETUS Afea Solver approach are subsequently used to resolve the sand interaction with the solid structure, which could not be observed visually because of sand flow around the test structure. We then use the experimentally verified simulation methodology to investigate the sand – structure interaction for the model event.

5.2.1. Vertical Pendulum Impulse Measurements

The impulse transmitted by sand to the solid aluminum block was first deduced from the pendulum mass and jump height data summarized in Table 5-1 using Equation (5.4). This impulse is shown (solid squares) as a function of standoff distance in Figure 5.6(a). The impulse was observed to decrease from approximately 14 kPa·s for a standoff distance of 14 cm, to approximately 8 kPa·s at a standoff distance of 40 cm. The error bars shown with the data were estimated from the uncertainty in pendulum height measurement during the exposure time of a high speed video image and estimates of the parallax error. The impulse decreased linearly with standoff distance with a slope of $-0.20\ kPa \cdot s \cdot cm^{-1}$.

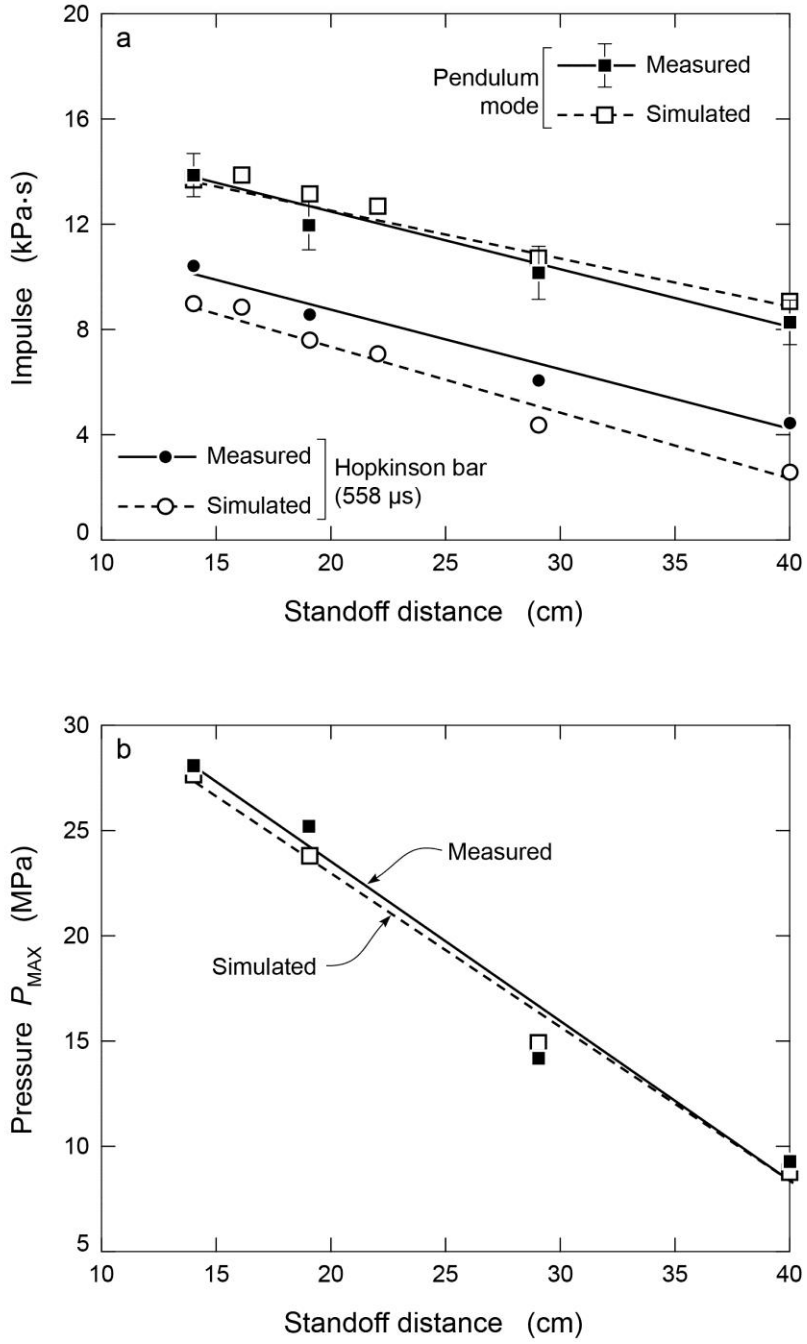

Figure 5.6. a) Dependence of impulse transmitted to a solid aluminum block upon the standoff distance. The transmitted impulse was determined from the jump height of the vertical pendulum. Impulse was also measured from the integration of the pressure-time curves in part b) for 0.558 ms from the initial rise in impulse. b) Dependence of pressure transmitted to the distal side of the solid aluminum block upon standoff distance.

5.2.2. Hopkinson Bar Pressure Measurements

The pressure-time signals measured with the Hopkinson bar test arrangement are shown in Figure 5.7 (solid black lines) for each standoff distance. Time *t=0*, corresponded to detonation of the test charge. All the pressure-time signals exhibited an initial sharp rise in pressure, terminating with a small pressure spike that decreased in strength with increasing standoff distance. Following the initial pressure peak, a period of slowly declining pressure was observed. Its slope decreased with standoff distance, and at the largest standoff distance, the slope of this region was almost zero (a plateau), Figure 5.7(d). This region was followed by an abrupt drop in pressure corresponding to the arrival of the first reflected signal at the sensor location, and was then followed by the second reflection, and eventually elastic reverberations of the Hopkinson bars. At the nearest standoff distance of 14 cm, the initial peak pressure was 28.2 MPa. This fell with increase in standoff distance to 9.3 MPa at a standoff distance of 40 cm. The peak pressures for each standoff distance are summarized in Table 5-2, and plotted against standoff distance in Figure 5.6(b).

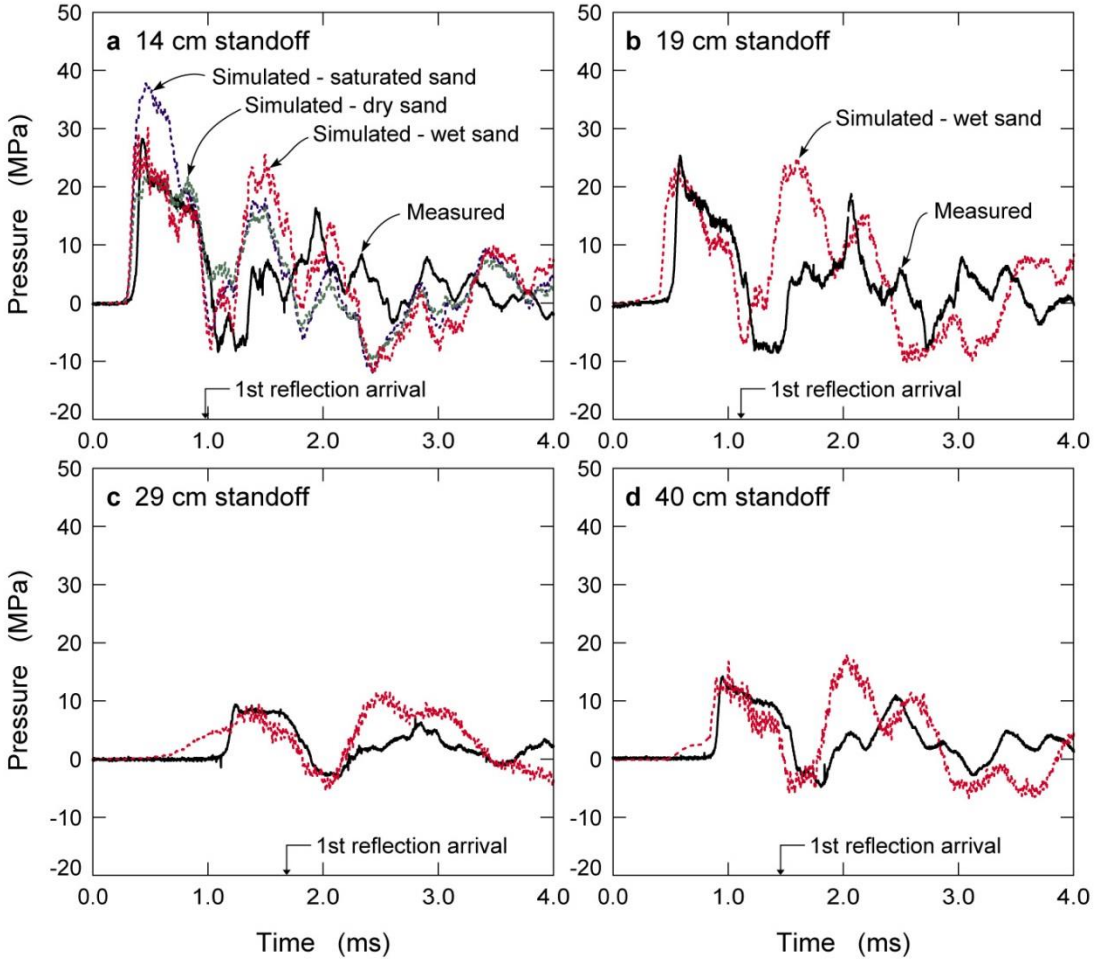

Figure 5.7. a) Comparison of the measured (black line) and simulated pressure-time waveforms at the strain gauge location on the Hopkinson bars at a standoff distance of 14cm. Simulations are shown for sand with three levels of moisture content. Measured and wet sand simulation results at other standoff distances are shown in b), c), and d).

The pressure-time curves shown in Figure 5.7 were integrated to calculate the impulse-time curves shown in Figure 5.8 (solid black lines). The time at which the first distal reflection ($558\ \mu s$ after the direct arrival) and the second reflection ($748\ \mu s$ after the first arrival) reached the sensor locations on the Hopkinson bars are shown for each

standoff distance. It can be seen that the impulse deduced from the pressure waveform decreased in the time interval between the first and second reflected arrivals due to sign conversion of the first reflected signal. The impulse began to rise again after the second reflected signal passed through the sensor locations. Since the reflection coefficients and bar attenuation processes are not well understood, the impulse obtained by integrating the pressure waveform for 558 μs after the first direct arrival was measured, and this is summarized in Table 5-2. It was approximately 3 kPa·s less than the impulse determined in the pendulum mode, Figure 5.6(a), indicating the time over which momentum was transferred exceeded the integration time.

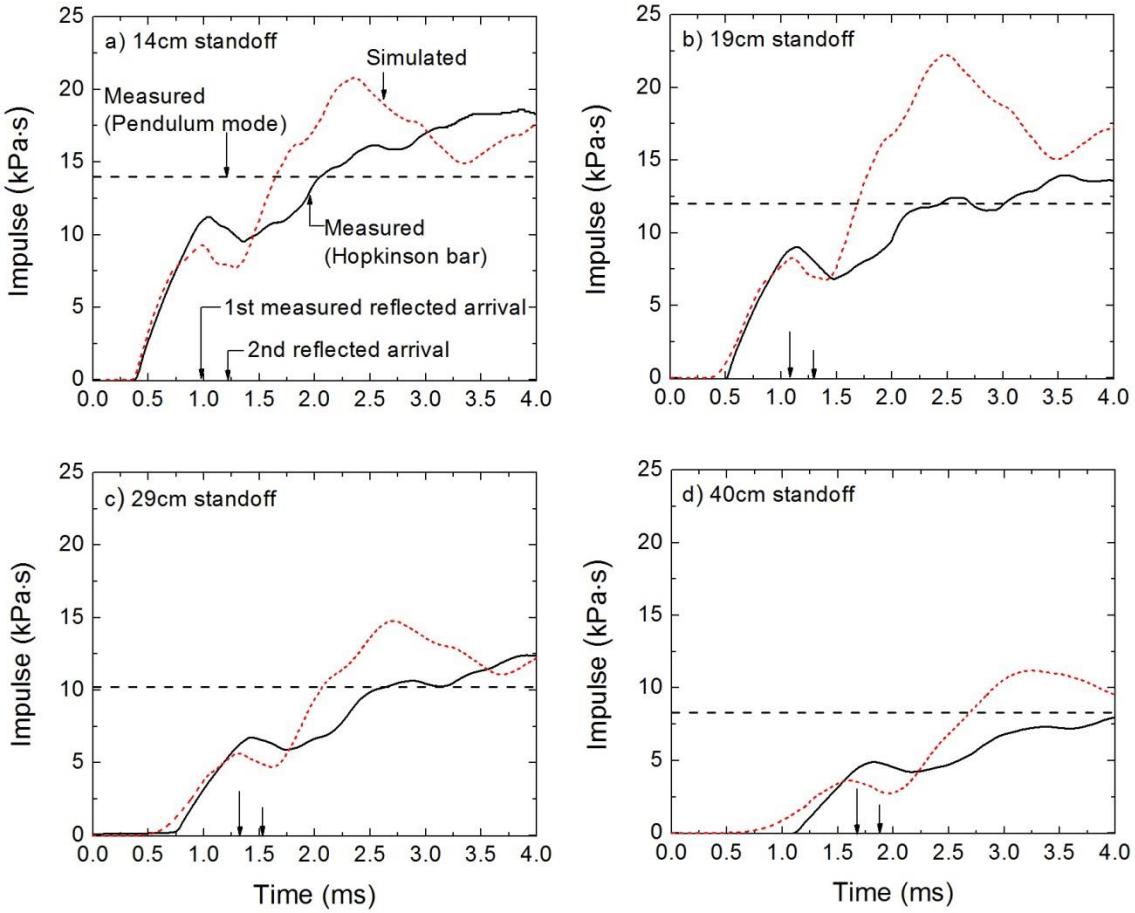

Figure 5.8. Measured and wet sand simulated impulse-time waveforms obtained by integration of the pressure-time waveforms for the solid block at standoff distances of a) 14 cm, b) 19 cm, c) 24cm, and d) 40 cm.

Table 5-2. Transmitted back pressure measured by Hopkinson bars.

Standoff Distance (cm)	***Initial Peak Pressure (MPa)***	***Transferred Impulse at 558 μs, I_t, (kPa-s)***	$\frac{dI}{dt} = \dot{I}$ ***(MPa)***
14	28.2	10.8	21.5
19	25.3	8.9	18.0
29	14.2	6.4	11.4
40	9.3	4.6	8.1

The impulse obtained by continued integration of the pressure waveform for 4 ms after detonation is shown also on Figure 5.8. It is interesting to note that the impulse measured in this way approached the impulse obtained with the vertical pendulum, Figure 5.6(a). Integration of the pressure data acquired up to the arrival of the first bar reflection, Figure 5.6(a), therefore captures a substantial fraction, but not all of the full impulse from the sand impact. It is finally noted that the initial slope of pressure time response gives the impulse rate $\dot{I}$. Using the data from Figure 5.8 it is found that $\dot{I}$ = 21.5 MPa at a 14 cm standoff distance, falling to 8.1 MPa at a 40 cm standoff distance; consistent with the average pressures measured during the first $558\ \mu s$ with the instrumented Hopkinson bars, Figure 5.7.

5.3. Numerical Simulations

The commercial IMPETUS Afea Solver [82] was used to simulate the experiments conducted with the vertical impulse test apparatus. The geometry of the modeled problem is shown in Figure 5.9. The approach is based on a discrete particle (or corpuscular) method first described by Olovsson et al [80] and Borvik et al. [127] The key features of the model, and the validity of its predictions for spherically symmetric C4 charges surrounded by dry and water saturated synthetic sand have been discussed by Borvik et al. [83] and successfully used to analyze the deflection and fracture of aluminum extrusions during impulsive loading by spherical symmetric sand encased charges [128].

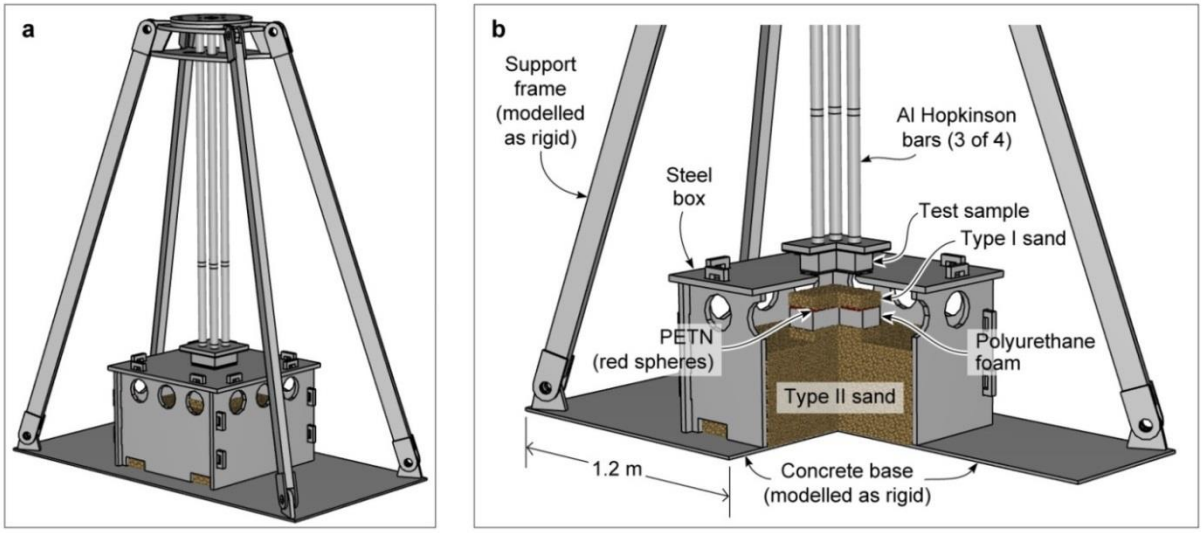

Figure 5.9. a) General view of vertical impulse test stand finite element model prior to charge detonation. b) A view of the lower part of the model with a quarter cut removed revealing the discrete particle arrangements which included 1,941,610 soil particles, 12,795 PETN particles, and 45,595 air particles (hidden from this view).

5.3.1. Modeling of High Explosive (PETN) and Air Particles

The IMPETUS Afea Solver represents explosive detonation products, and air by rigid, spherical particles that represent many (~10^{18}) actual molecules. These particles transfer momentum by particle-particle collisions defined by contact laws between the particles. The contact interactions of high explosive reaction and air particles are assumed to be elastic and accordingly follow Maxwell's molecular kinetic theory of gases [129]. Since at high densities, the co-volume effect can cause very large pressures to be predicted, the model incorporated co-volume effects when the particle fill fraction, b was large. The Maxwell-Boltzmann velocity distribution applied to the discrete particle model for the PETN high explosive used here was determined by selecting the PETN high explosive option in the IMPETUS Afea Solver code. This defined the PETN initial density, $\rho_0 = 1765\ kg/m^3$, its initial internal energy, $E_0 = 10.2\ GJ/m^3$, the ratio of heat capacities at constant pressure and volume, $\gamma = C_p/C_v = 1.4$, the initial solid-fill fraction of the particles, $b = 0.35$, and the detonation velocity, $V_D = 8350\, m/s$. This option was applied to the region occupied by the 300 g, 254 mm by 254 mm, by 3 mm thick Detasheet®. The code does not allow use of a second high explosive type, and since the parameters for C4 explosive are similar to those of PETN [83], the 50 g, C4 booster charges was approximated by an additional 0.5 mm thick layer of PETN placed at the lower surface of the charge. The particles remained stationary in the model until the explosive was initiated at the center of the bottom surface of the charge. The resulting PETN distribution of velocities was then applied to the region of high explosive particles that had been traversed by a detonation wave that propagated through the explosive at

speed V_D. The air was modeled as an ideal gas with a Maxwell-Boltzmann distribution of velocities and random initial directions. The velocities were governed by selection of an air pressure of 100 kPa (one atmosphere) with a density of 1.3 kg/m^3, an initial internal energy of 253 kJ/m^3, and a ratio of specific heats $\gamma = 1.4$.

5.3.2. Sand Model

The sand was also modeled by representative particles, but unlike the high explosive gases and air particles that were modeled as elastic collisions, the wet sand particles were modeled using a penalty based contact formulation that is described by Borvik et al.[83] During real sand particle impacts, energy can be dissipated by sliding friction at contacts between particles, by conversion of translational energy to particle rotation and by particle fracture. The model approach used in the IMPETUS Afea Solver does not treat particle rotation since it substantially increased the computational cost of the calculations, and fracture was also not explicitly addressed. However, the procedure used by Borvik et al. [83] to tune the model parameters to match soil properties is presumed to have accounted for these effects. To address dissipation, the same penalty contact stiffness, *k* for linear springs was used for both the normal and tangential components of a contact, Figure 5.10. In the IMPETUS Afea code, the penalty stiffness is dependent upon the scaled size of the unit cell, *L*, and that of the initial un-scaled unit cell, $L_o = 1\ m$. The penalty contact stiffness is defined by; $k = (\frac{L}{L_o})k_o$ where k_o is the particle-particle contact stiffness for the un-scaled unit cell. A linear dashpot with

damping constant, *c* that was proportional to a damping factor, ξ, acted in parallel with the normal contact spring while the tangential spring was limited by a Coulomb friction coefficient, μ. Recent observations by Deshpande et al [130] have indicated that the interparticle separation in dry sand quickly increases following detonation, but water saturated sand particles do not immediately form a loose spray when accelerated by a detonating charge. Wet sand remained clumped with semi-permanent contacts. This has led earlier studies [83, 128] to conclude that the damping coefficient, ξ, is important in water saturated soils while the friction coefficient, μ only mattered in dry sand.

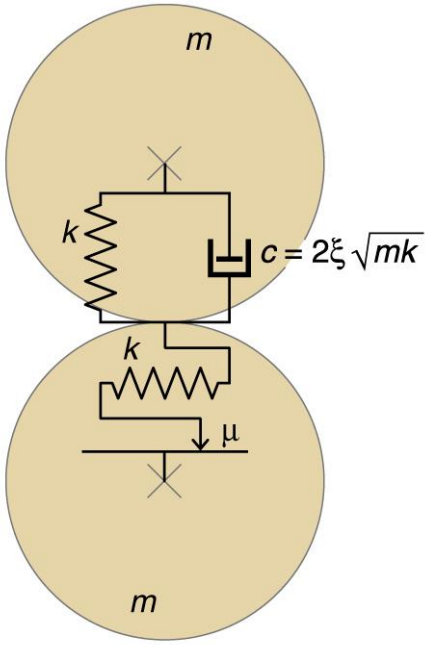

Figure 5.10. Rheological model used for simulating discrete sand particle interactions. The contact stiffness $k = 0.76\ GN/m$ and the damping coefficient $\xi = 0.005$. Friction was not included in the wet sand model.

The Type I sand used here consisted of the same silica micro-spheres (with a diameter of 150-200 μm and an amorphous silica density of 2700 kg/m^3) analyzed by Borvik et al. [83] The sand fill fraction for this synthetic sand was 60% and initial density was therefore 1620 kg/m^3. In the study by Borvik et al. [83] the remaining volume was either filled with water (water saturated sand), resulting in an increased initial sand density of 2020 kg/m^3 or was left unfilled for dry sand. The actual water was not modeled in the system; instead, the particle packing, friction coefficient, contact stiffness, and damping were adjusted so that simulations agreed with the experiments. The IMPETUS Afea Solver enables a user to specify dry or wet sand which in turn specifies default contact model parameters proposed by Borvik et al. [83] Selection of dry sand defines $\rho = 1620\ kg/m^3,\ k_o = 0.4\ GN/m, \xi = 0.0, and\ \mu = 0.1$ while selection of wet sand specifies $\rho = 2020\ kg/m^3,\ k_o = 4.0\ GN/m, \mu = 0.0, and\ \xi = 0.005$. The code also enables the user to specify other values of these parameters.

To investigate the effect of the Type I sand water content, we first used the default wet sand option which selected $\rho = 2020\ kg/m^3,\ k_o = 4.0\ GN/m, and\ \xi = 0.005$. The numerical results for this saturated sand case are shown as the dotted blue curve in Figure 5.7(a). Since water saturated sand has little free volume for compaction before pressure builds, this sand model resulted in significantly higher peak pressure than were observed experimentally. The other limiting case assigned the default parameters for the dry sand model to the Type I sand, and is shown as green dotted curve in Figure 5.7(a). It resulted in peak pressures below those observed experimentally. Since drainage of the originally water saturated sand occurred during set-up of the experiment, and we

estimated the water saturation to be 80%, and therefore used a sand model density, $\rho = 1940\ kg/m^3$ which lies between that of wet and dry sand. After several trials, it was found that the contact stiffness and damping coefficient parameters that gave best agreement with experimental pressure data also lay between those of the dry and water saturated sand, and so for all the subsequent simulations we used $k_o = 0.76\ GN/m$, $\mu = 0.0,\ and\ \xi = 0.005$.

A convergence study was also conducted to determine the optimum number of discrete particles. From this study convergence was reached with 2,000,000 discrete particles. The particles were distributed by the IMPETUS Afea Solver as 45,595 air particles, 1,941,610 soil particles, and 12,795 high energy explosive reaction product particles based on prior work by Borvik et al. [83]

To characterize the ejecta from a simulated event, twenty spherical virtual "monitors" each with a 0.508 cm radius were located at a distance of 2.5 cm from the location of the lower surface of the solid block at equal lateral distances between each other, Figure 5.11(a). These measured the discrete particle velocity and density within the monitors at 4 μs time step intervals. The sand density was calculated by summing the mass of all sand particles that passed through a monitor in each measured 4 μs time interval and dividing by the spherical monitor volume, (V):

$$\rho = \sum \frac{m_i}{V} \tag{5.9}$$

where m_i is the mass of the i-th particle. The sand particle velocity was calculated from the total momentum of each particle measured at each simulated time step interval divided by the total mass within the monitor during the same simulated time step:

$$v = \frac{\sum m_i v_i}{\sum m_i} \tag{5.10}$$

where v_i is the vector velocity of the i-th particle.

The hydrodynamic pressure (P_h) applied by the sand particles, could be calculated from the numerically measured values for sand density and velocity within the spherical monitors using:

$$P_h = \rho v^2 \tag{5.11}$$

By integrating the hydrodynamic pressure, the impulse-time relation for sand particles could also be calculated. The total pressure exerted by the particles on the sample front face 2.0 cm above the monitors could also be directly obtained during a simulation. The contact pressure responses are slightly delayed because of the extra distance travelled by the particles from the monitor location to the sample impact surface. The contact impulse was an output file created by the IMPETUS Afea post processor that automatically calculated the momentum transferred between sand particles and the solid blocks front face.

5.3.3. FE Modeling

5.3.3.1. Geometry

The test geometry shown in Figure 5.9(a) including the solid test sample modeled to its true dimensions by combining the test charge particle model with the finite element package in the IMPETUS Afea Solver. The solid block was modeled with a thin front face that was merged with the remaining sample thickness, defined in Figure 5.2, to calculate the force between the merged sections. The four Hopkinson bars were modeled as multiple merged cylindrical parts with the dimensions defined in Figure 5.2. The first short cylindrical part extended 2.54 cm and the second cylindrical part extended 48.3 cm from the base of the bars, to the location where the force was experimentally measured. Another 2.54 cm cylindrical section covered the length of the strain gauges used for the force measurements and the fourth cylindrical section ensured the full 2 m length of the bars was modeled. The top of the Hopkinson bars were merged with a cylindrical top plate with an artificial material viscosity to introduce dampening to the bars oscillatory response. The support structures, four tie downs, and concrete foundation were modeled as rigid structures with a fixed boundary condition. This approximation had negligible effect upon the results but significantly reduced the computational time. The steel box was modeled using the same dimensions as the test geometry. Top panel oscillations near the square aperture were particularly important to characterize since they affected the gap between the bottom of the sample and the upper surface of the top panel through which partially arrested sand particles escaped the test structure. A514 B steel material properties were therefore applied to the entire steel box. The pressure in the Hopkinson

bars was calculated at their sensor locations from the force-time response between the merged short cylindrical model section in each bar and its adjoining base section. These four force signals were summed and divided by the solid sample area. The vertical pendulum mode impulse was calculated from a post-processor output function that measured momentum transferred between discrete sand particles and the finite element model of the sample.

The FE model was constructed from 7,104 cubic and 19,608 linear hexahedra elements with 246,216 nodes. The Hopkinson bars and all connecting parts were modeled with a coarse mesh since material failure was not seen experimentally. The solid test block was modeled with a finer mesh since some local deformation (thought to be associated with sand fingers) was observed experimentally. The solid block was constructed from 16,944 8-node 3rd-order linear hexahedra elements. A mesh sensitivity study was performed to confirm solution convergence with this level of discretization.

5.3.3.2. Material

All the aluminum parts were fabricated from Al6061-T6 and were modeled as an isotropic material with a von Mises flow stress defined by a form of the Johnson-Cook constitutive model:

$$\sigma_y = (A + B(\epsilon_{eff})^n) \cdot \left(1 + C \cdot \ln\left(\frac{\dot{\epsilon}_{\text{eff}}}{\epsilon_0}\right)\right) \cdot \left(1 - \left(\frac{T - T_0}{T_m - T_0}\right)^m\right) \qquad (5.12)$$

where ϵ_{eff} is the equivalent plastic strain and A, B, n, C, and m are material constants. The first term on the right hand side of Eq. (5.12) governs the strain hardening and the constant A represents the initial yield strength, and B and n are both hardening parameters. The second term on the right hand side of Eq. (5.12) governs strain rate hardening and the constant *C* is the strain rate hardening parameter, and ϵ_0 is a user defined reference strain rate parameter. The last term of Eq. (5.12) controls thermal softening of the material. Al6061-T6 material parameters were obtained from a study by Wadley et al. [125] The A514 grade B steel was modeled in a similar manner using material properties from Johnson et al. [131] The coefficients used in conjunction with Eq. (5.12) to model both materials are provided in Table 5-3.

Table 5-3. Material constants for AA6061-T6 and A514 grade B

	Elastic constant and density			***Yield stress and strain hardening***			***Strain rate hardening***		***Temperature softening and adiabatic heating***		
Material	E (GPa)	ν	ρ $(kg \cdot m^{-3})$	A ***(MPa)***	B ***(MPa)***	n	ϵ_0 (s^{-1})	C	T_0 ***(K)***	T_m ***(K)***	m
AA6061	70.0	0.3	2700	270	98	6	$5 \cdot 10^{-4}$	0.001	293	893	1
A514-grade B	210.0	0.3	7850	796	510	0.26	$1 \cdot 10^{-2}$	0.014	293	1793	1

The option for aluminum alloy fracture was included by use of a Cockcroft-Latham failure criterion [132] even though it did not occur in the tests. Failure was defined to occur when a damage parameter, D, reached unity. The damage parameter was calculated as

$$D = \frac{1}{W_c}\int_0^{\epsilon_{eff}} \max(0, \sigma_1) d\epsilon_{eff} \qquad (5.13)$$

where $\sigma_1$is the first principle stress. The critical damage parameter, $W_c = 278\ MPa$. The general node splitting feature in the IMPETUS code was turned on. With this feature, the damage variable is allowed to evolve without any change to the constitutive response of the Al6061-T6 alloy until D=1. At that instant, the Al6061-T6 alloy is assumed to have failed and nodes of the elements where this failure has occurred are split apart. Material fracture was not introduced into the A514 steel material to improve computational speed.

To account for the two foam layers below the high explosive, Figure 5.3, the foam was explicitly included using a simple model for crushable foam built into the IMPETUS Afea code. The model is limited to isotropic elastic behavior under impact loading conditions with an assumed constant Young's modulus, E =0.9 MPa. A geometric strain failure criteria was introduced that required the foam to lose its shear strength once the failure strain, $\epsilon_{fail} = 0.1$ was reached and erode. Since both the polystyrene and polyurethane foams disintegrated quickly, and have similarly low densities (both measured at approximately 33 kg/m^3), only one generic layer of foam was modeled, with

a thickness equal to the sum of the two layers used in the tests. Figure 5.9 summarizes the test charge model geometry including the sand particles, high explosive particles, and foam for the specimen that was back-supported by four Hopkinson bars.

5.4. Simulation Results and Discussion

The simulated pressure waveform using the wet sand model with an 80% water saturation is shown as the red dotted curve in Figure 5.7(a). It can be seen that the simulated and measured waveforms prior to arrival of the first reflected signal were in remarkably good agreement at the short standoff distance. As the standoff distance increased, the simulated pressure signal began to rise above the quiescent back ground earlier than was observed in the experiments. The time gap between the simulated and measured pressure jump increased with standoff distance. However, apart from this shift in timing, the rest of the simulated pressure waveform was in good agreement with the experimental data. Beyond the first reflected arrival (shown on each waveform in Figure 5.7), the agreement between simulated and measured pressure response deteriorated, especially as bar reverberation began to dominate the response. This is thought to have been a consequence of an inadequate representation of the boundary conditions at the top and bottom of the bars, and of the dissipation mechanisms within them.

To investigate the phenomena governing the simulated pressure responses, Figure 5.11 shows the location of explosive and sand particles at various times after simulated detonation for the 14 cm standoff distance case. The test sample has been removed from the simulation to more clearly reveal the unimpeded motion of the particles though the aperture of the top lid of the sand containment box. The location of virtual monitors that were used to measure particle density and velocity are also shown in Figure 5.11(a). Highly time resolved observations of the initial stages of the event (Figure C1 of Appendix C) indicated that after detonation of the explosive, a compressive shock front propagated through the 5.08 cm thick wet sand layer and was reflected at the sand-air interface with sign conversion to a tension wave. This reflection occurred 50 μs after detonation, and was accompanied by ejection (spallation) of surface sand particles normal to the sand surface. Simultaneously, the pressure of the explosive reaction products began to push the wet Type I sand layer upwards. As the Type I sand slab moved upwards, it also began to laterally spread. Figure 5.11(a) shows the particle locations later at t=0.12 ms after detonation. Multiple collisions between the explosive reaction product and Type I sand particles resulted in motion of the sand particles in the upward direction. The velocity of sand particles at the leading edge of the sand front was higher than that at the tail, leading to stretching of the sand in the direction of upward propagation. Some widening in the transverse direction also occurred, Figure 5.11(b). The fast sand particles that were spalled from the surface by shock reflection can be seen passing through the monitor location in Figure 5.11(b), while those associated with the denser sand slab passed through the monitors latter, Figure 5.11(c). The majority of the upward moving Type I sand passed through the aperture of the top plate on the test apparatus within 1 ms

of detonation, Figure 5.11(e). The Type I sand particle impact with the sample support plate can be seen in the time sequence Figure 5.11(c) to (h), and was completed within about 5 ms of detonation. The back supported flat support plate arrested forward motion of the sand causing accumulation near the flight surface and then radial outward flow. There was little evidence of particle reflection back towards the sand source. Careful examination of the results indicate that lateral spreading of the Type I sand slab resulted in a small fraction of the Type I sand impacting the underside of the sand containment box lid near the aperture, Figure 5.11(c) to (e), setting it into oscillating deflection.

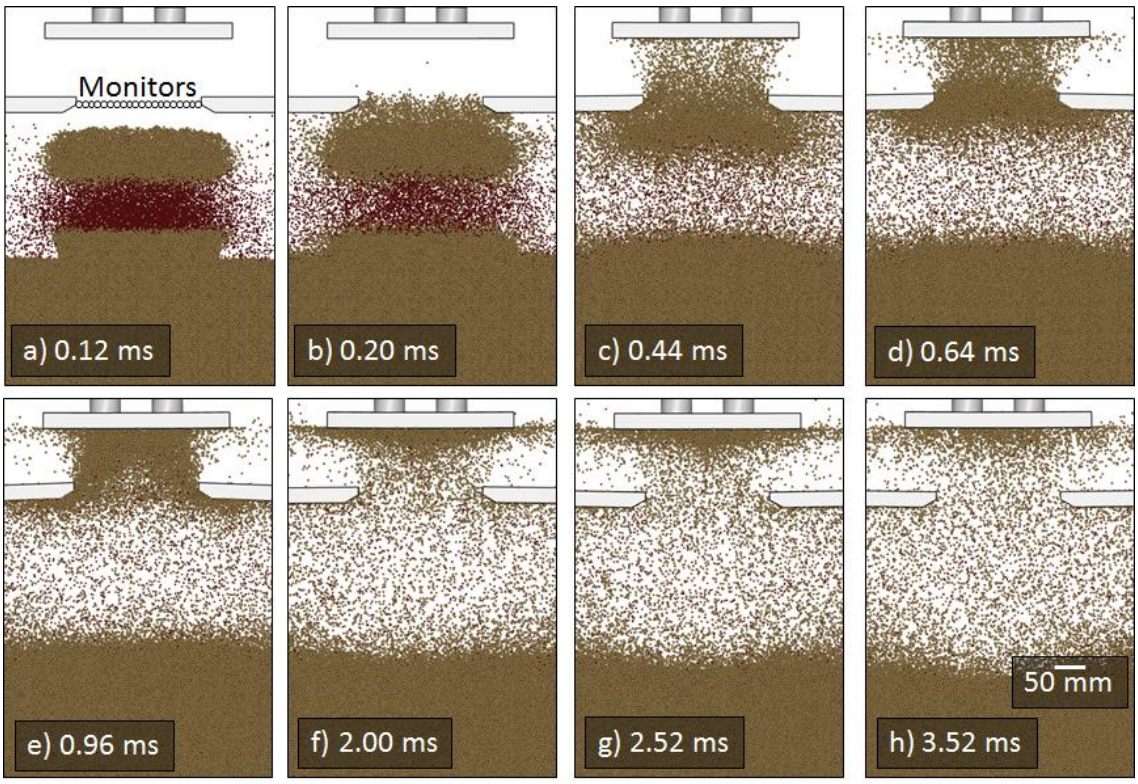

Figure 5.11. *A sand particle propagation sequence for simulations without a solid block sample attached to the test structure. The standoff distance was 14 cm. The burgundy particles correspond to the explosive gases while the brown particles correspond to sand. Air particles are not shown.*

Figure 5.12 shows a repeat of the simulation above, but with the solid aluminum test sample now attached to the apparatus. The sand monitor locations are again shown in Figure 5.12(a). It can be seen that most of the Type I sand particles passed through the aperture of the steel box, Figure 5.12(b), and impacted the bottom surface of the sample. Their upward motion was arrested at the sample surface, and the particles began to radially flow outwards and escape the system through the gap between the edges of the specimen and the top plate of the sand containment box. However, as the arriving Type I sand density increased, Figure 5.12(c), the rate of arriving particles began to exceed that of particle escaped through the gap, and a considerable compaction of sand against the sample occurred. This compacted sand was eventually vented through the gap between sample and steel box, but this required substantial time, Figure 5.12(d) through (h).

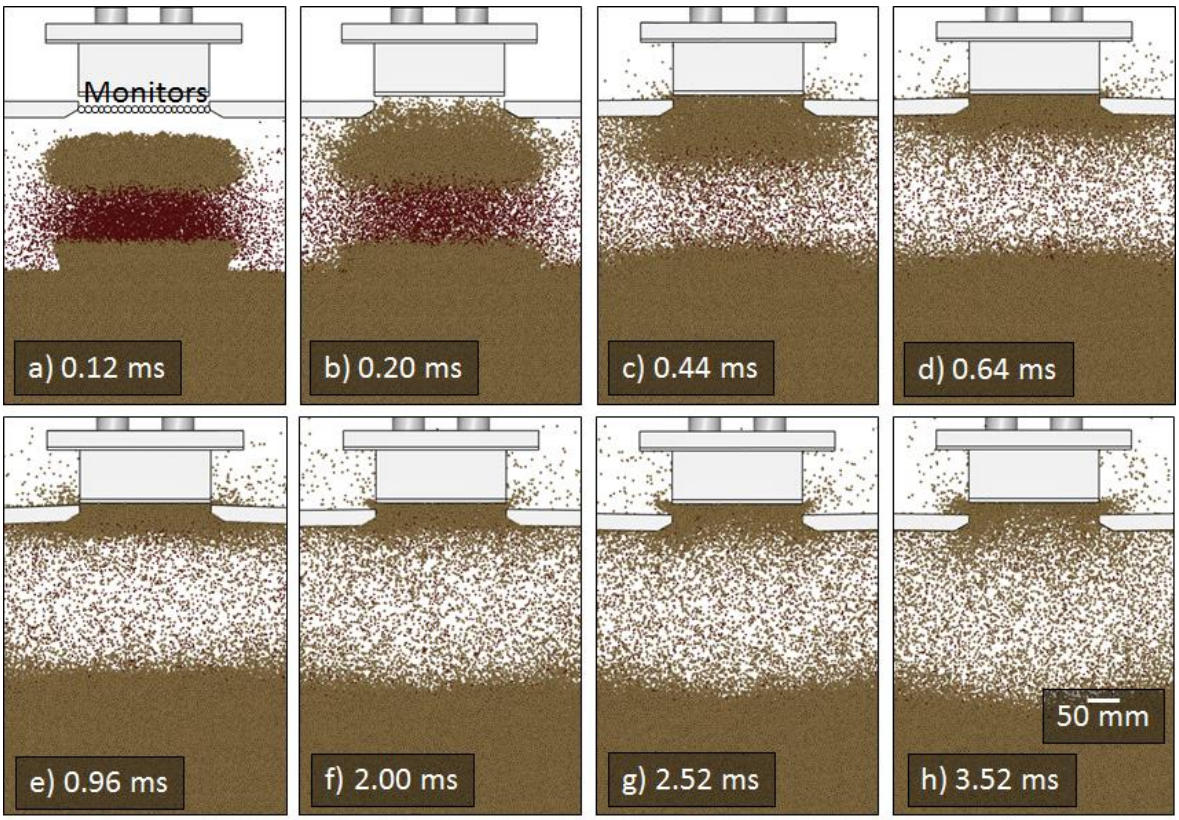

Figure 5.12. A sand particle propagation sequence for simulations with a solid block sample at a standoff distance of 14 cm.

The origin of the early simulated pressure signal arrival in Figure 5.7 can be most clearly resolved by examining simulations for the largest standoff distance test shown in Figure 5.13 (no test sample present) and Figure 5.14. At 0.4 ms after detonation, Figure 5.13(a), some Type I sand had advanced a significant distance upwards creating a diffuse leading edge and an axially stretched sand column. At 0.64 ms this leading edge sand had passed through the aperture of the sand containment box lid, and through the location of the monitors, Figure 5.13(b). Figure 5.14(b) shows that it had begun to impact the bottom surface of the test block at time t = 0.64 ms, which also corresponded to the start of the rise of the simulated pressure, Figure 5.7(d). The higher velocity of this fast sand resulted

from additional momentum supplied to surface sand particles by recoil of the compressive sand during (sign converting) shock reflection at the sand surface.

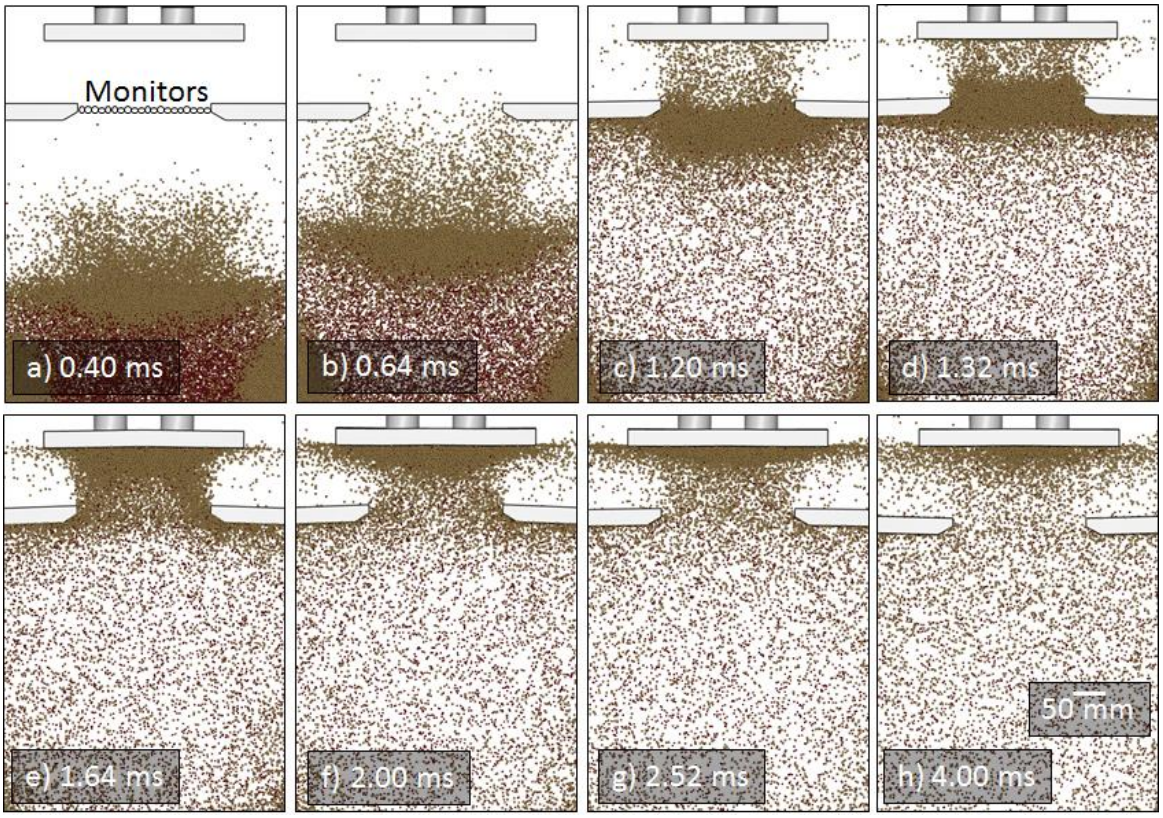

Figure 5.13. A simulated sand particle propagation sequence for a case without a solid block sample at a standoff distance of 40 cm.

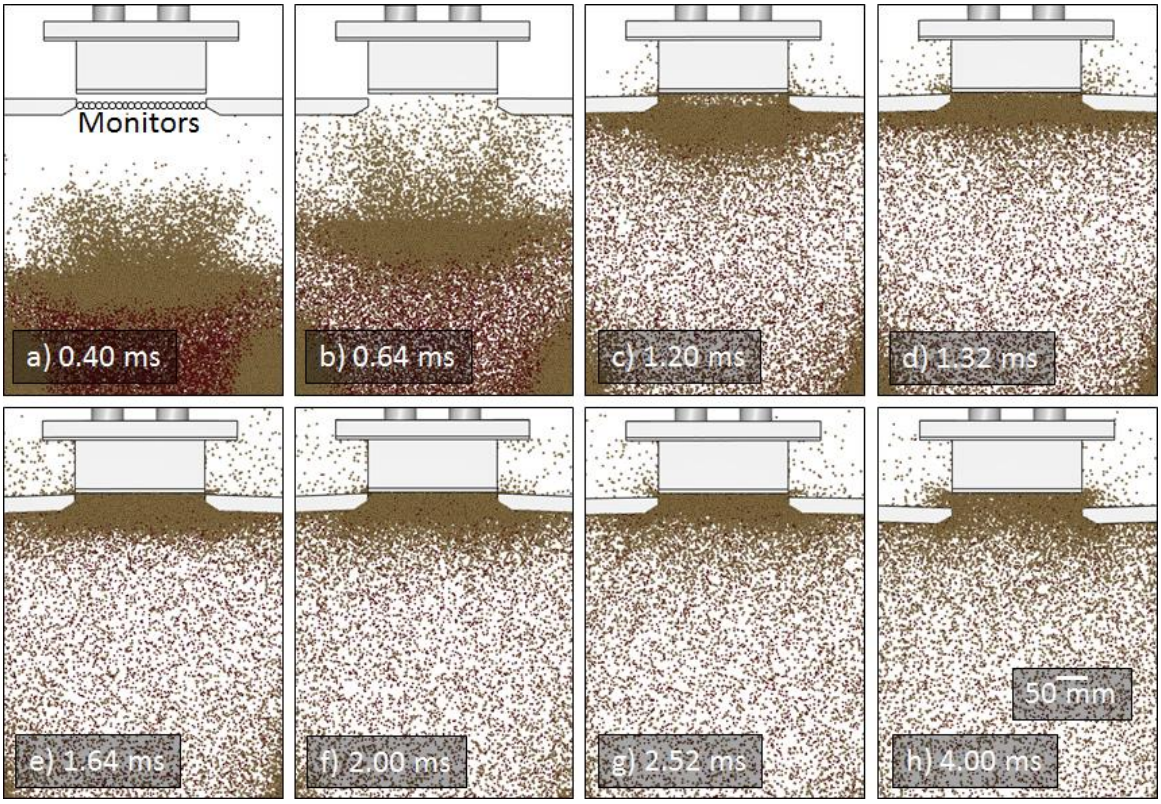

Figure 5.14. A sand particle propagation sequence for simulations with a solid block sample at a standoff distance of 40 cm.

The most significant effect of a longer standoff distance was to allow additional time for the spalled sand to separate from the axially stretching and laterally spreading Type I wet sand slab. The higher velocity of the spalled sand, Figure 5.14(b), resulted in sand-sample impact occurring well before the arrival of the axial stretched main sand slab, Figure 5.14(c and d). This fast spalled sand impact was the origin of the early simulated pressure signal arrival which became more prominent with increasing standoff distance. However, increasing the standoff distance also provided additional time for the sand slab stretching, and time for particles to escape through the gap between the side of the test sample and the cover plate of the apparatus, Figure 5.14(c) to (h). The additional

time also permitted more lateral stretching of the sand column, and resulted in an increased fraction of Type I sand particles impacting the lower surface of the cover plate.

To further investigate these phenomena, the sand particle velocity and density were determined at the sand monitor locations, and are shown as a function of time in Figure 5.15(a) and (b) and Figure 5.16(a) and (b) for standoff distances of 14 and 40 cm respectively. Sand velocities and densities are shown for simulations both with and without a test sample attached to the apparatus. It can be seen in Figure 5.15(a) that the fast (spalled) sand in the 14 cm standoff simulation had a monitor location velocity of about 500 ms^{-1} while that for the 40 cm case, Figure 5.16(a), was lower. In both cases the leading edge sand had the same initial velocity (1690 ms^{-1}) as it left the sand slab surface. Detailed examination of the simulation results indicated that the sand deceleration with distance of propagation was a consequence of momentum transfer from sand to air particles.

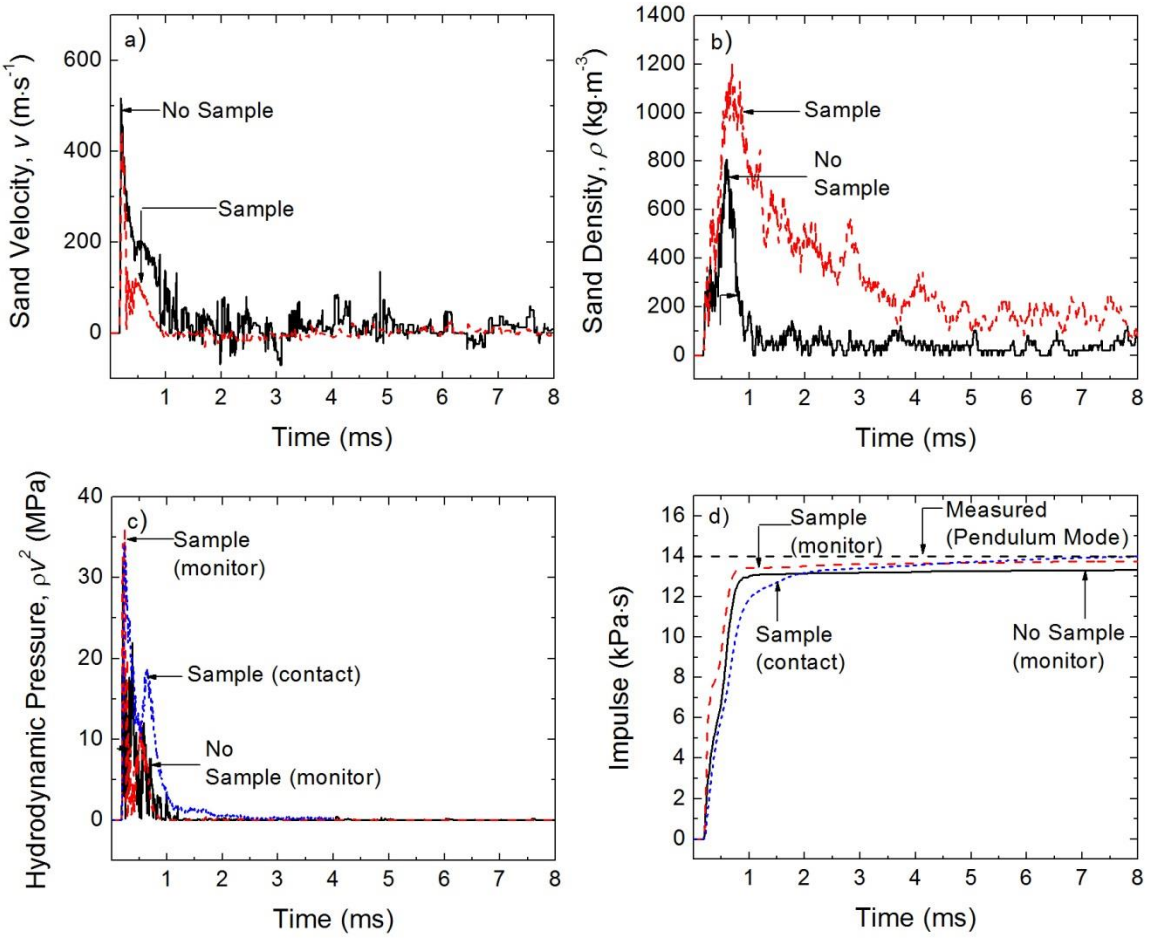

Figure 5.15. a) The sand velocity and b) sand density determined at monitors for simulation both with and without a sample for a standoff distance of 14 cm. The calculated sand hydrodynamic pressure c) and the sand impulse d) are also shown. The blue curves in c) and d) were directly calculated from the impact force on the sample front face using a contact algorithm.

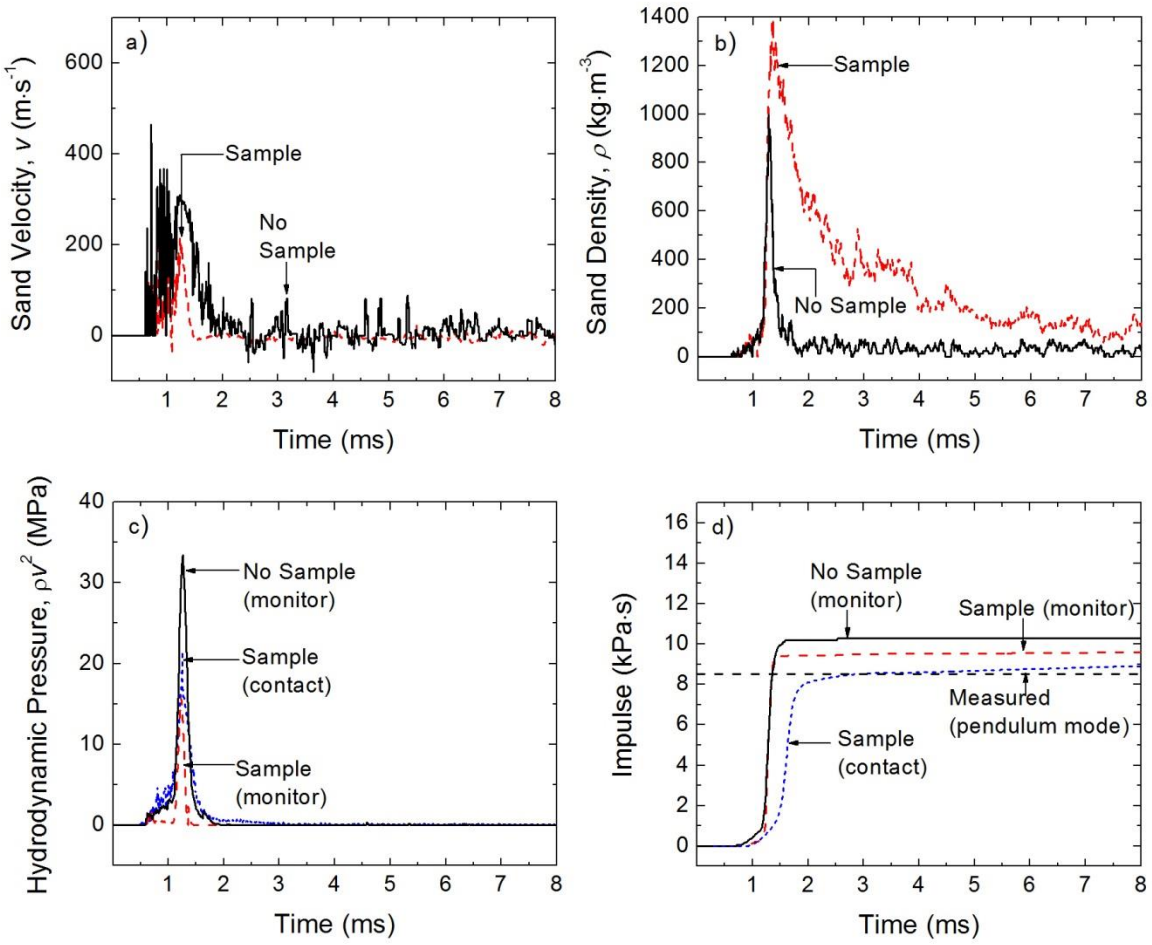

Figure 5.16. a) The particle velocity and b) sand density determined using the monitors for simulations with and without an attached sample for a standoff distance of 40 cm. The calculated hydrodynamic pressure c) and the impulse d) are also shown.

However, two experimental observations suggest that the sand-air deceleration mechanism was underestimated by the simulation methodology. First, high speed video observation of the sand fronts, Figure 5.4, show that the sand front velocity was 300 ms^{-1}; about 100-200 ms^{-1} slower than that predicted for the spalled sand. Secondly, the Hopkinson pressure bar pressure measurements, Figure 5.7(a) are consistent with sand arriving at the test samples with a sand velocity close to that observed by the high speed

video camera. It is possible that a substantial air drag acted on the fast (supersonic) spalled sand particles which was not accounted for in the simulations. It is also important to note that the density of the fast (first arriving) sand was less than $10\ kg\ m^{-3}$, Figure 5.15(b) and Figure 5.16(b); less than 1% of the original packed sand bed, and this may also have effected interactions with the air. This air drag might also have played a role in the formation of sand fingers observed ahead of the main sand front in Figure 5.4.

While the first arriving sand for both standoff distances had a velocity and density that was unaffected by the presence of the sample, later arriving sand was slowed, and its density increased when a sample was present. This reduced velocity is consistent with sand particle direction reversal during impact with accumulated sand at the lower surface of the sample, and collision of these reflected particles with later arriving particles. These collisions reduced the average incoming sand velocity measured by the monitors. As the density of arriving particles increased during the sand slab impact, sand continued to accumulate below the sample bottom surface since the particle escape rate through the gap at the sides of the sample was less than the particle arrival rate. This then resulted in a higher sand density at the monitor locations when a sample was present, Figure 5.15(b) and Figure 5.16(b).

Assuming that the hydrodynamic pressure exerted by sand that had stagnated against the test block is the product of sand density and the square of the velocity (equation 5.11), then the sand velocity and density data obtained with the monitors,

Figure 5.15 and Figure 5.16, can be used to estimate the pressure applied to the front of the sample, and compared to that directly determined by the contact algorithm in the simulation code. These pressures are shown as a function of time in Figure 5.15(c) for the 14 cm standoff distance simulation and Figure 5.16(c) for a 40 cm standoff distance. The pressure for the 14 cm standoff distance test rose rapidly to a first peak, and then decreased before rising again to a second peak. This two peak pressure response was observed at the monitor locations regardless of whether a sample was present or not. It was also present when the contact pressure on the sample bottom surface was directly determined from the sample contact algorithm in the IMPETUS software, Figure 5.15(c). The first pressure peak measured with the monitors and by the contact algorithm for the sample was 30 MPa. This was nearly identical to the pressure of the initial pressure spike measured using the Hopkinson pressure bars, Table 5-2 and Figure 5.7(a), and corresponded to arrival of the fast (spalled) sand at the sample surface. A second, lower pressure (8.3 MPa) peak occurred at 0.55 ms after detonation, and corresponded to the arrival of the more densely packed sand slab at the monitors. Increasing the standoff distance to 40 cm, led to substantial reductions in sand density (due to axial stretching of the sand) and velocity (from air drag effects), Figure 5.16(a) and (b), and replacement of the first pressure spike by a gradual ramp of pressure, Figure 5.16(c). This was consistent with the disappearance of the initial spike in pressure observed experimentally as the standoff distance was increased, Figure 5.7.

Integration of the pressure waveforms enables the impulse at the monitor locations to be determined and compared to that directly obtained from the sample contact algorithm. The impulse calculated at the monitor locations both with, and without the sample present are compared with that given by the sample contact algorithm for a standoff distance of 14 cm in Figure 5.15(d). At 14 cm, the incident impulse with no sample present rose rapidly upon arrival of the sand and reached a maximum plateau value of ~14 kPa.s within approximately 2 ms after detonation, and was approximately the same as that when the sample was present and determined by the contact algorithm. This impulse also agreed well with that measured by the vertical pendulum.

At the 40 cm standoff distance, Figure 5.16(d), the measured and contact algorithm predicted impulse were in very agreement. Both were slightly less than the predicted impulse of the sand that passed through the monitors. This appeared to be a consequence of the slower arrival rate of the sand particles which permitted a slightly higher fraction of the particles to undergo a glancing reflection and exit the system through the gap at the sample side. Similarly good agreement between the measured and simulated impulses using the contact algorithm was seen for the other two standoff distance experiments, and the negative slope of the simulated impulse verses standoff distance relation ($-0.17\ kPa \cdot s \cdot m^{-1}$) was similar to that observed experimentally ($-0.2\ kPa \cdot s \cdot m^{-1}$). Table 5-4 shows that that the ratio between incident impulse and transferred impulse was close to unity for the four tested standoff distances.

Table 5-4. Simulated ratio between incident impulse and transmitted impulse

Standoff Distance (cm)		***Incident Impulse, I_o, (kPa-s)***	***Transmitted Impulse I_t, (kPa-s)***	***Ratio I_o/I_t***
14	No sample	13.3	-	-
	Sample	13.7	13.9	1.02
19	No sample	12.5	-	-
	Sample	12.8	13.2	1.04
29	No sample	10.9	-	-
	Sample	10.4	10.8	1.04
40	No sample	10.2	-	-
	Sample	9.5	9.1	0.96

It is interesting to note that the impulse acquired during the first 0.558 ms of sand loading for the 14 cm standoff distance case was about 9 kPa.s. This was consistent with the impulse calculated by integration of the simulated pressure versus time response for $558\ \mu s$ in the Hopkinson bar test mode, and with the experimental data obtained by integration of the experimental pressure-time data. The three results indicate that 9/13 of the impulse was transferred to the solid block over a period of about 0.588 ms. Similarly good agreement with the experimental data and Hopkinson bar mode simulations was observed at the other standoff distances, Figure 5.6(a). The impulses obtained by integrating pressure data for the Hopkinson bar mode simulations for that experimentally recorded (4.0 ms after detonation) are shown on Figure 5.8 and agree surprisingly well with the experimental impulse data obtained using the pendulum test mode. It appears that interactions between the many bar modes excited in the Hopkinson bars eventually converge to the transmitted impulse.

The gradual decline in total impulse transferred to the solid samples as the standoff distance was increased was a result of a small decrease is sand velocity with propagation distance (compare Figure 5.15(a) and Figure 5.16(a)) by momentum transfer to air particles, and lateral spreading of the sand slab as the distance to the sample increased. The effect of lateral spreading can be seen by calculating the impulse intensity distribution across the underside of the sand containment box lid and bottom face of the test block. These impulse distribution maps for the 14 and 40 cm standoff distance simulations are shown in Figure 5.17 and Figure 5.18 respectively. Close examination of the results show the fast (spalled) sand impacted the test sample, Figure 5.17(a) and Figure 5.18(a). In the 14 cm case, most of the later arriving sand also impacted the sample, Figure 5.17(b) and (c) or the edge of the aperture. However, examination of the impulse map for the 40 cm standoff simulation, Figure 5.18, shows that substantial impulse was transferred to the underside of the cover plate by sand impact. The significance of the lateral spreading can be further quantified by plotting the specific impulse along a line that traversed the middle of the underside of the cover plate, Figure 5.19. The area of the specific impulse curve inside the aperture at 14 cm was 1.08 times that at a 40 cm standoff as a result of the additional lateral scattering.

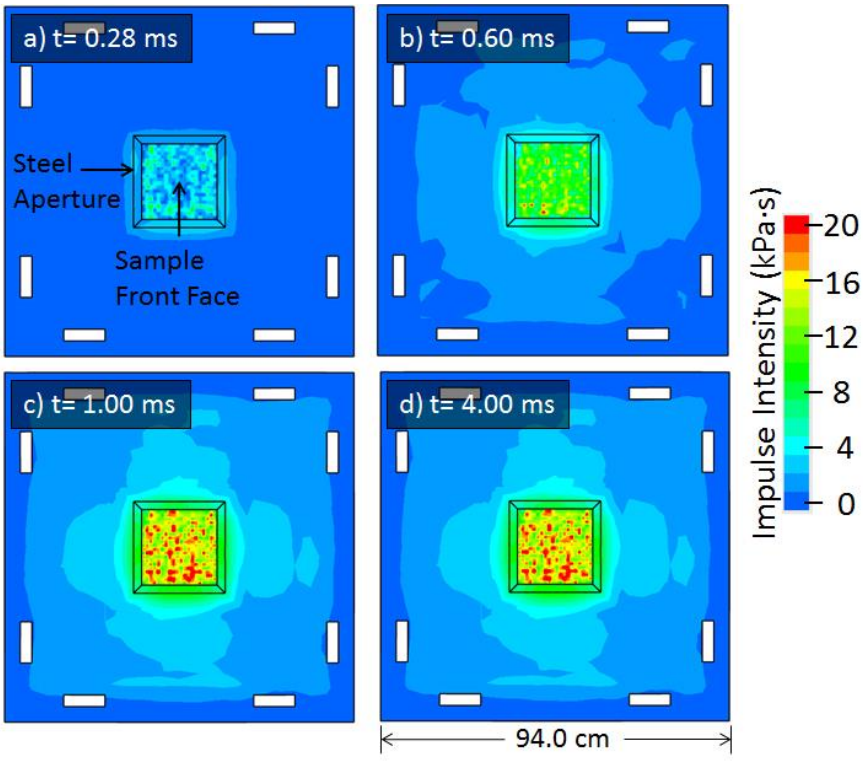

Figure 5.17. Impulse intensity distribution measured on the underside of the steel aperture opening for a 14 cm standoff distance.

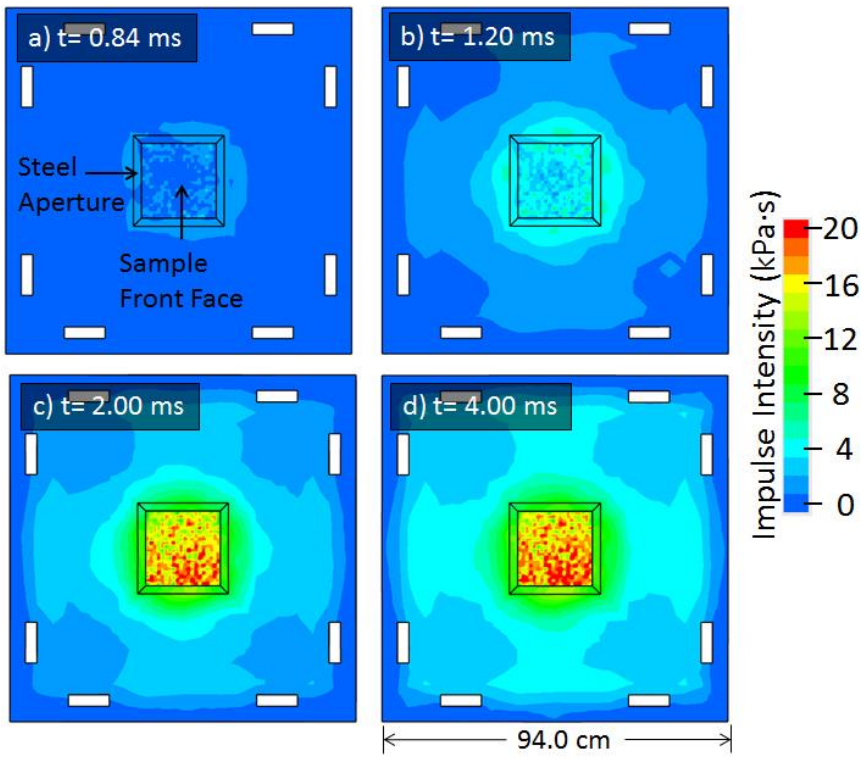

Figure 5.18. Impulse intensity distribution measured on the underside of the steel aperture opening for a 40 cm standoff distance.

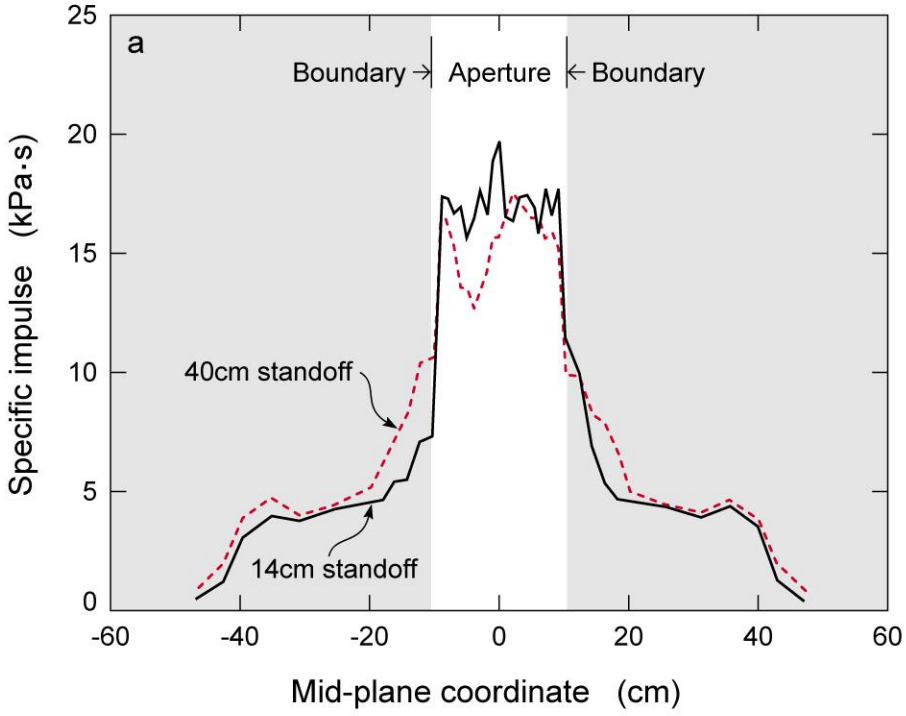

Figure 5.19. Specific impulse profile measured on the underside of the steel cover plate for standoff distances of 14 and 40 cm.

The sand particle impact with the underside of the lid caused it to suffer a displacement during the experiment. The underside of the test sample was also displaced vertically because of elastic compression (and extension) of the Hopkinson pressure bars. Figure 5.20(a) to (d) show these two sets of displacements, and reveal the effect they had upon the gap at the side of the test sample through which sand escaped. The combination of the two displacements resulted in a variation in the gap between the top of the steel lid and the bottom of the sand though which sand escaped the system, Figure 5.20(e). Initially, the distance between bottom of the sample and top surface of the sand

containment box lid was 8.15 mm. During the first 1.25 ms following detonation, the lid was displaced towards the sample by a greater distance than the upward displacement suffered by the sample. This led to a decrease in gap (between points b) and c) on the sample front face deflection curve) from 8.15 mm to about 3 mm at around 1.2 ms after detonation. This reduction in area through which the sand could escape resulted in more sand accumulation below the bottom surface of the sample, but had little effect upon transfer impulse transfer to the sample. At approximately 1.25 ms, the steel lid began to spring back towards its original location, and the gap for sand escape began to increase reaching a maximum width of 13 cm at 2.95 ms, Figure 5.20(d). This increased opening allowed the sand to escape from the sample front face, and relieve the pressure on the lower face of the sample.

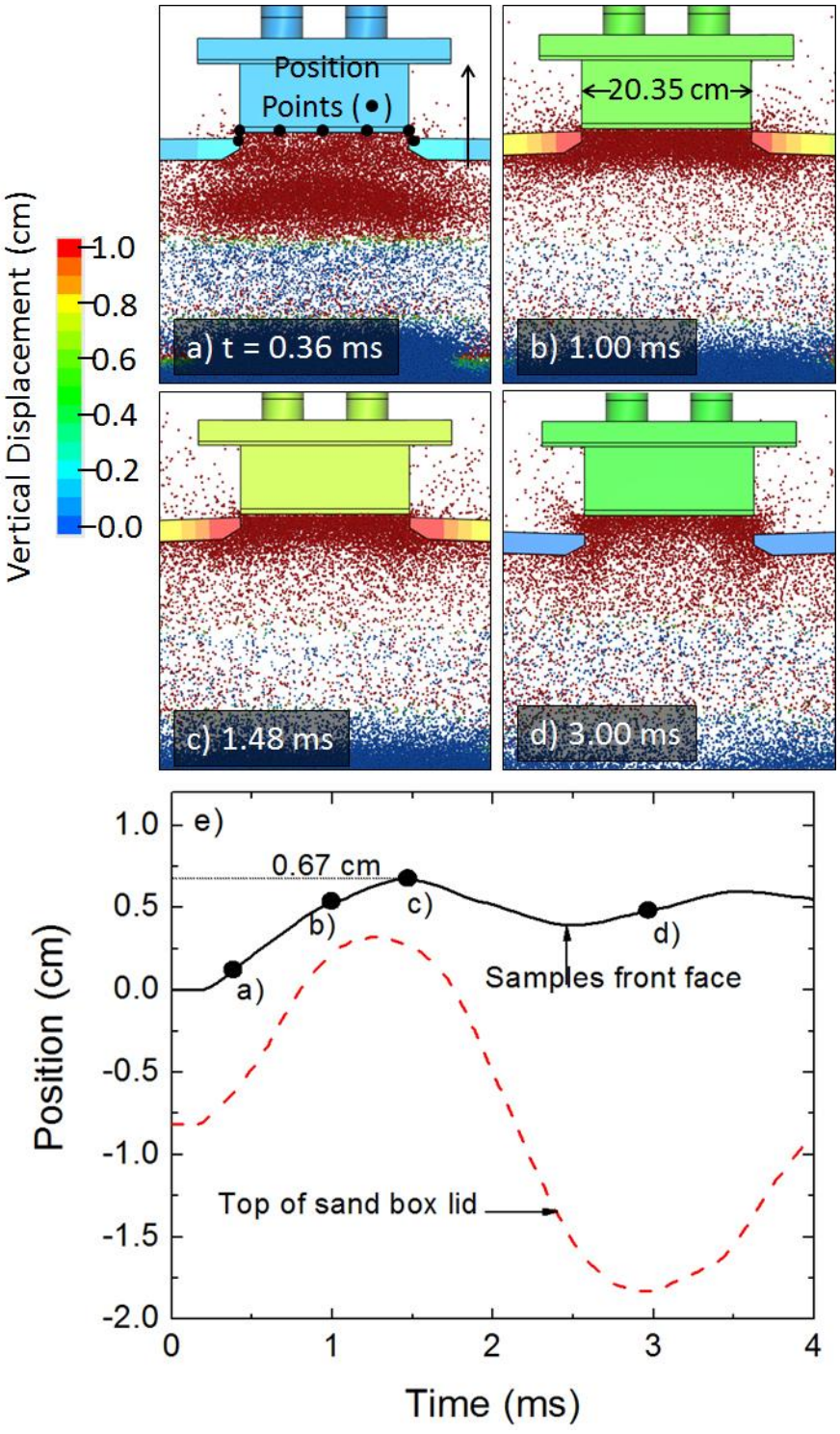

Figure 5.20. The simulated vertical displacement of the test blocks front face for the 14 cm standoff distance test. The displacement of the top of the aperture opening was also monitored (red dashed line). Detailed simulations (a-d) show the test structure and aperture vertical displacements and sand particle interaction at various stages of the loading process.

Chapter 6. Impulse Transfer during Sand Impact with a Cellular Structure

In Chapter 5 the pressure and momentum transferred to an incompressible, back-supported aluminum block was explored experimentally and numerically. Using the same impulsive loading facility that was discussed in Chapter 5, Chapter 6 will investigate the pressure and momentum transferred to a 3D cellular structure to understand the benefits for using cellular structures to mitigate impulsive sand loading. The results are also used in conjunction with the same discrete particle based simulation that were used in Chapter 5 to investigate the soil – structure interaction for cellular structures with a thin (weak) and thick (relatively rigid) front face. It is shown both experimentally and numerically that the cellular structures mitigated the impulse by approximately 10-15%. The validated model will be used in later Chapters to understand how the core, face sheet, and steel lids aperture affects the pressure and momentum transferred to the cellular structure.

6.1. Test Structure

The study utilized three test samples shown schematically in Figure 6.1. The solid block used in Chapter 5 of the soil – structure interaction is shown in Figure 6.1(a). The cellular structures were manufactured by first laying down a co-linear layer of 6061 aluminum alloy square tubes each spaced a tube width apart. A second, similarly spaced layer was then orthogonally placed on the first, and the assembly sequence repeated to create a $[0^o/90^o]_2$ structure. The 3D topology was assembled from the 2D array by inserting identical tubes in the out-of-plane (vertical) void space between the cross-ply oriented tubes. The 3D core was attached to either 12.7 mm or 4.7 mm thick front face sheets to create the two other sample types tested, Figure 6.1(b) and (c). All the structures were attached to 4.7 mm thick back face sheet with a pre-drilled set of holes that permitted attachment to the test rig. The out-of-plane tubes in the 3D cellular structure were notched to facilitate complete fluid penetration during a subsequent dip brazing operation used to bond the various components of the test structure, see Section 2.2. After brazing the structure was heat treated to the T6 (peak aged) condition. The geometry and mass of the 3D test structure investigated in this chapter is summarized in Table 6-1, and Figure 6.1. The core occupied a volume of $3.14x10^{-3}\ m^3$ while the aluminum in the 3D core occupied a volume of $6.3x10^{-4}m^3$ resulting in a core relative density $\bar{\rho} = 20.1\%$. The solid aluminum block, Figure 6.1(a), had the same volumetric dimensions as the tube core structure. Both structures in Figure 6.1(b) and (c) had identical cores; however, the different thickness front face sheets led to the thickness of the three structures to vary, as shown in Figure 6.1.

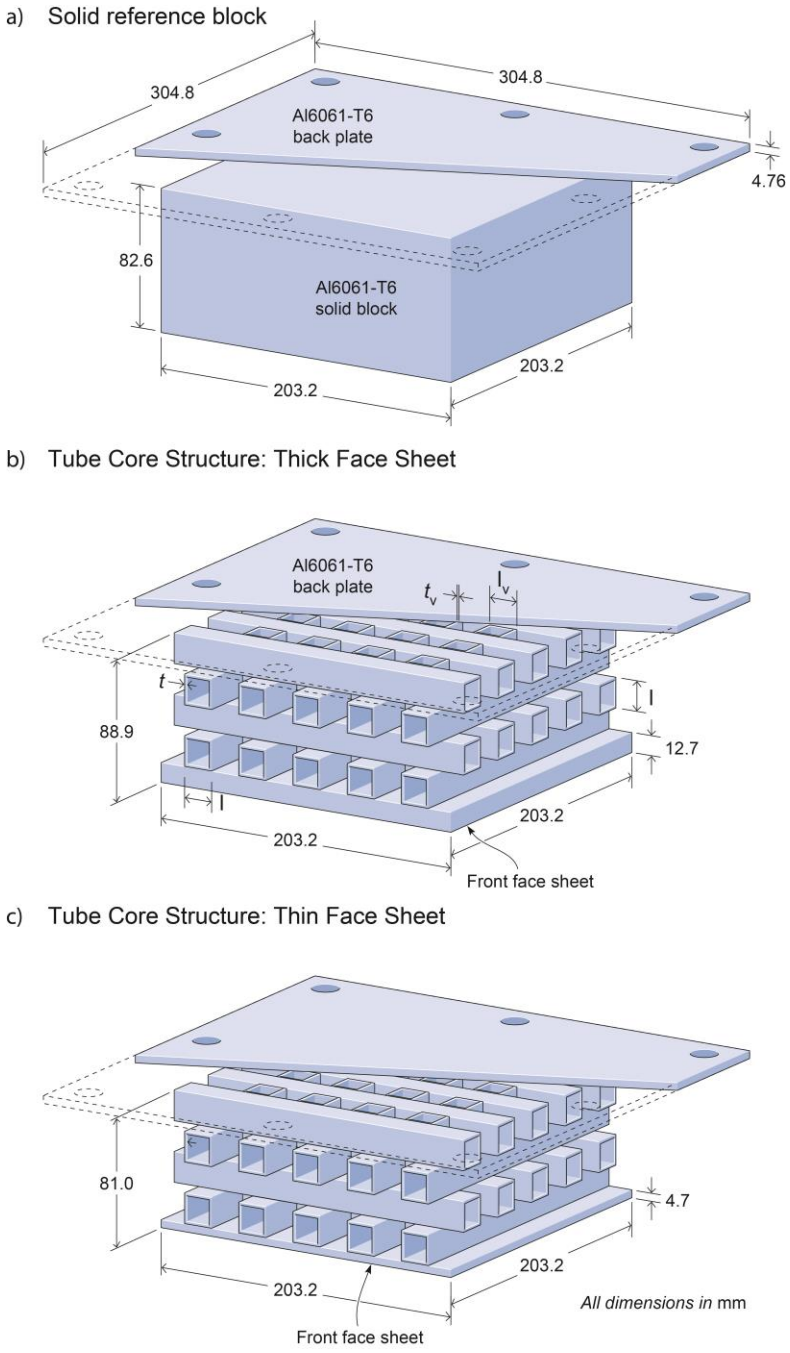

Figure 6.1. The back-supported test structures used for the sand impact loading experiments. (a) Solid Al6061-T6 reference block welded to 4.76 mm thick plate. The hole pattern on the back face sheet provided a means to bolt the specimen to the vertical impulse test apparatus. (b) The Al6061-T6 3D tube cellular structure with 12.7 mm thick front face and (c) the same cellular structure with a 4.7 mm thin front face.

Table 6-1. Core dimensions for back-supported test specimens

Sample	In-plane tube wall thickness, t (mm)	In-plane tube width, l (mm)	Out-of-plane tube wall thickness, t_v (mm)	Out-of-plane tube width, l_v (mm)	Face sheet thickness, t_{fs} (mm)	Specimen weight (kg)	Core weight (kg)	Relative density (%)
3D	1.45	19.05	1.45	19.05	4.7	3.22	1.51	20.1
3D	1.45	19.05	1.45	19.05	12.7	4.03	1.51	20.1

6.2. Blast Loading Test Procedures

The cellular structures were loaded by explosively accelerated wet synthetic sand in the same vertical impulse loading facility used to study impulse transfer to solid block samples, chapter 5. Figure 6.2 shows a schematic representation of the vertical impulse test apparatus. The reader is referred chapter 5 for a detailed description. The separation distance, δ, between the front face of the three test structures and the outside surface of the top plate of the steel sand box enclosure (Figure 6.2) varied during this study as a result of the varying test structure thicknesses, Figure 6.1. The gap, δ, for the solid block was 8.1 mm, while it was 9.7 mm for the thin face sheet cellular structure, and 1.8 mm for the thick face sheet cellular structure. Figure 6.2 illustrates the test geometry with a thin face sheet cellular structure attached.

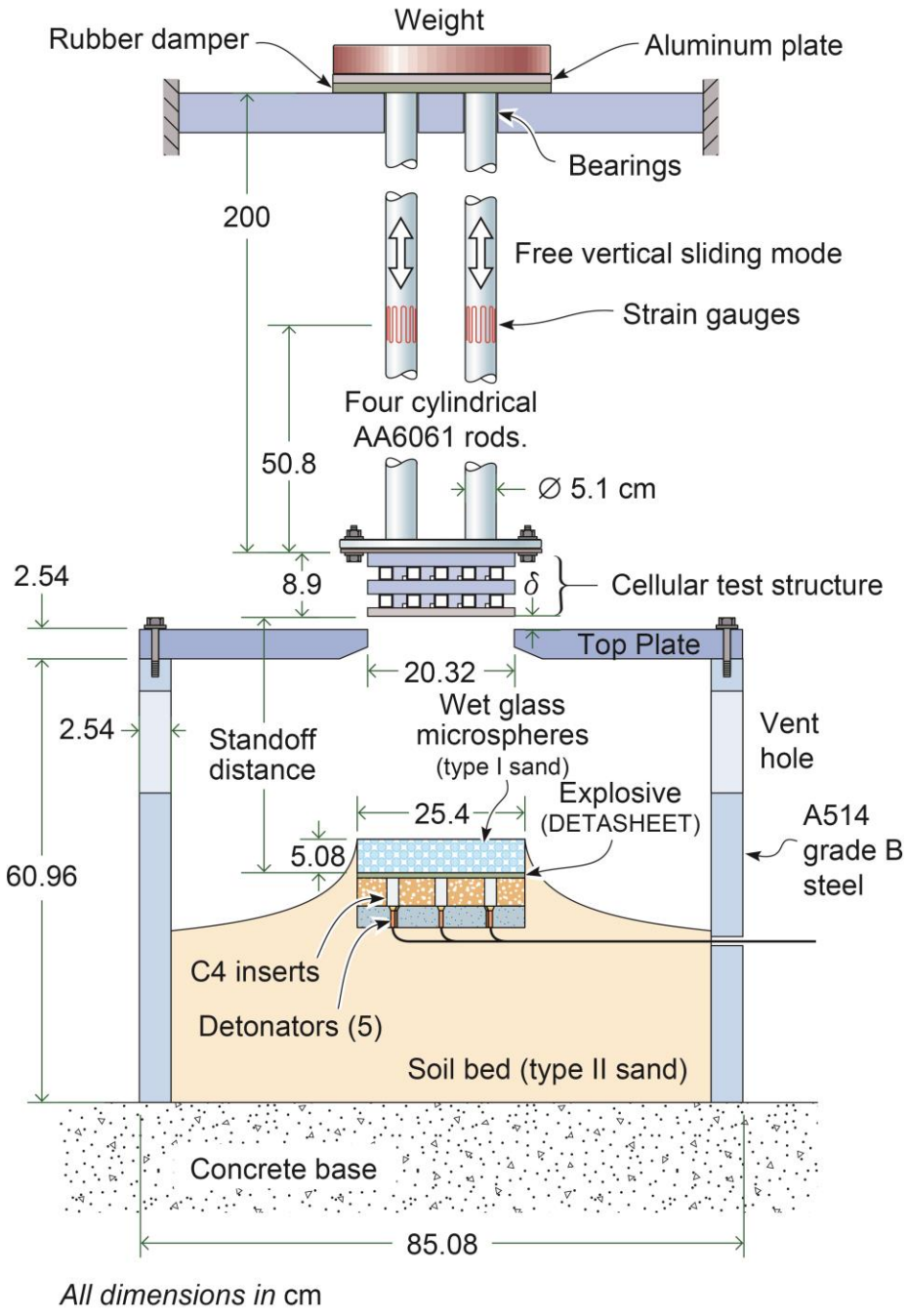

Figure 6.2. The vertical impulse test apparatus used to measure impulse and pressure transmission by the three test samples during synthetic sand impact. The standoff distance was varied by raising or lowering the location of the explosive sheet within the soil bed. The gap δ between sample surface and the sandbox top plate was 8.1 mm for the solid block, 9.7 mm for the thin face sheet cellular structure, and 1.8 mm for the thick face sheet samples.

6.3. Experimental Results

6.3.1. Vertical Pendulum Mode

The impulse transmitted by the sand to the cellular core sandwich structures were first deduced from the pendulum jump height and mass are summarized in Table 6-2 and compared with analogous data for the solid block sample. The impulse transferred to the solid aluminum block and cellular structure with a thick face sheet is shown as a function of standoff distance in Figure 6.3(a). The impulse applied to the solid block was experimentally observed to decrease from approximately 14 kPa·s, for a standoff distance of 14 cm, to approximately 8 kPa·s at a standoff distance of 40 cm. The impulse acquired by the cellular structure with a thick face sheet was less than that of the solid block; it decreased from approximately 12.5 kPa·s at a standoff distance of 14 cm, to approximately 8 kPa·s at a standoff distance of 40 cm. The error bars shown with the data were estimated from the uncertainty in pendulum height during the exposure time of a high speed video image and from estimates of the parallax error. The impulse transferred to the solid block decreased linearly with standoff distance, and had a slope $=-0.20\ kPa \cdot s \cdot cm^{-1}$. The impulse transferred to the thick front face covered cellular structure also decreased linearly with standoff distance, but with a slightly smaller slope $=-0.16\ kPa \cdot s \cdot cm^{-1}$. The impulse of the thin faced sandwich structure decreased from approximately 11.5 kPa·s at a standoff distance of 14 cm, to approximately 8 kPa·s at 40

cm, Figure 6.3(c). The impulse of the thin faced sandwich structure decreased linearly with standoff distance with a slope of $-0.14\ kPa \cdot s \cdot cm^{-1}$.

Table 6-2. Transmitted impulse for test specimens

Topology	***Standoff Distance (cm)***	***Charge Mass (C4 Insert Mass) (g)***	***Average Core Strain, ε_c (%)***	***Mass of Pendulum with Sample and Counterweights (kg)***	***Jump Height, h(t), (m)***	***Transferred Impulse $(kPa \cdot s)$***
Solid	14	300 (50)	_	106.6±0.15	1.49±0.17	13.9±0.8
3D (12.7mm)			18.6	106.3±0.15	1.22±0.15	12.6±0.8
3D (4.7mm)			20.1	106.9±0.15	1.05±0.16	11.7±0.9
Solid	19	300 (50)	_	92.3±0.15	1.46±0.21	12.0±0.9
3D (12.7mm)			14.5	92.0±0.15	1.31±0.17	11.3±0.8
3D (4.7mm)			18.1	92.7±0.15	1.18±0.19	10.8±0.9
Solid	29	300 (50)	_	85.1±0.15	1.26±0.24	10.2±1.0
3D (12.7mm)			6.8	85.4±0.15	1.11±0.17	9.6±0.8
3D (4.7mm)			8.9	85.3±0.15	1.05±0.21	9.4±1.0
Solid	40	300 (50)	_	85.1±0.15	0.84±0.17	8.3±0.8
3D (12.7mm)			3.2	85.4±0.15	0.78±0.15	8.1±0.8
3D (4.7mm)			3.4	85.3±0.15	0.69±0.13	7.9±0.7

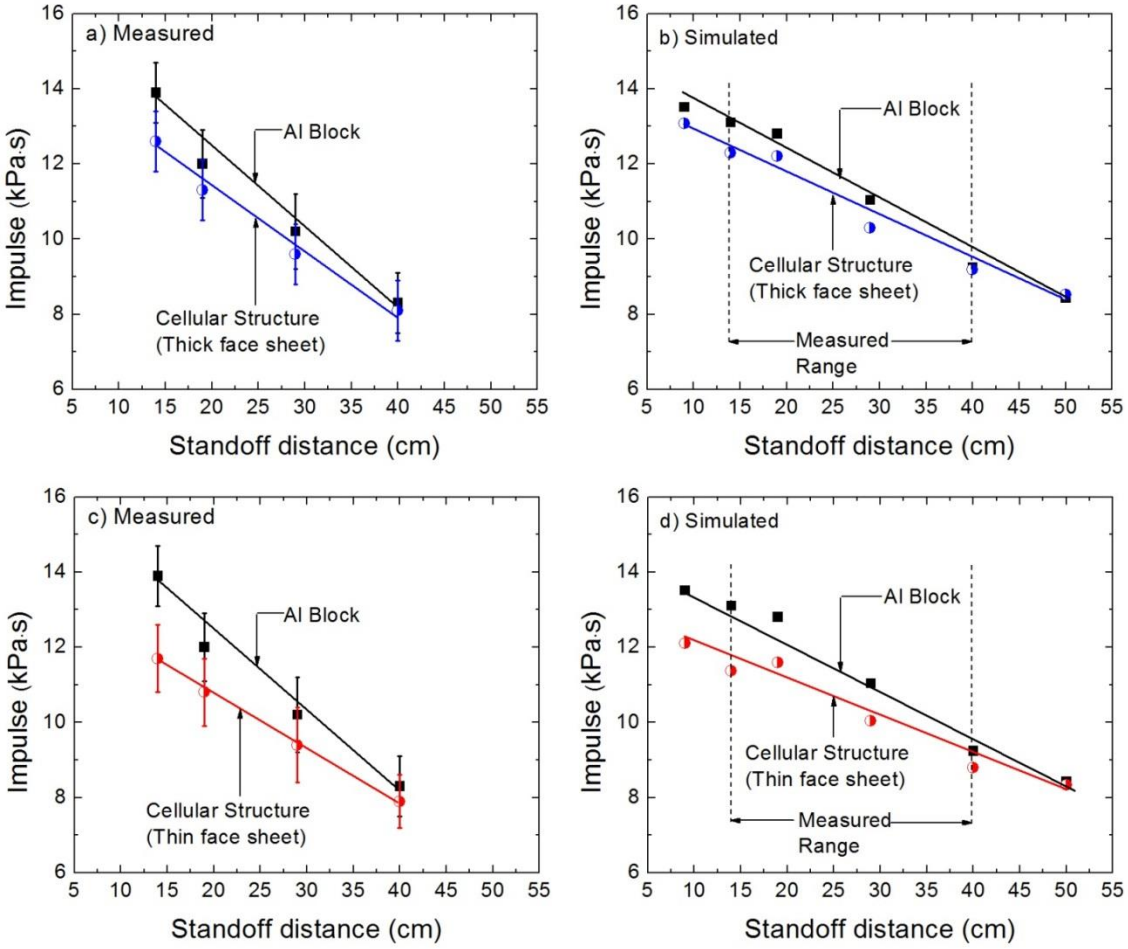

Figure 6.3. (a) Comparison between experimentally measured impulses transmitted by a solid aluminum block and the 3D cellular structure with a thick front face versus standoff distance. (b) Simulated results for the same experiments. (c) Comparison between experimentally measured impulses transmitted to a solid aluminum block and a 3D cellular sample with a thin front face versus standoff distance. (b) Simulated results for the same experiments together extensions to establish trends. Simulations at a shorter and a longer standoff distance have been added to confirm trends.

6.3.2. Hopkinson Pressure Bar Mode

The pressure-time responses for the thin face cellular structures (measured at the strain gauge locations on the four Hopkinson pressure bars) are shown in Figure 6.4 (solid black lines) for each standoff distance. Time *t=0*, corresponded to detonation of the test charge. All the pressure-time signals exhibited an initially sharp rise to a peak pressure that decreased with increasing standoff distance. Following the initial pressure peak, a period of declining pressure was observed before the first reflected signal arrived at the strain gauge locations (shown on the figures). Its slope decreased with standoff distance, and at the largest standoff distance, the slope of this region was almost flat (a plateau), Figure 6.4(d). There was an abrupt drop in pressure corresponding to the arrival of the first (sign converted) reflected signal at the sensor location, followed by elastic reverberations of the Hopkinson bars.

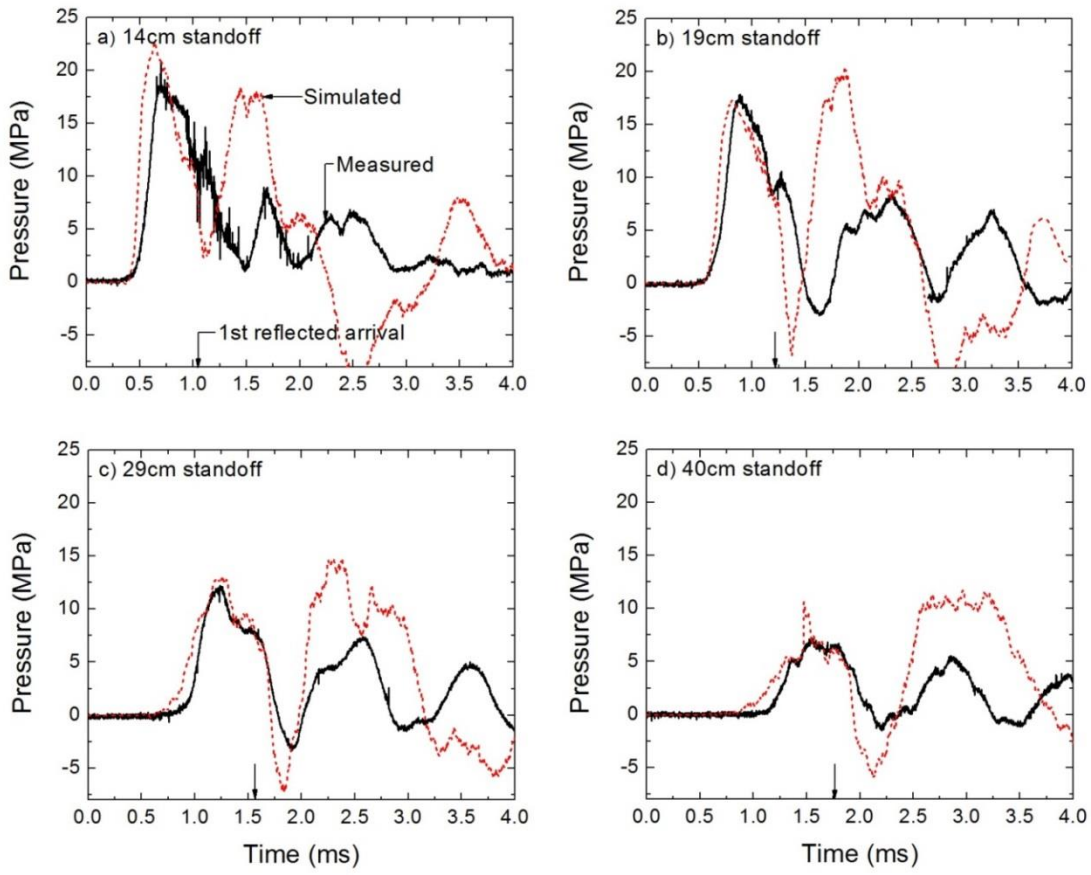

Figure 6.4. Measured (solid line) and simulated pressure-time waveforms for the thin face sheet, 3D cellular structure at standoff distances of a) 14 cm, b) 19 cm, c) 24cm, and d) 40 cm.

The pressure-time curves shown in Figure 6.4(a)-(d) were integrated to calculate the impulse-time curves shown in Figure 6.5 (solid black lines). The time at which the first distal reflection and the second reflected signals reached the sensors on the Hopkinson bars ($558\ \mu s$ and $748\ \mu s$ respectively) are shown for each standoff distance. The first refection was sign converted upon reflection from the top of the bar and its arrival caused a sharp drop in pressure, and inflection in the impulse –time response. The

second reflection had under gone two sign reversals, and was in phase with the continuing direct signal. Its arrival therefore caused the impulse to again start rising.

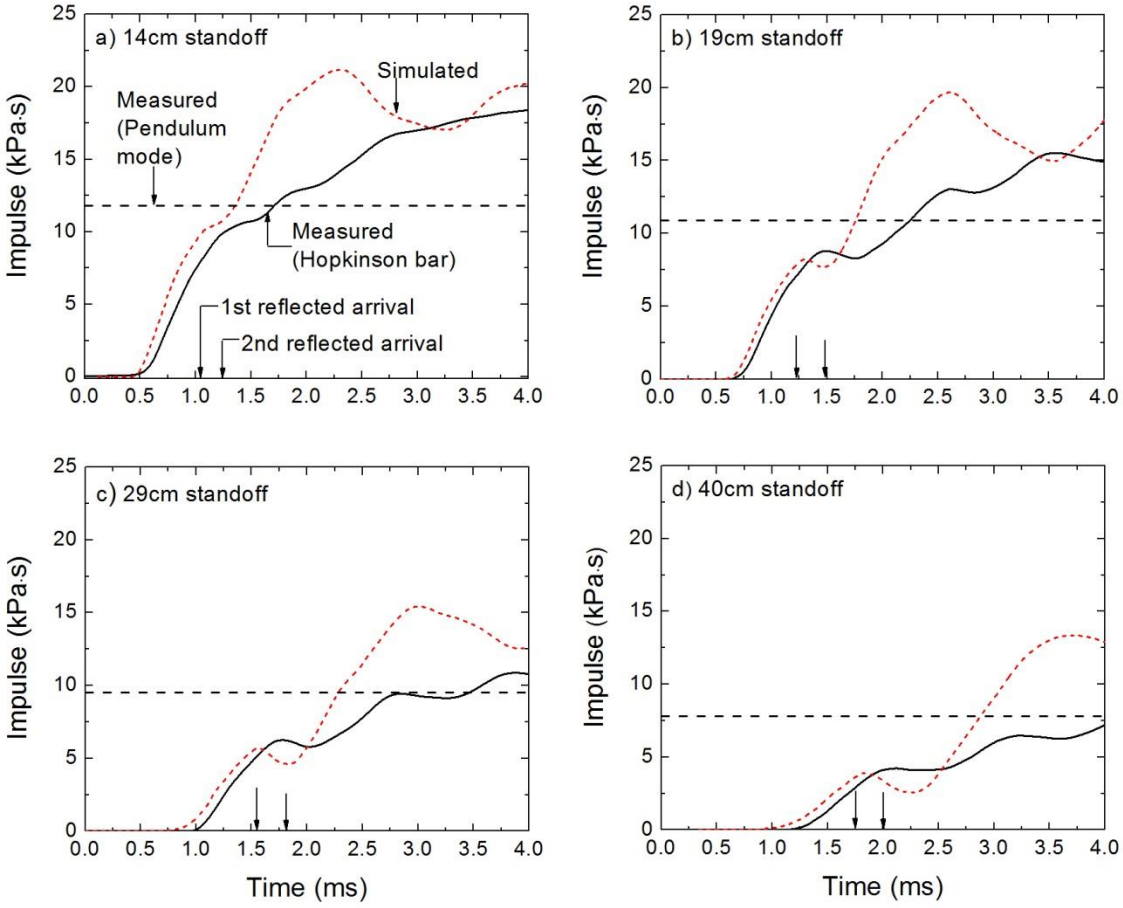

Figure 6.5. Measured and simulated transmitted impulse-time waveforms obtained by integration of the pressure-time waveforms for the thin face sheet, 3D cellular structure for standoff distances of a) 14 cm, b) 19 cm, c) 24cm, and d) 40 cm.

The peak pressures for each standoff distance are summarized in Table 6-3, and plotted against standoff distance in Figure 6.6(a). Table 6-3 and Figure 6.6(a) also shows that the peak pressures recorded for the solid aluminum block were greater than those for the cellular structure at the same standoff distance. The pressure applied to the solid

block was observed to decrease from approximately 28 MPa at a standoff distance of 14 cm, to approximately 10 MPa at a standoff distance of 40 cm. At the shortest standoff distance of 14 cm, the initial peak pressure transmitted by the cellular structure was 19.4 MPa. This fell with increase in standoff distance to 7.2 MPa at a standoff distance of 40 cm. The pressure applied by the solid block decreased linearly with standoff distance with a slope $=-0.7\ MPa \cdot cm^{-1}$. The pressure applied by the thin front face cellular structure also decreased linearly with standoff distance, but with a slope $= -0.5\ MPa \cdot cm^{-1}$. The cellular structures crush strength (21.8 MPa) has been previously reported in Chapter 3 and is shown on Figure 6.6(a).

Integration of the pressure data acquired up to the arrival of the first bar reflection, Figure 6.5, indicated that a substantial fraction of the full impulse was acquired during the first $558\ \mu s$ of sand impact. The initial slope of pressure time response gives an estimate of the impulse transfer rate, $\dot{I}$. Using the data shown in Figure 6.5, $\dot{I}$ = 18.8 MPa at a 14 cm standoff and fell to 6.9 MPa at a 40 cm standoff distance; consistent with the average pressure during the first $558\ \mu s$ pressure measured with the Hopkinson bars, Table 6-3. The impulse rate for the comparable solid aluminum block is also presented in Table 6-3 and exceeded that of the cellular structure. The impulse obtained by integrating the pressure waveform for 558 μs after the first direct arrival is summarized in Figure 6.6(c). The measured impulse transmitted by the cellular structure was 2-3 kPa·s lower than that transmitted by the solid block, Figure 6.3(c).

Table 6-3. Transmitted back pressures with Hopkinson bars.

Topology	***Standoff Distance (cm)***	***Average Core Strain, ε_c (%)***	***Peak Pressure (MPa)***	***Transferred Impulse at 558μs, I, (kPa-s)***	$\frac{dI}{dt} = \dot{I}$ ***(kPa)***
Solid		_	28.2	10.8	21.5
3D (4.7mm)	14	20.1	19.4	7.9	18.8
Solid		_	25.3	8.9	18.0
3D (4.7mm)	19	18.1	17.8	7.0	16.0
Solid		_	14.2	6.4	11.4
3D (4.7mm)	29	8.9	12.2	5.1	11.2
Solid		_	9.3	4.6	8.1
3D (4.7mm)	40	3.4	7.2	2.9	6.9

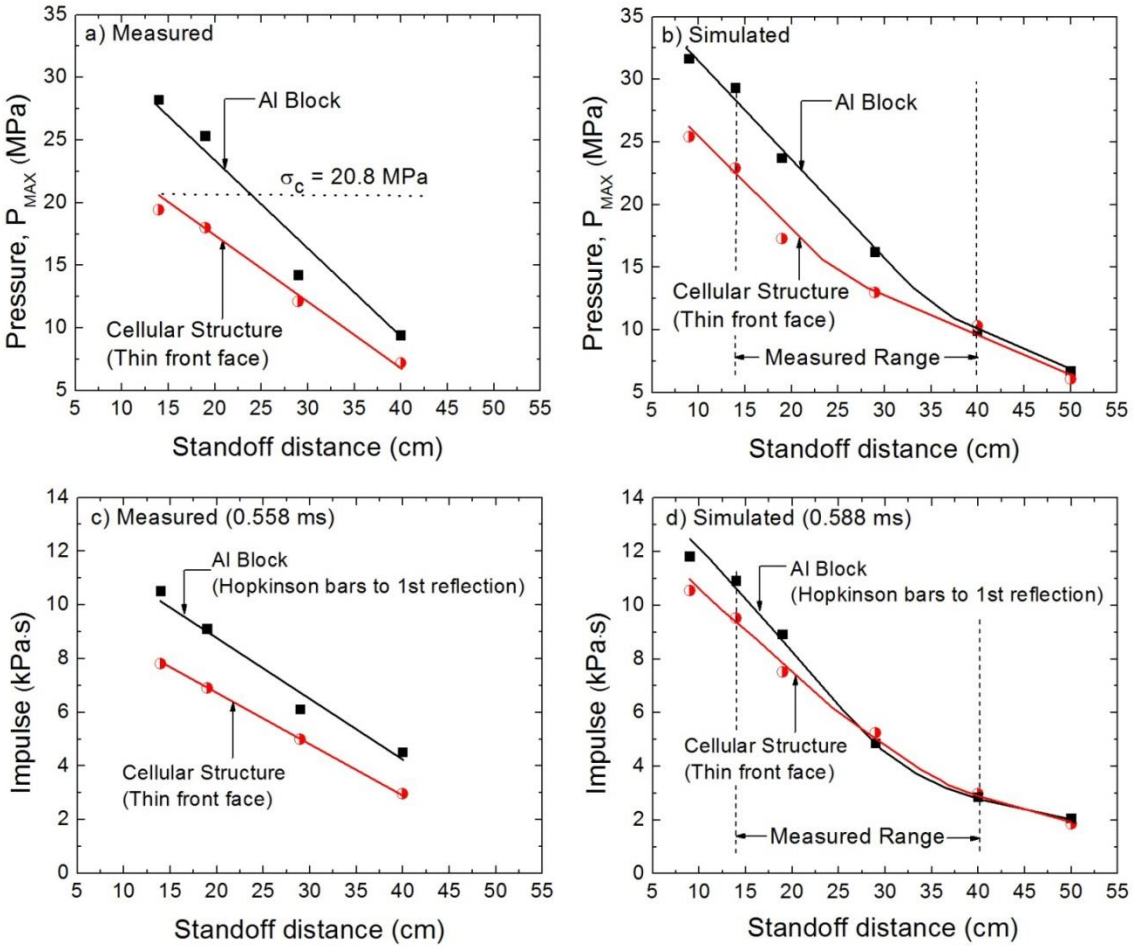

Figure 6.6. The dependence of pressure transmitted to the distal side of the solid aluminum block and thin faced cellular structure versus standoff distance: a) Measured and b) simulated. The dependence of impulse transmitted to a solid aluminum block and a thin faced cellular structure upon the standoff distance. c) Determined by integration of measured pressure - time response for 558 μs from the initial rise in impulse. d) Determined from the simulation results.

The test samples were sectioned and photographed to reveal their mid-plane deformation, Figure 6.7 and Figure 6.8. The collapse mechanisms shown in Figure 6.7 and Figure 6.8 are consistent with those found during the quasi-static and dynamic studies. Core crushing was initiated by the onset of buckling of the tubes oriented in the

through thickness direction, and was nucleated at the notches in the out of plane tubes. The vertical side walls of the in-plane tubes then began to buckle and constrained the amplitude of the vertical tube buckling. This led to repeated folding of the vertical tubes and a plateau-like stress-plastic strain response. The change in core thickness was used to calculate the core plastic strain caused by sand impact with both the thick and thin front faced cellular structures. These results are shown as a function of incident impulse (taken to be that transferred to the solid bock samples at each standoff distance) for both sample types in Figure 6.9(a) and (b). The core strains of the thin face samples were approximately the same as those of samples with a thick front face sheet. Examination of Figure 6.7 and Figure 6.8 show that the sides of the face sheets, especially for the most severely loaded samples, had been dent upwards by the sand impact, and the impacted surface therefore acquired a slightly convex shape (when viewed from below).

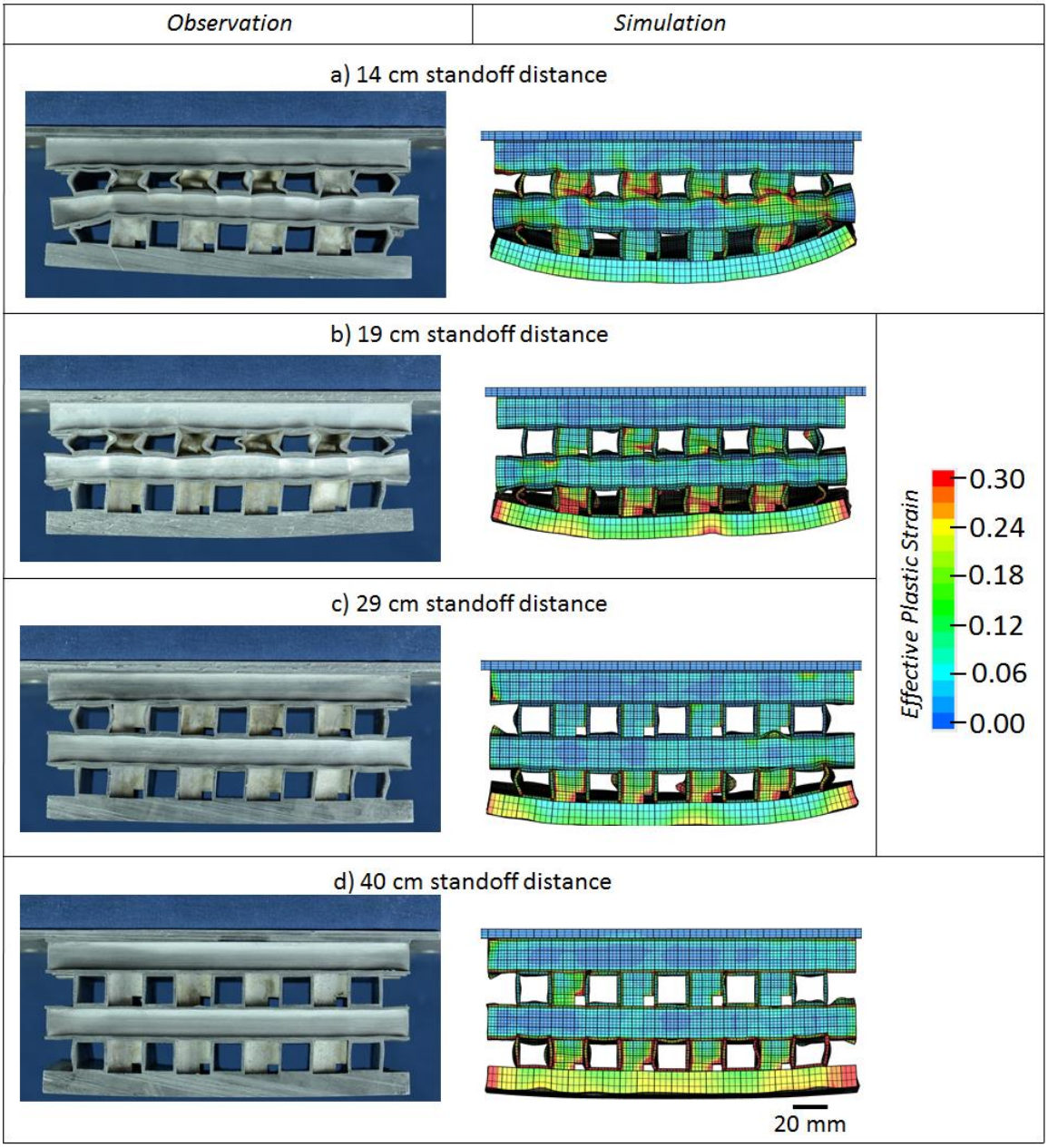

Figure 6.7. Measured and simulated deformations of a thick faced, 3D sandwich structure following impulsive sand loading (from below) using various standoff distances.

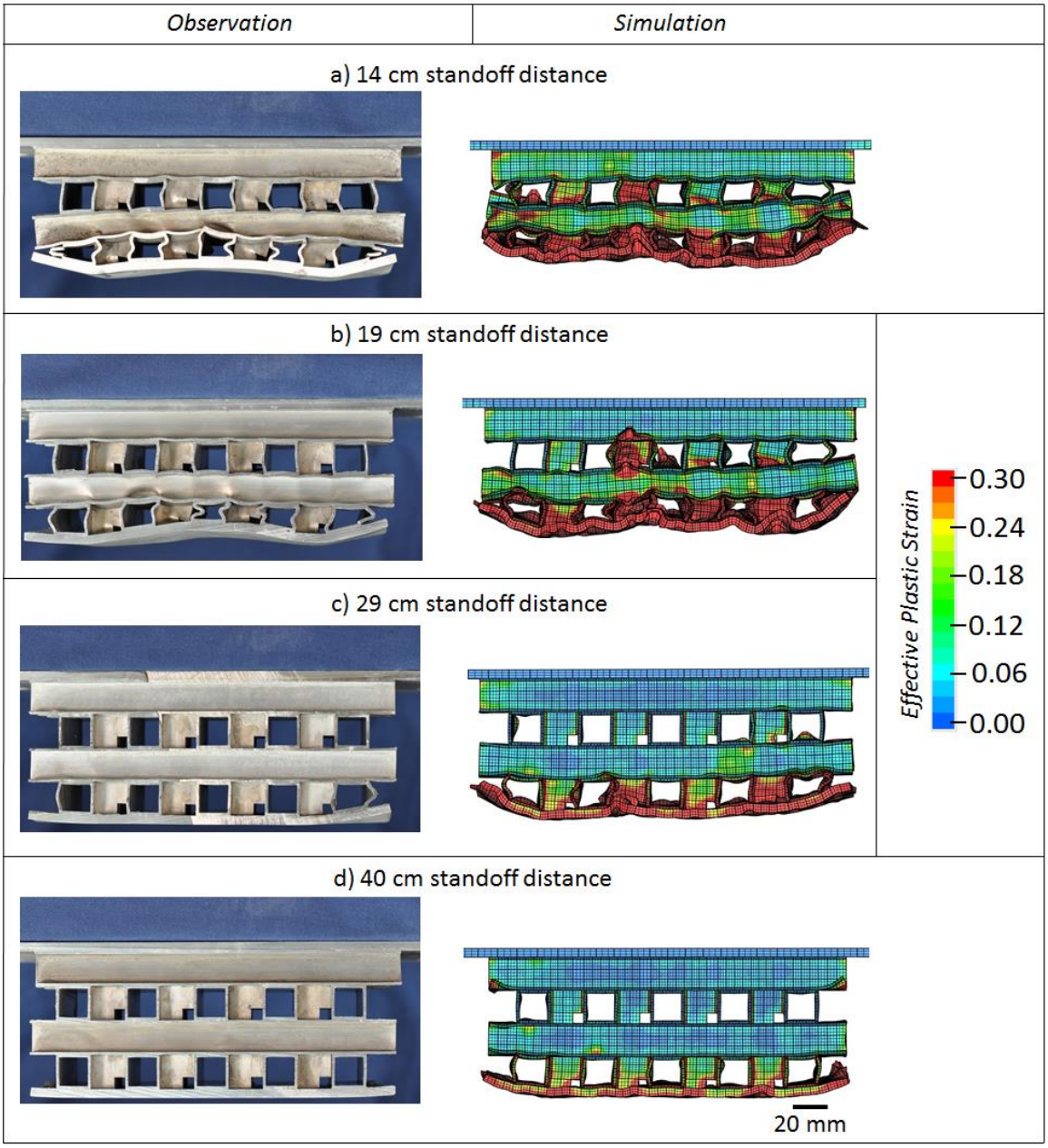

Figure 6.8. Measured and simulated cross-sectional images of the thin face, 3D test structrure after sand impact at stand off distances of a) 14cm, b) 19cm, c) 29cm, d) 40cm.

The difference in impulse transferred by the solid block and cellular structures (with thick and thin faces) has been divided by the impulse transferred by the solid block

and is plotted against incident impulse (again taken as that transferred to the solid block) in Figure 6.9(c) and (d). It can be seen that the reduction in impulse transferred by the cellular structures increased with incident impulse (reduction in standoff distance) and that samples with thinner face sheets suffered a large change.

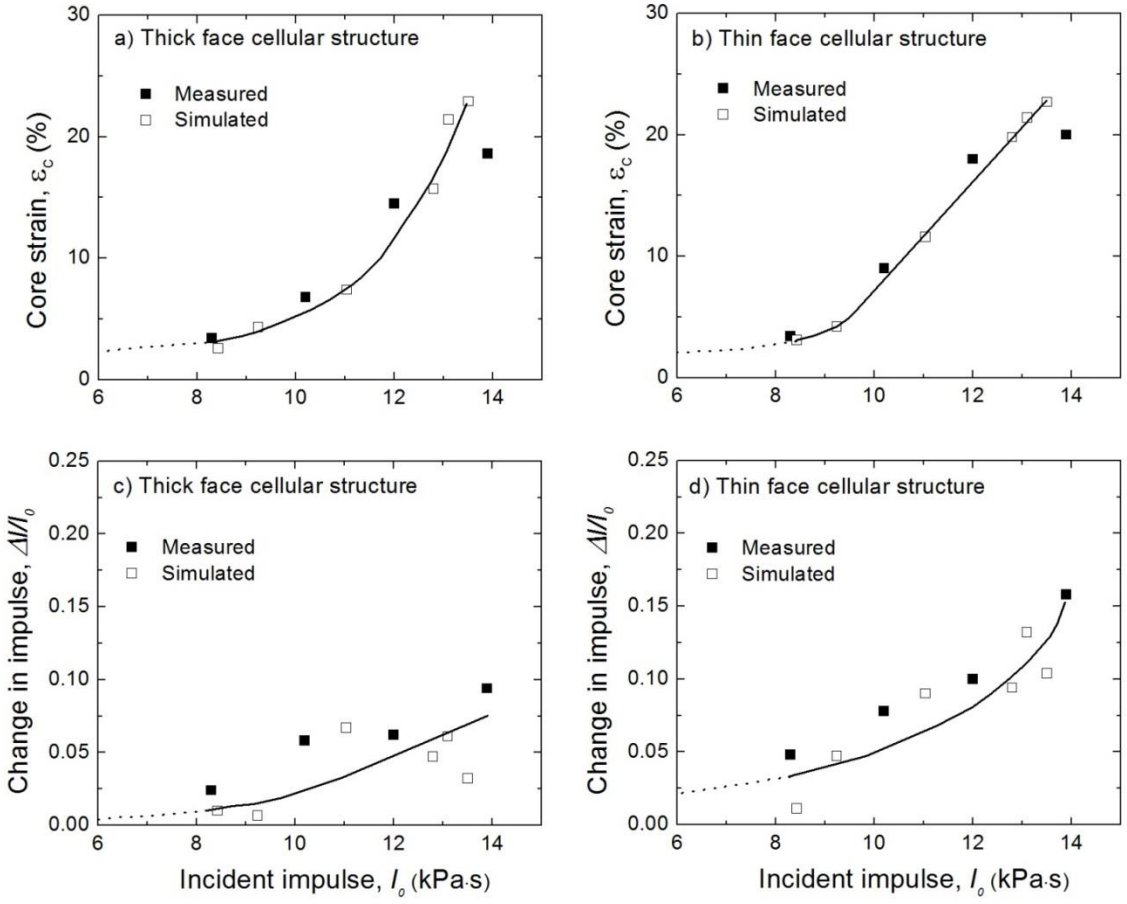

Figure 6.9. a) Core compressive strain versus incident impulse measured with solid block for the thick face 3D cellular structure, and for the b) thin face cellular structure. c) The difference in transmitted impulse between a solid aluminum block and the thick face cellular structure versus the incident impulse, and d) is shows the difference in transmitted impulse between a solid block and the thin face cellular structure.

6.4. Numerical Simulations

The commercial IMPETUS Afea Solver was used to simulate the experiments conducted with the vertical impulse test apparatus. A detailed description of its implementation to analyze the vertical impulse test facility and the earlier experiments with the solid block can be found Chapter 5.

6.4.1. The Cellular Structure Model

The geometry and relative density of the modeled tube specimens were designed to be the same as the measured specimens, reported in Table 6-1, but following the usual practice previously discussed in section 4.2.1, small imperfections were incorporated in the models to account for the manufacturing defects (such as tube misalignment and tube wall thickness variability) in the tested specimens that tripped tube wall buckling under compressive loading. The imperfections were introduced as a displacement to each tube wall with a spatial distribution corresponding to the lowest order measured eigenmode. For all modeled structures the first order eigenmode amplitude was set at 0.1 times the tube wall thickness.

6.4.2. Material Properties

The experimentally recovered Cauchy stress-true strain response of the Al 6061-T6 alloy used to make the test specimens was presented in Figure 2.6. The uniaxial Cauchy stress, σ, versus true strain, ε, relation for an elastic-plastic material under uniaxial straining can be written:

$$\varepsilon = \varepsilon_e + \varepsilon_p = \frac{\sigma}{E} + \varepsilon_p \tag{6.1}$$

where ε_e and ε_p are the elastic and plastic components of strain and E is Young's modulus. Having performed the uniaxial tensile test, the true stress versus plastic strain curve was tabulated and used to determine an isotropic strain hardening relation needed for FE simulations. The transition from elastic to plastic behavior was set at a Cauchy stress of 230.7 MPa. The hardening tabulation was implemented in the IMPETUS Afea Solver using the general piecewise linear hardening constitutive model with optional thermal softening and strain rate hardening. The yield stress of this model is defined in the form:

$$\sigma_y = f\left(\epsilon_{eff}^P\right)\left(1 - \left(\frac{T - T_0}{T_m - T_0}\right)^m\right)\left(1 + \frac{\dot{\epsilon}_{eff}^P}{\epsilon_0}\right)^c \tag{6.2}$$

where $f(\epsilon_{eff})$ is the piecewise linear hardening function of the effective deviatoric strain, which was obtained from the hardening curve behavior. The thermal softening component was defined by the current temperature, T, the reference temperature, T_0, the melting temperature, T_m, and the thermal softening parameter, m.

The strain rate hardening component of Eq (6.2) was defined by a reference strain rate, $\dot{\epsilon}_0$, and a strain rate hardening parameter, c. The coefficients used in conjunction with Equation 2 to model the material are given in Chapter 3.6.2. We note that the thermal softening and strain rate hardening components made a negligible contribution to the yield stress. This was primarily defined by the piecewise linear hardening function $f(\epsilon_{eff})$ modeled using a von Mises yield criterion with isotropic hardening.

To account for softening resulting from tube wall fracture on the tensile side of severely buckled tubes, the Cockcroft-Latham failure criterion was implemented for all the simulations. Failure was defined to occur when a damage parameter, D, reached unity. The damage parameter was calculated as:

$$D = \frac{1}{W_c}\int_0^{\epsilon_{eff}} \max(0, \sigma_1)\, d\epsilon_{eff} \qquad (6.3)$$

where σ_1 is the first principle stress. The critical damage parameter, W_c =85 MPa was obtained by fitting the simulated measured stress-strain response of a single laterally compressed tube tested Appendix B. The general node splitting feature in the IMPETUS code was turned on. In this feature the damage variable was allowed to evolve without any change to the constitutive response of the Al 6061-T6 alloy until D=1. At that instant, the Al6061-T6 alloy was assumed to have failed and nodes of the elements where this failure has occurred were split.

The FE model was constructed from 7,104 cubic and 19,608 linear hexahedra elements with 246,216 nodes. The Hopkinson bars and all connecting parts were modeled with a coarse mesh since material failure was not seen experimentally. The solid test block was modeled with a finer mesh since some local deformation (thought to be associated with sand fingers) was observed experimentally. The solid block was constructed from 16,944 8-node 3rd-order linear hexahedra elements. The cellular structure sample with a thin front face sheet was constructed with 19.278 8-node 3rd-order linear hexahedra elements and the cellular structure sample with a thick front face was constructed from 15,568 8-node 3rd-order linear hexahedra elements. A mesh sensitivity study was performed for all three sample types to confirm solution convergence with this level of discretization.

6.5. Simulation Results

6.5.1. Comparisons with Experiments

The IMPETUS code enables a direct computation of the momentum incident upon the front face of a test structure. This feature was used to calculate the impulse transferred to the solid Al block and to the cellular samples with thick and thin impact faces. The simulated impulse transferred to the solid block and thick front cellular samples is shown as a function of standoff distance in Figure 6.3(b). Similar data for the thin faced sample is shown in Figure 6.3(d). The magnitudes of the simulated impulses

for both the solid and cellular structures were in good agreement with those measured with the vertical pendulum, and declined with increasing standoff distance. Within the experimental range of standoff distances, the impulse transferred by the cellular structures was usually less than that transferred by the solid block, and the difference was slightly large for the thin faced samples, Figure 6.3(a) and Figure 6.3(c). To more clearly establish the trends with standoff distance, additional simulations were performed at shorter and longer standoff distances, and this data is shown on Figure 6.3(b) and Figure 6.3(d). These simulations show that at large standoff distances (low incident impulse levels), where no core compression occurs, there is no difference in the impulse transferred to the solid and cellular structures. Decreasing the standoff distance below 14 cm confirms that substantial impulse mitigation continues to occur, especially for the cellular structure with the thinner impact face.

Additional simulations were conducted to determine the pressure versus time history at the Hopkinson bar sensor locations. The average of the signals recorded on the four bars is shown in Figure 4 for the cellular structures with a thin impact face. Before the arrival of the first reflection, the simulated and measured pressure histories (and especially the peak pressures) are in good agreement. Past the first reflected wave, reverberations within the Hopkinson bar dominated the response, and it was difficult to accurately simulate the response in part because of poorly known reflection coefficients and dissipation processes of the bars. The most notable discrepancy between the measured and simulated pressure waveforms was the time at which the pressure began to rise. This occurred earlier in the simulations, and was most noticeable at longer standoff

distances. This phenomenon was observed in Chapter 5, during the study of the solid block response, and was attributed to the arrival of (anomalous) high velocity spalled sand, due to insufficient momentum transfer from sand to air particles. Figure 6.6(b) provides a summary of the simulated peak pressure predictions for the solid block and thin front face cellular structure. The simulated peak pressure was slightly higher than that observed experimentally as a consequence of the higher sand front velocity.

The impulse was obtained by integration of the simulated pressure waveforms, and is shown in Figure 6.5 for the cellular structures with a thin front face. Again, relatively good agreement with measured results was obtained up to the first reflected wave arrival. Following the first (sign reversed) reflected wave arrival, the impulse plateaued or decreased, before again rising when the twice reflected, non-sign reversed signal arrived ($190\ \mu s$) after the first reflected arrival. Reverberation and dissipation within the bars was not as well modeled by the simulation methodology, but even so, the general trend of rising impulse towards a final value was evident in the simulated data, Figure 6.5. The impulse obtained by integration (for 558 μs) of the measured and simulated pressure waveforms is plotted versus standoff distance in Figure 6.6(d). By extending the simulations to larger standoff distances than those used in experiments, it can be seen that the reduction in early stage impulse decreased to zero as the standoff distance was increased. The simulated change in impulse versus incident impulse for samples with a thick impact face is shown in Figure 6.9(c) and for those with a thin impact face in Figure 6.9(d). The simulated results again agree well with both sets of measurements.

The effective plastic strain distribution and overall deformation of the two sets of cellular test structures are shown in Figure 6.7 and Figure 6.8. The buckling collapse of the core and the convex deflection of the thin face sheet samples are well predicted. However, the simulations overestimated the convexity acquired by the impact face of the thick face samples. This may be a result of the use of a single (central) detonator location in the simulations rather than the five in the experiment which would have produced a slightly more spatially uniform impulse distribution. The plastic compressive strain of the cores is shown versus incident impulse in Figure 6.9(a) and (b) for both types of cellular structure. It can be seen that there was very good agreement between the measured and simulated core strains.

Chapter 7. Analysis of sand-structure interaction mechanisms

In Chapter 5 a particle-based model that investigated the nature of the soil – structure interaction was developed for an incompressible solid block. Chapter 6 provided further validation for the model by modeling a cellular structure in place of the solid block. The simulations provided good agreement between the experimental measurements obtained for pressure and momentum transfer to the solid and cellular structures. Here, simulations are used to explore in detail the cause for impulse mitigation for a cellular structure when compared to an incompressible solid block. Impulse mitigation is explored by: *(i)* removing the steel box top, *(ii)* changing the yield strength and modulus of the thin front face sheet, and *(iii)* by decreasing the yield strength of the cellular structures core material.

7.1. Sand Impact Visualization

A sequence of sand (brown) and detonation product (burgundy) particle position snap shots for the solid block, thin faced, and thick faced cellular structures are shown for the 14 and 40 cm standoff distance tests in Figure 7.1 and Figure 7.2. Twenty spherical virtual particle "monitors" each with a radius of 0.508 cm were positioned 2.5 cm below the lower surface of the solid block, and distributed in a line across the full mid-plane of the specimen, Figure 7.1(a) and Figure 7.2(a). The monitors (not shown in the simulations) were positioned at the same positions within the box lid aperture opening for the cellular structure simulations. This resulted in the monitors being initially located 2.7 cm below the thin face specimen front face sheet and 1.9 cm below the thick face sheet sample. In all three cases, it can be seen that the explosively accelerated sand above the explosive traveled in (predominantly) the upwards direction. A small lateral acceleration was also imparted to the synthetic sand layer causing it to widen over time (and distance of propagation). The upward accelerated sand acquired a range of velocities as a result of loading by a combination of shock reflection and the push from the expanding detonation products. It therefore increased in thickness with distance travelled.

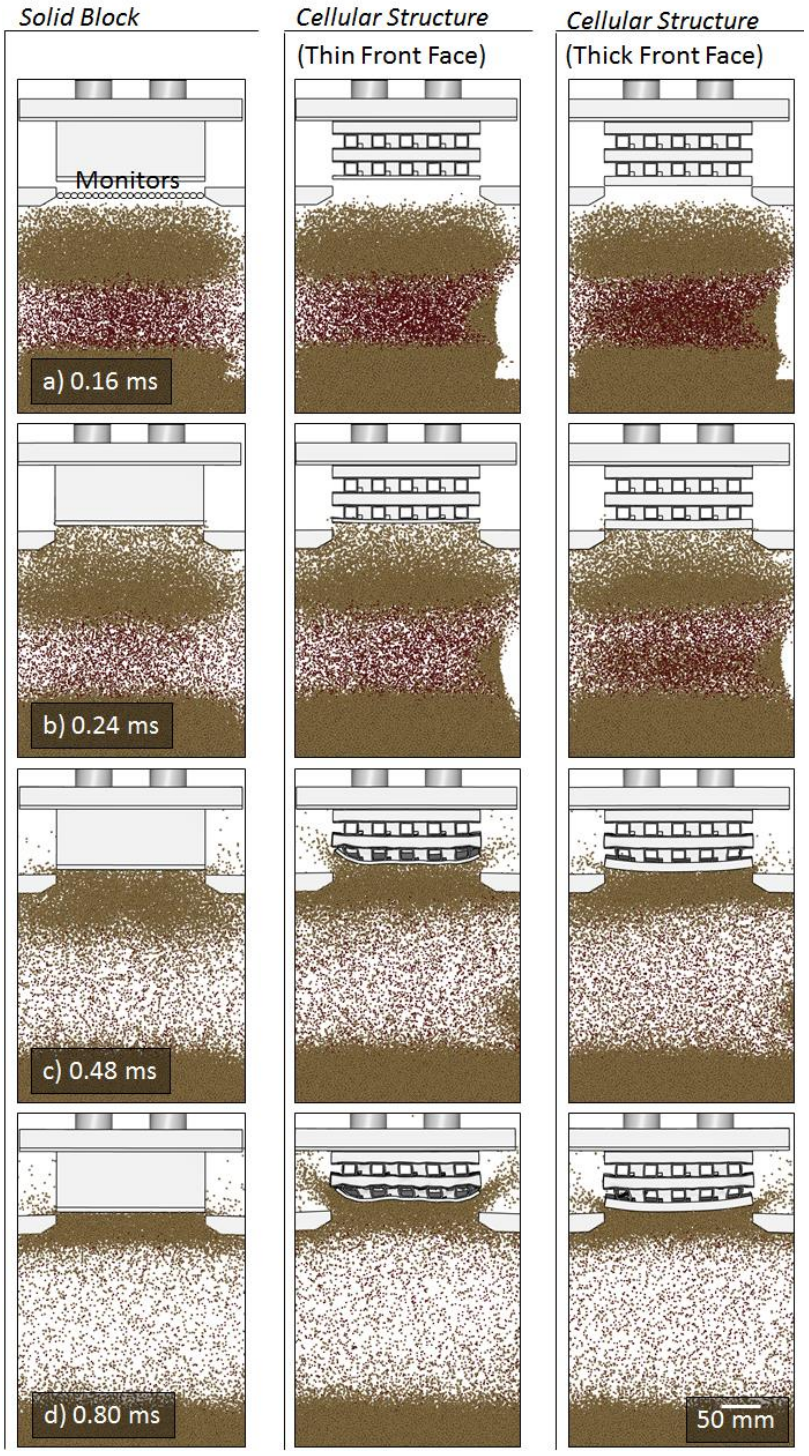

Figure 7.1. A simulated sand particle propagation sequence for a solid block, a thin faced sandwich structure and a thick faced sandwich structure at a nominal standoff distance of 14 cm.

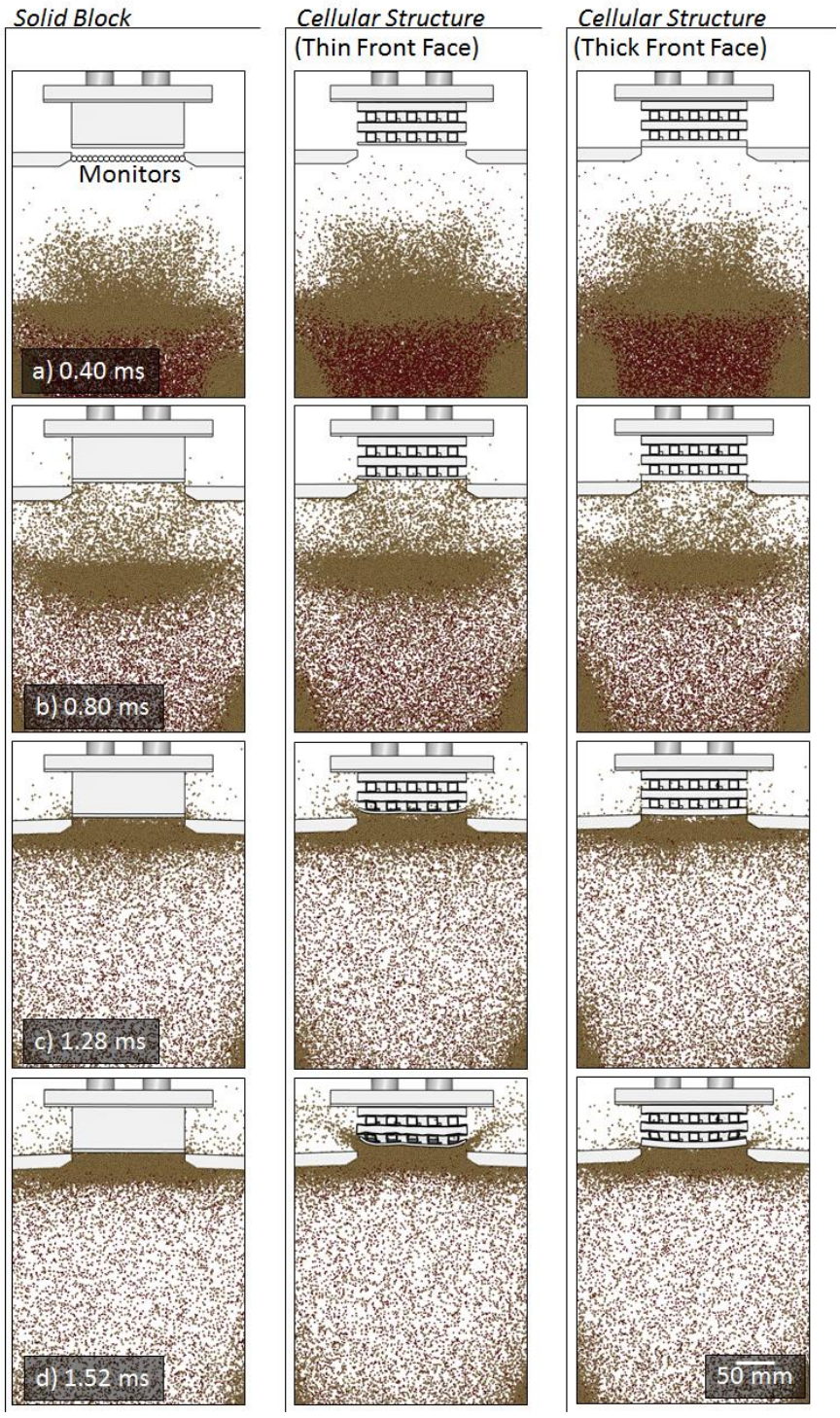

Figure 7.2. A sand particle propagation sequence for simulations with a solid block, a thin faced sandwich structure and a thick faced sandwich structure at a standoff distance of 40 cm.

At the 14 cm standoff distance, the fastest sand began to load the samples at ~0.24 ms after detonation, Figure 7.1(b), and at about 0.6 ms for the 40 cm standoff distance, Figure 7.2(a) and (b). The test samples then began to suffer an upwards displacement as the solid block and Hopkinson bars were elastically compressed, and the cellular structures began to plastically crush. The upward motion of the sand that impacted the solid block was arrested and displaced laterally across the flat surface. As it reached the sides of the sample it was forced to propagate through the narrow gap between the sand box lid and the bottom of the sample. Initially, sand accumulated just below the sample since the sand particle arrival rate exceeded that of escape through the gap. The upward motion of the impacted surface of the samples increased the gap with the lid and eventually enabled more rapid sand escape. However, sand particle impact with the underside of the lid also caused it to suffer an initially upward displacement during the experiment. The gap separation was controlled by vertical displacement of the sample (due to compression and extension of the samples and test structure) and oscillation of the sand box lid which are shown in Figure 7.3 for the three topologies at a 14 cm standoff distance. The evolution of the position of the lid and impacted surface of the samples is shown in Figure 7.4(a) and the gap separation in Figure 7.4(b). The gaps for the cellular samples were wider than those of the solid because of plastic core compression. The sides of the face sheet of the thin faced cellular sample were also more significantly bent by the escaping sand than the sample with the thick front face, Figure 7.3, and so their gaps with the sand box lid surface were larger throughout most of the sand loading process.

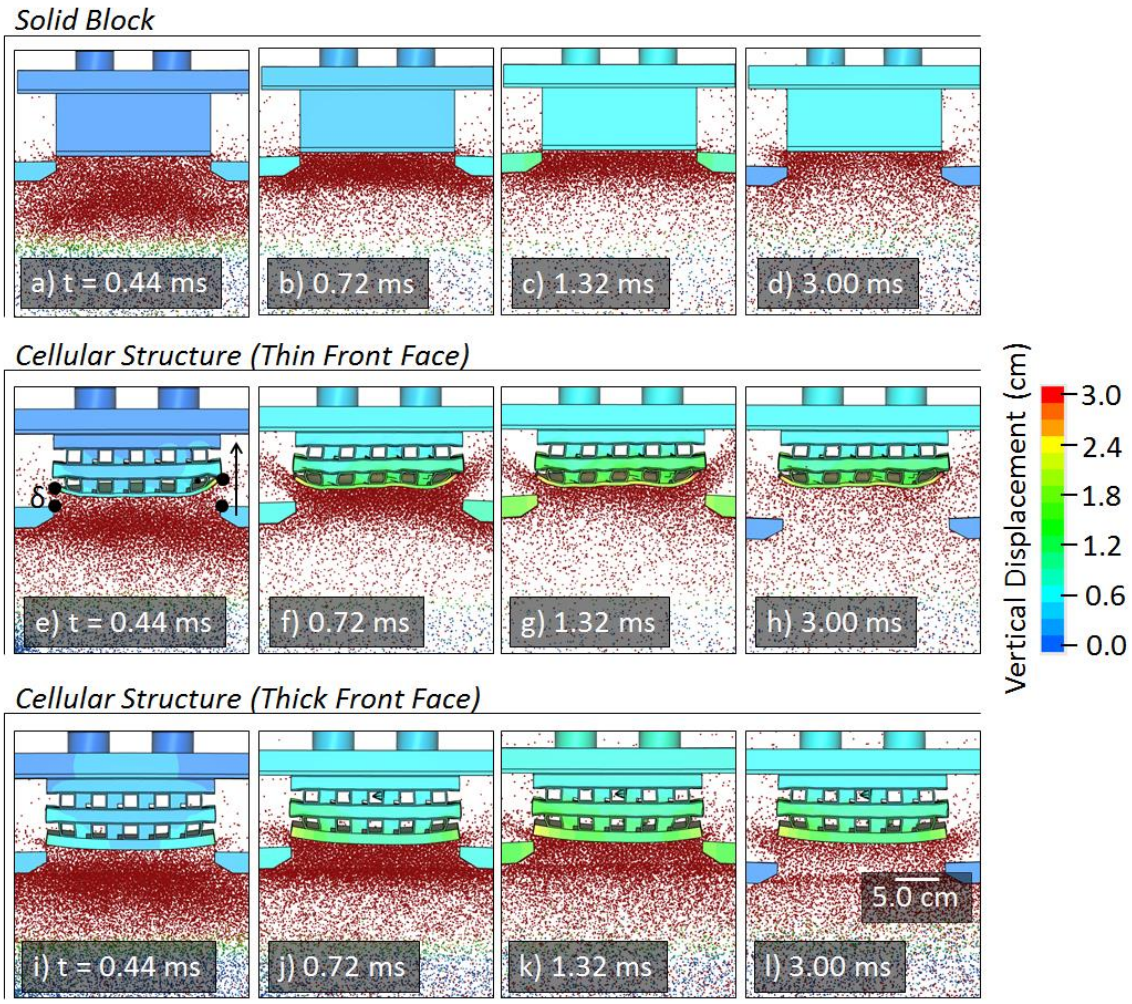

Figure 7.3. Detailed simulations (a-l) show the solid block and the two cellular test structures vertical displacement for a 14 cm standoff distance. Simultaneously, the lid is being displaced during the sand particle loading.

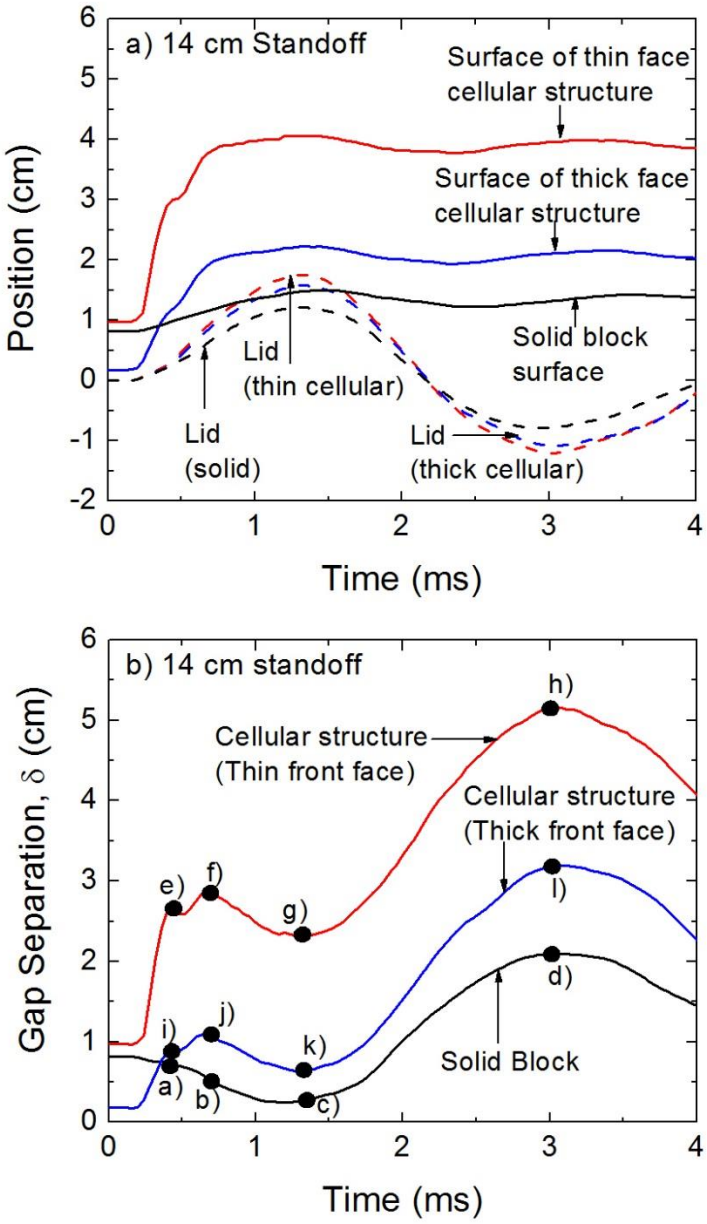

Figure 7.4. The simulated position change of the steel lid was monitored (dashed lines) and compared to the monitored position at the surface of the solid block and thin and thick cellular structures (solid lines). (b) The simulated vertical gap separation between the lid and the surface of the three tested samples for the 14 cm standoff test. The lettered dots correspond to images shown by Figure 7.3.

The effect of increasing the standoff distance can be seen by comparing Figure 7.1 and Figure 7.2. The sand layer was more significantly stretched as the standoff distance increased. This decreased the sand arrival rate, and in turn decreased the pressure on the test structure and its initial upward deflection, and also resulted in less plastic core compression for the two cellular structures, Figure 7.5. As a result of these off-setting effects, substantial sand accumulated beneath the three sample types, but was again more rapidly relieved in the thin front face structure by opening of the gap, Figure 7.6.

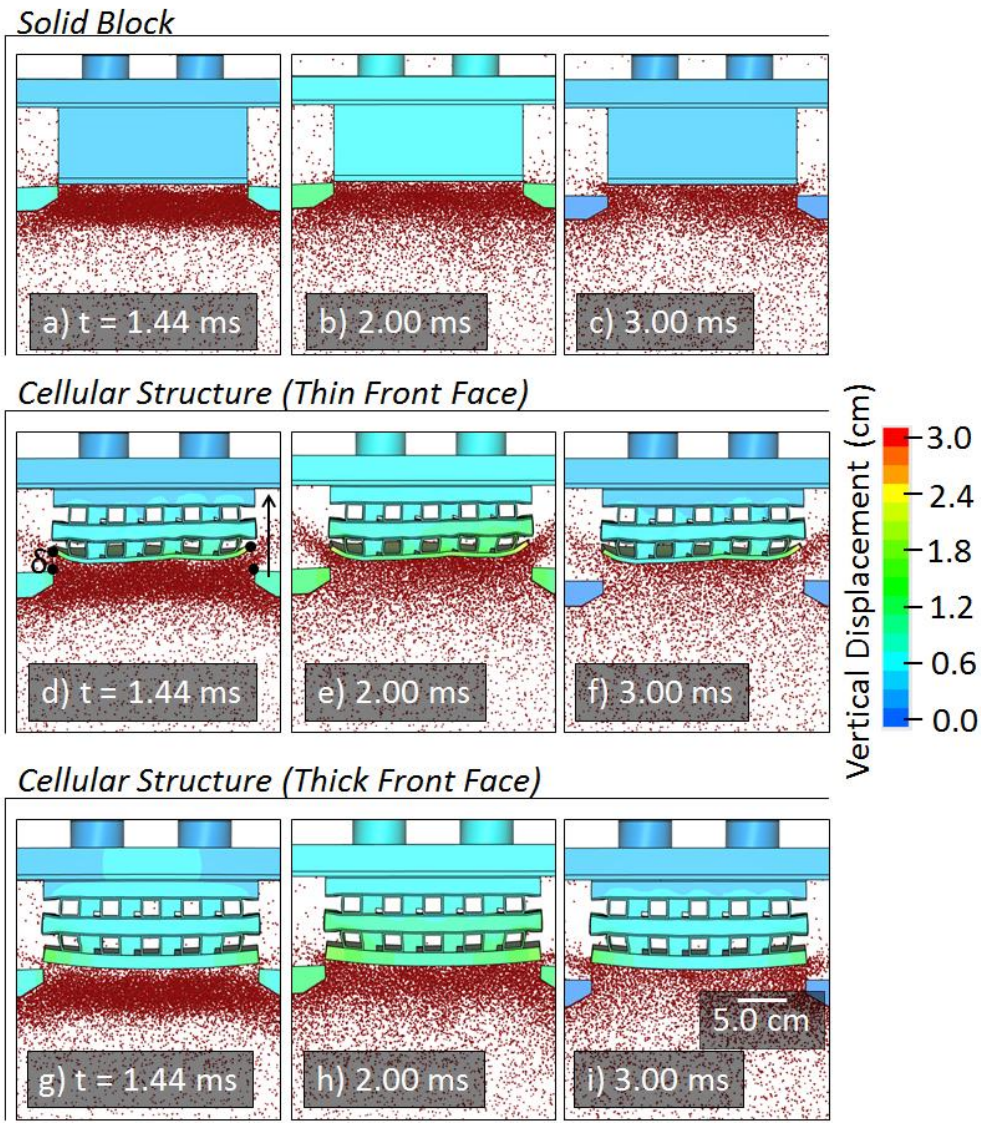

Figure 7.5. Detailed simulations (a-i) show the solid block and the two cellular test structures vertical displacement for a 40 cm standoff distance. Simultaneously, the lid is being displaced during the sand particle loading.

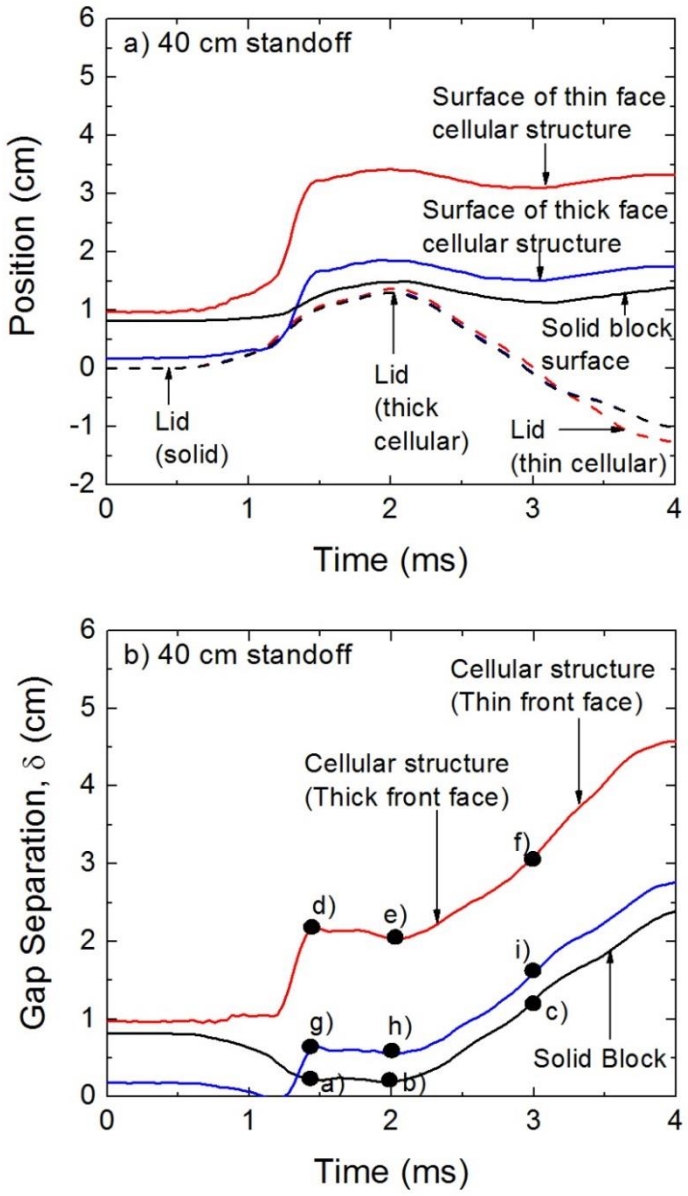

Figure 7.6. (a) The simulated position change of the steel lid was monitored (dashed lines) and compared to the monitored position at the surface of the solid block and thin and thick cellular structures (solid lines) at a 40 cm standoff. (b) The simulated vertical gap separation between the lid and the surface of the three tested samples for the 40 cm standoff test. The lettered dots correspond to images shown by Figure 7.5.

More insight into the sand loading process can be gained by examining the monitor deduced sand velocity – time profiles, Figure 7.7(a) and Figure 7.8(a). Apart from small random deviations and the slight difference in distance to the test sample, these were identical for the three sample types. At a 14 cm standoff distance the sand particles reached a peak velocity of approximately $400\ ms^{-1}$ at 0.2 ms after detonation. Figure 7.1(a-b) shows that this highest velocity was associated with spalled sand traveling at the sand front's leading edge. The most significant difference in the sand velocity of the three topologies was observed at ~0.4 ms after detonation when the main sand layer arrived. The monitors positioned below both cellular structures had a sand velocity of approximately $200\ ms^{-1}$ at this time, whereas the solid block sand velocity was substantially lower (approximately$100\ ms^{-1}$), consistent with extra accumulated sand that had stagnated against the sample. This difference is highlighted in Figure 7.1(d) where the sand contacting the solid block had limited opportunities to escape while the core crushing and the face sheet edge deformation allowed the sand to more easily flow past the steel box top. When the standoff distance was increased, the sand velocity exhibited less deviation between topologies, Figure 7.8(a). This is visually apparent in Figure 7.2(c and d) where less core crushing occurred, and the cellular structures acted more like the incompressible solid block.

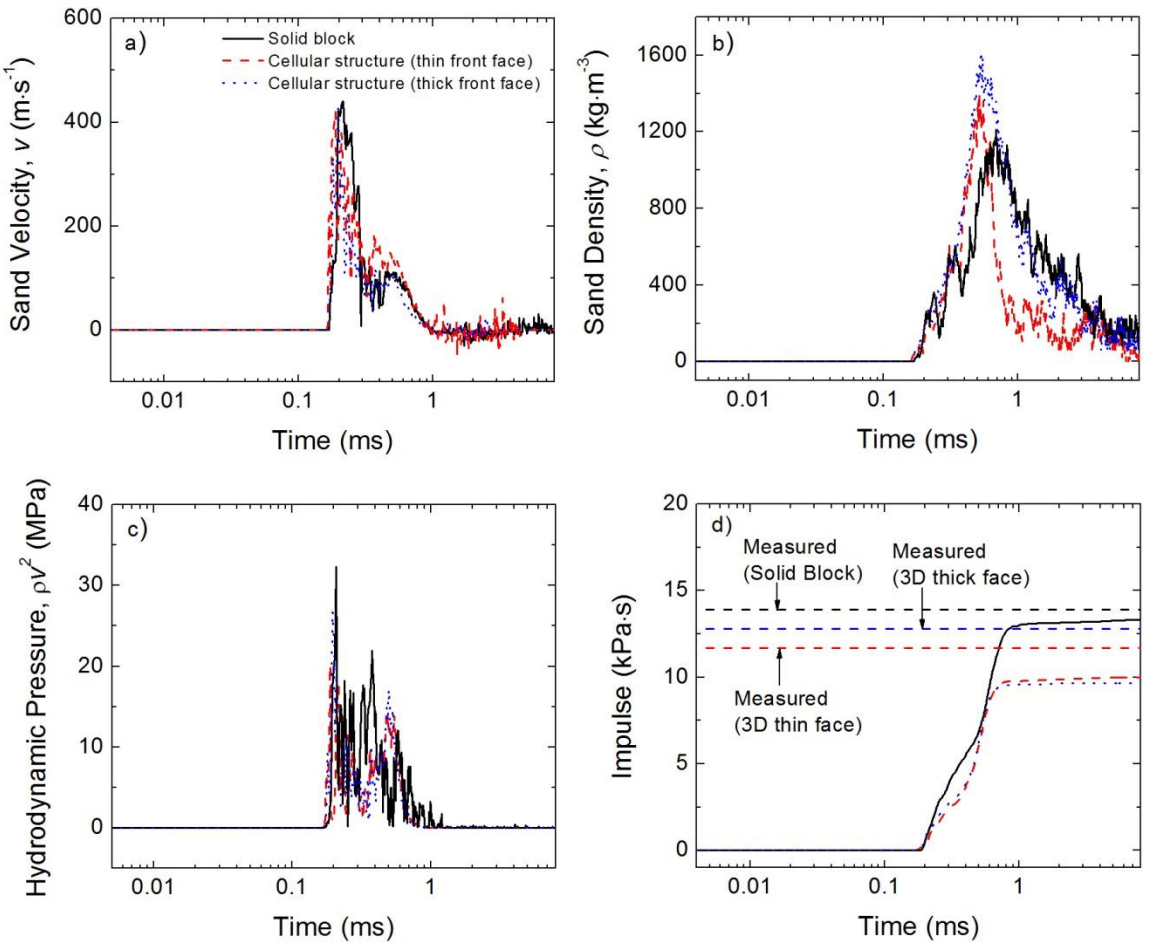

Figure 7.7. a) The sand velocity and b) sand density determined at monitors located 2.5 cm below the sample surface for a solid block (black), and thin (red) and thick (blue) faced sandwich structure for a standoff distance of 14 cm. The calculated hydrodynamic pressure c) and the sand impulse d) at the same monitor levels are also shown.

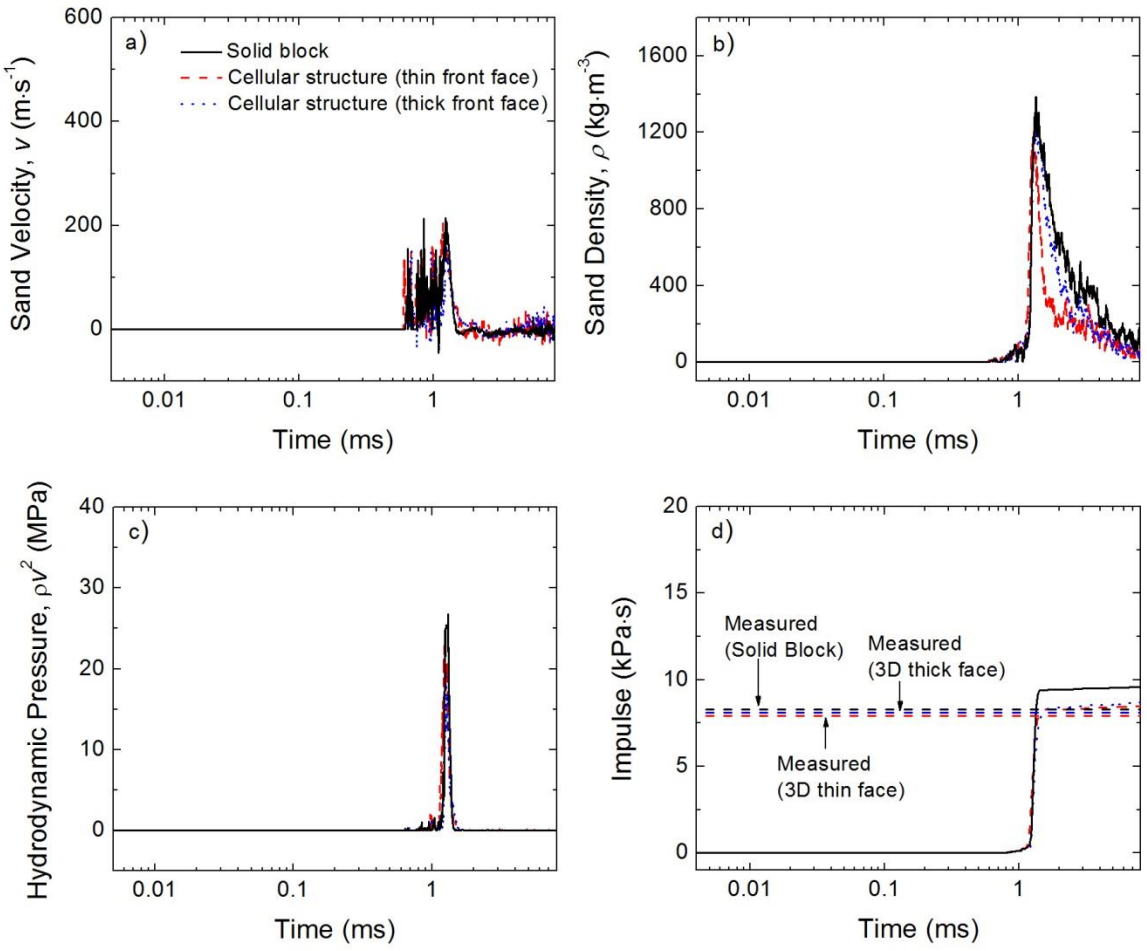

Figure 7.8. a) The sand velocity and b) sand density determined at monitors located 2.5 cm below the sample surface of a solid block (black), and thin (red) and thick (blue) faced sandwich structure for a standoff distance of 40 cm. The calculated hydrodynamic pressure c) and the sand impulse d) at the same monitor levels are also shown.

The sand density – time profiles at the monitors differed more significantly than the velocity – time outputs for the three topologies. At a 14 cm standoff distance the sand density at the monitors below the cellular structures reached a higher value (1400-1600 kgm^{-3}) than the solid block during the time (0.3-0.5 ms) of core crushing, Figure 7.7(b). After reaching a maximum, the sand density fell most rapidly for the thin faced cellular structure. The drop in density is visually apparent in Figure 7.1(c and d), and

corresponded with rapid sand flow from the steel box as the cores crushed and the gap, δ , increased. The incompressible solid block forced much of the sand to stagnate against the impact face. A similar effect occurred for the thick front face sheet sample which suffered smaller plastic compression than the sample with the thin face sheet. At the 40 cm standoff distance, the density – time outputs from the monitors exhibited similar trends, Figure 7.8(b). Once again, this was directly controlled by the separation distance with the sand box structure. The slower drop in sand density for the thin face sheet cellular structure at the 40 cm standoff distance (compared to that at 14 cm) was due to less core crushing.

The hydrodynamic pressure (P_h) applied by the sand particles, could be calculated from the numerically measured sand density, ρ, and velocity, v, with the spherical monitors using:

$$P_h = \rho v^2 \qquad (7.1)$$

The sand velocity and density data obtained with the monitors, Figure 7.7(a) and (b) and Figure 7.8(a) and (b) can be used to estimate the pressure applied to the front of the sample. This is shown in Figure 7.7(c) and Figure 7.8(c) for the two standoff distances. The pressure for the 14 cm standoff distance test increased rapidly to a first peak, and then decreased before rising again to a second peak for both cellular structures. This second peak was less apparent for the solid block. The first pressure peak amplitude was 30 MPa for the solid block, 25 MPa for the thick face cellular structure, and 20 MPa for the thin face cellular structure. These peak pressures were nearly identical to the

pressures of the initial pressure spike measured using the Hopkinson pressure bars, Table 6-3, and corresponded to arrival of the fast (spalled) sand at the sample surface. A second, lower pressure of approximately 15 MPa occurred at 0.5 ms after detonation for both cellular structures, and corresponded to the arrival of the more densely packed sand slab at the monitors. Increasing the standoff distance to 40 cm, led to a reduction in sand density (due to axial and lateral stretching of the sand) and a slightly reduced velocity (because of sand-air particle collisions), Figure 7.8(a) and (b). This resulted in disappearance of the first pressure spike, Figure 7.8(c); consistent with the disappearance of the initial spike in pressure observed experimentally, Figure 6.4, as the standoff distance was increased.

By integrating the hydrodynamic pressure, the impulse-time relation for sand particles could also be calculated, Figure 7.7(d) and Figure 7.8(d). At 14 cm, the impulse rose rapidly upon arrival of the sand, and for the solid block reached a maximum of ~13 kPa·s within approximately 2 ms of detonation. The impulse also rose rapidly for both cellular structures, but reached a lower maximum value of approximately 10 kPa·s. This agreed reasonably well with vertical pendulum measurements. Figure 7.8(d) shows that at a 40 cm standoff distance, the impulse's at the monitor locations were also similar to those measured with the vertical pendulum.

The impulse applied by the particles to the front face of the solid block (located 2.5 cm above the monitors) and both cellular structures (located at 2.7 cm and 1.9 cm

above the monitors for the thin and thick face cellular specimens respectively) could be directly obtained from an output file of the IMPETUS Afea post processor, Figure 7.9. Good agreement between the vertical pendulum measured and these simulated impulses was seen for all the standoff distances. The impulse-time signals calculated with the contact algorithm exhibit three distinct regions. Region I was associated with impact of the spalled sand at the sand front leading edge. For each standoff distance, the impulse acquired in Region I was almost identical for all three sample types. The slight differences were due to the differing thicknesses of the specimens which slightly changed the standoff distance from that of the solid block. Region II corresponded to impact by the dense sand slug, and was the region most responsible for the impulse differences between the three sample types. Figure 7.1(d) and Figure 7.2(d) indicate that Region II corresponds to the period where the separation gap between the steel top plate and the front face of the specimen was rapidly increasing. Recall that the gap for the solid block was smaller than for the cellular structures, and provided less room for sand to escape, and the impulse to remain higher than the crushable cellular structures. Sand loading rapidly decreased in Region III, and corresponded to a regime where the sample to sand box gap was the widest.

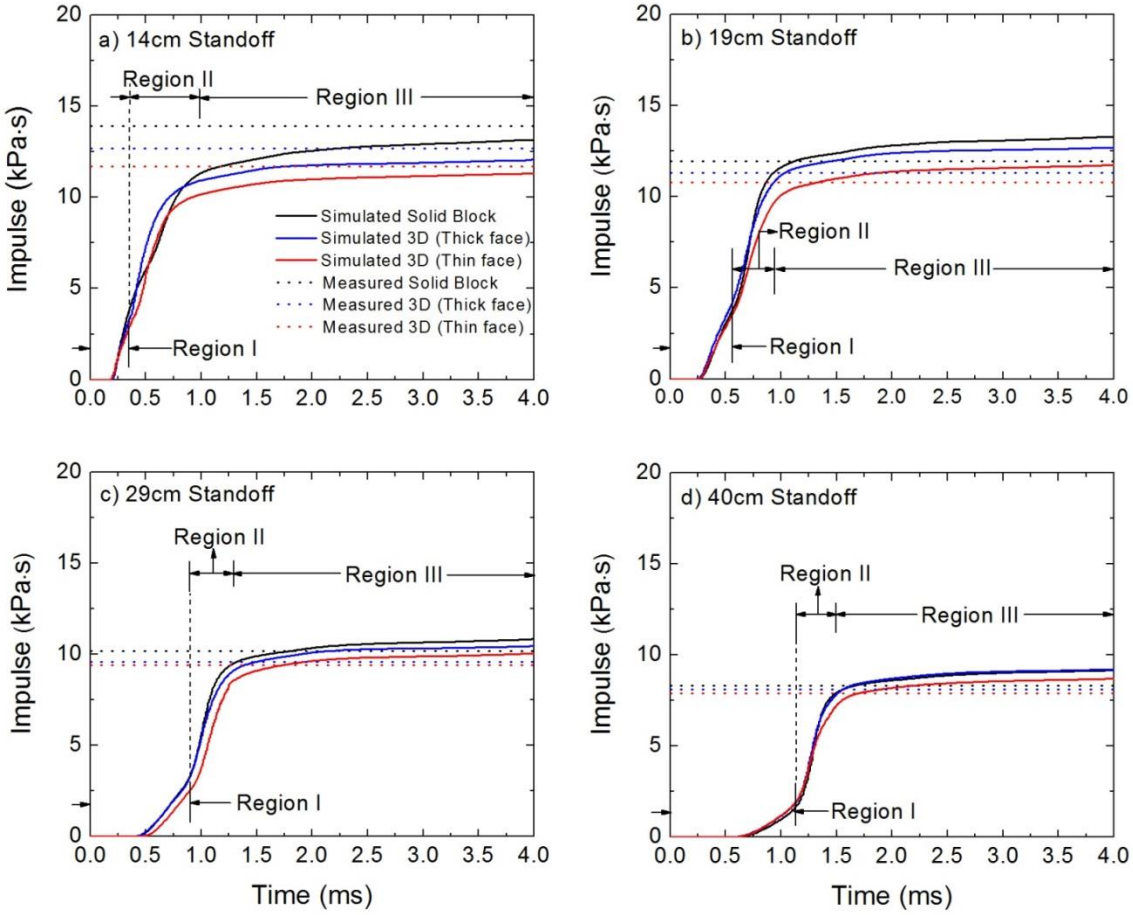

Figure 7.9. Simulated impulse-time responses determined from the sand particle contact with the front face of the solid block (black) and sandwich structures thin (red) and thick (blue) front faces for standoff distances of a) 14cm, b) 19cm, c) 29cand d) 40cm. The measured total impulse is shown as dashed lines whose colors correspond to those of the simulated structures.

7.2. Mechanisms of Impulse Transfer Reduction

7.2.1. Test Geometry Effects

It has been shown that the combination of the sand box lid deflection, core crushing, and elastic compression (and extension) of the Hopkinson bars all contribute to the gap through which sand flowed away from the sample and escaped the system. To better understand the consequences of this critical aspect of the experiment, the lid was removed from the simulations, keeping the rest of the model unchanged. This allowed the effect of the lid-sample aperture upon the transmitted impulse to be more clearly understood, and reveals the process by which the three samples interact with an unperturbed sand front. Figure 7.10 shows the transferred impulse (calculated using the sample contact algorithm) to the three sample types at standoff distances of 14 and 40 cm with the sand box lid removed. At a 14 cm standoff, Figure 7.10(a), the impulse for all three sample types was less than that with the lid in place, Figure 7.9(a) because of sand reflection from the inclined periphery of the sand box aperture towards the sample.

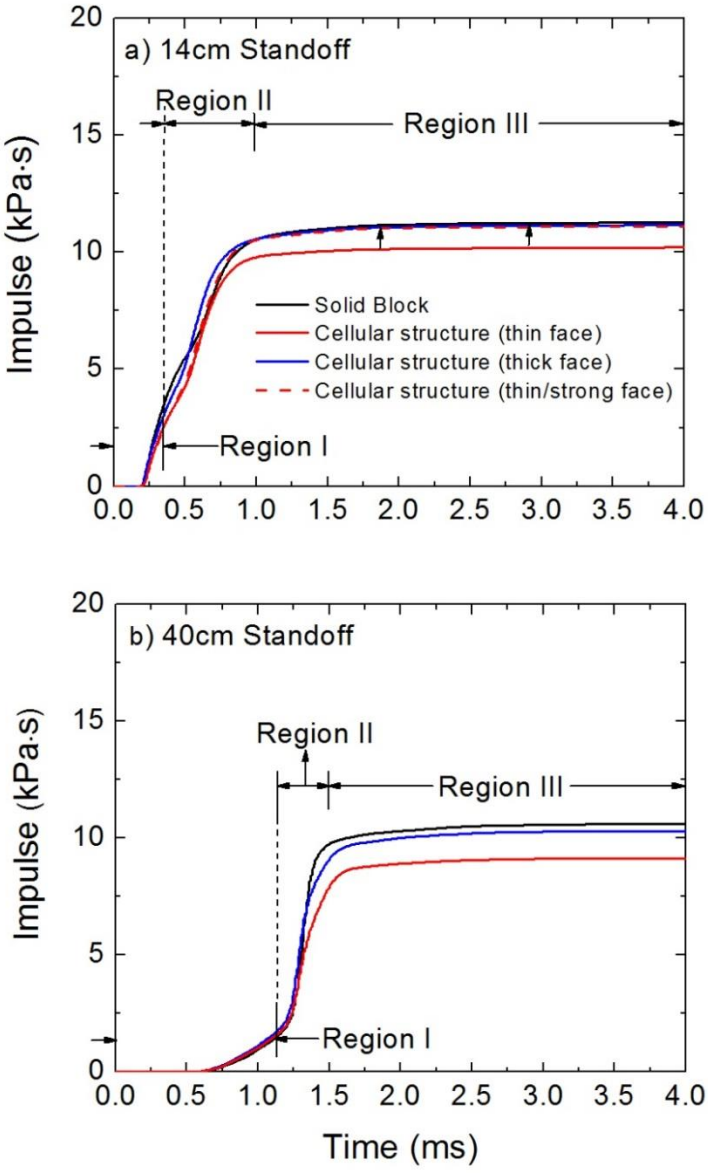

Figure 7.10. Simulated impulse-time responses determined from the sand particle contact with the front face of the solid block and thin and thick sandwich structures with no box top present for standoff distances of a) and d) 40cm.

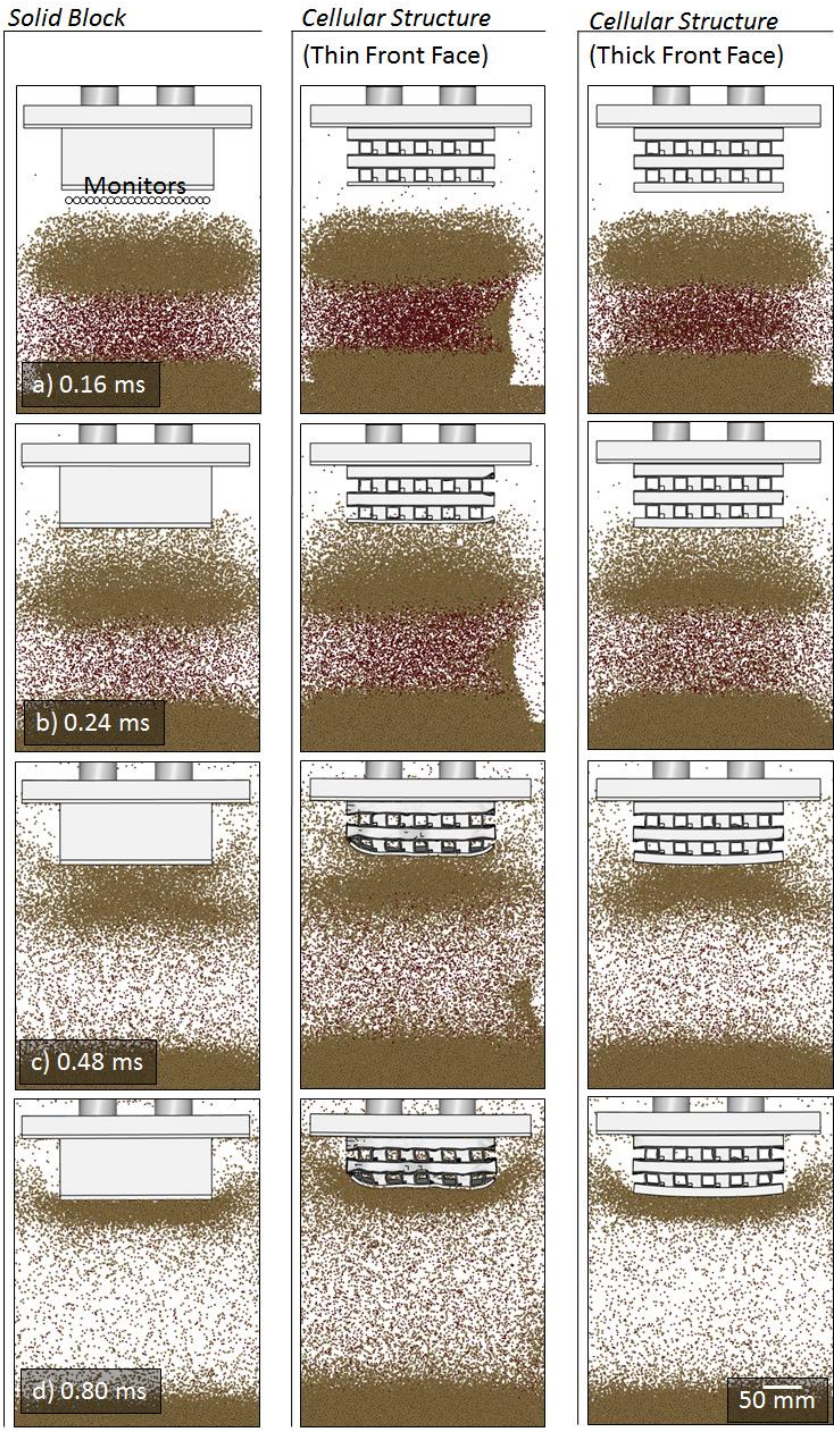

Figure 7.11. A sand particle propagation sequence for simulations with a solid block, a thin faced sandwich structure and a thick faced sandwich structure at a standoff distance of 14 cm

These results indicate that the lid aperture substantially affected the impulse transfer, and the mechanisms responsible for this are explored using sand position snap shots shown in Figure 7.11 and Figure 7.12. At the 14 cm standoff distance there is no noticeable difference between the simulation with a steel lid and without a steel lid at 0.16 ms after detonation, Figure 7.1(a) and Figure 7.11(a). At 0.24 ms after detonation, the spalled sand began to interact with the front face of the sample and the only noticeable difference between the simulation with and without a lid can be seen at the right and left edges of the sand front, Figure 7.1(b) and Figure 7.8(b), where the inclined surface defining the aperture is lid has reflected sand into the aperture. At 0.48 ms after detonation the sands peak density with a lid was calculated to be approximately $300\ kg \cdot m^{-3}$ higher than that with no lid present for the three test samples. The monitors calculated no noticeable sand velocity change when the lid was removed. A comparison between Figure 7.1(c) and Figure 7.11(c) shows the presence of inclined surface around the aperture of top lid forced some sand that would have otherwise missed the edge of the sample, to coalesce under and then impact the sample. Without a lid, the accumulated (densified) sand below the sample surface assumed a convex shape, and the edges of this dense sand front reflected some of the sand in a manner that allowed a fraction of its vertical impulse to be retained. Continued sand loading at 0.80 ms after detonation showed that without a lid the sand more easily rolled off the samples edge, Figure 7.11(d), rather than stagnating and eventually escaping as the gap separation increased, Figure 7.1(d). The formation of this virtual convex sand shape combined with the smaller fraction of the sand slug that impacted the sample resulted in reduced impulse transfer to the sample.

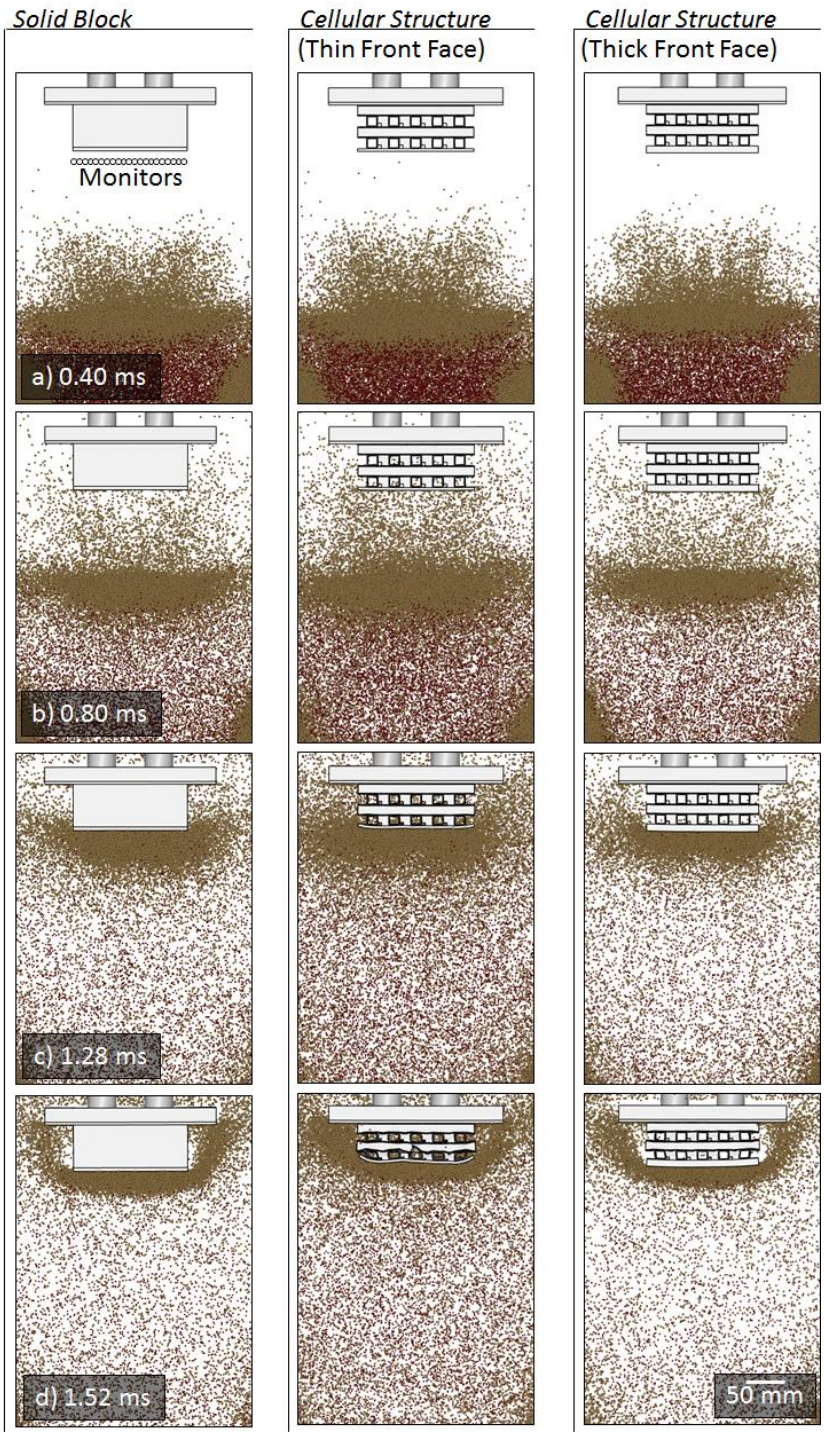

Figure 7.12. A sand particle propagation sequence for simulations with a solid block, a thin faced sandwich structure and the thick faced sandwich structure at a standoff distance of 40 cm with the box top removed.

7.2.2. Impact Face Deformation Effects

It is interesting to note that the solid block and the thick face cellular structure acquired a nearly identical impulse once the sand box lid was removed, Figure 7.10. Figure 7.11(d) shows that the thick face sheet sample remained nearly planar during sand loading, and the sand flowed off its surface in a similar fashion to the solid block. However, the impulse transmitted to the thin face sheet sample was less than that transmitted to the solid block, Figure 7.10. Examination of Figure 7.11(d) shows that the thin face sheet underwent significant deformation upon spalled sand impact, and its sides were quickly bent upwards to a shape that allowed the subsequent (Region II) sand slab to be only partially arrested before flowing around the specimen. To explore the consequence of this dynamic front face deflection phenomenon, the front face of the thin face cellular structure was again modeled as a 6061 aluminum alloy, but with a greatly increased yield strength (23 GPa) and modulus (7000 GPa) which caused it to remain rigid throughout the simulation.

The red dashed (thin/strong face) line in Figure 7.10(a) represents the impulse-time response for a cellular sample with a strong thin face sheet that was not allowed to deform. The impulse at 14 cm was increased to that of the solid block, and the thick face cellular structure. It is therefore clear that face sheet deformation was able to promote sand flow around the sample and only partial vertical momentum transfer to the specimen. It is noted that even though the impulse-time response of the three samples

reached the same plateau value when the face sheet did not deform, a slight difference in the slope in Region II of the impulse-time response remained, Figure 7.10(a). The impulse-time response in Region II occurs during core compression, and so the core's contribution to impulse transfer was explored next.

7.2.3. Core Strength Effects

The cellular structure core has been simulated to this point using an aluminum alloy yield strength of 230 MPa resulting in a core peak crush strength of 21.8 MPa. Since the crush strength of the core scales linearly with that of the alloy's yield strength, the alloy yield strength was progressively decreased in the simulations to investigate how easier core collapse affected the transmitted impulse and applied pressure. The alloy yield strength was decreased to half (115 MPa), a fourth (58 MPa), and an eighth (29 MPa) of its original value, and the core compressive strength calculated using the finite element model developed in Chapter 3. These core strengths are summarized in Table 7-1. The sand impact simulations were then repeated without a sandbox lid and a rigid front face was used for all simulations.

Table 7-1. Material yield and cellular compressive strength, and impulse transfer rate and maximum transmitted pressure

Sample	***Material Yield Strength (MPa)***	***Compressive Strength (MPa)***	***Impulse rate (MPa)***
Solid Block	350.0	-	20.7
3D cellular	230.7	21.8	13.7
3D cellular	115.4	10.9	7.9
3D cellular	57.7	5.5	6.9
3D cellular	28.8	2.5	6.4

Figure 7.13(a) shows the impulse-time response for cellular structure cores with core compressive strengths between 21.8 and 2.8 MPa. Decreasing the compressive strength of the cellular structure resulted in a slightly reduced plateaued impulse from 11 kPa·s (for the original core strength of 21.8 MPa) to approximately 10.5 kPa·s for weakest core samples. The approximately 5% decrease in impulse only occurred when the core was sufficiently weak to permit significant core crushing, Figure 7.13(b-d). The majority of the core crushing occurred during Region I by impact of the spalled sand at the sand front. This allowed the distance between the impact face and the explosive charge original location to rapidly increase (by the product of the original core height and the compressive strain). This increased the standoff distance for later arriving (Region II) sand, and was responsible for the reduction in impulse. To illustrate, if a 7.6 cm thick core were compressed 50%, the increased standoff distance would be 3.8 cm, and using the slope of the impulse – standoff response for the solid block, Figure 6.3(a) of *0.2 kPa.s.cm*$^{-1}$, the reduction of impulse if all the sand had impacted at the longer standoff distance would be 0.76 *kPa.s* compared to the 0.5 *kPa.s* change of the simulation.

The collapse sequence in Figure 7.13(b-e) shows that cellular structures with lower compressive strengths were fully densified 0.8 ms after detonation at a 14 cm standoff distance, Figure 7.13(e). The maximum velocity attained by the front face during the core crushing Region I response was ~100 ms^{-1}. During the Region I response, the rate of impulse transfer decreased with reduction of core strength, Table 7-1, because of the decrease in sand impact velocity (and thus stagnation pressure) measured in the front face sheet frame of reference. This result indicates that when a core can be easily compressed by sand impact, the pressure transmitted to the structures distal side can be decreased. We also note no slap enhancement of impulse was observed, even when the core was compressed beyond its densification strain.

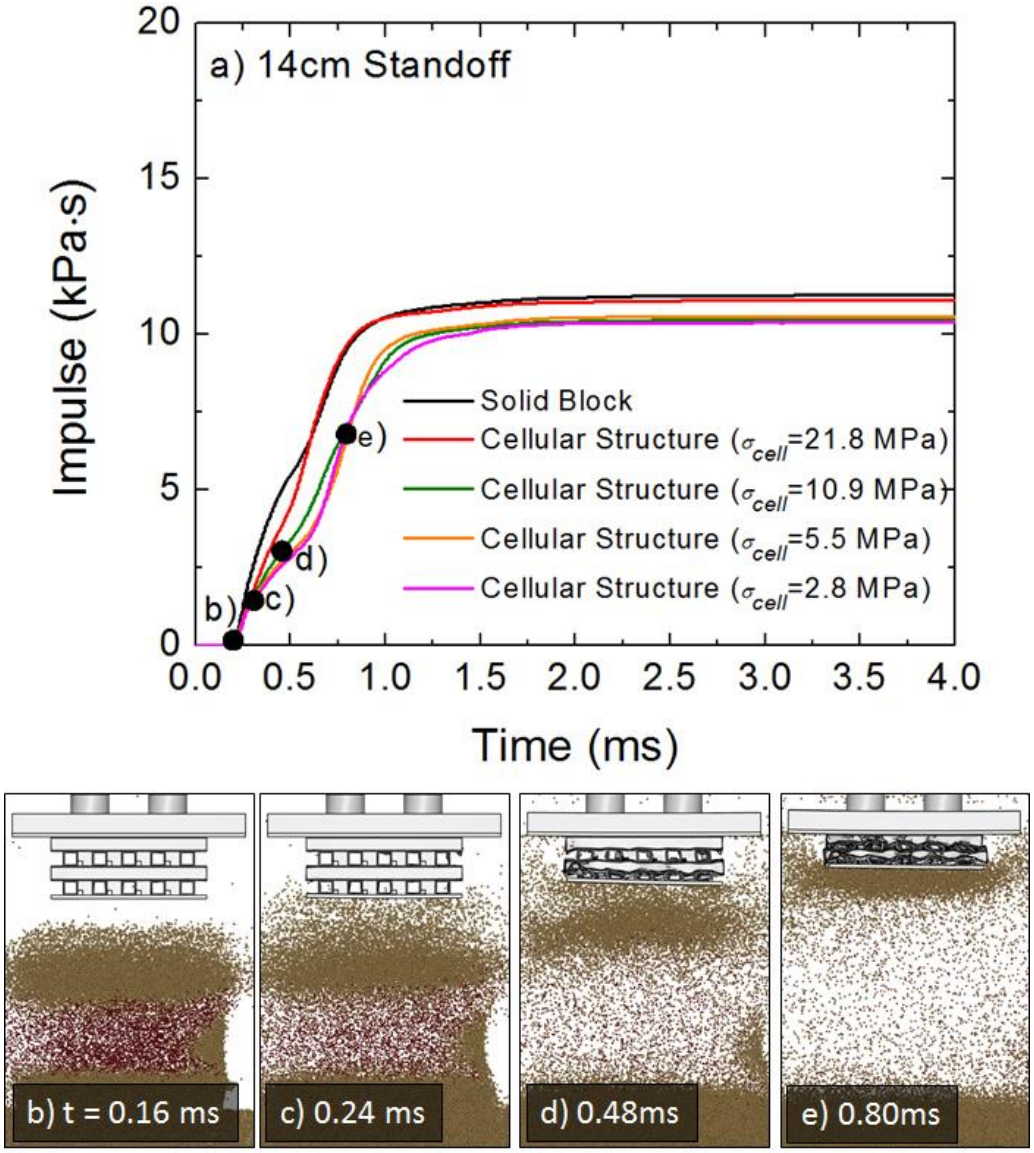

Figure 7.13. a) Predicted transferred impulse-time responses at a 14 cm standoff distance without a box top lid for the solid block (black), a thin face cellular structure with rigid front face (red) and cellular structures with cores made from materials of differeing strengths(green, orange and pink). (b-e) Show snap shots of the sand loading against a rigid thin face cellular structure made from a material with a core yield strength of 115 MPa (green curve in (a)).

Chapter 8. Discussion

Simply put, the goals of the dissertation were to design and develop a method for making a lightweight cellular structure that was well suited for impact mitigation applications, and then use it to explore the interactions of explosively accelerated wet sand with crushable structures, both experimentally and by quantitatively precise simulation.

8.1. Cellular Structure Design and Characterization

A lightweight three-dimensional orthogonal tube cellular structure for impact mitigation applications has been designed, Figure 2.1(c). The structure can most inexpensively be fabricated from aluminum tubes made from highly extrudable alloys such as medium strength, corrosion resistant Al 6061, 6063, and 6082 or higher strength 7075. Since the tubes must be robustly bonded to each and to face sheets for most

applications, the Al 6061 system was selected since it has good weldability and can be brazed by a variety of methods. The decision was also driven by the intent of the research to model the cellular structures deformation under quasi static and dynamic loading, and high rate constitutive models have been previously developed for this alloy.

The 3D tube based cellular structure was made by using a simple dip brazing approach to join square extruded tubes made of aluminum alloy 6061 and heat treating the structure to the peak aged (T6) condition. The array of out-of-plane tubes provided an efficient energy absorbing element to control impact. The co-linear tubes that were laced between the out-of-plane tube array were introduce to provide the cellular structure with stretch resistance, which is important for applications like that shown in Figure 1.4. The dip brazing method used to join the tubes proved to be relatively simple and cost effective; however, the method required the introduction of notch cut-outs into the out-of-plane tubes at every in-plane layer to provide channels to remove salts used during fabrication. This was necessary to avoid post-braze corrosion and to relieve pressure buildup in external cavities when they dipped into a molten salt bath at a temperature in the 500^{o}C range. However, under compressive loading, these notches acted as the nucleation sites for global buckling of the structure, Figure 3.4(a). Alternative fabrication methods, such as vacuum brazing or laser welding might eliminate the need for notches in the out-of-plane tube, but these methods are more costly and complicated to successfully implement.

The 3D orthotropic structures out-of-plane compressive strength was proportional to that of the alloy from which it was made and dependent upon its relative density. At a relative density of ~10%, the 3D structure yields at a stress of about 5 MPa, but this increases with relative density to about 50 MPa at a relative density of ~40%, Figure 3.5. The 3D structure appeared well suited for impact mitigation applications because of the prolonged extent of plateau response, and the high densification strain of the structure. The finite element package within the IMPETUS Afea Solver when combined with a piecewise linear hardening model and a Mises yield surface was able to successfully simulate the response of the structures to quasi-static compression.

Both the compression experiments and the FEM analysis reveal the 3D structure to have a high specific energy absorption that increased with the structures compressive strength (or relative density) from about 10 kJ/kg for structures with a compressive strength of ~10 MPa to 30 kJ/kg at strengths of 60 MPa. This was only slightly less than the specific strength of arrays of vertical tubes, which are considered to be ideal structures for low velocity impacts in which the impact forces are aligned with the axis of the tubes (such as in frontal vehicle collisions). Although excellent energy absorbers, a tube array of vertical tubes has no stretch resistance perpendicular to the axis of the tubes, and so is not an ideal core topology for an edge clamped sandwich panel subject to localized impact that can be as important for localized loading applications, Figure 1.3. The 3D orthogonal tube structure invented here clearly has considerable stretch resistance as well as excellent through thickness compressive strength and energy absorption. In

addition, the 3D structures specific energy absorption was shown to exceed attainable with any metal foam, Figure 3.8.

It was experimentally determined and numerically verified that the elastic modulus of the 3D tube based cellular structure had a linear dependence upon the solid material modulus, E_s, and structures relative density given by: $E_{cell}/E_s = 3.6\bar{\rho}$, that was consistent with an initially stretch dominated response, Figure 3.12. Stretch-dominated structures tend to be much stiffer and stronger than comparable density bending-dominated structures made from the same material. However, their deformation mechanisms involve tension and compression (hard modes), and their initial peak strength is typically followed by softening, which draws into question their use as ideal energy absorbers. This has been overcome here by synergistic interactions with the in-plane tube array during large strain buckling deformation, Figure 3.7. The modulus of 3D orthogonal tube structures developed here was significantly higher than that of metal foams of a similar relative density and material.

The peak strength of the cellular structure was found to be proportional to that of the solid material and exhibited a power law dependence upon relative density, given by: $\sigma_{cell}/\sigma_s = 1.05\bar{\rho}^{5/3}$. In-situ experimental observations and finite element simulations clearly showed that the crush strength was controlled by the initiation of buckling of the tubes oriented in the applied load direction. This was tripped by the notches used to facilitate brazing. When the notches were omitted from the structure, the peak strength could be increased substantially. For example, the strength of a 3D structure with a

relative density of ~20% increased from 22 to 27 MPa, Table 3.1. However, when buckling was eventually initiated large load drops occurred and the stress strain response was oscillatory (not plateau-like), Figure 3.3, and the specific energy absorption only increased slightly from 19 to 22 J/g, Table 3.1. This leads us to conclude that the use of notches to enable implementation of an inexpensive dip brazing fabrication approach has not been too detrimental to the mechanical response, and appears to have led to a smoother plateau behavior better suited for impact applications in which the transmission of pressure pulses associated with unstable tube collapse is not desirable.

The dynamic of the 3D tube structure was experimentally investigated using a combination of instrumented Hopkinson bar impact experiments and high speed video imaging located in the Cambridge University Engineering Department. The study revealed that the 3D tube structure dynamically compressed at a near constant crush stress to the densification strain of about 60%. Furthermore, the initial compressive strength was independent of impact velocity for compression strain rates up to 2000 s^{-1}, which greatly simplifies the design of impact protection systems. Once again, the finite element analysis module in the IMPETUS Afea Solver, when combined with a Johnson-Cook rate dependent, piecewise linear hardening model with a von Mises multi-axial yield surface and a simplified failure criterion constitutive model, was shown to predict the flow stress –displacement response and deformation modes of the 3D structures very well.

Under dynamic loading, the core strength again exhibited a power law dependence upon relative density, given by $\sigma_p/\sigma_s = (\bar{\rho})^{5/3}$, consistent with crush strengths controlled by the buckling of tubes oriented in the applied load direction, Figure 4.18(a). However, the peak strength of each 3D structure was independent of loading rate, Figure 4.18(a). Under dynamic loading, the buckling mode of the vertical tubes was constrained by the walls of the in-plane tubes and this appeared to have been a significant contribution to the relatively rate insensitive compressive response. When an isolated tube was axially compressed, its response was rate dependent due to activation of a tube rotation mechanism at low impact velocities. This mode was inhibited in the 3D structure and forced the system into less inertially sensitive shorter length scale microbuckling collapse, like that seen under quasi-static loading.

The finite element simulations of the high rate loading experiments revealed that the impact face pressure increased from that transmitted at the back structure as the displacement rate increased, Figure 4.19. The ratio of the impact to back face stress also increased with reduction in core density. This effect arises because there is insufficient time during the impact process for communication (by elastic wave propagation) between the impact face and that supporting the back of the sample. This effect does have considerable consequence for impact mitigation applications since an object impacting the front face would be decelerated by the reaction forces present at the impact face.

8.2. Vertical Impulse Test Facility and Observations

Following the dynamic compressive study, a vertical pendulum test facility was developed and constructed at the Newtec Test Range in Edgefield (South Carolina), and used to experimentally investigate the impact of explosively accelerated wet sand with a flat sided, back supported solid 6061-T6 aluminum reference block and the 3D cellular structure. The apparatus used the (typically 70 kg mass) pendulum jump height (against gravity) to determine the impulse transferred to the specimen following detonation of a 300 g sheet of explosive (with 50 g of explosive booster) that accelerated a 5.08 cm thick layer of wet silica particles (synthetic sand) towards the sample against which impact occurred at normal incidence, Figure 5.2. The facility also enabled the pressure applied to the rear face of the samples to be measured for about 4 ms during the sand impact process using a set of four Hopkinson pressure bars. However, reflections from the upper end of the bars limited the period of accurate measurement to 558 μs after first sand arrival.

High speed video imaging, Figure 5.4 indicated that the model landmine launched the 5.08 cm thick wet sand layer normal to the soil surface with a leading edge velocity of ~ 300 ms^{-1}. However, small fingers of faster sand could be observed ahead of the main sand front. These were thought to be associated with fast sand that was spalled from the top of the sand layer by shock reflection at the sand air interface. Within the resolution of the measurements performed here, the leading edge sand speed did not significantly change with height during the first half meter of propagation.

Experiments with a solid (incompressible sample) indicated that the transmitted impulse and pressure decreased with increasing standoff distance between the top of the layer of explosive and the lower surface of the test sample. The pressure transmitted by the distal end of the 3D cellular structures was usually less than that transmitted by the solid block except at large standoff distance. However, the experiments alone were unable to resolve the reasons for these effects. Since the pressure applied by the stagnation of sand against a rigid target scales with the sand density and the square of its impact velocity, one or both of these must have changed with standoff distance. Obviously, air drag and even gravity will cause the explosively launched sand to eventually slow down as it propagates from the site of detonation. However, high speed video imaging, Figure 5.4 of the sand as it propagated away from the explosive event could not resolve a reduction in sand velocity sufficiently large to account for the impulse reduction with standoff distance. It was clear that the sand column that impacted the samples had stretched, and therefore its density must have been decreased as it propagated greater distances, and if lateral spreading also occurred, this would further reduce the density.

The experiments with (compressible) cellular structure indicated that the 3D structures transferred up to 15% less impulse than the solid block at the closest standoff distances, Figure 6.3, but showed minimal difference at the furthest standoff distance where the cellular structure was not significantly deformed. The peak pressure

transmitted by the cellular structures was also less than that transmitted by the solid block. However, such large impulse mitigation is inconsistent with previous numerical and laboratory studies of sand column impacts with cellular structures [77, 79]. These indicated that usually little or no impulse reduction occurred unless the core suffered substantial crushing, and in the most optimal scenario where the core collapsed to a strain of about 50%, only a 5% reduction of impulse was predicted to occur. These earlier studies also predicted that substantial impulse enhancement would occur if the impact caused the core strain to significantly exceed the densification strain. However, this regime could not be accessed experimentally since the resulting loads on the vertical impulse facility would have caused Taylor impact plastic flow and the lower end, and perhaps buckling, of the Hopkinson bars. These issues led to a decision to invest a significant effort in numerical simulations of the model landmine event and its interactions with the test samples and structure that supported them.

8.3. Particle Method Simulation Assisted Analysis

The particle based simulation method implemented in the IMPETUS Afea Solver was used to model the detonation of the explosive, the acceleration of the sand by the shock that propagated through the sand and the more gradual “push” of the expanding detonation products, and the sand and detonation particles impact with the test structure. Using sand particle contact models developed in other studies of the same synthetic silica

sand [83, 125], the modeling approach has been used to investigate the sand–structure interaction during the experiments and to predict the impulse and pressure measurements. After accounting for the partially water saturated sand used in the experiments, this combined approach was able to successfully predict both the impulse transferred during the vertical pendulum mode tests and the pressure waveforms recorded with the instrumented Hopkinson pressure bars. The simulated impulse transferred to solid and cellular samples were in very good agreement with measurements for all the test structures and standoff distances investigated in the dissertation. The pressure – time waveforms recorded with the Hopkinson bars was also well predicted by the particle based simulation methodology. The peak pressure and general shape of the waveforms prior to the arrival of the reflected signals was exceptionally well predicted. Past the first reflected wave, reverberations within the Hopkinson bar dominated the response, and difficulty of adequately defining the dissipation mechanisms within the bars and the reflection coefficients at the top and the bottom of the bars, precluded accurate predictions.

Once the model was validated, by comparison with measured impulse and pressure waveforms for both solid and the compressible cellular structure, it was used to investigate the fundamental processes involved during the impact of sand against various test structures. These simulations revealed the existence of three regions of impulse transfer. The first region corresponded to the arrival of fast sand that had spalled from the top surface of the sand layer during reflection at the air-sand surface of the compressive shock launched into the sand by the explosive event. Appendix C contains the results of

highly time resolved simulations of this process. They reveal that when the detonation front reached the sand, a compressive shock was propagated through the sand with a velocity comparable to the speed of sound in the wet sand. This shock was reflected and sign converted to a tensile disturbance at the sand air interface, and caused some sand particles to be emitted perpendicular to the sand surface at high velocity. This process continued as the shock returned towards the detonation until it met with the rear surface of the sand that was being accelerated (to a much lower velocity than the spalled sand) by the expanding (high pressure and temperature) detonation products. The fast, but low density spalled sand appears to experimentally correlate with the sand fingers observed in the high speed video images. The pressure (and impulse) applied during this region decreased rapidly with standoff, and appears to be a consequence of sand stretching (density reduction) due to a substantially velocity gradient in the sand, and to momentum transfer from the sand particles to those representing the air.

The second region of loading corresponded to impact by the main body of sand which was pushed towards the sample by the expanding explosive reaction products. This much higher density sand had a range of velocities centered around 300 ms^{-1}; in the range observed experimentally. The simulations revealed that it stretched in length, and to a lesser extend in lateral width, as it propagated upwards perpendicular the surface of the explosive sheet. The third region corresponded to impact of explosive reaction product and slow sand particles with the sample. In the experiments conducted here this third regime contributed little additional impulse to the sample, and indicated that the majority of the impulse was transferred by the sand located above the explosive charge.

As the standoff distance increased, the simulated pressure waveforms began to show progressively earlier pressure rises compared to those of the experiments as the standoff distance increased. This first arriving signal was from spalled sand impact and indicates that the simulations overestimated the speed of the sand in this regime. There are two possible explanations. The first is that the spalled sand speed was correctly predicted but that the forces that caused it to slow during propagation were underestimated. These sand particles were moving at speeds of order 1,000 ms^{-1} which is above Mach 3 for the test site location. Such hypersonic sand is likely to suffer a substantial drag force resulting from the air shock created ahead of each isolated sand particle. Further treatment of this issue was beyond the scope of the dissertation. The second rationale for the discrepancy is that the simulation overestimated the velocity of the spalled sand. The details of this process, including the possibility that's clusters of sand particles might have been launched in practice, was also beyond the scope of the dissertation, but would be an interesting area for further explorations.

The simulations revealed that the standoff effect occurred because of a small reduction in axial sand particle velocity (due to momentum transfer to air particles) and more time for lateral spreading of the sand particles as the standoff distance increased, Figure 5.19. This lateral spreading resulted in a smaller fraction of the sand passing through the aperture in the sand box lid and impacting the bottom surface of the test samples. The simulations also indicated that the momentum transferred to the solid, back

supported structure whose flat impact face was perpendicular to the sand propagation direction was almost identical to that of the incident sand. This affirms the conclusion of a previous laboratory study utilizing lower velocity sand columns [77], and indicates that the beneficial fluid structure interaction effect (that results from significant reflected momentum from rigid surfaces) that present in underwater impulse transfer processes was absent for wet sand impacts studied here with impact velocities of 300 ms^{-1}. There may be caveats that could be investigated in future work. For instance, if the structure is closer to the explosive, detonation product and air shock loading may be more significant and could influence the effective FSI. It is also possible that higher impact velocity sand might behave differently during impact with the structure or sand already accumulated against it.

The simulation methodology provided a means to investigate the soil interaction with the sand box lid aperture and nearby test structure. Studies of this interaction revealed that the gap created between the four edges of square samples front face and the steel box top significantly affected impulse transfer to the solid block. The gap acted as a valve, and controlled the rate of sand venting from region beneath the sample where it accumulated during the impact process. This venting in turn controlled the pressure exerted on the sample by the sand. Because both the sample surface and the top surface of the sand box lid both moved during the approximately 2-4 ms period of sand impact, Figure 5.20, this gap also varied during the loading event.

Upon removal of the steel box top, the simulations revealed that the transferred impulse was reduced at the closest standoff distance. This occurred because sand accumulated near the center of the impact face creating a virtual convex surface against which later arriving sand impacted. Those later impacts near the sides of the sample were only partially arrested and did not transfer their entire vertical momentum to the test sample. However, as the standoff distance was increased, this impulse reduction effect was lost and the impulse with the lid removed exceeded that with it present. This appears to have occurred because the impacting sand retained a higher velocity with no lid present. This seemed to have occurred because less stagnated sand accumulated near the impact and sand particles therefore impacted and their forward momentum fully transferred before they laterally flowed over the sample surface and escape the system. It is important to note that that the sand which appears to be leaving the sample at ~45^{o} in Figure 7.11(d) is the result of collisions between laterally reflected particles (with no upward momentum) and upward moving particles (that had not impacted the sample).

The dynamic deformation of the face sheet impacted by sand also had an effect on the impulse transfer process to cellular structures. When the (unsupported) edges of the face sheet were deflected upwards by early sand impacts, later arriving sand was reflected with only partial upward momentum transfer. This effect was responsible for most the difference in impulse reduction between the thin and thick face sheet cellular samples, Figure 6.9(c) and (d).

The contribution of just core crushing to the impulse transfer process was investigated by making the thin front face sheet of cellular core samples to be effectively rigid. This then resulted in a transferred impulse that was identical to that of the solid block; a key finding of the dissertation that supports previous investigations with sand columns [77, 79].

Reducing the core strength so that it was substantially less than the pressure applied by the sand was shown to decrease the transferred impulse by ~5% compared to that transferred to a solid block. The origin of this sand structure effect has been linked to a subtle interplay between the dynamic increase in effect standoff distance as the core compressed and the development of a convex shaped layer of densified sand against the samples impact face which resulted in only partial vertical momentum transfer during impacts near the sides of the samples. Weak cellular structures were also shown to decrease the pressure on the distal end of the specimen and the acceleration of the test apparatus. When the core was so weak that it allowed the core to reach/exceed its densification strain, the front sheet failed to “slap” the back face, and cause a significant pressure rise as predicted in some previous calculations [79]. This appears to be a result of the gradual increase in the post densification strain hardening of the cellular structure developed and tested here.

Chapter 9. Conclusion

The findings of this work have been grouped into categories relating to : *(i)* the cellular structures characterization and compressive response, *(ii)* experimental studies of the soil-structure interaction, and *(iii)* insights from particle based simulations.

9.1. Characterization and Compressive Response

- The elastic modulus of the 3D tube based cellular structure has an approximately linear dependence upon the solid material modulus, E_s, and structures relative density given by: $E_{cell}/E_s = 3.6\bar{\rho}$ consistent with an initially stretch dominated

response. The modulus of 3D orthogonal tube structures is significantly higher than that of metal foams of similar relative density and material.

- The peak strength of the cellular structure was proportional to that of the solid material and exhibited a power law dependence upon relative density, given by: $\sigma_{cell}/\sigma_s = 1.05\bar{\rho}^{5/3}$. In-situ experimental observations and finite element simulations reveal the crush strength to be controlled by buckling of the tubes oriented in the applied load direction.

- The specific energy absorption increased with compressive strength from about 10 kJ/kg for structures with a compressive strength of ~10 MPa to 30 kJ/kg at strengths of 60 MPa. This was slightly less than the specific strength of arrays of vertical tubes, but was off-set by the existence of a non-zero in-plane compressive strength for the 3D structure. In addition, the co-linear aligned tubes provide the structure with stretch resistance, which is also important for impact applications.

- A 3D tube structure of a given relative density has a near constant crush strength to a crush strain of about 60%. The initial compressive strength was independent of impact velocity for compression strain rates up to 2000 s^{-1},and was shown, using the finite element model, to be a consequence of the rate independent plastic response of the aluminum 6061-T6 alloy.

- Under dynamic loading, the core strength again exhibited a power law dependence upon relative density, given by $\sigma_p/\sigma_s = (\bar{\rho})^{5/3}$, consistent with crush strengths controlled by the buckling of tubes oriented in the applied load direction.

- The vertical tube response of the isolated tubes was rate dependent due to tube rotation at low impact velocities.

- The vertical tube collapse mode changes when placed inside the in-plane tube lay-up, leading to a synergistic interaction in the energy absorption between the co-linear aligned and vertical tubes at dynamic loading, which was also observed with quasi-static loading.

- The finite element simulations reveal that the ratio of the impact to back face stresses increased with strain rate and core density, which is a valuable result for shock load mitigation problems.

9.2. Experimental Soil-Structure Interactions

- A vertical impulse test apparatus has been constructed to enable the impulse applied by detonation of a small 350 g sheet of explosive buried in wet synthetic

sand to be measured. The facility also enabled the pressure applied to the rear face of the samples to be measured using a set of Hopkinson pressure bars.

- The model landmine launched 5.08 cm thick wet sand layers normal to the soil surface at leading edge velocities in the 300 ms^{-1} range. Small fingers of faster sand could be observed ahead of the main sand front. These have been associated with fast sand that was spalled from the top of the sand layer by shock reflection at the sand air interface.

- Analysis of the experiments with a solid (incompressible sample) indicated that the transmitted impulse decreased with increasing standoff distance.

- Experiments with the cellular structure indicated that the 3D structures transferred up to 15% less impulse than the solid block at the closest standoff distances, but showed minimal difference at the furthest standoff distances where the cellular structure was not significantly deformed.

- The pressure transmitted by the distal end of the 3D cellular structures was usually less than that transmitted by the solid block except at large standoff distance.

9.3. Insights from Particle-Based Simulations

- Comparison of the simulated impulse transferred to solid and cellular samples were in very good agreement with measurements for all the test structures and standoff distances investigated in the dissertation.

- The pressure – time waveforms recorded with the Hopkinson bars was well predicted by the particle based simulation methodology. The peak pressure and general shape of the waveforms prior to the arrival of the reflected signals was exceptionally well predicted.

- The simulations reveal three regions of impulse transfer. The first region corresponded to the arrival of fast sand that had spalled from the top surface of the sand layer during reflection at the air-sand surface of the compressive shock launched into the sand by the explosive event. This fast sand appears to correlate with the sand fingers observed in the high speed video images. The pressure (and impulse) applied in this region decreased rapidly with standoff, and appears to be a consequence of sand stretching (density reduction) due to a velocity gradient in the sand, and to momentum transfer from the sand particles to those representing the air. The second region of loading corresponded to impact by the main body of sand which was pushed towards the sample by the expanding explosive reaction products. The third region corresponded to impact of explosive reaction product

and slow sand particles with the sample. In the experiments conducted here this third regime contributed little additional impulse to the sample.

- As the standoff distance increased, the simulated pressure waveforms began to show progressively earlier pressure rises compared to those of the experiments as the standoff distance increased. This is attributed to either a failure of the simulation model to correctly capture the drag phenomena that slow the motion of sand in air or an overestimation of the spalled sands initial velocity.

- The simulated transmitted impulse and peak pressure decrease with increasing standoff distance was in good agreement with those observed in experiments. The simulations revealed that the standoff effect occurred because of a small reduction in axial sand particle velocity (due to momentum transfer to air particles) and more time for lateral spreading of the sand particles as the standoff distance increased. This spreading resulted in a smaller fraction of the sand impacting the (finite) area of the test samples impact face.

- The experimentally validated simulations also indicate that the momentum transferred to a solid back supported planar structure inclined perpendicular to the sand propagation direction is almost identical to that of the incident sand. This affirms the conclusion of a previous study utilizing lower velocity sand columns,

and indicates that the beneficial fluid structure interaction effect present in underwater impulse transfer processes is absent for wet sand impacts at velocities of 300 ms^{-1}.

- The simulation methodology provided a means to investigate the soil structure interaction and revealed that the gap separation created between the samples front face and the steel box top was largely responsible for a reduction in impulse. The gap separation acted as a valve for release of the sand pressure. Crushable structures that provided a more significant opening allowed for more impulse reduction.

- Upon removal of the modeled steel box top, simulations revealed that the transferred impulse decreased at the closest standoff distance due to later arriving sand reflection with only partial momentum transfer from accumulated sand below the impact surface. At the largest standoff distance, the impulse was increased the steel box top was removed because the velocity remained higher when the early sand impacts had time to laterally flow across the sample impact face and escape the system.

- Modeling the thin front face sheet of strong core samples to be effectively rigid resulted in a similar transferred impulse to that of the solid block. A weaker front face was found to deform at its edges resulting in a convex sample impact face

that did not fully transfer all the sand particle vertical momentum to the test structure.

- Reducing the core strength so that it was substantially less than the pressure applied by the sand was shown to decrease the transferred impulse by ~5% compared to that transferred to a solid block. The origin of this sand structure effect has been linked to a subtle interplay between the dynamic increase in effect standoff distance as the core compressed and the development of a convex shaped layer of densified sand against the samples impact face which resulted in only partial vertical momentum transfer during impacts near the sides of the samples. Weak cellular structures were also shown to decrease the pressure on the distal end of the specimen and the acceleration of the test apparatus.

- When the core was so weak that it allowed the core to reach/exceed its densification strain, the front sheet failed to “slap” the back face, and cause a significant pressure rise (as predicted in some previous calculations). This appears to be a result of the gradual increase in the post densification strain hardening of the cellular structure developed and tested here.

Appendix A. Tube Upper Bound Derivation

The axial crushing of both square [133] and circular [134] tubes has been widely studied. The following design formula is an expression for the average crush force for a hollow extrusion [135].

$$F_{avg}^{0} = C_0 \varphi^{2/3} \sigma_o A_s \qquad (A1)$$

The parameters involved are:

C_0 cross section dependent dimensionless constant

φ $\frac{A_s}{A_f}$ solidity ratio (A_s: solid (net) extrusion cross section, A_f: gross cross section area)

σ_o $\sigma_0 = 0.5(\sigma_{02} + \sigma_u)$ characteristic stress of extrusion material (σ_{02}: nominal stress at 0.2% plastic strain, σ_u: ultimate nominal stress)

The compressive peak stress for a crushed extruded tube is described as the average crush force over the tubes gross cross sectional area. Starting from equation (A1), the compressive peak stress is defined by

$$\sigma_p = \frac{F_{avg}^0}{A_f} = C_0 \varphi^{5/3} \sigma_0 \tag{A2}$$

Parameters in Equation (A2) can be organized to re-define, φ, with measurable values, as:

$$\varphi = \left[\frac{\sigma_p}{C_0 \sigma_0}\right]^{3/5} \tag{A3}$$

The energy absorbed (E) by the crushed extruded tube is dependent on the average crush force and the tubes axial displacement (w), and is written as

$$E = F_{avg}^0 w \tag{A4}$$

This energy absorbed per unit crush mass (E_m) is described by:

$$E_m = \frac{F_{avg}^0 w}{\rho_s A_s w} = \frac{F_{avg}^0}{\rho_s A_s} \tag{A5}$$

where ρ_s is the density of the tube material. The ratio for the tube energy absorbed per unit mass, Equation (A5), over the tube peak stress, Equation (A2), is expressed by

$$\frac{E_m}{\sigma_p} = \frac{\frac{F_{avg}^0}{\rho_s A_s}}{\frac{F_{avg}^0}{A_f}} = \frac{A_f}{\rho_s A_s} = \frac{1}{\rho_s \varphi} \tag{A6}$$

Rearranging Equation (A6) to define the tube energy absorbed per unit mass $(E_m)$with respect to the tube peak stress (σ_p) and substituting φ with Equation (A3) results in the expression used to graphically obtain the tube upper limit shown in Figure 3.8.

$$E_m = \frac{\sigma_p}{\rho_s \varphi} = \sigma_p \left[\rho_s \frac{\sigma_p}{C_0 \sigma_0}\right]^{3/5} \quad \textit{(A7)}$$

Appendix B. Lateral Compression of Tube

To test the validity of the modeling approach prior to simulating quasi-static compression of the 3D topologies we set up a simple single square tube compression experiment and compared the measured and simulated response using the material model described above. We also tuned the critical damage parameter (W_c) with this simulation to 85MPa, which was applied to all 3D simulations to initiate node splitting.

The dimensions of the measured and modeled tube are outlined in Table B1. The tested tube underwent the same thermal processes as outlined in Section 2.2, rendering an age-hardened AA6061-T6 tube. The Specimen was compressed in a 50kN Instron universal testing machine (Instron Corp, Model 4208, Canton, MA, USA) at a strain rate of $\dot{\varepsilon} = 4*10^{-3}\ s^{-1}$ and temperature of 25^{o}C. A laser extensometer (Electronic Instrument Research, Model LE-01, Irwin, PA, USA) was used to measure the displacement of the tube walls. It should be noted that the tube was not brazed to a face sheet material like the 3D orthogonal tube samples in the study. Instead, the tube walls directly contacted

the load platens, which resulted in a different collapse mode to that of tubes that were brazed to face sheets.

B1. Measured dimensions of single tube profile sample studied under quasi-static compressive lateral loading.

	Wall Thickness				Outer Width			
	Top Wall (mm)	Right Wall (mm)	Left Wall (mm)	Bottom Wall (mm)	Right to Left Wall (mm)	Top to Bottom Wall (mm)	Relative Density, $\bar{\rho}$	Peak Stress, σ_p (MPa)
Measured	1.59	1.57	1.58	1.58	18.99	18.95	28.74	48.83
Numerical Model	1.575	1.575	1.575	1.575	19.05	19.05	30.34	49.15

The meshed tube structure was built from 3,240 cubic hexahedra elements with 112,112 nodes. The simulated stress-strain curve in Figure 2.6 demonstrates a good fit to the measured sample. A comparison of Figure B1(b) and (c) shows near identical collapse mode predictions for the experimental and simulated single tube profiles. Thus, the material properties were deemed satisfactory for the 3D orthogonal tube assemblies. Besides providing verification of the material approach, this model also provided evidence of the sensitivity between tube wall thickness and predicting the force curves. No imperfections were necessary with a single tube since the wall thickness of the numerical models fell within 1% or less of each other. This observation suggests that there was a combination of 1) variability in the thickness of each tube that formed the 3D structure and 2) the misalignment caused by fabrication resulted in the large imperfections that were required to trip the simulated 3D structures buckling.

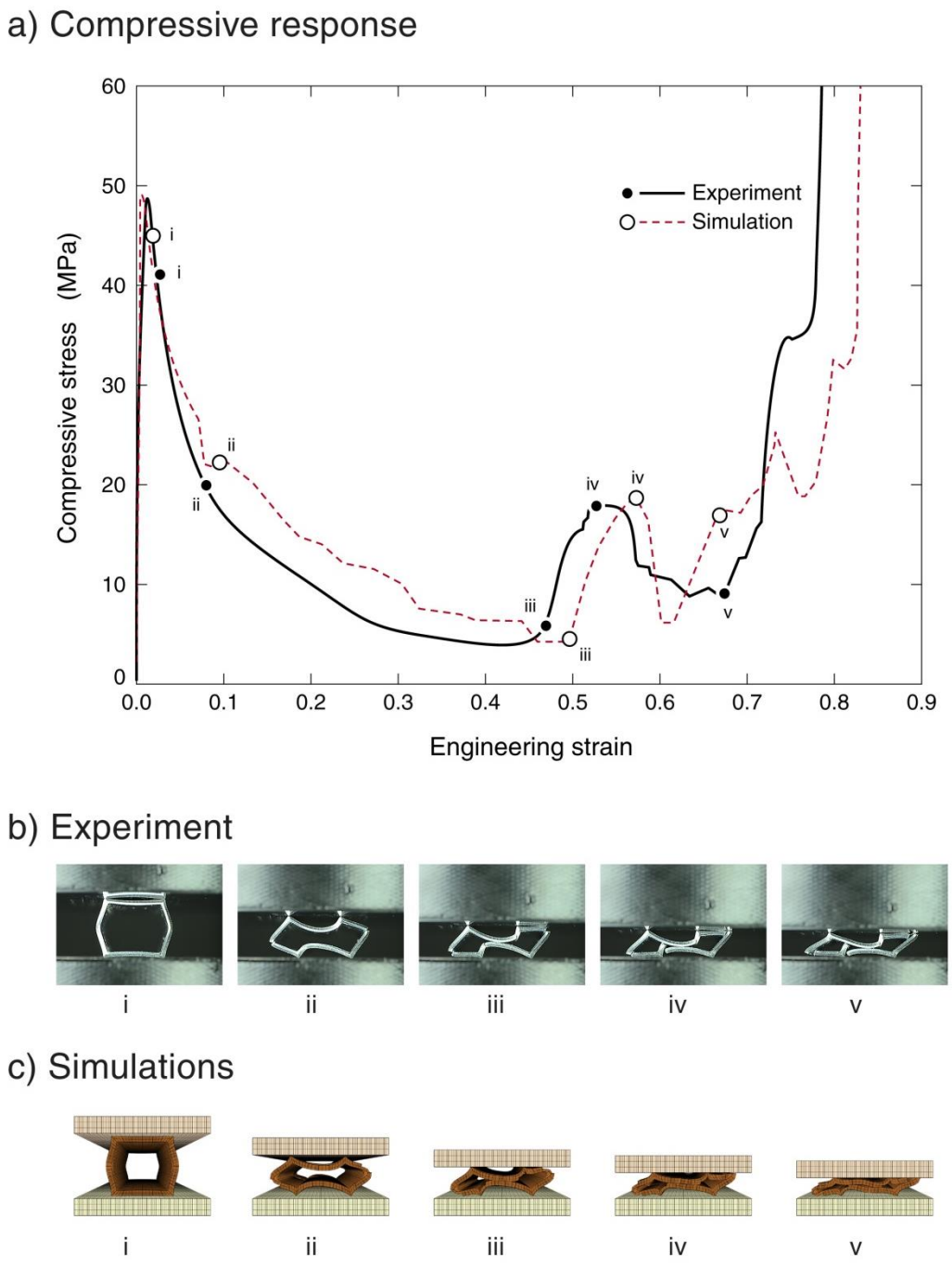

Figure B1. a) A stress-strain curve for a single tube under lateral compression. b) The experimentally observed sequence of the tested collapse modes. c) The sequence of simulated collapse modes.

Appendix C. Initial Stages of Detonation

Time resolved simulations following the initial stages of the detonation indicated that a compressive shock front propagated through the 5.08 cm thick wet sand layer and was reflected at the sand-air interface with sign conversion to a tension wave, Figure C1. The detonation point was centrally located at the base of the simulated particles. Upon detonation the explosive particles are shown to flow radially downward into the low density foam region and began to radially compress the wet Type I sand layer upward, Figure C1(a). The compression wave travelled through the wet sand layer until it began to reflect at the sand-air interface at approximately 30.0 μs, Figure C1(e). The shock traveled through the 5.08 cm layer of wet sand at a velocity of 1690 ms^{-1}, which is consistent with prior studies [136]. Once the sand was reflected at the sand-air interface, it was transformed to a tension wave enabling elastic particle recoil from the surface. Figure C1(g) shows that after 40.0 μs, the reflection was accompanied by sand ejecta from the leading edge of the Type I sand. At 50.0 μs the reaction products are pushing the wet Type I sand upward and the reflective shock wave began pushing the Type II sand downward, causing it to compact and undergo transverse shear, Figure C1(h).

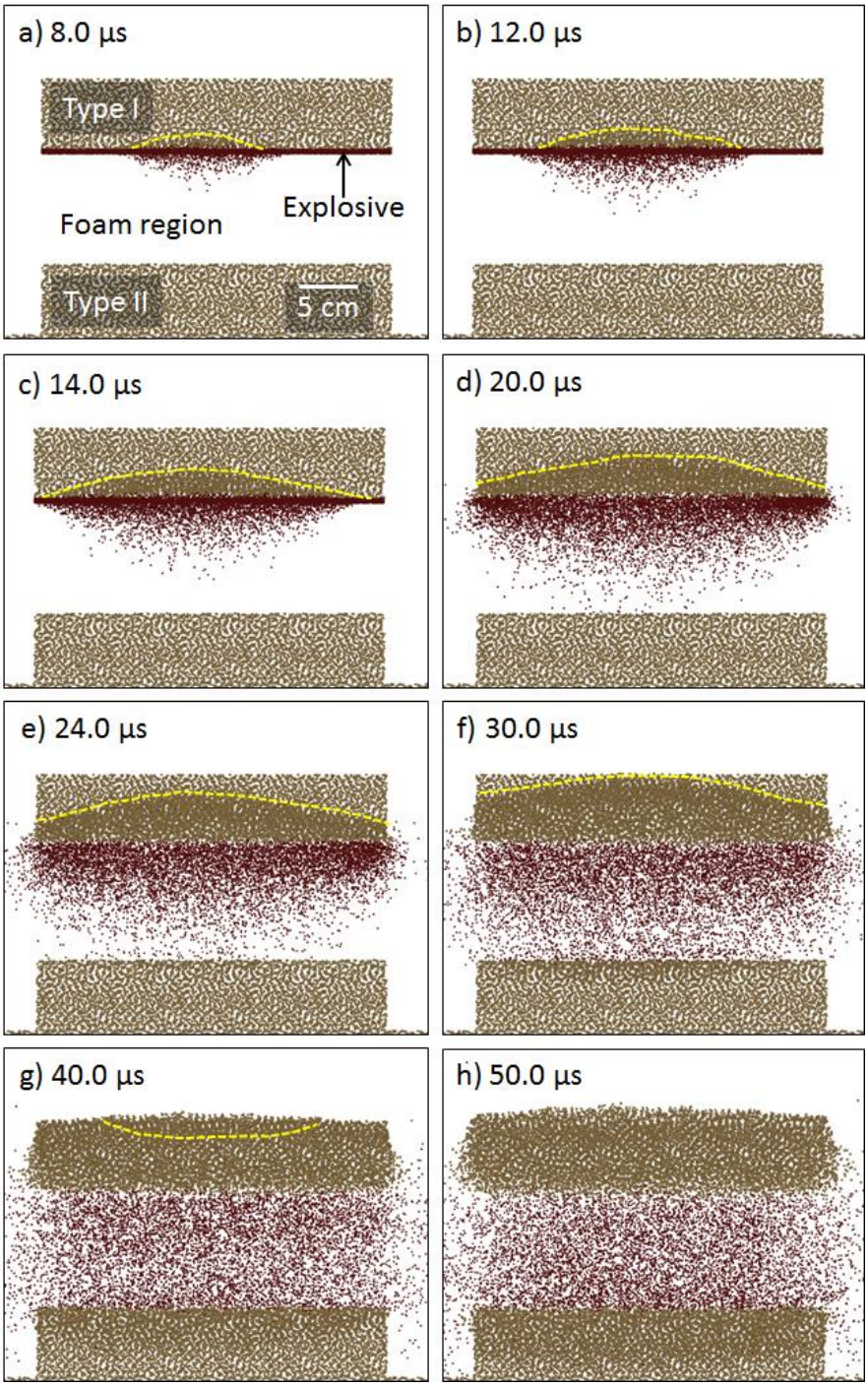

Figure C1. Time resolved simulation sequence of the initial explosive event that demonstrates a compressive shock front propagated through the Type I sand (a-f) and being reflected at the sand-air interface into a tension wave (g-h). The yellow dotted curve highlights the shock front (a-f) and tension wave (g).

Chapter 10. References

[1] Smith, P. D. *Blast and Ballistic Loading of Structures*. Oxford ; Boston: Butterworth-Heinemann, 1994.

[2] Wierzbicki, T. *Optimum Design of Integrated Front Panel against Crash*. Report for Ford Motor Company. Vehicle Component Department. July 15, 1983.

[3] Langseth, M., and A.G. Hanssen. *Aluminum Structural Design*. New York: SpringerWien, 2003.

[4] Mori, L. F., D. T. Queheillalt, H. N. G. Wadley, and H. D. Espinosa. "Deformation and Failure Modes of I-Core Sandwich Structures Subjected to Underwater Impulsive Loads." *Experimental Mechanics* 49, no. 2 (September 4, 2008): 257–275.

[5] Wadley, Haydn, Kumar Dharmasena, Yungchia Chen, Philip Dudt, David Knight, Robert Charette, and Kenneth Kiddy. “Compressive Response of Multilayered Pyramidal Lattices during Underwater Shock Loading.” *International Journal of Impact Engineering* 35, no. 9 (September 2008): 1102–1114.

[6] Gibson, L.J., and M.F. Ashby. *Cellular Solids: Structure and Properties*. 2nd ed. Cambridge: Cambridge University Press, 1997.

[7] Alghamdi, A.A.A. “Collapsible Impact Energy Absorbers: An Overview.” *Thin-Walled Structures* 39, no. 2 (February 2001).

[8] Gibson, L.J. “The Mechanical Behaviour of Cancellous Bone.” *Journal of Biomechanics* 18, no. 5 (January 1985): 317–328.

[9] Ashby, M. F., and R. F. Mehl Medalist. “The Mechanical Properties of Cellular Solids.” *MetallurgicalTransactions A* 14, no. 9 (September 1983): 1755–1769.

[10] Easterling, K. E., R. Harrysson, L. J. Gibson, and M. F. Ashby. “On the Mechanics of Balsa and Other Woods.” *Proceedings of the Royal Society A: Mathematical, Physical and Engineering Sciences* 383, no. 1784 (September 8, 1982): 31–41.

[11] Timoshenko, S. P., J. N. Goodier, and H. Norman Abramson. “Theory of Elasticity (3rd Ed.).” *Journal of Applied Mechanics* 37, no. 3 (1970): 888.

[12] Wadley, H. “Fabrication and Structural Performance of Periodic Cellular Metal Sandwich Structures.” *Composites Science and Technology* 63, no. 16 (December 2003): 2331–2343.

[13] Ashby, M.F., A.G. Evans, N. A. Fleck, L.J. Gibson, J.W. Hutchinson, and H.N.G. Wadley. *Metal Foams: A Design Guide*. Butterworth-Heinemann, 2000.

[14] Wadley, H. N.G. “Multifunctional Periodic Cellular Metals.” *Philosophical Transactions of the Royal Society A: Mathematical, Physical and Engineering Sciences* 364, no. 1838 (January 15, 2006): 31–68.

[15] Maiti, S.K., L.J. Gibson, and M.F. Ashby. “Deformation and Energy Absorption Diagrams for Cellular Solids.” *Acta Metallurgica* 32, no. 11 (November 1984): 1963–1975.

[16] Evans, A.G., J.W. Hutchinson, N.A. Fleck, M.F. Ashby, and H.N.G. Wadley. “The Topological Design of Multifunctional Cellular Metals.” *Progress in Materials Science* 46, no. 3–4 (January 2001): 309–327.

[17] Deshpande, V.S., M.F. Ashby, and N.A. Fleck. “Foam Topology: Bending versus Stretching Dominated Architectures.” *Acta Materialia* 49, no. 6 (April 2001): 1035–1040.

[18] Evans, K.E. “The Design of Doubly Curved Sandwich Panels with Honeycomb Cores.” *Composite Structures* 17, no. 2 (January 1991): 95–111.

[19] Blitzer, T. *Introduction, Honeycomb Technology, Materials, Design, Manufacturing, Applications and Testing*. 1st edn. London, UK: Chapman & Hall, 1997.

[20] Gibson, L. J., M. F. Ashby, G. S. Schajer, and C. I. Robertson. “The Mechanics of Two-Dimensional Cellular Materials.” *Proceedings of the Royal Society A: Mathematical, Physical and Engineering Sciences* 382, no. 1782 (July 8, 1982): 25–42.

[21] Fleck, N. A., and V. S. Deshpande. “The Resistance of Clamped Sandwich Beams to Shock Loading.” *Journal of Applied Mechanics* 71, no. 3 (2004): 386.

[22] Valdevit, L., J.W. Hutchinson, and A.G. Evans. “Structurally Optimized Sandwich Panels with Prismatic Cores.” *International Journal of Solids and Structures* 41, no. 18–19 (September 2004): 5105–5124.

[23] Côté, F., V.S. Deshpande, N.A. Fleck, and A.G. Evans. “The Compressive and Shear Responses of Corrugated and Diamond Lattice Materials.” *International Journal of Solids and Structures* 43, no. 20 (October 2006): 6220–6242.

[24] McShane, G. J., V. S. Deshpande, and N. A. Fleck. “The Underwater Blast Resistance of Metallic Sandwich Beams With Prismatic Lattice Cores.” *Journal of Applied Mechanics* 74, no. 2 (2007): 352.

[25] Rathbun, H. J., Z. Wei, M. Y. He, F. W. Zok, A. G. Evans, D. J. Sypeck, and H. N. G. Wadley. “Measurement and Simulation of the Performance of a Lightweight Metallic Sandwich Structure with a Tetrahedral Truss Core.” *Journal of Applied Mechanics* 71, no. 3 (2004): 368.

[26] Sypeck, D.J., and H. N. G. Wadley. “Multifunctional Microtruss Laminates: Textile Synthesis and Properties.” *J. Mater. Res* 16, no. 3 (March 2001): 890–897.

[27] Sypeck, David J., and Haydn N. G. Wadley. “Cellular Metal Truss Core Sandwich Structures.” *Advanced Engineering Materials* 4, no. 10 (2002): 759–764.

[28] Wadley, Haydn, Kumar Dharmasena, Doug Queheillalt, Yung Chia Chen, Philip Dudt, David Knight, Ken Kiddy, Zhenyu Xue, and Ashkan Vaziri. “Dynamic Compression of Square Honeycomb Structures During Underwater Impulsive Loading.” *Journal of Mechanics of Materials and Structures* 2, no. 10 (December 1, 2007): 2025–2048.

[29] Wei, Z., V.S. Deshpande, A.G. Evans, K.P. Dharmasena, D.T. Queheillalt, H.N.G. Wadley, Y.V. Murty, et al. “The Resistance of Metallic Plates to

Localized Impulse." *Journal of the Mechanics and Physics of Solids* 56, no. 5 (May 2008): 2074–2091.

[30] Dharmasena, K.P., H.N.G. Wadley, K. Williams, Z Xue, and J.W. Hutchinson. "Response of Metallic Pyramidal Lattice Core Sandwich Panels to High Intensity Impulsive Loading in Air." *International Journal of Impact Engineering* 38, no. 6 (May 2011): 275–289.

[31] Rimoli, J.J., B. Talamini, J.J. Wetzel, K.P. Dharmasena, R. Radovitzky, and H.N.G. Wadley. "Wet-sand Impulse Loading of Metallic Plates and Corrugated Core Sandwich Panels." *International Journal of Impact Engineering* 38, no. 10 (October 2011): 837–848.

[32] Kooistra, Gregory W., Douglas T. Queheillalt, and Haydn N.G. Wadley. "Shear Behavior of Aluminum Lattice Truss Sandwich Panel Structures." *Materials Science and Engineering: A* 472, no. 1–2 (January 2008): 242–250.

[33] Hanssen, A G, O S Hopperstad, and M Langseth. "Design of Aluminium Foam-filled Crash Boxes of Square and Circular Cross-sections." *International Journal of Crashworthiness* 6, no. 2 (January 2001): 177–188.

[34] Hanssen, A G, L Lorenzi, K K Berger, O S Hopperstad, and M Langseth. "A Demonstrator Bumper System Based on Aluminium Foam Filled Crash Boxes." *International Journal of Crashworthiness* 5, no. 4 (January 2000): 381–392.

[35] Pingle, S. M., N. A. Fleck, V. S. Deshpande, and H. N. G. Wadley. “Collapse Mechanism Maps for a Hollow Pyramidal Lattice.” *Proceedings of the Royal Society A: Mathematical, Physical and Engineering Sciences* 467, no. 2128 (October 13, 2010): 985–1011.

[36] Abramowicz, W., and N. Jones. “Transition from Initial Global Bending to Progressive Buckling of Tubes Loaded Statically and Dynamically.” *International Journal of Impact Engineering* 19, no. 5–6 (May 1997): 415–437.

[37] Reyes, G. “Static and Low Velocity Impact Behavior of Composite Sandwich Panels with an Aluminum Foam Core.” *Journal of Composite Materials* 42, no. 16 (August 1, 2008): 1659–1670.

[38] Hanssen, A.G., M. Langseth, and O.S. Hopperstad. “Static and Dynamic Crushing of Square Aluminium Extrusions with Aluminium Foam Filler.” *International Journal of Impact Engineering* 24, no. 4 (April 2000): 347–383.

[39] Baumeister, J, J Banhart, and M Weber. “Aluminium Foams for Transport Industry.” *Materials & Design* 18, no. 4–6 (December 1997): 217–220.

[40] Reid, S.R. “Plastic Deformation Mechanisms in Axially Compressed Metal Tubes Used as Impact Energy Absorbers.” *International Journal of Mechanical Sciences* 35, no. 12 (December 1993): 1035–1052.

[41] Deshpande, V. S., and N. A. Fleck. “High Strain Rate Compressive Behavior of Aluminum Alloy Foams.” *International Journal of Impact Engineering* 24, no. 3 (March 2000): 227–298.

[42] Dannemann, Kathryn A, and James Lankford Jr. “High Strain Rate Compression of Closed-cell Aluminium Foams.” *Materials Science and Engineering: A* 293, no. 1–2 (November 30, 2000): 157–164.

[43] Calladine, C.R., and R.W. English. “Strain-rate and Inertia Effects in the Collapse of Two Types of Energy-absorbing Structure.” *International Journal of Mechanical Sciences* 26, no. 11–12 (January 1984): 689–701.

[44] Graff, Karl F. *Wave Motion in Elastic Solids*. Courier Dover Publications, 1975.

[45] Cole, R.H. *Underwater Explosions*. Princeton, NJ: University Press, 1948.

[46] Kambouchev, N., L. Noels, and R. Radovitzky. “Nonlinear Compressibility Effects in Fluid-Structure Interaction and Their Implications on the Air-Blast Loading of Structures.” *Journal of Applied Physics* 100, no. 6 (2006): 063519.

[47] Swisdak, M.M. *Explosion Effects and Properties. Part I. Explosion Effects in Air*. Silver Spring, MD: Naval Surface Weapons Center, 1975.

[48] Wadley, H.N.G., K.P. Dharmasena, M.Y. He, R.M. McMeeking, A.G. Evans, T. Bui-Thanh, and R. Radovitzky. “An Active Concept for Limiting Injuries Caused by Air Blasts.” *International Journal of Impact Engineering* 37, no. 3 (March 2010): 317–323.

[49] Neuberger, A., S. Peles, and D. Rittel. “Scaling the Response of Circular Plates Subjected to Large and Close-Range Spherical Explosions. Part I: Air-Blast Loading.” *International Journal of Impact Engineering* 34, no. 5 (May 2007): 859–873.

[50] Wei, Z., K.P. Dharmasena, H.N.G. Wadley, and A.G. Evans. “Analysis and Interpretation of a Test for Characterizing the Response of Sandwich Panels to Water Blast.” *International Journal of Impact Engineering* 34, no. 10 (October 2007): 1602–1618.

[51] Taylor, G.I. *The Pressure and Impulse of Submarine Explosion Waves on Plates*. Vol. III. Cambridge, UK: Cambridge University Press, 1941.

[52] Hutchinson, John W., and Zhenyu Xue. “Metal Sandwich Plates Optimized for Pressure Impulses.” *International Journal of Mechanical Sciences* 47, no. 4–5 (April 2005): 545–569.

[53] Zhu, Feng, Zhihua Wang, Guoxing Lu, and Longmao Zhao. “Analytical Investigation and Optimal Design of Sandwich Panels Subjected to Shock Loading.” *Materials & Design* 30, no. 1 (January 2009): 91–100.

[54] Qiu, X., V. S. Deshpande, and N. A. Fleck. “Dynamic Response of a Clamped Circular Sandwich Plate Subject to Shock Loading.” *Journal of Applied Mechanics* 71, no. 5 (2004): 637.

[55] Xue, Zhenyu, and John W. Hutchinson. “Preliminary Assessment of Sandwich Plates Subject to Blast Loads.” *International Journal of Mechanical Sciences* 45, no. 4 (April 2003): 687–705.

[56] Arora, H., P. A. Hooper, and J. P. Dear. “The Effects of Air and Underwater Blast on Composite Sandwich Panels and Tubular Laminate Structures.” *Experimental Mechanics* 52, no. 1 (June 24, 2011): 59–81.

[57] Deshpande, V.S., A. Heaver, and N.A. Fleck. “An Underwater Shock Simulator.” *Proceedings of the Royal Society A: Mathematical, Physical and Engineering Sciences* 462, no. 2067 (March 8, 2006): 1021–1041.

[58] Espinosa, H. D., S. Lee, and N. Moldovan. “A Novel Fluid Structure Interaction Experiment to Investigate Deformation of Structural Elements Subjected to Impulsive Loading.” *Experimental Mechanics* 46, no. 6 (December 8, 2006): 805–824.

[59] Tilbrook, M.T., V.S. Deshpande, and N.A. Fleck. “Underwater Blast Loading of Sandwich Beams: Regimes of Behaviour.” *International Journal of Solids and Structures* 46, no. 17 (August 2009): 3209–3221.

[60] Xue, Zhenyu, and John W. Hutchinson. “A Comparative Study of Impulse-Resistant Metal Sandwich Plates.” *International Journal of Impact Engineering* 30, no. 10 (November 2004): 1283–1305.

[61] Liang, Yueming, Alexander V. Spuskanyuk, Shane E. Flores, David R. Hayhurst, John W. Hutchinson, Robert M. McMeeking, and Anthony G. Evans. “The Response of Metallic Sandwich Panels to Water Blast.” *Journal of Applied Mechanics* 74, no. 1 (2007): 81.

[62] Kambouchev, Nayden, Raul Radovitzky, and Ludovic Noels. “Fluid–Structure Interaction Effects in the Dynamic Response of Free-Standing Plates to Uniform Shock Loading.” *Journal of Applied Mechanics* 74, no. 5 (2007): 1042.

[63] Rathbun, H.J., D.D. Radford, Z. Xue, M.Y. He, J. Yang, V. Deshpande, N.A. Fleck, J.W. Hutchinson, F.W. Zok, and A.G. Evans. “Performance of Metallic Honeycomb-Core Sandwich Beams under Shock Loading.” *International Journal of Solids and Structures* 43, no. 6 (March 2006): 1746–1763.

[64] Pickering, E.G., Steeve Chung Kim Yuen, and G.N. Nurick. “The Influence of the Height of Burial of Buried Charges – Some Experimental Observations.” *International Journal of Impact Engineering* 58 (August 2013): 76–83.

[65] Fox, D.M., X. Huang, D. Jung, W.L. Fourney, U. Leiste, and J.S. Lee. “The Response of Small Scale Rigid Targets to Shallow Buried Explosive Detonations.” *International Journal of Impact Engineering* 38, no. 11 (November 2011): 882–891.

[66] Pickering, E.G., S. Chung Kim Yuen, G.N. Nurick, and P. Haw. “The Response of Quadrangular Plates to Buried Charges.” *International Journal of Impact Engineering* 49 (November 2012): 103–114.

[67] Neuberger, A., S. Peles, and D. Rittel. “Scaling the Response of Circular Plates Subjected to Large and Close-Range Spherical Explosions. Part II: Buried Charges.” *International Journal of Impact Engineering* 34, no. 5 (May 2007): 874–882.

[68] Bergeron, Denis, Robert Walker, and Clay Coffey. “Detonation of 100-Gram Anti-Personnel Mine Surrogate Charges in Sand - A Test Case for Computer Code Validation.” *Tech.Rep. Canada Defence Reserach Establishment Suffield* DRES-SR-668 (1998): A2–A20.

[69] Deshpande, V.S., R.M. McMeeking, H.N.G. Wadley, and A.G. Evans. "Constitutive Model for Predicting Dynamic Interactions between Soil Ejecta and Structural Panels." *Journal of the Mechanics and Physics of Solids* 57, no. 8 (August 2009): 1139–1164.

[70] Tremblay, J.E., D.M. Bergeron, and R. Gonzalez. *Protection of Soft-Skinned Vehicle Occupants from Landmine Blasts*. The Technical Cooperation Program, Subcommittee on Conventional Weapons Technology, Techincal Panel W-1, 1998.

[71] Wang, Zhongqi, Hong Hao, and Yong Lu. "A Three-Phase Soil Model for Simulating Stress Wave Propagation due to Blast Loading." *International Journal for Numerical and Analytical Methods in Geomechanics* 28, no. 1 (January 2004): 33–56.

[72] Wang, Zhongqi, and Yong Lu. "Numerical Analysis on Dynamic Deformation Mechanism of Soils under Blast Loading." *Soil Dynamics and Earthquake Engineering* 23, no. 8 (December 2003): 705–714.

[73] Lu, Yong, Zhongqi Wang, and Karen Chong. "A Comparative Study of Buried Structure in Soil Subjected to Blast Load Using 2D and 3D Numerical Simulations." *Soil Dynamics and Earthquake Engineering* 25, no. 4 (June 2005): 275–288.

[74] Drucker, D.C., and W. Prager. “Soil Mechanics and Plastic Analysis or Limit Design.” *Quarterly of Applied Mathematics* 10 (1952): 157–165.

[75] Laine, P, and A. Sandvik. “Derivation of Mechanical Properties for Sand.” In *Fourth Asia-Pacific Conference on Shock and Impact Loads of Structures*, 361–368. Singapore: CI-Premier PTE LTD., 20001.

[76] Grujicic, M., B. Pandurangan, R. Qiao, B.A. Cheeseman, W.N. Roy, R.R. Skaggs, and R. Gupta. “Parameterization of the Porous-Material Model for Sand with Different Levels of Water Saturation.” *Soil Dynamics and Earthquake Engineering* 28, no. 1 (January 2008): 20–35.

[77] Park, S., T. Uth, N.A. Fleck, H.N.G. Wadley, and V.S. Deshpande. “Sand Column Impact onto a Kolsky Pressure Bar.” *International Journal of Impact Engineering* 62 (December 2013): 229–242.

[78] Pingle, S.M., N.A. Fleck, H.N.G. Wadley, and V.S. Deshpande. “Discrete Element Calculations of the Impact of a Sand Column against Rigid Structures.” *International Journal of Impact Engineering* 45 (July 2012): 74–89.

[79] Liu, T., H.N.G. Wadley, and V.S. Deshpande. “Dynamic Compression of Foam Supported Plates Impacted by High Velocity Soil.” *International Journal of Impact Engineering* 63 (January 2014): 88–105..

[80] Olovsson, L., A.G. Hanssen, T. Børvik, and M. Langseth. “A Particle-Based Approach to Close-Range Blast Loading.” *European Journal of Mechanics - A/Solids* 29, no. 1 (January 2010): 1–6..

[81] Børvik, T., A.G. Hanssen, M. Langseth, and L. Olovsson. “Response of Structures to Planar Blast Loads – A Finite Element Engineering Approach.” *Computers & Structures* 87, no. 9–10 (May 2009): 507–520.

[82] “Welcome to IMPETUS AFEA.” Accessed February 11, 2014. http://www.impetus-afea.com/.

[83] Børvik, T., L. Olovsson, A.G. Hanssen, K.P. Dharmasena, H. Hansson, and H.N.G. Wadley. “A Discrete Particle Approach to Simulate the Combined Effect of Blast and Sand Impact Loading of Steel Plates.” *Journal of the Mechanics and Physics of Solids* 59, no. 5 (May 2011): 940–958.

[84] Smith, P.D., and J.G. Hetherington. *Blast and Ballistic Loading of Structures*. Oxford: Butterworth-Heinemann, 1994.

[85] Mills, N. *Polymer Foams Handbook: Engineering and Biomechanics Applications and Design Guide*. 1st ed. Oxford: Butterworth-Heinemann, 2007.

[86] Wei, Z., K.P. Dharmasena, H.N.G. Wadley, and A.G. Evans. “Analysis and Interpretation of a Test for Characterizing the Response of Sandwich Panels to

Water Blast.” *International Journal of Impact Engineering* 34, no. 10 (October 2007): 1602–1618.

[87] Deshpande, V, and N Fleck. “One-dimensional Response of Sandwich Plates to Underwater Shock Loading.” *Journal of the Mechanics and Physics of Solids* 53, no. 11 (November 2005): 2347–2383.

[88] Chen, Yong, Z.P. Tong, H.X. Hua, Y. Wang, and H.Y. Gou. “Experimental Investigation on the Dynamic Response of Scaled Ship Model with Rubber Sandwich Coatings Subjected to Underwater Explosion.” *International Journal of Impact Engineering* 36, no. 2 (February 2009): 318–328.

[89] Chen, Yong, ZhiYi Zhang, Yu Wang, and Hongxing Hua. “Crush Dynamics of Square Honeycomb Thin Rubber Wall.” *Thin-Walled Structures* 47, no. 12 (December 2009): 1447–1456.

[90] Schiffer, A., and V. L. Tagarielli. “The Response of Rigid Plates to Blast in Deep Water: Fluid-structure Interaction Experiments.” *Proceedings of the Royal Society A: Mathematical, Physical and Engineering Sciences* 468, no. 2145 (May 9, 2012): 2807–2828.

[91] Dharmasena, Kumar, Doug Queheillalt, Haydn Wadley, Yungchia Chen, Philip Dudt, David Knight, Zhensong Wei, and Anthony Evans. “Dynamic Response of

a Multilayer Prismatic Structure to Impulsive Loads Incident from Water." *International Journal of Impact Engineering* 36, no. 4 (April 2009): 632–643.

[92] Dharmasena, K.P., D.T. Queheillalt, H.N.G. Wadley, P. Dudt, Y. Chen, D. Knight, A.G. Evans, and V.S. Deshpande. "Dynamic Compression of Metallic Sandwich Structures During Planar Impulsive Loading in Water." *European Journal of Mechanics - A/Solids* 29, no. 1 (January 2010): 56–67.

[93] Mori, L.F., S. Lee, Z.Y. Xue, A. Vaziri, D.T. Queheillalt, K.P. Dharmasena, H.N.G. Wadley, J.W. Hutchinson, and H.D. Espinosa. "Deformation and Fracture Modes of Sandwich Structures Subjected to Underwater Impulsive Loads." *Journal of Mechanics of Materials and Structures* 2, no. 10 (2007): 1981–2006.

[94] Mori, L. F., D. T. Queheillalt, H. N. G. Wadley, and H. D. Espinosa. "Deformation and Failure Modes of I-Core Sandwich Structures Subjected to Underwater Impulsive Loads." *Experimental Mechanics* 49, no. 2 (September 4, 2008): 257–275.

[95] McShane, G.J., D.D. Radford, V.S. Deshpande, and N.A. Fleck. "The Response of Clamped Sandwich Plates with Lattice Cores Subjected to Shock Loading." *European Journal of Mechanics - A/Solids* 25, no. 2 (March 2006): 215–229.

[96] Radford, D.D., G.J. McShane, V.S. Deshpande, and N.A. Fleck. "The Response of Clamped Sandwich Plates with Metallic Foam Cores to Simulated Blast

Loading.” *International Journal of Solids and Structures* 43, no. 7–8 (April 2006): 2243–2259.

[97] Luccioni, Bibiana, Daniel Ambrosini, Steeve Chung Kim Yuen, and Gerald Nurick. “Effects of Large and Spread Explosives Loads.” *International Journal of Protective Structures* 1, no. 3 (September 1, 2010): 319–344.

[98] Dharmasena, Kumar P., Haydn N.G. Wadley, Tao Liu, and Vikram S. Deshpande. “The Dynamic Response of Edge Clamped Plates Loaded by Spherically Expanding Sand Shells.” *International Journal of Impact Engineering* 62 (December 2013): 182–195.

[99] Liu, T., N.A. Fleck, H.N.G. Wadley, and V.S. Deshpande. “The Impact of Sand Slugs Against Beams and Plates: Coupled Discrete Particle/finite Element Simulations.” *Journal of the Mechanics and Physics of Solids* 61, no. 8 (August 2013): 1798–1821.

[100] McShane, G.J., V.S. Deshpande, and N.A. Fleck. “A Laboratory-scale Buried Charge Simulator.” *International Journal of Impact Engineering* 62 (December 2013): 210–218.

[101] Evans, A.G., J.W. Hutchinson, N.A. Fleck, M.F. Ashby, and H.N.G. Wadley. “The Topological Design of Multifunctional Cellular Metals.” *Progress in Materials Science* 46, no. 3–4 (January 2001): 309–27.

[102] Tian, J., T.J. Lu, H.P. Hodson, D.T. Queheillalt, and H.N.G. Wadley. "Cross Flow Heat Exchange of Textile Cellular Metal Core Sandwich Panels." *International Journal of Heat and Mass Transfer* 50, no. 13–14 (July 2007): 2521–36.

[103] *Brazing of Aluminum Alloys*. Materials Park, OH: ASM international, 2003.

[104] Fleming, K.M., A. Zhu, and J.R. Scully. "Corrosion of AA6061 Brazed with an Al-Si Alloy: Effects of Si on Metallurgical and Corrosion Behavior." *Corrosion* 68, no. 12 (December 2012): 1126–1145.

[105] Braithwaite, D., 2008, http://www.colemanmw.com. Personal communication.

[106] Hatch, J.E. (editor). *Aluminum: Properties and Physical Metallurgy*. Metals Park, OH: American Society of Metals, 1984.

[107] Chakrabarti, D.J, and David E Laughlin. "Phase Relations and Precipitation in Al–Mg–Si Alloys with Cu Additions." *Progress in Materials Science* 49, no. 3–4 (January 2004): 389–410.

[108] Chen, Weigang. "Experimental and Numerical Study on Bending Collapse of Aluminum Foam-Filled Hat Profiles." *International Journal of Solids and Structures* 38, no. 44–45 (November 2001): 7919–7944.

[109] Hall, I.W., M. Guden, and C.-J Yu. “Crushing of Aluminum Closed Cell Foams: Density and Strain Rate Effects.” *Scripta Materialia* 43, no. 6 (2000): 515–521.

[110] Miyoshi, T., M. Itoh, S. Akiyama, and A. Kitahara. “ALPORAS Aluminum Foam: Production Process, Properties, and Applications.” *Advanced Engineering Materials* 2, no. 4 (April 2000): 179–183.

[111] Hanssen, A G, O S Hopperstad, and M Langseth. “Design of Aluminium Foam-Filled Crash Boxes of Square and Circular Cross-Sections.” *International Journal of Crashworthiness* 6, no. 2 (January 2001): 177–188.

[112] IMPETUS, “IMPETUS Afea Solver®”, 2014, http://www.impetus-afea.com

[113] Cockcroft, M.G., and D.J Latham. “Ductility and Workability of Metals.” *J. Inst. Met.* 96 (1968): 33–39.

[114] Hanssen, A.G., M. Langseth, and O.S. Hopperstad. “Static and Dynamic Crushing of Square Aluminium Extrusions with Aluminium Foam Filler.” *International Journal of Impact Engineering* 24, no. 4 (April 2000): 347–383.

[115] Wierzbicki, T., and W. Abramowicz. “On the Crushing Mechanics of Thin-Walled Structures.” *Journal of Applied Mechanics* 50, no. 4a (1983): 727.

[116] Hopkinson, H. “An Investigation of the Mechanical Properties of Materials at Very High Rates of Loading.” *Proc. Phys. Soc B.* 62, no. 11 (1949): 676–700.

[117] Johnson, W. *Impact Strength of Materials*. London: Edward Arnold, 1972.

[118] Russell, Benjamin, Adam Malcom, Haydn Wadley, and Vikram Deshpande. "Dynamic Compressive Response of Composite Corrugated Cores." *Journal of Mechanics of Materials and Structures* 5, no. 3 (October 15, 2010): 477–493.

[119] Hanssen, A.G., and L. Olovsson. *Impetus-AFEA*. Flekkefjord, Norway: IMPETUS-AFEA, n.d. http://www.impetus-afea.com/.

[120] Zok, F. W., H. Rathbun, M. He, E. Ferri, C. Mercer, R. M. McMeeking, and A. G. Evans. "Structural Performance of Metallic Sandwich Panels with Square Honeycomb Cores." *Philosophical Magazine* 85, no. 26–27 (September 11, 2005): 3207–3234.

[121] Radford, D. D., G. J. McShane, V. S. Deshpande, and N. A. Fleck. "Dynamic Compressive Response of Stainless-Steel Square Honeycombs." *Journal of Applied Mechanics* 74, no. 4 (2007): 658.

[122] Fyllingen, ø., O.S. Hopperstad, A.G. Hanssen, and M. Langseth. "Modeling of Tubes Subjected to Axial Crushing." *Thin-Walled Structures* 48, no. 2 (February 2010): 134–142.

[123] Holloman, Ryan L., Vikram Deshpande, Arve G. Hanssen, Katherine M. Fleming, John R. Scully, and Haydn N. G. Wadley. "Tubular Aluminum Cellular

Structures: Fabrication and Mechanical Response." *Journal of Mechanics of Materials and Structures* 8, no. 1 (2013): 65–94.

[124] Jaspers, S.P.F.C, and J.H Dautzenberg. "Material Behaviour in Conditions Similar to Metal Cutting: Flow Stress in the Primary Shear Zone." *Journal of Materials Processing Technology* 122, no. 2–3 (March 2002): 322–330.

[125] Wadley, H.N.G., T. Børvik, L. Olovsson, J.J. Wetzel, K.P. Dharmasena, O.S. Hopperstad, V.S. Deshpande, and J.W. Hutchinson. "Deformation and Fracture of Impulsively Loaded Sandwich Panels." *Journal of the Mechanics and Physics of Solids* 61, no. 2 (February 2013): 674–699.

[126] Johnson, G.R., and W.H. Cook. "A Constitutive Model and Data for Metals Subjected to Large Strains, High Strain Rates and High Temperatures." In *Proceedings of the 7th International Symposium on Ballistics*, 541–547. The Hague, The Netherlands, 1983.

[127] Børvik, T., A.G. Hanssen, M. Langseth, and L. Olovsson. "Response of Structures to Planar Blast Loads – A Finite Element Engineering Approach." *Computers & Structures* 87, no. 9–10 (May 2009): 507–20.

[128] Wadley, H.N.G., T. Børvik, L. Olovsson, J.J. Wetzel, K.P. Dharmasena, O.S. Hopperstad, V.S. Deshpande, and J.W. Hutchinson. "Deformation and Fracture of

Impulsively Loaded Sandwich Panels." *Journal of the Mechanics and Physics of Solids* 61, no. 2 (February 2013): 674–699.

[129] Maxwell, J.C. "Illustrations of the Dynamical Theory of Gases." *Philosophical Magazine* 19 (1860): 19–32.

[130] Deshpande, V.S., R.M. McMeeking, H.N.G. Wadley, and A.G. Evans. "Constitutive Model for Predicting Dynamic Interactions between Soil Ejecta and Structural Panels." *Journal of the Mechanics and Physics of Solids* 57, no. 8 (August 2009): 1139–64.

[131] Johnson, G.R., and W.H. Cook. "A Constitutive Model and Data for Metals Subjected to Large Strains, High Strain Rates and High Temperatures." In *Proceedings of the 7th International Symposium on Ballistics*, 541–547. The Hague, The Netherlands, 1983.

[132] Cockcroft, M.G., and D.J Latham. "Ductility and the Workability of Metal." *J. Inst. Metals* 1 (1996): 33–39.

[133] Hanssen, A.G., M. Langseth, and O.S. Hopperstad. "Static Crushing of Square Aluminium Extrusions with Aluminium Foam Filler." *International Journal of Mechanical Sciences* 41, no. 8 (August 1999): 967–93.

[134] Hanssen, A.G., M. Langseth, and O.S. Hopperstad. “Static and Dynamic Crushing of Circular Aluminium Extrusions with Aluminium Foam Filler.” *International Journal of Impact Engineering* 24, no. 5 (May 2000): 475–507.

[135] Jones, Norman. *Structural Impact*. 2nd ed. New York: Cambridge University Press, 2012.

[136] Bourbié, Thierry. *Acoustics of Porous Media*. Paris: Editions Technip, 1987.